A Numerical Model of an Active Magnetic Regenerator Refrigerator with Experimental Validation

by

Kurt Engelbrecht

A dissertation submitted in partial fulfillment of the requirements for the degree of

Doctor of Philosophy

(Mechanical Engineering)

at the

UNIVERSITY OF WISCONSIN-MADISON

2008

Abstract

Active magnetic regenerative refrigeration (AMRR) systems represent an environmentally attractive alternative to vapor compression systems that do not use a fluorocarbon working fluid. A one-dimensional transient numerical model that solves the governing energy equations of an AMRR has been developed. The governing equations are solved by starting from an initial temperature distribution and stepping the model forward in time until cyclical steady state has been achieved, and using the results to calculate cooling power and total input power to the system. This thesis describes the numerical model and details how it was verified numerically and experimentally. The model was verified in the limit of a passive regenerator against an analytic solution and was verified experimentally against data taken on a prototype AMRR system. The model was also used to analyze transient operation of a practical AMRR system and was used to evaluate different methods of controlling an AMRR system.

Acknowledgements

Most importantly, I would like to thank my advisors Greg Nellis and Sanford Klein for their guidance on this project and for their overall contributions to my education. I would also like to thank Doug Reindl, John Pfotenhauer, Christopher Rutland, and Daniel Klingenberg for being on my committee and for their technical assistance.

I would like to thank my father Martin for his continuing encouragement and my mother Susan for her support and thanks to my sisters Sarah, Claire, and Rosie for always being there for me. I would also like to thank my grandparents for their continued love and support.

Astronautics has provided experimental data and technical support that helped make this thesis possible. I would like to thank Steve Russek, Andre Boeder, Jeremy Chell, Carl Zimm and Alexander Sternberg for their contributions to this work. I would also like to thank Takenori Numazawa and Koji Kamiya from Tsukuba Magnet Laboratory for their help. Thanks to Nini Pryds, Thomas Petersen, Britt Hansen, Inge Biering, Stinus Jeppesen, and Christian Bahl for the opportunity to compare our numerical models and for their help. I would like to thank Steve Meitner for his help in the lab, Mike Frischmann and Jeff Laundre for the work on this project and Harrison Skye and Ryan Taylor for their technical assistance.

Finally, I would like to thank Astronautics, the American Society of Heating Refrigeration and Air-conditioning Engineers, and the UW-Madison mechanical engineering department for their financial support.

Table of contents

Abstract ..... **i**
Acknowledgements ..... **ii**
Table of contents ..... **iii**
List of Figures ..... **v**
List of Tables ..... **x**
Nomenclature ..... **xi**
1 Introduction **1**
1.1 Thermodynamics of the AMRR System 1
1.2 Magnetic Cooling System Configurations 6
1.2.1 Adiabatic Demagnetization Refrigerators 6
1.2.2 Active Magnetic Regenerative Refrigerators 7
1.3 Developments in Magnetocaloric Materials 9
1.3.1 Gadolinium and Its Alloys 13
1.3.2 $Gd_5Si_{4-x}Ge_x$ 15
1.3.3 $LaFe_{13-x}Si_xH_y$ 16
1.3.4 $MnAs_{1-x}Sb_x$ 17
1.3.5 MnFeP Materials 18
1.3.6 Other Materials 19
1.4 Developments in Magnetocaloric Materials 20
1.4.1 University of Victoria Prototype 24
1.4.2 Chubu Electric and Toshiba Device 25
1.4.3 Astronautics Reciprocating and Rotary Prototypes 25
1.4.4 Nanjing University Device 27
1.4.5 Institute of Technology and Chubu Rotary Device 28
1.4.6 Other Systems 29
1.5 Practical AMRR Issues 30
1.6 AMRR Modeling Work Outside of UW-Madison 34
1.6.1 Zero-Period AMR Models 34
1.6.2 Time Dependent AMRR Models 35
1.6.3 Zero-Period AMR Models 35
1.7 Research Objectives 36
2 Numerical Model Description **39**
2.1 Governing Equations 39
2.2 Numerical Solution Algorithm 52
2.3 Model Verification 53
2.3.1 Validation of the Magnetic Work Interaction 60
2.4 Magnetocaloric Material Properties 62
2.4.1 Interpolation of Empirical Data 63
2.4.2 Mean Field Model of the Magnetocaloric Effect 65
2.4.3 Curve Fitting Specific Heat Curves 70
2.5 Heat Transfer Fluid Properties 73
2.6 Regenerator Correlations 77
2.6.1 Packed Sphere Regenerator Correlations 77

2.6.2 Parallel Plate Regenerator Correlations 80
2.7 Correction for Internal Temperature Gradients in a packed sphere regenerator .. 83
2.7.1 Governing Equations for the Internal Temperature Gradient Study..... 84
2.7.2 Numerical Solution for the Internal Temperature Gradient Model 89
2.7.3 Verification of Internal Temperature Gradients Model 90
2.7.4 Results for a Passive Regenerator 92
2.7.5 Temperature Gradient Results for an Active Magnetic Regenerator..... 101
2.8 Correction for Internal Temperature Gradients in a Parallel Plate regenerator .. 105
3 Active Magnetic Regenerative Refrigeration System Modeling Results..... 109
3.1 Modeling Transient AMRR Operation 109
3.2 Part Load Performance 116
3.3 Comparison to a 2D Numerical AMRR Model 122
3.3.1 Cycle Characteristics for the Model Comparison 122
3.3.2 2D Model Description and Governing Equations..... 125
3.3.3 Model Comparison Results..... 128
4 Description of Passive Regenerator Experiment and Experimental Results..... 138
4.1 Experiment Design..... 138
4.2 Experimental Measurements..... 145
4.3 Modifications to the Numerical AMRR Model for Single Blow Data Analysis 151
4.4 Experimental Data Analysis 152
4.5 Experimental Data Analysis for Individual Regenerator Pucks 163
4.5.1 Reynolds Number and Prandtl Number Used for the Nusselt Number .....
Correlation 167
4.6 Experimental Results 170
4.6.1 Fitting Curve Fitting of Experimental Measurements 177
4.6.2 Testing the Effects of Heat Transfer to the Outer Shell..... 181
5 Modeling the Astronautics Rotary AMRR Prototype 187
5.1 Description of the Experimental Apparatus..... 187
5.2 Prototype AMRR Modeling Parameters..... 191
5.2.1 Thermal Capacity of the AMRR Housing 195
5.3 Prototype Experimental Runs 198
5.4 Initial Model Predictions Compared to Experimental Results 199
5.5 Improving Model Agreement with Experimental Results 202
5.6 Modeling and Experimental Uncertainty..... 212
5.6.1 Experimental Uncertainty 212
5.6.2 Modeling Uncertainty 212
5.7 Modeling Results Using the New Nusselt Number Correlation..... 215
6 Conclusions 220
6.1 Suggestion for Future Work 222
References..... 224
Appendix A1..... 233
Appendix A2..... 253
Appendix A3..... 265

List of Figures

Figure 1.1 Temperature-entropy diagram for $Gd_{0.94}Er_{0.06}$ with lines of constant applied magnetic field shown 4

Figure 1.2 Adiabatic temperature change with magnetization for $Gd_{0.94}Er_{0.06}$ 5

Figure 1.3 Temperature-entropy diagram for a one-shot refrigeration cycle 7

Figure 1.4 Conceptual drawing showing the processes that make up rotary AMRR system, (a) magnetization, (b) cold to hot flow, (c) demagnetization, and (d) hot to cold flow. 9

Figure 1.5 Schematic of the University of Victoria reciprocating AMRR device: (1) fluid displacer, (2) hot heat exchanger, (3) AMR, (4) cold heat exchanger, (5) magnet (Rowe et al., 2006) 21

Figure 2.1 Conceptual drawing of a 1D AMR model showing the important modeling parameters 40

Figure 2.2 Differential segment of entrained fluid with energy terms indicated 43

Figure 2.3 Differential segment of regenerator with energy terms indicated 45

Figure 2.4 Numerical grid used for fluid and regenerator temperature solutions 48

Figure 2.5 Fluid temperature predicted by the AMRR model and Schumann solution for the conditions in Table 2.1 56

Figure 2.6 Mass flow rate variation for an idealized regenerator 57

Figure 2.7 Numerical model predictions and published results for ε_t as a function of *NTU* and various values of *U* in the ideal regenerator limit 59

Figure 2.8 Numerical model predictions and published results from Figure 2.7 in the region $\varepsilon_t > 0.9$ 60

Figure 2.9 Adiabatic temperature change of gadolinium vs. temperature when magnetized from 0 to 1 Tesla determined from AMRR model and property values 61

Figure 2.10 Isothermal entropy change of pure gadolinium when magnetized from 0 to 1.5 Tesla predicted by the mean field model and based on experimental data. 69

Figure 2.11 Plot of heat capacity vs. temperature with the lattice and magnetic portions indicated. 71

Figure 2.12 Actual and Curve Fit Data for k_f vs. T/T_{ref} 75

Figure 2.13 Specific heat as a function of temperature for some possible working fluids 76

Figure 2.14 Schematic of a simple parallel plate regenerator with characteristic dimensions shown. 80

Figure 2.15 Reduced temperature as a function of reduced time for various values of reduced radius with $Bi = 2.5$ and $Fo = 0.25$. 91

Figure 2.16 Total efficiency as a function of *Fo Bi* for various values of *Fo*. Also shown is the efficiency in the limit of infinite thermal conductivity. 95

Figure 2.17 Reduced temperature as a function of $\tilde{r}$ for various values of $\tilde{t}$ for *Fo* = 0.1 and *Fo Bi* = 1.0. Note that the cycle time is insufficient to allow the entire sphere to participate in the energy storage process and so only the outer edge temperature is affected by the fluid. 95

Figure 2.18 Efficiency predicted by the numerical model and using lumped capacitance model corrected with the Jeffreson and Hausen degradation factor. Efficiency is shown as a function of the product of the Biot and Fourier number for various values of the Fourier number. 98

Figure 2.19 Degradation factor predicted by the numerical model as a function of the product of the Biot and Fourier number for various values of the Fourier number. 100

Figure 2.20 Total efficiency computed using the corrected degradation factor presented in Eqs. (2.128) and (2.129) and predicted by the numerical model as a function of the product of the Biot and Fourier number for various values of the Fourier number. 101

Figure 2.21 Reduced temperature as a function of reduced time for various values of reduced radius for a sphere with (a) *Bi* = 0.2, *Fo* = 5.0, (b) *Bi* = 5.0, *Fo* = 5.0, and (c) *Bi* = 5.0, *Fo* = 0.2. 103

Figure 2.22 Total efficiency for the active and passive processes as a function of the product of the Biot and Fourier number for various values of the Fourier number. Note that the behavior of these processes is identical when normalized in this manner. 105

Figure 3.1 Schematic of heat exchanger modeled in transient operation 110

Figure 3.2 Refrigeration capacity of a system started from a uniform temperature of 300 K 114

Figure 3.3 Reservoir temperature as a function of time for the system that is shut off and restarted 115

Figure 3.4 *COP* as a function of cooling power for various values of cycle time and fluid mass flow rate 118

Figure 3.5 Optimum fluid flow rate and cycle time as a function of refrigeration capacity 120

Figure 3.6 Fluid flow rate and cycle time corresponding to the optimum control strategy shown in Fig. 3.5 for a desired cooling power 121

Figure 3.7 Schematic of regenerator geometry used for the 1D and 2D model comparison 123

Figure 3.8 Profile of (a) mass flow rate as a function of time and (b) magnetic field as a function of time for the model comparison 124

Figure 3.9 Predicted adiabatic temperature change using the 1D model compared to the adiabatic change from Gd material properties 127

Figure 3.10	Predicted refrigeration capacity of the 1D and 2D models as a function of regenerator plate thickness	129
Figure 3.11	Predicted heat rejection to ambient of the 1D and 2D models as a function of regenerator plate thickness	129
Figure 3.12	Predicted magnetic work input of the 1D and 2D models as a function of regenerator plate thickness	131
Figure 3.13	Predicted COP of the 1D and 2D models as a function of regenerator plate thickness	131
Figure 3.14	Average temperature gradient in (a) the regenerator and (b) the heat transfer fluid	133
Figure 3.15	Fluid temperature as a function of regenerator location (a) before the cold blow and (b) before the hot blow for a 0.1 mm plate thickness and 0.05 mm flow channel height	134
Figure 3.16	Fluid temperature as a function of regenerator location (a) before the cold blow and (b) before the hot blow for a 3 mm plate thickness and 1.5 mm flow channel height	136
Figure 4.1	Flow schematic of the single blow passive regenerator test stand	139
Figure 4.2	Photograph of the single blow experimental apparatus	141
Figure 4.3	Photograph of the manual three-way valves and solenoid valve mounted near the inlet of the regenerator	144
Figure 4.4	Single blow experimental volumetric flow rate as a function of time	147
Figure 4.5	Schematic of temperature sensors in the regenerator test section	148
Figure 4.6	Schematic of temperature sensors in the regenerator test section	149
Figure 4.7	Experimental inlet and outlet temperature profiles for both pure water and a mixture of 20% propylene glycol and water at a flow rate of 2 L/min.	150
Figure 4.8	Nusselt number as a function of Reynolds number for a regenerator with a porosity of 0.36	154
Figure 4.9	Root mean squared error between the predicted and measured temperature profile for the single blow regenerator experiment for water at a 1 L/min flow rate when the entire regenerator is considered.	156
Figure 4.10	Experimental inlet and outlet temperatures as a function of time as well as the best-fit predicted outlet temperature when all seven regenerator pucks are considered	157
Figure 4.11	Temperature in the regenerator after a long flow time. The temperature drop across the regenerator is an indicator of the heat loss to the room.	158
Figure 4.12	Drawing of the single blow regenerator test section showing the regenerator puck construction and flow area between pucks	159
Figure 4.13	Root mean squared error between the predicted and measured temperature profile for the single blow regenerator experiment for water at a 1 L/min flow rate when the only puck 1 in the regenerator is considered.	161

Figure 4.14 Experimental inlet and outlet temperatures as a function of time as well as the best-fit predicted outlet temperature when only puck 1 is considered 162
Figure 4.15 Nusselt number predicted by the numerical model for 1 L/min flow rate of water as a function of number of time steps. Also shown is the Richardson extrapolation curve. 165
Figure 4.16 Nusselt number predicted by the numerical model for 1 L/min flow rate of water as a function of number of the number of spatial steps 167
Figure 4.17 Reynolds number calculated by the model for a 1 L/min flow of water for puck 1 in the regenerator. 168
Figure 4.18 Prandtl number calculated by the model for a 1 L/min flow of water for puck 1 in the regenerator. 169
Figure 4.19 Measured Nusselt number for each regenerator puck for water at a flow rate of 1 L/min. Also shown is the average Nusselt number for the seven regenerator pucks. 170
Figure 4.20 Measured average Nusselt number and uncertainty for four repeated experiments using a 40% propylene glycol and water mixture with a flow rate of 3 L/min 172
Figure 4.21 Measured average Nusselt number as a function of Reynolds number for experiments using water as a heat transfer fluid 173
Figure 4.22 Measured average Nusselt number as a function of Reynolds number and Prandtl number for experiments using water as a heat transfer fluid 174
Figure 4.23 Measured average Nusselt number as a function of Reynolds number and Prandtl number for experiments using a mixture of 20% propylene glycol and water as a heat transfer fluid 175
Figure 4.24 Measured average Nusselt number as a function of Reynolds number for experiments using 30% propylene glycol and water as a heat transfer fluid 176
Figure 4.25 Measured average Nusselt number as a function of Reynolds number for experiments using 40% propylene glycol and water as a heat transfer fluid 177
Figure 4.26 Nusselt number as a function of Reynolds number for a Prandtl number of 6.8 and a regenerator with a porosity of 0.36 178
Figure 4.27 Nusselt number as a function of Reynolds number for a Prandtl number of 30 and a regenerator with a porosity of 0.36 179
Figure 4.28 Nusselt number predicted by Eq. (4.9) as a function of measured Nusselt number. Also shown is a line indicating a perfect curve fit and lines indicating ±20% of the measured values. 180
Figure 4.29 Measured Nusselt number for a hot soaked regenerator (experiments 1 and 2) and for a cold soaked regenerator (experiments 3 and 4) 182
Figure 4.30 Measured Nusselt number when the PVC outer shell is heated (experiments 1 and 2) and when the outer shell is not heated (experiment 3). Also shown is the prediction from the new Nusselt number correlation. 184

Figure 4.31 Measured Nusselt number when the PVC outer shell is heated (experiments 1 and 2) and when the outer shell is not heated (experiment 3) 185
Figure 5.1 Rotary AMRR experiment at Astronautics 188
Figure 5.2 Part drawing of the regenerator wheel used in the prototype device (all dimensions in mm) 189
Figure 5.3 Test schematic of the rotary AMRR apparatus at Astronautics 190
Figure 5.4 Form of the mass flow rate and magnetic field functions as a function of dimensionless time for a bed that is magnetized from the cold end ($x=L$) to the hot end. Positive mass flow is defined as flow from the hot reservoir to the cold reservoir. 194
Figure 5.5 Ratio of the thermal capacity of the regenerator housing to the thermal capacity of the regenerator material as a function of cycle time 196
Figure 5.6 Predicted cooling power vs. experimental cooling power for a range of operating conditions. Also shown is a line indicating a perfect prediction 200
Figure 5.7 Predicted cooling power for a type 1 and type 2 bed vs. measured cooling power for a range of operating conditions 201
Figure 5.8 Experimental and predicted cooling power for a regenerator rotation rate of 120 rev/min, T_H = 298 K 202
Figure 5.9 Predicted cooling power for cases 1-4 when the maximum magnetic field is varied. Also shown are the experimental cooling powers for each case 209
Figure 5.10 *RMSE* of the predicted cooling power for a range of maximum for varying maximum magnetic field used by the model 210
Figure 5.11 Predicted cooling power vs. experimental cooling power using a maximum effective magnetic field of 1.2 Tesla. Also shown is a line indicating a perfect prediction 211
Figure 5.12 Predicted cooling power vs. experimental cooling power using the Nusselt number developed in Chapter 4 and a maximum effective magnetic field of 1.2 Tesla. Also shown is a line indicating a perfect prediction 216
Figure 5.13 Modeling results from Fig. 5.12 with error bars shown. 217
Figure 5.14 Difference between the predicted and measured cooling power as a function of operating temperature span 218

List of Tables

Table 1.1 Summary of properties of selected magnetocaloric materials 13
Table 1.2 Summary of experimental performance of recently built AMRR systems 23
Table 2.1 Parameters used for model comparison with the Schumann solution. 55
Table 2.2 Inputs used in the mean field magnetic model to calculate the material properties of pure gadolinium 68
Table 2.3 Coefficients of property functions for water 74
Table 3.1 Calculated system heat capacities 112
Table 3.2 System parameters used for transient study 113
Table 3.3 Parameters used for space cooling part load performance. 117
Table 3.4 Modeling parameters used to compare the 1D model described in this thesis to a 2D model developed by Petersen et al. (2007) 123
Table 4.1 Experimental equipment list 140
Table 4.2 Experimental operating conditions for the single blow regenerator 146
Table 4.3 Properties of the regenerator housing 160
Table 5.1 Experimentally measured and controlled parameters for experimental data provided by Astronautics 190
Table 5.2 Modeling parameters used to simulate the rotary AMRR device at Astronautics 192
Table 5.3 Properties of the AMRR regenerator housing 195
Table 5.4 Summary of experimental data sets 198
Table 5.5 Summary of the representative data sets chosen to study the effects of modeling parameters on predicted values 203
Table 5.6 Loss of cooling power compared to a perfect regenerator due to regenerator losses for the representative experimental runs 204
Table 5.7 Predicted cooling power for a normal system from Table 5.5 compared to the predicted cooling power for a regenerator with a Nusselt number scaling factor of 0.5 205
Table 5.8 Predicted cooling power for a system with a 12.5% flow compared to the predicted cooling power for a system with a 50% flow ramp 213
Table 5.9 Predicted cooling power for a system with a 5% flow unbalance and the predicted cooling power for a system with no flow unbalance 214

Nomenclature

A_c	cross-sectional area (m^2)
a_s	specific surface area (m^2/m^3)
b	half thickness of a plate in a parallel plate regenerator (m)
Bi	Biot number
B_J	Brillouin function
c	specific heat capacity (J/kg-K)
$c_{\mu_o H}$	specific heat capacity at constant magnetic field (J/kg-K)
CFL	characteristic fluid length
DF	heat transfer degradation factor
D_y	plate thickness in a parallel plate regenerator (m)
d_h	hydraulic diameter (m)
d_p	particle diameter in a packed sphere or crushed particle regenerator (m)
f	friction factor
Fo	Fourier number
k	thermal conductivity (W/m-K)
k_{eff}	effective static thermal conductivity of regenerator and fluid (W/m-K)
k_{disp}	thermal conductivity of the fluid due to axial dispersion (W/m-K)
$\dot{g}'''$	volumetric heat generation (W/m^3)
h	heat transfer coefficient (W/m^2-K) or enthalpy (J/kg-K)
h^*	modified heat transfer coefficient (W/m^2-K)
h_V	volumetric heat transfer coefficient (W/m^3-K)
i	spatial subscript
j	temporal subscript
L	length (m)
m	mass (kg)
$\dot{m}$	mass flow rate (kg/s)
M	magnetic intensity (A/m)
Nt	number of steps used in numerical solution
Nx	number of axial control volumes used in numerical solution
NTU	number of transfer units
Nu	Nusselt number
p	pressure (Pa)
Pe	Peclet number
Pr	Prandtl number
P_x	distance between plates in a parallel plate regenerator (m)
$\dot{q}''$	heat flux (W/m^2)
$\bar{\dot{q}}$	average heat transfer rate (W)
Re	Reynolds number
s	entropy (J/kg-K)
t	time (s)

tol	relaxation tolerance (K)
T	temperature (K)
T_{Curie}	Curie temperature (K)
u	specific internal energy (J/kg)
U	internal energy (J) or utilization factor
v	specific volume (m^3/kg)
W	work (J)
x	axial position (m)
y	parameter used in the Schumann solution
z	parameter used in the Schumann solution

Greek

ε	porosity of the regenerator bed
ε_t	thermal effectiveness
μ	viscosity (N-s/m^2) or magnetic permeability (H/m)
$\mu_o H$	applied field (Tesla)
ρ	density (kg/m^3)
σ	standard deviation
τ	cycle duration (s)

Subscripts

eff	effective
el	electron
C	cold or refrigeration temperature
f	fluid
H	hot or heat rejection temperature
lat	lattice
mag	magnetic
max	maximum
r	regenerator material
ref	reference
s	surface

Chapter 1 Introduction

Active magnetic regenerative refrigeration (AMRR) systems represent an attractive alternative to vapor compression refrigeration and air-conditioning systems. AMRR systems do not use a fluorocarbon working fluid; instead, a solid refrigerant is used. The solid refrigerant, a magnetocaloric material, communicates with the environment via a heat transfer fluid. Because the solid refrigerant has essentially zero vapor pressure, AMRR systems have no Ozone Depletion Potential (ODP) and no direct Global Warming Potential (GWP). The heat transfer fluid will likely be aqueous and will therefore have minimal environmental impact. In theory, a well-designed AMRR system can be competitive with or even more efficient than vapor compression systems, provided that the volume of the active magnetic regenerator is sufficiently large.

1.1 THE THERMODYNAMICS OF THE AMRR CYCLE

Magnetic refrigeration is driven by the magnetocaloric effect, which is a change in entropy of a material with magnetization. The temperature and magnetic field of a magnetocaloric material are highly coupled over certain, typically limited, operating ranges; this characteristic allows them to be used within energy conversion systems. The magnetocaloric effect is maximized at the Curie temperature where a material changes from a ferromagnetic to a paramagnetic state. There are two types of magnetic phase changes that may occur at the Curie point, first order magnetic transition (FOMT) and second order magnetic transition (SOMT). For SOMT materials, the magnetic moments of the material become aligned during the transformation from a ferromagnet to a paramagnet. There is no discontinuous jump in magnetization and no latent

heat at the transition associated with the transition. FOMT materials experience a simultaneous ordering of magnetic dipoles and a latent heat associated with the transition. Some FOMT materials experience a change in the crystal sub-lattice associated with the phase change at the Curie point. According to Gschneidner et al. (2005), the temperature change for SOMT materials upon magnetization is almost instantaneous (on the order of nanoseconds). However, for FOMT materials that experience a change in structure, atoms are displaced during the change in crystal structure and therefore the time required to achieve a temperature change when magnetizing some FOMT materials can be many orders of magnitude larger than the time-scale associated with SOMT materials. According to Gschneidner et al. (2005), SOMT materials generally exhibit very low hysteresis (where material properties are dependent on the history of the magnetic field), but FOMT materials can exhibit significant hysteresis.

A thermodynamic substance can change its internal energy (U) as a result of either work or heat, leading to the differential energy balance:

$$dU = T\,dS + dW \tag{1}$$

The 1st term in Eq. (1) corresponds to an inflow of heat ($T\,dS$) and the 2nd to an inflow of work (dW). In general, work can flow in many forms (e.g., mechanical, electrical, etc.). The familiar fundamental property relationships that describe most fluids result when only volumetric compression work (P-V) is considered; however, for magnetocaloric materials, the integral of the applied field ($\mu_o H$) and magnetic moment (M) form the work term in Eq. (1). This is appropriate provided that magnetic hysteresis effects are ignored (Guggenheim, 1967) .

$$dU = T\,dS + \mu_o H\,dM \tag{2}$$

Increasing the applied field for magnetic materials tends to align the magnetic dipoles, which requires work and reduces entropy. Using this relationship between entropy, internal energy, and magnetic field, it becomes possible to apply all of the typical thermodynamic results and identities that are ordinarily used in the context of a pure compressible substance to a magnetocaloric material. For example, Maxwell's relations (Guggenheim, 1967) can be used to describe relationships between the partial derivatives of properties and a magnetocaloric material will be characterized by an equation of state that describes the magnetization as a function of temperature and applied field. A temperature-entropy diagram for a magnetic material will include lines of constant applied magnetic field rather than isobars; however, the diagram is otherwise analogous to a more familiar T-s diagram characterizing a compressible working fluid. For example, Figure 1.1 illustrates the temperature-entropy diagram for $Gd_{0.94}Er_{0.06}$ (Zimm and Gschneidner, 2003).

.

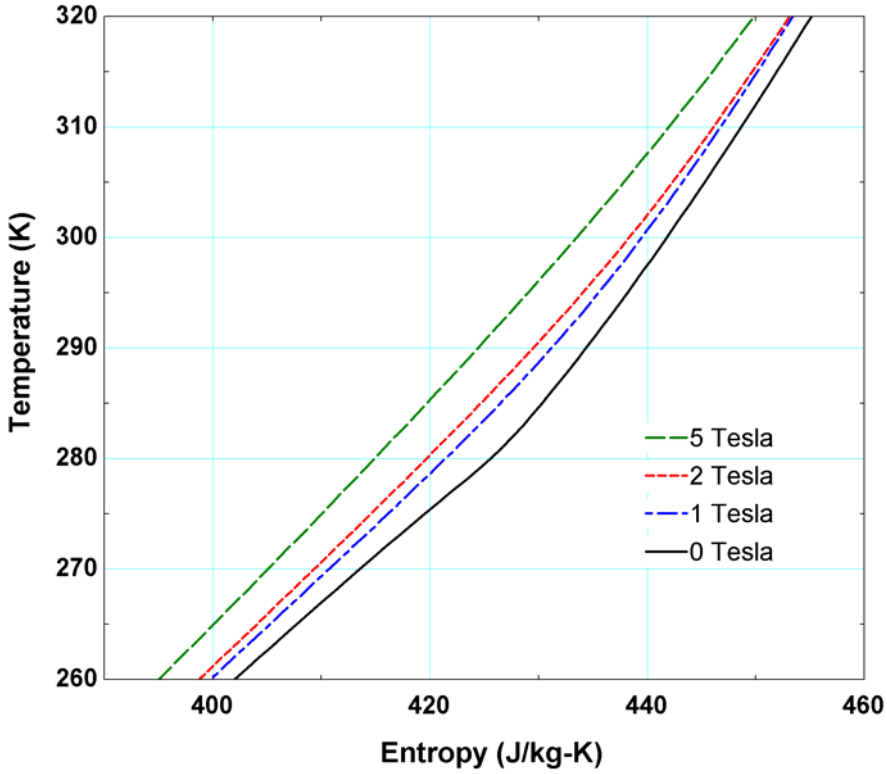

Figure 1.1. Temperature-entropy diagram for $Gd_{0.94}Er_{0.06}$ with lines of constant applied magnetic field shown.

Closer examination of Figure 1.1 reveals that it is possible to change the temperature of a magnetic material in an adiabatic process by changing the applied magnetic field. Figure 1.2 illustrates the adiabatic temperature change of an alloy of 94% Gadolinium and 6% Erbium, $Gd_{0.94}Er_{0.06}$, when the magnetic field is increased from 0 Tesla to 2 Tesla and from 0 Tesla to 5 Tesla. Figure 1.2 shows that the adiabatic temperature change (which is a direct indicator of the magnetocaloric effect) depends on the initial temperature of the material, notice that a large magnetocaloric effect is only exhibited for a relatively limited temperature span. In a material such as $Gd_{0.94}Er_{0.06}$ that exhibits a second order phase transition above the magnetic ordering temperature, magnetic hysteresis is negligible. In this case, adiabatic magnetization and

demagnetization are isentropic processes; therefore, when the material is subsequently demagnetized, its temperature will return to its original, zero-field value.

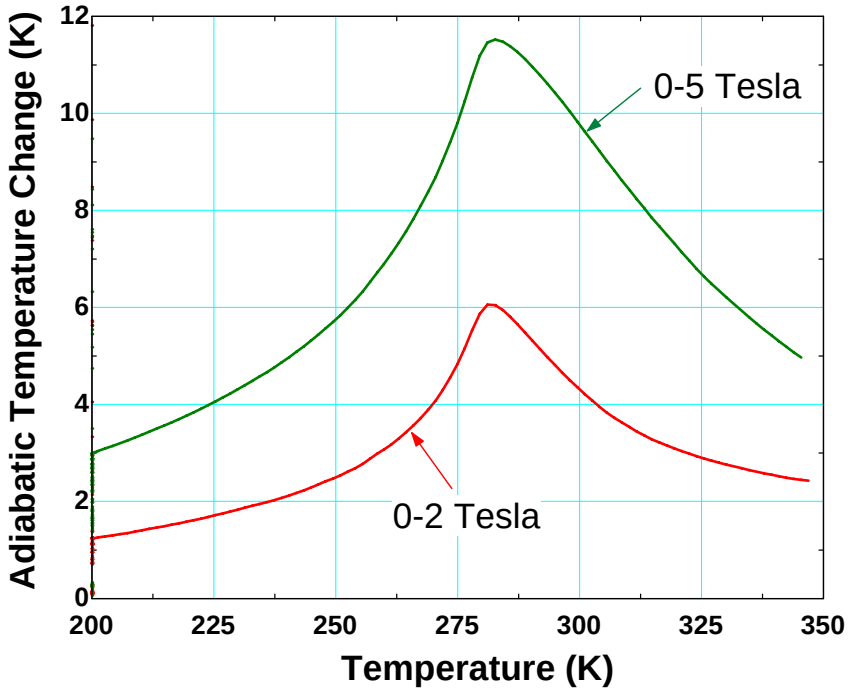

Figure 1.2. Adiabatic temperature change with magnetization for $Gd_{0.94}Er_{0.06}$

Figure 1.2 reveals several details that are relevant to practical AMRR systems. First, the adiabatic temperature change is relatively small compared to the temperature span required for most practical cooling systems. This characteristic necessitates the use of a regenerative cycle in order to provide a cooling load over a useful temperature span. Second, the magnetocaloric effect is largest over a relatively narrow temperature range. In order to maximize the magnetocaloric effect and therefore the performance of the AMRR system, it is desirable to

construct a regenerator bed from several materials which have Curie temperatures that are tailored to match the local operating temperature.

1.2 MAGNETIC COOLING SYSTEM CONFIGURATIONS

1.2.1 Adiabatic Demagnetization Refrigerators

Early magnetic coolers were used to achieve extreme cryogenic temperatures; these devices used an adiabatic demagnetization refrigeration (ADR), or "one-shot," cycle. Giauque and MacDougall (1933) used an ADR system to reach temperatures below 1 K, breaking the temperature barrier that had previously been imposed by the properties of cryogenic fluids. The ADR system that they and other researchers used consisted of a solid piece of magnetocaloric alloy and utilized an isothermal magnetization, in which the material is placed into contact with a hot reservoir, followed by an adiabatic demagnetization. All of the material in an ADR cycle undergoes the same thermodynamic cycle and therefore the temperature lift is limited to the adiabatic magnetization temperature change exhibited by the material. Figure 1.3 shows a one-shot refrigeration cycle on a T-s diagram. ADR cycles also require complex heat switches with limited heat flux capacities. For these reasons, the ADR cycle is not a practical alternative for near room temperature, commercial devices.

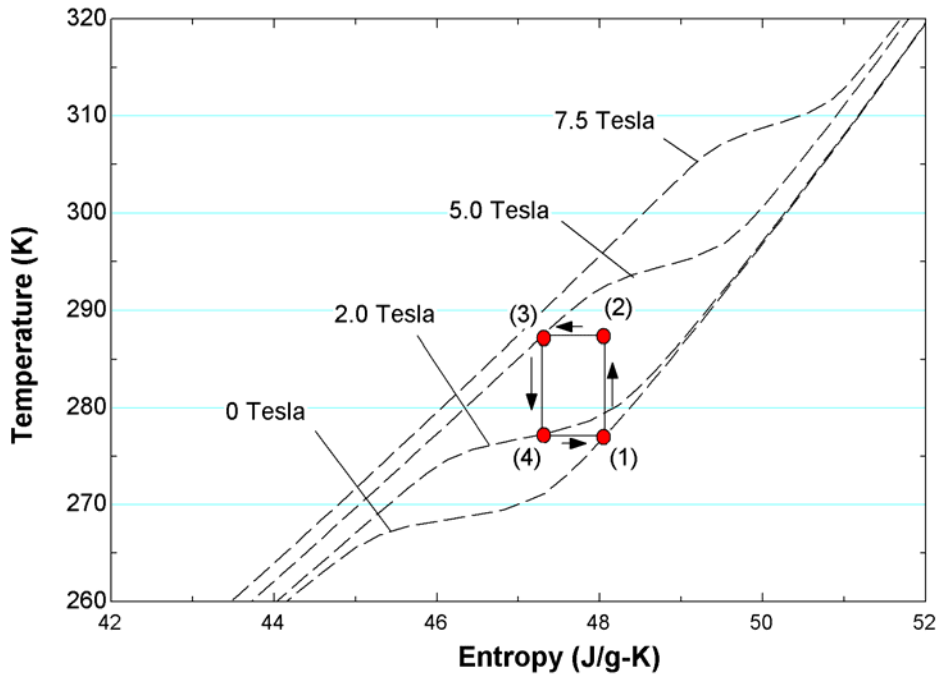

Figure 1.3. Temperature-entropy diagram for a one-shot refrigeration cycle

1.2.2 Active Magnetic Regenerative Refrigerators

The technical barriers associated with the ADR cycle have been overcome by the use of a regenerator within the active magnetic regenerative refrigeration (AMRR) cycle. Brown (1976) first constructed a regenerative magnetic refrigerator and demonstrated that the use of a regenerative configuration can provide a no-load temperature span that is much greater than the adiabatic temperature change of the magnetocaloric material that is used to construct the regenerator. The device described by Brown used a stationary fluid column with a moving regenerator. Green et al (1986) constructed the first successful AMRR using a bed subjected to a fluid flow and achieved a 40 K temperature span. In an AMRR system, a porous bed of magnetic material is exposed to a time-varying magnetic field and a time-varying flow of heat transfer fluid. Each segment of the bed undergoes a unique refrigeration cycle and interacts with

the adjacent material via the heat transfer fluid. The net result of these cascaded refrigeration cycles is a temperature lift that is much larger than can be achieved by an ADR cycle.

The AMRR cycle consists of four processes. A conceptual drawing illustrating the processes that make up the operation of a rotary AMRR, such as is described by Zimm et al. (2006), is shown in Figure 1.4. A regenerator consisting of six individual beds is discussed here; one of the six beds is highlighted in Figure 1.4 and is considered in the following discussion. The bed is magnetized by rotating it into the field of a permanent magnet, Figure 1.4(a). The magnetocaloric effect causes the material in the bed to increase in temperature when it is magnetized. While the bed is in the magnetic field, it experiences a flow of heat transfer fluid from its cold end to its hot end; this flow causes a heat rejection in the hot heat exchanger, Figure 1.4(b), because the temperature of the fluid leaving the hot end is hotter than the ambient temperature. The bed is demagnetized as it rotates out of the permanent magnet, Figure 1.4(c), causing the temperature of the bed to decrease. The regenerator then experiences a flow of heat transfer fluid from its hot end to its cold end while it is out of the magnetic field, Figure 1.4(d), which causes a cooling load to be accepted at the cold heat exchanger because the temperature of the fluid leaving the cold end is less than the refrigeration load temperature.

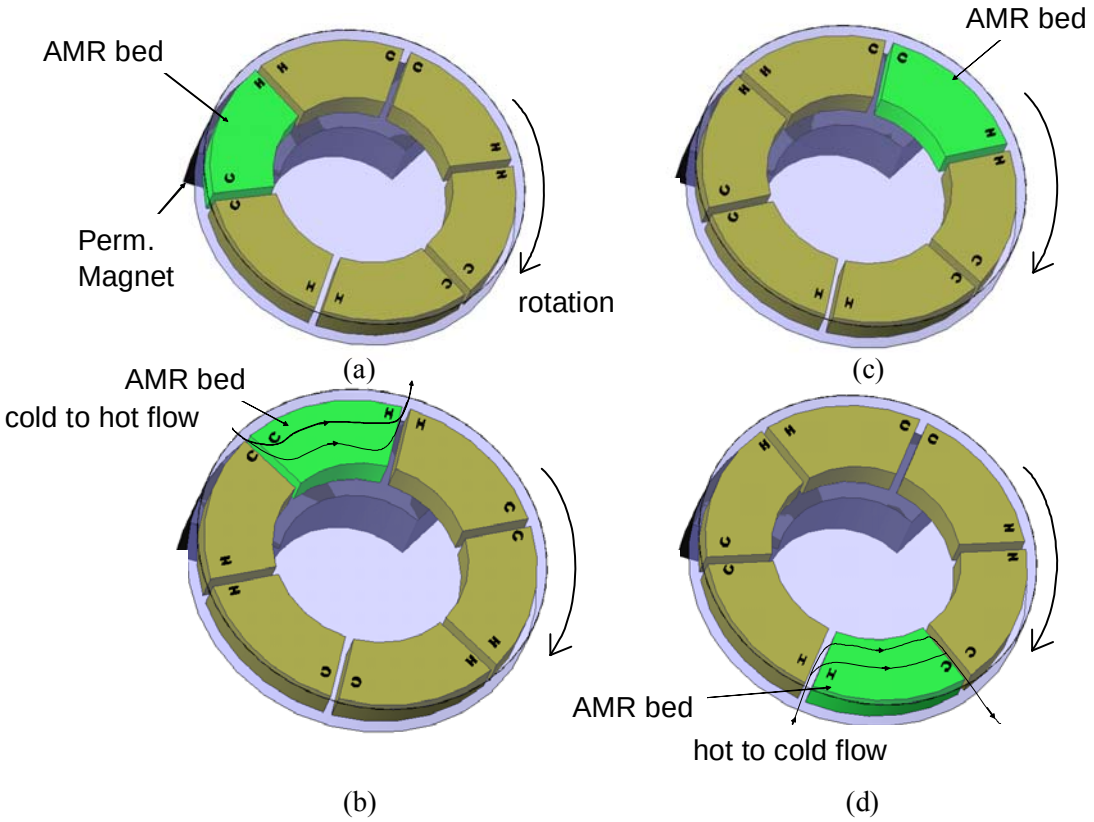

Figure 1.4. Conceptual drawing showing the processes that make up rotary AMRR system, (a) magnetization, (b) cold to hot flow, (c) demagnetization, and (d) hot to cold flow.

1.3 DEVELOPMENTS IN MAGNETOCALORIC MATERIALS

The properties of the magnetocaloric material that is used in an AMRR system are primarily responsible for the system performance that can be achieved. A review of recently developed materials for room-temperature refrigeration is given by Brueck (2005). Researchers have developed several promising materials with large magnetocaloric effects and tunable Curie temperatures that may be suitable for room-temperature applications (Gschneidner et al., 2005).

Magnetocaloric materials generally have non-linear properties that are highly dependent on temperature; therefore evaluating the relative potential performance of one material compared to another in an AMRR system is not straightforward. A rigorous comparison of materials would require that the properties be integrated with a detailed model of the AMRR system and even then, the results would depend on the regenerator geometry, operating temperatures, heat transfer fluid properties and several other system or operating parameters.

Although no simple set of properties can define the performance of a magnetocaloric material used in an AMRR, the two parameters that provide the most meaningful basis for comparison are the adiabatic temperature change with magnetization (ΔT_{ad}) and the mass specific entropy change with magnetization (Δs_M). Many magnetocaloric materials exhibit magnetic hysteresis; that is, the material properties are dependent on the history of the magnetic field experienced by the material. Hysteresis will reduce the performance of an AMRR system and therefore should also be considered when selecting a magnetocaloric material. The thermal conductivity of the magnetocaloric material also has an important, albeit less intuitive, impact on the performance of AMRR devices. A material with a large thermal conductivity could lead to a regenerator that is plagued by large axial conduction, which can be a major loss mechanism for AMRRs. However, it is possible to reduce axial conduction losses by placing low conductivity spacers in the regenerator. Conversely, a material with a low conductivity will not interact completely with the heat transfer fluid during each cycle; the diffusive conduction wave that transfers energy between the material and the fluid will travel too slowly (as compared to the cycle time) and therefore the material in the center of the solid matrix (e.g., at the center of a spherical particle) will not participate thermally in the AMRR cycle (or the frequency of operation must be reduced,

which carries its own penalty). Regenerators characterized by high fluid-to-solid heat transfer coefficients or high operating frequency are particularly susceptible to losses related to temperature gradients that are internal to the solid material (Engelbrecht et al. 2006a). Therefore, materials with either very high or very low thermal conductivity may not be well-suited for some AMRR applications; the threshold conductivities depend strongly on the particular geometry of the regenerator that is being considered.

The Curie point is the temperature where a material changes from a ferromagnetic to a paramagnetic state; this temperature is significant because a material will exhibit its greatest magnetocaloric effect near the Curie temperature (in Figure 1.2, the Curie point is about 277 K). There are two types of magnetic phase changes that may occur at the Curie point, first order magnetic transition (FOMT) and second order magnetic transition (SOMT). As discussed above, the time required to realize a magnetization induced temperature change in some FOMT materials can be many orders of magnitude larger than the time required in SOMT materials. This time lag between the application or removal of a magnetic field and the associated thermal response of an FOMT material may decrease cycle performance by 30-50% when FOMT materials are used in an AMRR that operates at frequencies from 1-10 Hz. However, according to Russek and Zimm (2006), even with this penalty, FOMT materials with large magnetocaloric effects that use less expensive raw materials have the potential to be more cost effective in AMRR devices than SOMT materials such as Gd.

Figure 1.2 shows that magnetic materials exhibit a large magnetocaloric effect only over a narrow temperature range that is near the Curie temperature (T_{Curie}) of the material. As a result,

there is only a small temperature range where an AMR composed of a single magnetic material can maintain its otherwise potentially high performance. In order to maximize the magnetocaloric effect over a larger temperature span, a regenerator bed composed of several materials may be constructed with an engineered, spatial variation in the Curie temperature along the length of the regenerator; the local Curie temperature of the material at any position is selected (through changes in the composition of the alloy) in order to match the local, average regenerator temperature. A regenerator constructed of several magnetocaloric materials is referred to as a layered regenerator, and AMRR systems that utilize layered regenerators have the potential to achieve higher system performance than single material AMRR systems. Therefore, researchers are working towards the development of families of material compounds which have similar properties, but whose Curie temperature can be shifted by changing the material composition. For example, the Curie temperature of alloys of gadolinium, Gd, and dysprosium, Dy, can be adjusted by varying the fraction of Gd in the alloy. A thorough review of available magnetocaloric materials can be found in Gschneidner et al. (2005). In this section, some of the most promising families of materials that were presented in Gschneidner et al. (2005) as well as more recently developed materials that were not included in that review are discussed.

According to Allab et al. (2006), the upper limit of the magnetic field strength that can be achieved using a permanent magnet today is approximately 2 Tesla; therefore, the properties of magnetocaloric materials are compared using a magnetic field change from 0 to 2 Tesla. A summary of the magnetic properties of selected materials is presented in Table 1.1. Note that in

Table 1.1, hysteresis is defined as the temperature shift that is observed as the magnetic field increases as compared to when the magnetic field decreases.

Table 1.1. Summary of properties of selected magnetocaloric materials.

Material	T_{Curie} (K)	Type	$-\Delta s_M$ (0-2 Tesla) (J/kg-K)	ΔT_{ad} (0-2 Tesla) (K)	Hysteresis (K)	Reference
Gd	294	SOMT	5.8	5.5	~0	Dan'Kov (1998)
$Gd_5Si_{4-x}Ge_x$						
x=0.5	269	FOMT	27	7	2	Pecharsky et al. (2003)
$LaFe_{13-x}Si_xH_y$						
x=1.3, y=1.1	287	FOMT	28	7.1	1	Fujita et al. (2003)
$La_{1-w}Ce_wFe_{13-x}Si_xH_y$						
w=0.1, x=1.3, y=1.6	334	FOMT	30			Fujieda et al. (2004)
$MnAs_{1-x}Sb_x$						
x=0	318	FOMT	32	5	6	Wada and Tanabe (2001)
x=0.1	287	FOMT	30	3 (0-1.45 Tesla)	1	Wada et al. (2005)
$Mn_{1.1}Fe_{0.9}P_{1-x}Ge_x$						
x=0.2	206	SOMT	13		~0	Yan et al. (2005)
x=0.22	280	FOMT	16		11	Dagula et al. (2005)
$Mn_{1.1}Fe_{0.9}P_{0.5}As_{0.5}$	282	FOMT	25			Tegus et al. (2004)
$Pr_{13}Fe_{87}$	288	SOMT	3			Pawlik et al. (2006)
$Gd_{1-x}Tb_xCo_2$						
x=0.6	300	SOMT	2.5			Zhou et al (2006)
x=1	230	SOMT	3.5			Zhou et al (2006)
$Ni_{2+x}Mn_{1-x}Ga$						
x=0.16	314	FOMT	11 (0-1.8 Tesla)		7	Cherechukin et al. (2004)
x=0.18	333	FOMT	21 (0-1.8 Tesla)		7	Cherechukin et al. (2004)

1.3.1 Gadolinium and its alloys

Gadolinium, Gd, is an SOMT material with a Curie temperature of approximately 293 K. It is the only pure substance with a Curie point near room temperature that exhibits a significant

magnetocaloric effect over a large temperature span. Dan'kov et al. (1998) studied the magnetocaloric properties of high-purity Gd and found the maximum ΔT_{ad} to be approximately 5.8 K when magnetized from 0 to 2 Tesla using a direct measurement of ΔT_{ad}. The isothermal entropy change with magnetization is approximately -5.5 J/kg-K for high-purity Gd. Ames Laboratories measured the properties of a commercial grade gadolinium and determined an entropy change with magnetization of -4.9 J/kg-K (Zimm et al., 2003). The magnetic hysteresis exhibited by gadolinium is quite low and Dan'kov et al. reported that there was no detectable hysteresis in single gadolinium crystals. The thermal conductivity of Gd near room temperature is approximately 10 W/m-K (Fujieda et al., 2004). Because gadolinium has a relatively large magnetocaloric effect and low hysteresis, it has been used in many prototype room temperature AMRR systems (Yu et al., 2003). Gadolinium can corrode in the presence of water at room temperature, which could affect the long-term performance and durability of an AMRR system using Gd-based alloys. However, Zhang et al. (2005) found that by adding NaOH to the water, this corrosion problem can be eliminated; practical AMRR systems using Gd-based alloys will likely require some type of corrosion inhibitor in the heat transfer fluid.

Gadolinium can be alloyed with terbium (Tb) (Gschneidner and Pecharsky, 2000), dysprosium (Dy) (Dai et al., 2000), or erbium (Er) (Nikitin et al., 1985) in order to lower the Curie temperature. Canepa et al. (2002) report that palladium (Pd) can be added to Gd to form Gd_7Pd_3, which has a higher Curie point than pure Gd. The properties of all of these Gd alloys exhibit magnetocaloric properties that are similar to pure Gd and these families of Gd alloys can be used to construct a layered regenerator bed.

1.3.2 $Gd_5Si_{4-x}Ge_x$

Alloys composed of gadolinium, silicon and germanium exhibit a magnetocaloric effect that is significantly larger than that of gadolinium alone and have a phase transition temperature that is near room temperature (Pecharsky and Gschneidner 1997). The Curie temperature of the material can be adjusted by varying the fraction of silicon and compounds with a wide range of Curie temperatures can be synthesized (Pecharsky and Gschneidner 1997a). Unlike gadolinium, most $Gd_5Si_{4-x}Ge_x$ compounds are FOMT materials and the entropy change with magnetization is larger than that of gadolinium but is also much sharper, occurring over a narrower temperature range. The FOMT involves a change in crystal symmetry, with a magnetic hysteresis that is larger than that of gadolinium, with a value of 2 K reported for $Gd_5Si_2Ge_2$ (Pecharsky and Gschneidner, 1997). The thermal conductivity of $Gd_5Si_2Ge_2$ was experimentally determined to be approximately 5-7 W/m-K near room temperature (Fujieda et al., 2004). The hysteresis can be greatly reduced by alloying with other elements, but the material then becomes an SOMT (Pecharsky and Gschneidner, 1997b; Shull et al, 2006).

Pecharsky et al. (2003) found that by using high-purity starting components and a different heat treatment (compared to what was used in the previous work by Pecharsky and Gschneidner (1997)), the entropy change with magnetization and the adiabatic temperature change for $Gd_5Si_2Ge_2$ could both be increased by more than 50%. The magnetic entropy change, Δs_M, of this optimally prepared material was approximately -27 J/kg-K and the adiabatic temperature change, ΔT_{ad}, was approximately 7 K when the material was magnetized from 0 to 2 Tesla. The adiabatic temperature change was determined from heat capacity and magnetization measurements and was not measured directly. $Gd_5 (Si_{1-x}Ge_x)_4$ materials have the potential to be

high performance AMRR refrigerants because they possess a relatively high entropy change with magnetization as well as a large adiabatic temperature change. Families of these materials with similar magnetic properties can be fabricated with large spans of Curie temperature.

1.3.3 $LaFe_{13-x}Si_xH_y$

Alloys of lanthanum, iron, silicon and hydrogen undergo a first order magnetic phase transition and exhibit a magnetocaloric effect that is larger in magnitude than gadolinium but is much sharper (i.e., it occurs over a narrower temperature span), as discussed by Fujieda et al. (2002). The properties of the material can be adjusted by substituting iron for silicon (Gschneidner et al. 2005) or by adding hydrogen (Fujita et al. 2003). The Curie temperature of this family of materials has been reported in the temperature range from 195 K to 336 K (depending on composition). $La(Fe_{11.7}Si_{1.3})H_{1.1}$ has a Curie temperature of 287 K and experiences an entropy change of -28 J/kg-K and an adiabatic temperature rise of 7.1 K when magnetized from 0 to 2 Tesla. The adiabatic temperature rise was measured indirectly using heat capacity and magnetization data. The hysteresis for $LaFe_{11.44}Si_{1.56}$ is approximately 1 K according to Fujita et al. (2003); however, the hysteresis can vary widely with material composition. The thermal conductivity of these materials is approximately 10 W/m-K near room temperature (Fujieda et al., 2004). Lanthanum is one of the most common rare earth elements, with a cost that is significantly less than Gd, making these materials potentially more economical than Gd.

The performance of the lanthanum, iron, silicon family of materials can be enhanced by substituting other elements for lanthanum. For example, by substituting cerium (Ce) for lanthanum, Fujieda et al. (2004) were able to increase the magnetic entropy change to -30 J/kg-K

for a compound with 10% cerium substitution. Fujieda et al. (2006) found that substituting praseodymium (Pr) for lanthanum increases the entropy change and adiabatic temperature change when magnetized from 0 to 5 Tesla by more than 30% compared to a similar material with no lanthanum substitution. No data was found for a 2 Tesla magnetic field change for the material with praseodymium substituted for lanthanum; however, it likely has a similar advantage over the un-substituted material at 2 Tesla. The hysteresis is not affected by substituting praseodymium for lanthanum.

1.3.4 $MnAs_{1-x}Sb_x$

The recently developed $MnAs_{1-x}Sb_x$ compounds are FOMT materials that may be suitable for magnetic refrigeration systems. MnAs has a Curie temperature of approximately 318 K, an entropy change with magnetization, Δs_M, of approximately -31 J/kg-K, and an adiabatic temperature change, ΔT_{ad}, of approximately 5 K when magnetized from 0 to 2 Tesla (Wada and Tanabe, 2001). The adiabatic temperature was measured indirectly using heat capacity measurements. MnAs has a relatively large hysteresis of 5 K and a low thermal conductivity of approximately 2 W/m-K near room temperature (Fujieda et al., 2004). The Curie temperature of this alloy can be adjusted between 230 K and 318 K by substituting antimony (Sb) for arsenic (As). When the fraction of Sb (x) is greater than or equal to 0.05, the thermal hysteresis becomes quite small while the magnetocaloric effect remains approximately unchanged (Wada et al., 2005). For the material containing Sb, ΔT_{ad} was determined to be 3 K when magnetized from 0 to 1.45 Tesla using a direct measurement of adiabatic temperature change. These materials are attractive as magnetic refrigerants because they have a large entropy change with magnetization, the Curie temperature can be adjusted over a large temperature range and the hysteresis becomes

relatively small with the addition of antimony. However, the adiabatic temperature change is relatively low for this family of materials and the thermal conductivity is significantly lower than that of gadolinium and the other magnetocaloric materials that have been discussed; these properties may decrease performance under some AMRR operating conditions.

1.3.5 MnFeP Materials

The properties of this family of materials can be modified with the addition of the elements As, Mn, Ge, cobalt (Co), and chromium (Cr) (Tegus et al., 2004). The Curie temperature of $Mn_{1.1}Fe_{0.9}P_{1-x}Ge_x$ can be adjusted between 250 K and 380 K by varying x, the fraction of germanium (Ge) in the compound (Dagula et al., 2005). Yan et al. (2006) report that the properties of this alloy are strongly dependent on the material processing technique that is used. The Curie temperature of a melt-spun alloy was found to be 18 K higher than that of an annealed bulk alloy with the same composition. The melt-spun materials also exhibited higher entropy change with magnetization and lower hysteresis. This family of materials are generally FOMT; however, when x=0.2, the material becomes SOMT with no detectable hysteresis. The Curie temperature for the x=0.2 alloy is approximately 206 K and therefore it is not well-suited for space cooling applications; however, it may be useful for some low temperature refrigeration applications. As germanium is substituted for phosphorus (P), the thermal hysteresis increases and reaches a value of approximately 8 K for compounds with x>0.2. The entropy change with magnetization is approximately -16 J/kg-K for a 0 to 2 Tesla applied field change for materials that have a Curie temperature near room temperature. The Curie temperature of $Mn_{1+x}Fe_{1-x}P_{1-y}As_y$ can be adjusted by varying the fraction of As. The maximum entropy change for these materials from Brueck et al. (2005) is -20 J/kg-K for $Mn_{1.1}Fe_{0.9}P_{0.47}As_{0.53}$, which has a Curie

temperature of 289 K. Tegus et al. (2004) reported an entropy change with magnetization of approximately -25 J/kg-K for $Mn_{1.1}Fe_{0.9}P_{0.5}As_{0.5}$, which has a Curie temperature of 282 K. These materials have a substantial magnetocaloric effect and the Curie temperature can be adjusted over a wide temperature range, which makes them attractive as possible magnetic refrigerants. The thermal hysteresis for these materials is larger than other materials mentioned above, which could reduce performance in an AMRR system.

1.3.6 Other Materials

Compounds of $Ni_{2+x}Mn_{1-x}Ga$ have Curie temperatures that lie between 315 K and 380 K and have a relatively large magnetocaloric effect. Cherechukin et al. (2004) reports that these materials exhibit a magnetic entropy change of -20.7 J/kg-K when magnetized from 0 to 1.8 Tesla for $Ni_{2.18}Mn_{0.82}Ga$. These materials have a relatively high hysteresis of 7 K (Gshneidner et al., 2005), which makes them less desirable than other materials with large magnetocaloric effects. However, new fabrication processes may reduce this hysteresis, making these materials well-suited for coolers operating at higher temperatures, for example between 300 and 350 K.

Several other materials have been developed recently, but none seem as promising as the materials discussed above. Dinesen et al. (2005) studied the magnetic properties of $La_{0.67}Ca_{0.33}$-$Sr_xMnO_{3\pm\delta}$ and found that the adiabatic temperature change of these materials is significantly lower than that of gadolinium. For a Sr fraction of 0.55, ΔT_{ad} is 1 K and Δs_M is -2.8 J/kg-K when magnetized from 0 to 1.2 Tesla. Pawlik et al. (2006) studied alloys of praseodymium and iron (Fe) and found that the maximum magnetocaloric effect occurred in $Pr_{13}Fe_{87}$, with an entropy change of magnetization of approximately -3 J/kg-K, which is less than that of Gd. Compounds

of Gd, Tb, and Co were studied by Zhou et al. (2006) and the maximum entropy change with magnetization was found to be -3.6 J/kg-K, which is also significantly lower than that of pure Gd.

1.4 AMRR PROTOTYPE SYSTEMS

Different mechanical realizations of the AMRR cycle are possible and several types of prototype systems have been constructed. For example, the magnetic material may be stationary and the field varied by controlling the current in a solenoid; however, this configuration is currently only practical at very low temperatures or where superconductors can be used to efficiently handle the large currents that are required to generate useful magnetic fields. Practical AMRR systems used for residential and other smaller scale applications will likely use a permanent magnet to generate a magnetic field, because the power required by the cryogenic equipment necessary to maintain the superconducting temperature of a solenoid magnet can greatly exceed the cooling power of small to medium scale AMRR devices (Zimm et al., 2006). However, for large scale systems, the increased performance that is possible for an AMRR energized by a superconducting magnet may offset the additional power required to maintain the magnet at a cryogenic temperature. Systems using permanent magnets can achieve variations in applied field by physically moving either the magnetic regenerator relative or the magnet relative to one another, either linearly in a reciprocating device, or rotationally in a rotary device (e.g., Figure 1.4); a schematic of a reciprocating AMRR system is shown in Figure 1.5.

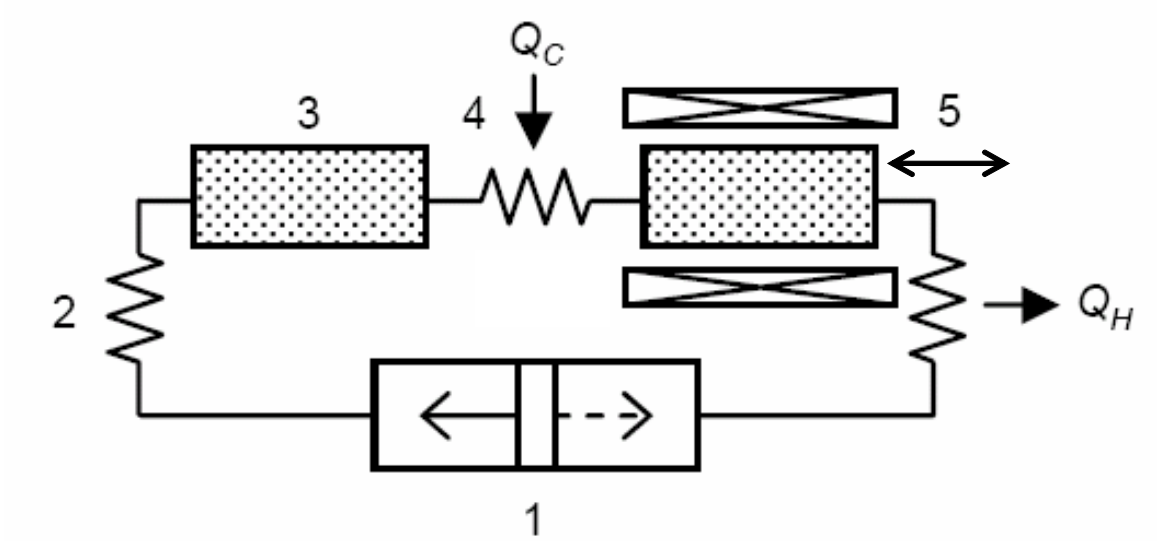

Figure 1.5. Schematic of the University of Victoria reciprocating AMRR device: (1) fluid displacer, (2) hot heat exchanger, (3) AMR, (4) cold heat exchanger, (5) magnet (Rowe et al., 2006).

Several AMRR prototypes have been built and their measured performance has been published. Some of these prototypes have implemented layered regenerator beds in an attempt to increase performance and many of these newer systems are using the more practical option of permanent magnets rather than superconducting solenoid magnets to generate the magnetic field. Yu et al. (2003) provide a summary of the prototype systems and their associated performance that covers the period of time up to 2003; only the most significant systems that were discussed in that paper are cited here. More recent results for new prototype systems and new system configurations are summarized in Table 1.2 and discussed below. Examination of Table 1.2 shows that the performance of AMRR systems is highly dependent on the operating conditions used for the tests and the materials used to fabricate the regenerator. In every case, the maximum value of the cooling power that can be produced by a system (Q_C) will occur as the temperature span of the system (ΔT) approaches zero and the maximum temperature span will occur when no

refrigeration load is produced. One must therefore pay close attention to the system operating conditions when evaluating and comparing the performance of the prototype AMRR systems presented in Table 1.2 and discussed in this section.

Table 1.2. Summary of experimental performance of recently built AMRR systems.

System	Config.	$\mu_o H_{max}$ (Tesla)	# Beds	Regen. volume (cm^3)	Freq. (Hz)	Regen. material	Q_C (W)	ΔT (K)	Regenerator geometry	Reference
US Navy	Recip	7 (E)	1	173	0.01	Gd	0	40	Embossed ribbon (0.2mm)	Green (1986)
University of Victoria	recip.	2 (S)	2	74	1	Gd, GdTb & GdEr	0	50	crushed part. (0.25-0.65mm)	Rowe et al. (2006)
		2 (S)		49	0.8	Gd	0	15.5	spheres (0.2mm)	Rowe et al. (2004)
		2 (S)		25	0.6		7	14		
Chubu Electric/ Toshiba	recip.	4 (S)	2	484	0.167	Gd	100	26	spheres (0.3 mm)	Hirano et al. (2002)
		2 (S)					40	24		
Astronautics Recip.	recip.	5 (S)	2	~600	0.167	Gd	100	38	spheres (0.15-0.3mm)	Zimm et al (1998)
							600	0		
Astronautics Rotary Regenerator	rotary	1.5 (P)	6	33	4	Gd	15	14	spheres (0.43-0.5mm)	Zimm et al. (2006)
						Gd & GdEr	27	14	spheres (0.25-0.355mm)	
							0	25		
Astronautics Rotary Magnet	rotary	1.5 (P)	12	242	2	Gd	220	0	stacked plates	Zimm et al. (2007)
							155	8		
Grenoble	recip.	0.8 (P)	1	32	0.42	Gd	9	4	parallel plates (1.0mm)	Clot et al. (2003)
Nanjing University	recip.	1.4 (P)	2	~200	<0.25 Hz	Gd	0	23	spheres (0.2mm)	Lu et al. (2005)
						Gd5Si2Ge2	0	10		
						GdSiGeGa	0	25		
							40	5		
Tokyo Institute of Technology/Chubu	rotary	1.1 (P)	4	~844	0.39	layered Gd1-xDyx	540	0.2	spheres (0.5mm)	Okamura et al. (2007)
					0.42		150	5.2		
Xi'an Jiaotong University	recip.	2.18 (S)	1	~200	~0.1 Hz	Gd	19	4	spheres (0.3mm)	Yu et al. (2006)
						Gd5Si2Ge2	10	3	irregular part. (0.3-0.75mm)	

[a] $\mu_o H_{max}$: S, superconducting magnet, E, electromagnet, P, permanent magnet

1.4.1 University of Victoria Prototype

The University of Victoria AMRR consists of two regenerator beds that are moved linearly through a magnetic field that is generated by a stationary superconducting solenoid magnet (Rowe et al. 2004); a schematic of the system is shown in Figure 1.5 The maximum magnetic field generated by the magnet is 2 Tesla. The regenerator is constructed by stacking together up to three "pucks" of magnetocaloric material. Each puck is 2.5 cm in diameter and 2.5 cm long and can be composed of different materials with different matrix geometry. The heat transfer fluid is helium at 10 bar and flow is controlled by a displacer. The cooling load is controlled by two 25 W finned heaters that are mounted between the two regenerator beds. The device can operate from 0.2 to 1 Hz; the maximum frequency is constrained by the inertial forces.

The University of Victoria prototype has been tested with several layered regenerator beds over a range of operating frequencies. The performance of a layered bed was compared directly to a single-material bed by first running the system with 2 Gd pucks and then with one Gd puck and one $Gd_{0.74}Tb_{0.26}$ puck. The layered bed produced a no-load temperature span of approximately 19 K, while the single material bed produced a span of approximately 15.5 K (Rowe et al., 2004). Using a single "puck" of Gd, the prototype produced 7 W of cooling over a temperature range of 288-302 K. Rowe et al. (2006) constructed a bed of three "pucks" consisting of Gd, $Gd_{0.74}Tb_{0.26}$, and $Gd_{0.85}Er_{0.15}$ in order of decreasing Curie temperature. Operating at a frequency of 1 Hz, a no-load temperature span of 51 K was achieved, showing that layered beds allow AMRR systems to operate over a substantially larger temperature span than can be achieved using a single material regenerator.

1.4.2 Chubu Electric and Toshiba Device

The Chubu Electric/Toshiba AMRR has two regenerator beds that are moved linearly in the presence of a 4 Tesla magnetic field that is generated by a superconducting solenoid. Each regenerator has diameter of 6.2 cm and a length of 8 cm and is comprised of packed spheres of Gd. The heat transfer fluid is a mixture of water and ethanol. Fluid flow is controlled by two valves and a variable speed pump. Hirano et al. (2002) report a cooling power of 100 W with a COP of 5.6 when the system operates between 302 K and 276 K. However, the reported COP is somewhat misleading because it does not include any motor or pump inefficiencies and also neglects the power that is required to cool the superconducting solenoid. When the maximum magnetic field is decreased to 2 Tesla, the cooling power drops to approximately 40 W between 298 K and 274 K, showing that the strength of the magnetic field can significantly affect AMRR performance.

1.4.3 Astronautics Reciprocating and Rotary Prototypes

Astronautics Corporation of America's first near room temperature AMRR prototype was a reciprocating device with a 5 Tesla magnetic field generated by a superconducting solenoid. Two regenerators were made of packed Gd spheres with diameters ranging from 0.15 mm to 0.30 mm. The regenerator material occupied a total volume of approximately 600 cm^3. The maximum cooling power for this device is 600 W, which is obtained as the temperature span approaches 0 and a cooling power of 100 W was achieved with a temperature span of 38 K (Zimm et al., 1998). Although the original device produced a relatively large cooling power over a large temperature span, the device itself was quite large and used a superconducting magnet and therefore would not be practical as a commercial product (Zimm et al., 2006).

Astronautics has recently built two rotary devices that use a more practical, 1.5 Tesla $Nd_2Fe_{14}B$ permanent magnet. The device described by Zimm et al. (2006) uses a rotating regenerator wheel with a stationary permanent magnet. The regenerator is divided into six separate beds that rotate through the field of the permanent magnet, as shown in Fig. 1.4. The heat transfer fluid is water-based and the fluid flow rate is controlled using a variable speed pump and two rotary valves. The plumbing of the system is set up so that the pump runs continuously and flow through the external piping and heat exchangers is unidirectional, while the flow through each individual bed reverses direction during operation. The rotary configuration allows the device to operate at frequencies up to 4 Hz (240 RPM), which is higher than any reciprocating AMRR built to date.

Zimm et al. (2006) studied the performance of a layered bed of Gd and $Gd_{0.94}Er_{0.06}$ and a single-material bed of a LaFeSiH material using the rotating regenerator device. They found that the layered bed is capable of producing a larger cooling load than a similar bed made of Gd when the temperature span is large. The rotary device achieved a maximum no-load temperature span of approximately 25 K with the layered bed and a no-load temperature span of less than 19 K with a single material, Gd bed. The cooling power over a 14 K span for the layered bed was 80% higher (27 W) than the 15 W cooling load that was produced by the single material regenerator. However, the cooling power is greater for the single material Gd bed as the temperature span approaches zero; the layered bed was capable of producing 41 W of cooling at zero temperature span while the Gd bed produced 44 W of cooling under the same condition. This behavior was expected, since the magnetocaloric effect of Gd is greater than that of $Gd_{0.94}Er_{0.06}$ at room

temperature. A regenerator made of irregular particles of $La(Fe_{11.44}Si_{1.56})H_{1.0}$ with sizes in the range of 0.25 mm to 0.5 mm was also studied using the rotary device. The LaFeSiH material produced a higher cooling load than either the Gd or the Gd and GdEr regenerator beds at zero temperature span. However, the LaFeSiH material produced lower cooling power when the temperature span was increased. Based on this result, Zimm et al. concluded that LaFeSiH materials are promising materials for AMRR systems, but that a layered bed would be necessary if these alloys are to achieve high performance over a useful temperature span.

A more recent rotary device that uses a rotating permanent magnet with stationary regenerator beds is described by Zimm et al. (2007). The regenerator is comprised of 12 stationary beds made of stacked plates of Gd. Detailed information about the regenerator geometry is not given; however, the porosity of the beds is approximately 0.52 and there is a total of 0.916 kg of Gd which is consistent with a regenerator volume of 116 cm^3 Initial test results for this rotary magnet device show a maximum zero temperature cooling power of 220 W and 155 W of cooling over an 8 K temperature span.

1.4.4 Nanjing University Device

Nanjing University built a reciprocating device consisting of two regenerator beds that are moved linearly into and out of the magnetic field generated by a stationary, 1.4 Tesla permanent magnet. The regenerators fit within the 3 cm diameter bore of the magnet. Lu et al. (2005) have operated the system with Gd regenerators as well as several recently developed, more advanced magnetocaloric materials. The maximum reported cooling power for this system is 40 W at a temperature span of 5 K when using a regenerator made of $Gd_5Si_{1.895}Ge_{1.89}Ga_{0.03}$. The no-load

temperature span for this device is 23 K for a single material Gd regenerator, 25 K for a $Gd_5Si_{1.895}Ge_{1.89}Ga_{0.03}$ regenerator, and 10 K for a $Gd_5Si_2Ge_2$ regenerator. It is not clear why the $Gd_5Si_2Ge_2$ regenerator achieved a lower temperature span than the pure Gd regenerator. However, Shull et al. (2006) found that adding small amounts of materials such as gallium (Ga) to $Gd_5Si_{4-x}Ge_x$ materials changes the magnetic characteristics from FOMT to SOMT, increases the Curie temperature of the material, and greatly reduces hysteresis. The reduced hysteresis and increased Curie temperature of the $Gd_5Si_{1.895}Ge_{1.89}Ga_{0.03}$ material may account for the dramatic improvement in the no-load temperature span, which is more than double that achieved by the device when operating with a bed material that does not include Ga.

1.4.5 Tokyo Institute of Technology and Chubu Rotary Device

The Chubu system is a rotary device that uses a rotating magnet with a stationary regenerator described by Okamura et al. (2006). The regenerator consists of four packed regenerator beds composed of 0.5 mm diameter spheres, each bed consists of four layers of different materials. The layers are, from the cold end to the hot end, $Gd_{0.91}Y_{0.09}$, $Gd_{0.84}Dy_{0.16}$, $Gd_{0.87}Dy_{0.13}$, and $Gd_{0.89}Dy_{0.11}$. In total, the mass of Gd in the regenerator is 4 kg. During operation, the 1.1 Tesla neodymium permanent magnet rotates over a regenerator bed and then stops while fluid flows though the bed. The magnet then rotates 90º to the next regenerator bed and the process is continued in this manner. The heat transfer fluid is water and its flow is controlled by a rotary valve and variable speed pump. The system produces a maximum cooling power of 540 W at a frequency of 0.39 Hz and a fluid flow rate of 13.3 L/min as the temperature span approaches 0 K (Okamura et al. 2007). For a temperature span of 5.2 K, a maximum cooling power of 150 W was achieved at a frequency of 0.42 Hz and a fluid flow rate of 13.3 L/min.

1.4.6 Other Systems

Clot et al. (2003) built a reciprocating AMRR using 1 mm parallel plates of Gd that are separated by a 0.15 mm gap to allow fluid flow. The magnetic field is provided by a 0.8 Tesla permanent magnet and the system operates at 0.42 Hz. A cooling load of 8.8 W is obtained for a temperature span from 298.5 K to 302.5 K with a COP of 2.2; the COP includes all power inputs to the system. Xi'an Jiaotong University built a reciprocating AMRR with a single regenerator bed that uses a 2.18 Tesla electromagnet (Yu et al. 2006). The dimensions of the bed were not reported, but the bed holds 930 g of Gd particles. Assuming a porosity of 0.4, the volume of the regenerator is approximately 200 cm^3. Using Gd spheres as the refrigerant, this device produced up to 18.7 W of cooling between 294.5 K and 291.4 K with a fluid flow rate of 3.5 L/min. The same device was operated using a regenerator made of irregular particles of $Gd_5Si_2Ge_2$ and the cooling power dropped to a maximum value of 10.3 W between the temperatures of 300.1 K and 297.1 K with a fluid flow rate of 3.6 L/min. The reason for the lower cooling power measured with the $Gd_5Si_2Ge_2$ material is not known; however, it is likely because the system is not operating near the Curie point of the material. Vasile and Muller (2006) describe a prototype using a rotating permanent magnet and stationary regenerator. The regenerator is composed of a series of parallel plate regenerator "inserts" that are thermally isolated from one another and can be made of different magnetocaloric materials in order to construct a layered regenerator. However, there is currently little published performance data for this prototype.

1.5 PRACTICAL AMRR ISSUES

Magnetic refrigeration is not a mature field and there will be issues that must be overcome before AMRR devices become practical for commercial applications. Recent prototypes have addressed some of the practical issues associated with the previous experiments. For example, some recent systems have demonstrated relatively large cooling powers using permanent magnets; this eliminates the need for a cryocooler and superconducting solenoids. The maximum operating frequency of AMRR systems has been increased by using rotary rather than reciprocating configurations; the increase in the operating frequency allows smaller and therefore more economically viable beds and magnets to be used. Despite these advances, there are still several practical issues that should be considered.

System Size

Prototype AMRR systems are currently much larger than the equivalent vapor compression systems that they would replace. For example, Lu et al. (2005) report using a permanent magnet with an outer diameter of 14 cm (5.5 in) and a length of 20 cm (7.9 in) for a system that provides a maximum cooling power of 40 W. The system, including the magnet, regenerator, pumps, plumbing and electric motor, is significantly larger than the compressor and electric motor that would be required for a comparably sized vapor compression system; note that the AMRR system would require heat exchangers that are approximately the same size as the evaporator and condenser in a vapor compression system.

As AMRR systems become more efficient through material selection and regenerator design, their size will decrease; however, even a well-designed and advanced AMRR system using an

SOMT material will likely be larger than an equivalent vapor compression system. In order for an AMRR with a packed sphere regenerator of Gd to produce 8.8 kW cooling at an efficiency that is competitive with vapor compression, Engelbrecht et al. (2006b) has shown that a total regenerator volume of approximately 4 L will be required. This regenerator volume does not include the volume associated with the magnet, the pump, the valves, or the regenerator housing. Therefore the total volume of the AMRR system will likely be significantly higher than a vapor compression system that is sized to meet the same load. However, Engelbrecht (2005) also showed that the regenerator volume can be reduced substantially without sacrificing performance if a layered bed composed of low hysteresis FOMT material compounds is used in conjunction with more sophisticated regenerator geometries. If the material operates in the region of its FOMT, the high latent heat of the materials offers important advantages. First, the latent heat will minimize the reduction in effective ΔT_{ad} by the pore fluid volume, allowing the use of a more porous bed with lower pressure drop and lower longitudinal conduction which reduces losses. Second, the large latent heat will allow higher volume specific fluid flow rates for a given AMRR frequency, allowing the use of a much smaller regenerator bed and correspondingly smaller magnet.

High Fluid Mass Flow Rate

Unlike vapor compression systems, the fluid in an AMRR cycle does not undergo a phase change. As shown in Table 1.1, the adiabatic temperature rise of current magnetocaloric materials is less than 8 K for a reasonable magnetic field swing and the temperature change of the heat transfer fluid will be lower than this value due to heat transfer losses as well as the specific heat of the fluid entrained in the bed. The heat transfer from the fluid to the load is the

product of the mass flow rate, the temperature change of the fluid, and the specific heat of the fluid. Therefore, for a given cooling capacity, the fluid mass flow rate in an AMRR system must be substantially larger than the flow rate of refrigerant in a vapor compression cycle.

Zimm et al. (2006) reported an AMRR cooling power of 30 W over an 8 K temperature span which required a fluid flow rate of approximately 0.7 kg/min; this equates to a cooling power to fluid mass flow rate ratio of approximately 43 W-min/kg. Engelbrecht et al. (2006b) predict that the flow rate of water in a packed sphere AMRR that produces 8.8 kW of cooling is approximately 84 kg/min, which leads to a cooling power to fluid flow ratio of approximately 105 W-min/kg. These two data points suggest that the cooling power to mass flow rate ratio of an AMRR system will be in the range of 25-150 W-min/kg depending on the cycle design and magnetocaloric material that is used.

For a vapor compression system, the cooling power to fluid mass flow rate ratio will be much higher due to the latent heat of vaporization of the refrigerant. For example, the DOE/ORNL Heat Pump model (Rice, 2006) predicts that a vapor compression system sized to produce 8.8 kW of cooling will require a refrigerant flow rate of 3.3 kg/min; this corresponds to a cooling power to fluid mass flow rate ratio of approximately 2700 W-min/kg. For an equal cooling power, the predicted fluid flow rate for a well-designed AMRR is approximately 25 times higher than the value predicted for a vapor compression system, and fluid flow rate for the experimental value reported by Zimm et al. (2006) is approximately 60 times the predicted flow rate for a vapor compression system.

The high fluid mass flow rates that are required must be considered carefully in the design of an AMRR system in order to prevent excessive pumping losses in the heat exchangers and connecting piping. Proper care must be taken in the heat exchanger circuiting and the design of the connecting piping and valves associated with an AMRR system in order to limit parasitic pumping losses. The single phase fluid of the AMRR can allow the use of improved heat exchanger designs that may make up for the higher fluid flow rate in some applications. In air conditioning applications, the heat exchange is dominated by the air side heat exchange resistance, so the increased fluid flow rate may not have much effect on heat exchanger size or cost. Also, because the pressure in AMRR systems is much lower than vapor cycle systems, use of plastic piping becomes possible, which may reduce connecting piping and installation costs.

Material Processing

Processing of magnetocaloric materials may be an issue for commercial AMRR devices. Most of the magnetocaloric materials that have been developed have only been produced in laboratory scale quantities, and many of these require lengthy heat treatments or high-purity starting materials in order to achieve optimum magnetocaloric properties. For example, arc-melted samples of $LaFe_xSi_{1-x}H_y$ were annealed for 10 days at 1323 K (Fujita et al., 2003) and $MnAs_{1-x}Sb_x$ compounds were heat-treated for 7 days (Wada et al. 2005) in order to achieve desired results. Many magnetocaloric materials are sensitive to the purity of the starting elements that are used to synthesize the material (Tishin, 2005), which may make the cost of the raw materials very high. Pecharsky et al. (2003) reported significant increases (greater than 50%) in magnetic entropy change and adiabatic temperature change with magnetization when using 99.9% pure Gd instead of Gd with a purity of 95-98%. The requirement of high purity materials, long heat

treatments, and expensive raw materials may make the commercial production of some types of magnetocaloric materials impractical.

1.6 AMRR MODELING WORK OUTSIDE OF UW-MADISON

1.6.1 Zero-Period AMR Models

There are several, time independent models of AMRR systems; these models are sometimes referred to as zero-period models. Zero-period models are useful for qualitative investigations of AMRR cycle characteristics; for example, the evaluation of the magnetocaloric properties of various materials in the context of an AMRR cycle or the parametric investigation of the impact of a particular cycle parameter. The major benefits of these zero-period models are their computational efficiency as well as their illumination of underlying physical phenomena; however, the predictive capability of a zero-period model is limited.

Zhang et al. (2000), He et al. (2003), Zhang et al. (1993), and papers by Yan and Chen (1991, 1992) all present zero-period models that can be used to understand the characteristics of various AMRR cycle configurations. Shir et al. (2003) have used a time independent model to show how magnetic nanocomposites may be used to obtain an ideal magnetic refrigerant, one in which the local adiabatic temperature change is proportional to the local absolute temperature. The major shortcomings of all zero-period models are their heuristic approach to capturing the effect of material properties, particularly for layered beds, and their macroscopic approach to estimating losses.

1.6.2 Time Dependent AMRR Models

Researchers at Astronautics have presented the Finite Reduced Period (FRP) model; this AMRR model is one-dimensional and time dependent, but it requires that the heat capacity of the entrained fluid in the regenerator be negligible compared to that of the magnetic material (DeGregoria et al., 1989 and DeGregoria, 1991). In this limit, the conventional regenerator equations are solved during the flow portions of the cycle and instantaneous temperature changes are imposed at the conclusion of these processes. These temperature changes represent the magnetization and demagnetization processes which are assumed to occur reversibly and adiabatically. The pumping loss, axial conduction, and dispersion losses are calculated separately and then subtracted from the predicted refrigeration power (Johnson and Zimm, 1996). The FRP model has been applied primarily to the design of low temperature AMRR systems that use a gas as the heat transfer fluid, as described by Janda et al. (1991), and therefore the assumption of negligible entrained fluid heat capacity is not overly restrictive.

Kirol and Mills (1984) describe a one-dimensional transient model of a magnetic cycle that assumes perfect regeneration. Smaïli and Chahine (1998) describe a one dimensional transient model in which only the flow processes are considered; the magnetization and demagnetization processes are assumed to happen instantaneously and reversibly. The heat transfer coefficient is assumed to be everywhere constant and the impact of axial conduction and entrained heat capacity are not considered. Hu and Xiao (1995) present an analysis of AMRR systems that is based on small perturbation theory; a technique that is used for pulse-tube type refrigeration systems, as described by several researchers including Hooijkaas and Benschop (1999). The

governing equations are linearized and the fluctuating parameters are written in complex form, implying a sinusoidal variation of all such quantities.

A two-dimensional model of a flat plate AMRR is described by Petersen et al. (2007). The model uses an FEM approach to solve for fluid flow profiles and temperature gradients in the solid. Because of the increased complexity of the model, the computation time is much higher for the two-dimensional model than equivalent one-dimensional models. The geometry is fixed as a flat plate regenerator and modeling other regenerator geometries would require significant modifications to the existing model.

With the exception of the 2D model presented by Petersen et al., the models described above are either overly simplified and therefore non-physical or, in the case of the models reported by DeGregoria or Barclay, not accessible to the public due to proprietary or other reasons, and computationally slow. Most of these models do not consider the impact of entrained fluid heat capacity. The 2D FEM model by Petersen et al. does include entrained fluid heat capacity, but the computation time may be prohibitive for some design applications and the regenerator geometry is currently limited.

1.7 RESEARCH OBJECTIVES

The primary goal of this research is to develop a sophisticated, flexible, and physics-based numerical model of an AMRR system that has been validated against experimental data under both active and passive operating conditions and is available as a distributable code with a useful user interface. The model that has been developed is one-dimensional and numerically solves

the coupled partial differential equations for both the solid regenerator and heat transfer fluid in an AMRR. The model is flexible with regard to modeling inputs such as regenerator geometry, fluid flow profile, variations in magnetic field, and material properties. A description of the model is provided in Chapter 2 and a summary of some of the most interesting modeling results is provided in later chapters. The numerical model is a flexible modeling tool that can predict the performance of an AMRR over a range of operating conditions, fluid and solid properties, and regenerator geometries and therefore can be used to assess and design this technology for a wide range of applications. For example, the model has been used to analyze room temperature AMRR systems for residential cooling (Engelbrecht et al. 2005), analyze a prototype AMRR, predict performance of transient and cyclical passive room temperature regenerators, and analyze cryogenic temperature AMRR systems that use gas heat transfer fluids (Utaki et al., 2007).

The model has been compared to experimental data collected at Astronautics Corporation of America using the AMRR experiment described by Zimm et al. (2005). These data were collected at various operating conditions for a regenerator comprised of six beds of packed gadolinium spheres operating in the field of a 1.5 Tesla permanent. Acceptable agreement was achieved between the model and experiment for a range of operating conditions. A comparison of the numerical model to experimental data is given in Chapter 6.

One of the shortcomings of AMRR data is that the experiment is not precisely controlled; the complexity associated with an AMRR operating at several Hertz necessarily precludes the measurement of details such as the temperature and flow as a function of time and does not allow precise knowledge of the boundary conditions required by the model. Therefore, disagreement

between experiment and model can be attributed to either a failure to model the underlying physics of the problem or incorrect boundary conditions. For this reason, the numerical model has also been used to design a single-blow, passive regenerator experiment. The single-blow experiment is simple and can be precisely instrumented and controlled. The experiment allows important aspects of the model to be verified precisely, including the heat transfer coefficient, the impact of internal temperature gradients, axial dispersion, viscous dissipation, and the effect of the entrained fluid heat capacity. The model was used to determine the regenerator geometry and operating conditions that provide the most meaningful experimental information. This single-blow setup has been constructed at the UW-Madison and has been used to measure the heat transfer in a packed sphere regenerator. A modified version of the numerical AMRR model was used to analyze experimental data. Disagreement between the model prediction and experimental measurements can be attributed to the Nusselt number correlation used in the AMRR model; therefore, a set of experiments have been carried out and used to generate a Nusselt number correlation for a packed sphere regenerator using a liquid heat transfer fluid.

Chapter 2 Numerical Model Description

2.1. GOVERNING EQUATIONS

This chapter presents a one dimensional (1D) model of an active magnetic regenerative refrigerator (AMRR). A diagram of the system that is being simulated and some of the important modeling parameters are shown in Fig. 2.1. The equipment that is external to the bed (e.g., the pumps, heat exchangers, and permanent magnets), are not explicitly modeled; however, their effect on the cycle is felt through an imposed time variation of the mass flow rate ($\dot{m}(t)$) and the variation of the magnetic field in time and space ($\mu_o H(x,t)$). The time variation of these quantities is related to the fluid-mechanical-magnetic processes associated with the cycle implementation. The interface between these imposed boundary conditions and the characteristics of these auxiliary pieces of equipment can be handled by system-level models that interact with this component-level model.

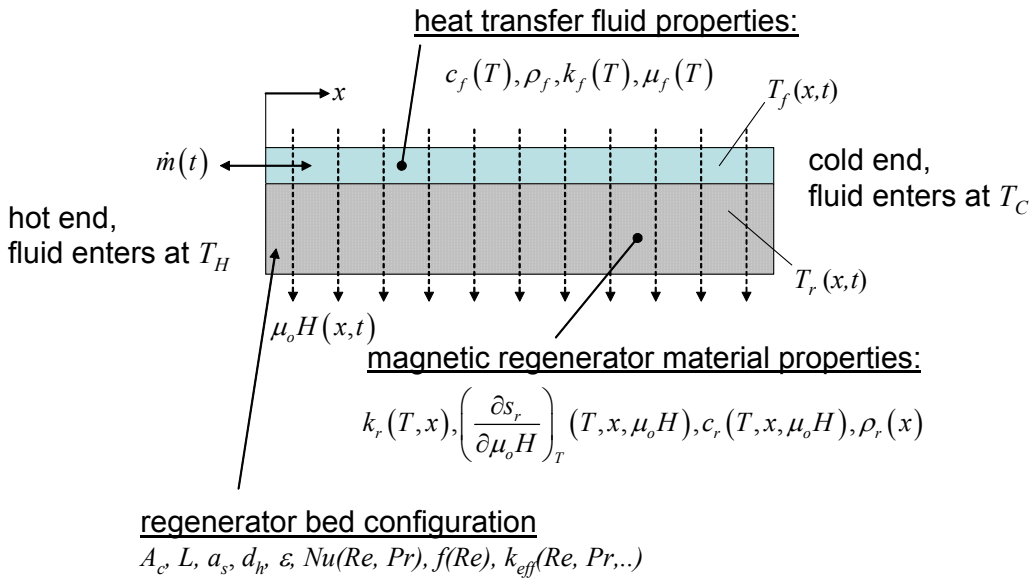

Figure 2.1. Conceptual drawing of a 1D AMR model showing the important modeling parameters

A positive fluid mass flow rate indicates that flow is in the positive x direction and therefore enters the hot end of the regenerator bed and flows towards the cold end. When flow is negative, fluid enters at the cold end and flows towards the hot end. The fluid is a liquid and is assumed to be incompressible; therefore the mass of fluid entrained in the bed is time invariant. Continuity indicates that the mass flow rate must be spatially uniform within the bed for an incompressible fluid; therefore, the specification of the mass flow rate at the boundaries alone is sufficient to determine the mass flow rate throughout the bed. The flow entering the bed is assumed to have the temperature of the adjacent thermal reservoir, T_H or T_C depending on whether the flow rate is positive or negative, respectively. It is possible to specify this temperature as a function of time during a cycle if that information is available, for example, from an auxiliary model of the heat exchangers that interface the fluid to the heat rejection reservoir and refrigeration load. The required fluid properties include the density (ρ_f), specific heat capacity (c_f), viscosity (μ_f), and

thermal conductivity (k_f); these properties are assumed to be a function of temperature but not pressure. The density of the fluid is assumed to be unaffected by either temperature or pressure, consistent with the assumption of an incompressible fluid.

The fluid flows within a regenerator matrix that is composed of a magnetic material. The magnetic material may be layered; this layering may be represented most simply as a spatial variation in the Curie temperature ($T_{Curie}(x)$) or, in a more exact model, by using different material properties for different types of materials depending on the axial location within the bed. The partial derivative of the specific entropy of the magnetic material with respect to applied field at constant temperature and the specific heat capacity of the material at constant applied field are assumed to be functions of the temperature of the material and of the applied magnetic field ($\frac{\partial s_r}{\partial \mu_o H}_T (T, \mu_o H)$ $c_{\mu_o H}(T, \mu_o H)$). The conductivity is assumed to be a function of temperature ($k_r(T)$). Some rare earth compounds, such as CeSb and $EuNi_2Si_{0.3}Ge_{1.7}$, show a change in entropy corresponding to a change in pressure, or a barocaloric effect (Strassle and Furrer, 2005). However, these materials are not currently being investigated as possible refrigerants in AMRR systems and the pressure change needed to realize the full barocaloric effect is near 20 bar, which is an order of magnitude greater than the pressure drop that can be tolerated in an efficient AMRR device. The magnetic material is assumed to have a constant density (ρ_r). Since most magnetocaloric materials are either metals or ceramics, the change in density over the typical temperature range spanned by an AMRR system (less than 100 K) should be very low.

The geometry of the matrix must consist of many small passages that place the fluid into intimate thermal contact with the regenerator material. Regenerator geometries ranging from packed beds of spheres to screens to perforated plates may be considered by this model by adjusting the thermal-fluid correlations and the geometric parameters that are used in the simulation. In order to maintain the flexibility to simulate any geometry, the regenerator geometry is characterized by a hydraulic diameter (d_h), porosity (ε), and specific surface area (a_s). For a particular geometry, the Nusselt number of the matrix is assumed to be a function of the local Reynolds number of the flow and Prandtl number of the fluid ($Nu(Re_f, Pr_f)$) and the friction factor is assumed to be a function of the local Reynolds number of the flow ($f(Re_f)$).

The matrix is characterized by an effective static thermal conductivity (k_{eff}) that relates the actual rate of axial conduction through the composite magnetic material/fluid matrix in the absence of fluid flow to the rate of conduction heat transfer that would be experienced by a comparable solid piece of material. Axial dispersion due to the eddy mixing of the fluid that occurs when fluid flows is treated as an augmentation of the thermal conductivity in the fluid (k_{disp}). The values of these thermal conductivity parameters depend on the particular geometry, materials, and flow conditions that are simulated. The overall size of the regenerator is specified by its length (L) and total cross-sectional area (A_c).

The variations of the fluid and regenerator temperature over a steady-state cycle, ($T_f(x,t)$ and $T_r(x,t)$, respectively), are the eventual outputs of the model. These temperature distributions, coupled with the prescribed mass flow rate and material properties, allow the calculation of

various cycle performance metrics including the refrigeration load and the magnetic power requirement.

The behavior of the bed is predicted by solving a set of coupled, partial differential equations in time and space. The governing partial differential equations are obtained from energy balances on the fluid and the matrix. Figure 2.2 illustrates a differential segment of the fluid with the various energy flows indicated.

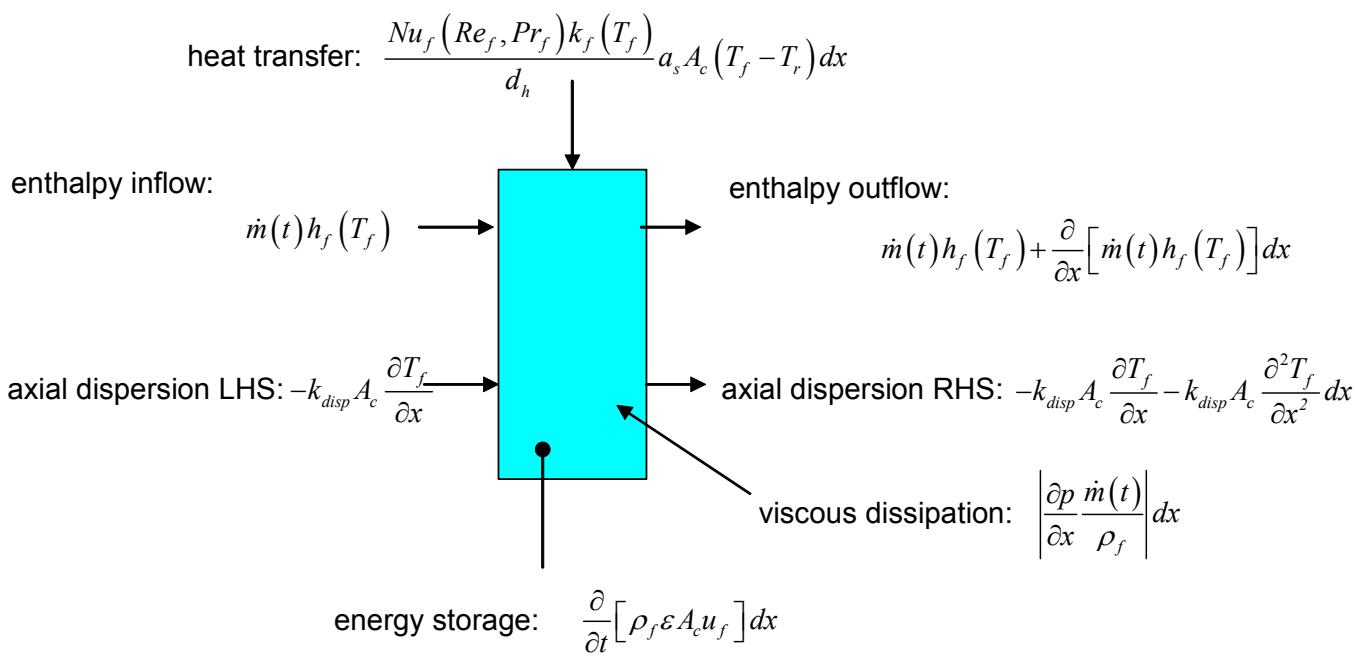

Figure 2.2. Differential segment of entrained fluid with energy terms indicated

After some simplification, the energy balance on the fluid suggested by Fig. 2.2 is:

$$k_{disp} A_c \frac{\partial^2 T_f}{\partial x^2} - \dot{m}\frac{\partial h_f}{\partial x} - \frac{Nu\, k_f}{d_h} a_s\ A_c \left(T_f - T_r\right) + \left|\frac{\partial p}{\partial x}\frac{\dot{m}}{\rho_f}\right| = \rho_f\ A_c\ \varepsilon \frac{\partial u_f}{\partial t} \qquad (2.1)$$

The first term in Eq. (2.1) represents conduction due to axial dispersion; the second term represents the change in the enthalpy carried by the fluid; the third term is the convective heat transfer between the fluid and the regenerator material; the fourth term represents viscous dissipation in the fluid, and the right side of the equation represents energy stored due to the heat capacity of the fluid entrained in the matrix. Note that static axial conduction through the fluid is considered together with the axial conduction in the bed (these components cannot be separated) and appear in the governing equation for the magnetic material. Conduction in the fluid may be non-negligible in an AMRR device due to the relatively high fluid thermal conductivity. Although axial conduction through the static fluid does not appear in Eq. (2.1), it is applied to the matrix and modeled using the concept of an effective static bed conductivity. The dispersive conductivity that does appear in Eq. (2.1) is much higher than the static conductivity of the fluid whenever the fluid is flowing.

After expanding the derivatives in Eq. (2.1) under the assumption that material properties are independent of pressure, assuming an incompressible fluid and substituting the definition of the friction factor in terms of the pressure gradient, the energy balance becomes:

$$k_{disp} A_c \frac{\partial^2 T_f}{\partial x^2} - \dot{m}\, c_f \frac{\partial T_f}{\partial x} - \frac{Nu\, k_f}{d_h} a_s\, A_c \left(T_f - T_r\right) + \left| \frac{f_f\, \dot{m}^3}{2\, \rho_f^2\, A_c^2\, d_h} \right| = \rho_f\, A_c\, \varepsilon\, c_f \frac{\partial T_f}{\partial t} \quad (2.2)$$

which is the final form of the governing differential equation for the fluid.

Figure 2.3 illustrates a differential segment of the regenerator material with the various energy flows indicated:

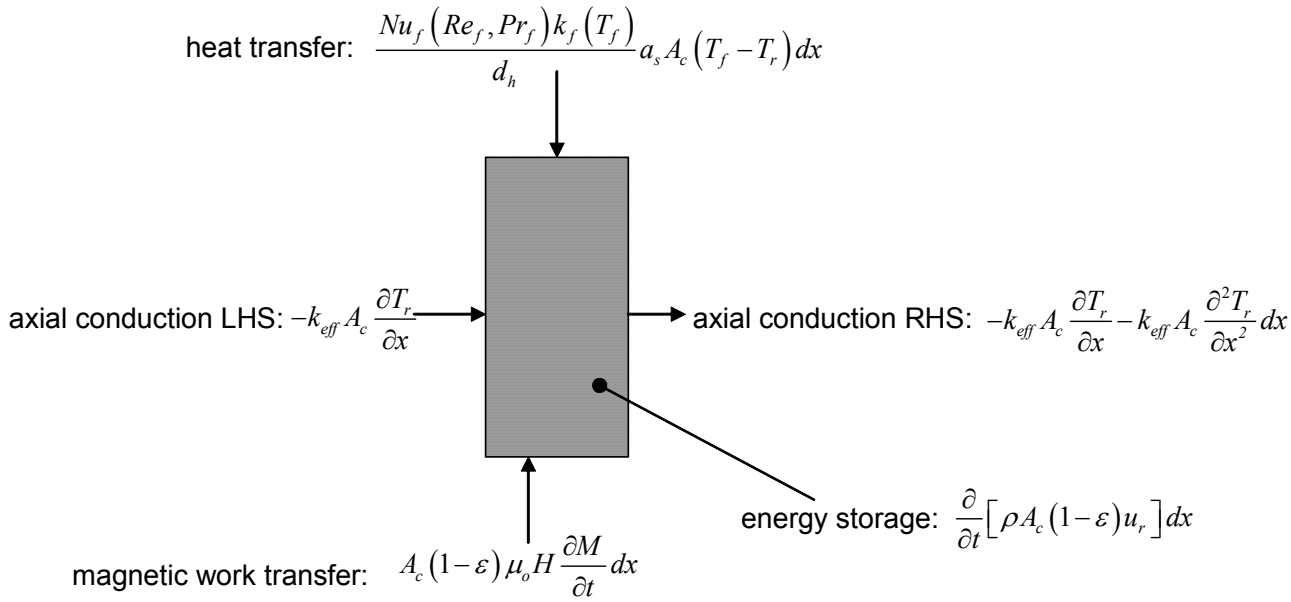

Figure 2.3. Differential segment of regenerator with energy terms indicated

The energy balance suggested by Figure 2.3 is:

$$\frac{Nu\, k_f}{d_h} a_s\ A_s \left(T_f - T_r\right) + A_c \left(1-\varepsilon\right) \mu_o H \frac{\partial M}{\partial t} + k_{eff} A_c \frac{\partial^2 T_r}{\partial x^2} = \rho_r\ A_c \left(1-\varepsilon\right) \frac{\partial u_r}{\partial t} \quad (2.3)$$

The magnetic work term is grouped with the change in the internal energy of the regenerator in order to obtain:

$$\frac{Nu\, k_f}{d_h} a_s\ A_s \left(T_f - T_r\right) + k_{eff} A_c \frac{\partial^2 T_r}{\partial x^2} = A_c \left(1-\varepsilon\right) \rho_r \left(\frac{\partial u_r}{\partial t} - \mu_o H \frac{\partial \left(v_R M\right)}{\partial t} \right) \quad (2.4)$$

The right hand side of Equation (2.4) is the difference between a differential change in internal energy and a differential magnetic work transfer; this difference must be equal to a differential heat transfer, which is related to a change in the entropy of the material. Therefore, assuming that the magnetization and demagnetization processes are internally reversible, Equation (2.4) may be rewritten according to:

$$\frac{Nu\, k_f}{d_h} a_s\, A_s \left(T_f - T_r\right) + k_{eff} A_c \frac{\partial^2 T_r}{\partial x^2} = A_c \left(1-\varepsilon\right) \rho_r\, T_r \frac{\partial s_r}{\partial t} \tag{2.5}$$

The change in regenerator entropy is divided into its temperature and magnetic field-driven components in order to yield the final form of the governing equation for the regenerator:

$$\frac{Nu\, k_f}{d_h} a_s\, A_s \left(T_f - T_r\right) + k_{eff} A_c \frac{\partial^2 T_r}{\partial x^2} = A_c \left(1-\varepsilon\right) \rho_r\, T_r \frac{\partial s_r}{\partial \mu_o H}_T \frac{\partial \mu_o H}{\partial t} + A_c \left(1-\varepsilon\right) \rho_r\, c_{\mu_o H} \frac{\partial T_r}{\partial t} \tag{2.6}$$

The fluid is assumed to enter the matrix at the temperature of the associated heat reservoir, providing the required spatial boundary conditions:

$$\begin{aligned} &\text{if } \dot{m}\left(t\right) \geq 0 \text{ then } T_f\left(x=0,t\right) = T_H \\ &\text{if } \dot{m}\left(t\right) < 0 \text{ then } T_f\left(x=L,t\right) = T_C \end{aligned} \tag{2.7}$$

The governing equations are integrated forward in time using a spatially implicit technique. A periodic steady state is achieved when the total energy change of the bed material (ΔU_r) and fluid entrained in the bed (ΔU_f) from the end of cycle k to the end of the previous cycle, k-1, normalized by the difference between the maximum and minimum value of the energy in the regenerator during a cycle (U_{max} and U_{min}, respectively) is within a convergence tolerance (*tol*). The convergence criterion is based on the total energy in the bed rather than the temperature for this model because the energy flows, such as cooling capacity and heat rejection, are the main outputs of this model. Therefore, it makes sense to consider whether the solution has converged with respect to the total energy rather than the fluid and solid temperatures. However, temperature and energy are closely related. Convergence is achieved when

$$\frac{\Delta U_f + \Delta U_r}{U_{max} - U_{min}} < tol \qquad \text{steady state} \tag{2.8}$$

where the change in fluid energy is calculated by integrating the absolute value of the energy change over the length of the bed:

$$\Delta U_f = \rho_f \varepsilon A_c \int_0^L \left| u_{f\,k} - u_{f\,k-1} \right| dx \tag{2.9}$$

and the change in regenerator energy is evaluated in a similar manner:

$$\Delta U_r = \rho_r \left(1-\varepsilon\right) A_c \int_0^L \left| u_{r\,k} - u_{r\,k-1} \right| dx \tag{2.10}$$

Rewriting Eq. (2.10) using the definition of the specific heat of the regenerator material yields

$$\Delta U_r = \rho_r \left(1-\varepsilon\right) A_c \int_0^L \left| T_{r,Nt}\, c_{\mu_o H,\,Nt} - T_{r,1}\, c_{\mu_o H,1} \right| dx \tag{2.11}$$

where Nt is the final time step in the cycle. Because the magnetic field is equal at the beginning and end of cycle, the energy change due to the magnetic work interaction is zero. The internal energy of the fluid at any time is

$$U_f = \rho_f \varepsilon A_c \int_0^L u_f dx \tag{2.12}$$

The internal energy of the regenerator material is .

$$U_r = \rho_r \left(1-\varepsilon\right) A_c \int_0^L u_r \left(\mu_0 H = 0, T\right) dx \tag{2.13}$$

As shown in Eq. (2.13), the internal energy of the regenerator is evaluated assuming the material is in a magnetic field of 0 Tesla for simplicity. U_{max} in Eq. (2.8) is defined as the maximum value of the sum of the fluid and regenerator energy during one complete cycle and U_{min} is the minimum value of the sum of fluid and regenerator energy during the cycle. The numerical

solution for the fluid and regenerator temperature is obtained over a spatial grid that extends from 0 to L and the fluid and regenerator temperatures at each node correspond to their values at the center of each control volume as shown in Figure 2.4.

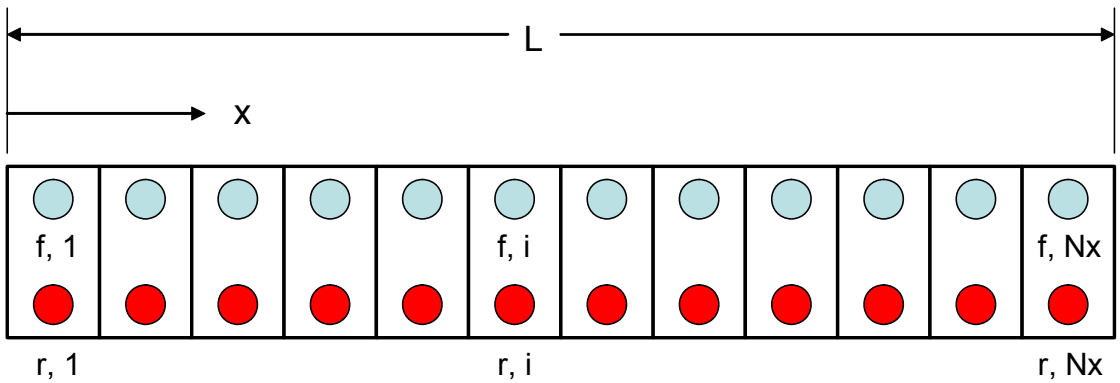

Figure 2.4. Numerical grid used for fluid and regenerator temperature solutions

The axial location of each fluid and regenerator temperature node (x_i) is given by:

$$x_i = \left(i - \frac{1}{2}\right)\frac{L}{Nx} \quad i=1..Nx \tag{2.14}$$

where i is the axial subscript and Nx is the total number of axial control volumes that are used. The cycle time is discretized according to:

$$t_j = j\frac{\tau}{Nt} \quad j=0..Nt \tag{2.15}$$

where j is the temporal subscript and Nt is the total number of time steps that are used. Initial values for the temperatures at each spatial node ($T_{r\,i,1}$ and $T_{f\,i,1}$) can be assigned arbitrarily. One possibility is an assumed linear temperature profile, although other options have been explored in order to speed the convergence to a cyclic steady state.

$$T_{r\,i,1} = T_H - \frac{x_i}{L}\left(T_H - T_C\right) \quad i=1..Nx \tag{2.16}$$

$$T_{f\,i,1} = T_H - \frac{x_i}{L}\left(T_H - T_C\right) \quad i=1..Nx \tag{2.17}$$

The changes in fluid and regenerator properties over a small time step are neglected so that the temperatures at time step j+1 are obtained using the discretized governing equations with constant properties that are evaluated using the temperatures at time step j. The fluid energy balance from Eq. (2.2) is discretized and written for each control volume.

$$\begin{aligned}
&\frac{Nu_{i,j}\,k_{f\,i,j}}{d_h}\frac{a_s\,A_c L}{Nx}\left(T_{r\,i,j+1} - T_{f\,i,j+1}\right) + \dot{m}\left(t_j\right)c_{f\,i,j}\left(\frac{T_{f\,i,j+1} + T_{f\,i-1,j+1}}{2} - \frac{T_{f\,i+1,j+1} + T_{f\,i,j+1}}{2}\right) \\
&+\left|\frac{f_{f\,i,j}\,\dot{m}\left(t_j\right)^3 L}{2\,\rho_f^2\,A_c^2\,d_h\,Nx}\right| + k_{disp\,i,j}A_c\frac{Nx}{L}\left(T_{f\,i-1,j+1} - T_{f\,i,j+1}\right) + k_{disp\,i,j}A_c\frac{Nx}{L}\left(T_{f\,i+1,j+1} - T_{f\,i,j+1}\right) \\
&= \rho_f A_c \varepsilon c_f \frac{L\,Nt}{Nx\,\tau}\left(T_{f\,i,j+1} - T_{f\,i,j}\right) \qquad\qquad i = 2..Nx-1
\end{aligned} \tag{2.18}$$

where $Nu_{i,j}$ is the Nusselt number based on the fluid temperature values in the node,

$$Nu_{i,j} = Nu\left(Re_{f\,i,j}, Pr_{f\,i,j}\right) \tag{2.19}$$

$Re_{f\,i,j}$ is the Reynolds number for the fluid computed using the fluid temperature and the free flow velocity and $Pr_{f\,i,j}$ is the Prandtl number of the fluid:

$$Re_{f\,i,j} = \frac{d_h\left|\dot{m}\left(t_j\right)\right|}{A_c\,\mu_{f\,i,j}} \tag{2.20}$$

$$Pr_{f\,i,j} = \frac{c_{f\,i,j}\mu_{f\,i,j}}{k_{f\,i,j}} \tag{2.21}$$

The friction factor ($f_{f\,i,j}$) in Equation (2.18) is evaluated in terms of the local Reynolds number, which depends upon the fluid temperatures within the node:

$$f_{f\,i,j} = f_f\left(Re_{f\,i,j}\right) \tag{2.22}$$

The boundary conditions for the fluid temperature governing equation are assigned such that the fluid that enters at either edge of the regenerator has the temperature of the corresponding reservoir, that the boundaries of the bed are adiabatic with respect to dispersive heat transfer, and there is no heat loss through the regenerator walls. At the boundaries of the regenerator bed, the energy balance depends upon the fluid flow direction. The discretized fluid equations at the hot end of the regenerator bed are:

$$\begin{aligned}
&\textit{if } \dot{m}\left(t_j\right) \geq 0 \quad \textit{then} \\
&\frac{Nu_{1,j}\, k_{f\,1,j}}{d_h}\frac{a_s\, A_c L}{Nx}\left(T_{r\,1,j+1} - T_{f\,1,j+1}\right) + \dot{m}\left(t_j\right) c_{f\,1,j}\left(T_H - \frac{T_{f\;2,j+1} + T_{f\;1,j+1}}{2}\right) \\
&+\left|\frac{f_{f\;1,j}\,\dot{m}\left(t_j\right)^3 L}{2\,\rho_f^2\, A_c^2\, d_h\, Nx}\right| + k_{disp\;1,j} A_c \frac{Nx}{L}\left(T_{f\;2,j+1} - T_{f\;1,j+1}\right) = \rho_f A_c \varepsilon\, c_f \frac{L\,Nt}{Nx\,\tau}\left(T_{f\;1,j+1} - T_{f\;1,j}\right) \quad \text{for } i = 1
\end{aligned} \tag{2.23a}$$

$$\begin{aligned}
&\textit{if } \dot{m}\left(t_j\right) < 0 \quad \textit{then} \\
&\frac{Nu_{1,j}\, k_{f\,1,j}}{d_h}\frac{a_s\, A_c L}{Nx}\left(T_{r\,1,j+1} - T_{f\,1,j+1}\right) - \dot{m}\left(t_j\right) c_{f\,1,j}\left(\frac{T_{f\;2,j+1} + T_{f\;1,j+1}}{2} - \left(\frac{3}{2}T_{f\;1,j+1} - \frac{1}{2}T_{f\;2,j+1}\right)\right) \\
&+\left|\frac{f_{f\;1,j}\,\dot{m}\left(t_j\right)^3 L}{2\,\rho_f^2\, A_c^2\, d_h\, Nx}\right| + k_{disp\;1,j} A_c \frac{Nx}{L}\left(T_{f\;2,j+1} - T_{f\;1,j+1}\right) = \rho_f A_c \varepsilon\, c_f \frac{L\,Nt}{Nx\,\tau}\left(T_{f\;1,j+1} - T_{f\;1,j}\right) \quad \text{for } i = 1
\end{aligned} \tag{2.23b}$$

Note that the temperature of each node is evaluated at the center of the node. Therefore, the temperature of the fluid exiting the hot end of the bed is approximated by extrapolating the

temperatures in nodes 1 and 2 down to $x = 0$. For node Nx (the cold end of the bed), the energy balances are:

$$if\ \dot{m}\left(t_j\right) \geq 0 \quad then$$

$$\frac{Nu_{Nx,j}\, k_{f\,Nx,j}}{d_h} \frac{a_s\, A_c L}{Nx} \left(T_{r\,Nx,j+1} - T_{f\,Nx,j+1}\right) + \dot{m}\left(t_j\right) c_{f\,Nx,j} \left(\frac{T_{f\,Nx,j+1} + T_{f\,Nx\text{-}1,j+1}}{2} - \left(\frac{3}{2} T_{f\,Nx,j+1} - \frac{1}{2} T_{f\,Nx\text{-}1,j+1} \right) \right)$$

$$+ \left| \frac{f_{f\,Nx,j}\, \dot{m}\left(t_j\right)^3 L}{2\, \rho_f^2\, A_c^2\, d_h\, Nx} \right| + k_{disp\,Nx,j}\, A_c \frac{Nx}{L} \left(T_{f\,Nx\text{-}1,j+1} - T_{f\,Nx,j+1}\right) = \rho_f A_c \varepsilon\, c_f \frac{L\, Nt}{Nx\, \tau} \left(T_{f\,Nx,j+1} - T_{f\,Nx,j}\right) \qquad \text{for } i{=}Nx$$

(2.24a)

$$if\ \dot{m}\left(t_j\right) < 0 \quad then$$

$$\frac{Nu_{Nx,j}\, k_{f\,Nx,j}}{d_h} \frac{a_s\, A_c L}{Nx} \left(T_{r\,Nx,j+1} - T_{f\,Nx,j+1}\right) - \dot{m}\left(t_j\right) c_{f\,Nx,j} \left(T_C - \frac{T_{f\,Nx,j+1} + T_{f\,Nx\text{-}1,j+1}}{2} \right)$$

$$+ \left| \frac{f_{f\,Nx,j}\, \dot{m}\left(t_j\right)^3 L}{2\, \rho_f^2\, A_c^2\, d_h\, Nx} \right| + k_{disp\,Nx,j} A_c \frac{Nx}{L} \left(T_{f\,Nx\text{-}1,j+1} - T_{f\,Nx,j+1}\right) = \rho_f A_c \varepsilon\, c_f \frac{L\, Nt}{Nx\, \tau} \left(T_{f\,Nx,j+1} - T_{f\,Nx,j}\right) \qquad \text{for } i{=}Nx$$

(2.24b)

The regenerator energy balances are likewise discretized and written for each control volume:

$$\frac{Nu_{f\,i,j}\, k_{f\,i,j}}{d_h} a_s\, A_s \frac{L}{Nx} \left(T_{r\,i,j+1} - T_{f\,i,j+1}\right) + A_c \frac{L}{Nx} (1-\varepsilon)\, \rho_r\, c_{\mu_o H\,i,j} \frac{\left(T_{r\,i,j+1} - T_{r\,i,j}\right) Nt}{\tau}$$

$$+ \frac{Nx\, k_{eff\ i,j}\, A_c}{L} \left[T_{r\,i,j+1} - T_{r\,i-1,j+1} \right] + \frac{Nx\, k_{eff\ i,j}\, A_c}{L} \left[T_{r\,i,j+1} - T_{r\,i+1,j+1} \right] =$$

$$-A_c\, (1-\varepsilon)\, \rho_r T_{r\,i,j} \left(\frac{\partial s_r}{\partial \mu_o H} \right)_{i,j} \frac{\partial \mu_o H}{\partial t} \left(x_i, \frac{t_{j+1} + t_j}{2} \right) \qquad i = 2..Nx-1$$

(2.25)

Note that the 3rd and 4th terms in Eq. (2.25) represent conduction to the neighboring control volumes on the left- and right-hand sides, respectively. The hot and cold ends of the regenerator are assumed adiabatic. Neglecting conduction at the edge of the bed, the energy balance at the hot end is:

$$\frac{Nu_{f\,1,j}\,k_{f\,1,j}}{d_h}a_s\,A_s\frac{L}{Nx}\left(T_{r\,1,j+1}-T_{f\,1,j+1}\right)+A_c\frac{L}{Nx}(1-\varepsilon)\,\rho_r\,c_{\mu_o H\,1,j}\frac{\left(T_{r\,1,j+1}-T_{r\,1,j}\right)Nt}{\tau}$$
$$+\frac{Nx\,k_{eff\,1,j}\,A_c}{L}\left[T_{r1,j+1}-T_{r2,j+1}\right]=-A_c\,(1-\varepsilon)\,\rho_r\,T_{r\,1,j}\left(\frac{\partial s_r}{\partial\mu_o H}\right)_{1,j}\frac{\partial\mu_o H}{\partial t}\left(x_1,\frac{t_{j+1}+t_j}{2}\right) \tag{2.26}$$

Neglecting conduction at the cold end, the energy balance at the cold end is:

$$\frac{Nu_{f\,Nx,j}\,k_{f\,Nx,j}}{d_h}a_s\,A_s\frac{L}{Nx}\left(T_{r\,Nx,j+1}-T_{f\,Nx,j+1}\right)+A_c\frac{L}{Nx}(1-\varepsilon)\,\rho_r\,c_{\mu_o H\,Nx,j}\frac{\left(T_{r\,Nx,j+1}-T_{r\,Nx,j}\right)Nt}{\tau}$$
$$+\frac{Nx\,k_{eff\,m,j}\,A_c}{L}\left[T_{r\,Nx,j+1}-T_{r\,Nx-1,j+1}\right]=-A_c\,(1-\varepsilon)\,\rho_r\,T_{r\,Nx,j}\left(\frac{\partial s_r}{\partial\mu_o H}\right)_{Nx,j}\frac{\partial\mu_o H}{\partial t}\left(x_{Nx},\frac{t_{j+1}+t_j}{2}\right) \tag{2.27}$$

2.2. NUMERICAL SOLUTION ALGORITHM

Equations (2.18), (2.23), (2.24) and (2.25)-(2.27) form a system of linear equations in terms of each of the nodal regenerator and fluid temperatures that are shown in Figure 2.4 at one step forward in time (i.e., at time j+1). These equations are solved using a sparse matrix decomposition algorithm in order to take an implicit step forward in time. The model is first order accurate in time and, because it uses an implicit integration technique, the solution is unconditionally stable with respect to time step duration. The solution process is repeated in order to determine the fluid and regenerator temperatures at all spatial nodes and for each time

step over an entire cycle. At the end of each cycle, the change in energy in the regenerator and fluid is evaluated by performing the integration presented in equations (2.9) and (2.11) numerically and compared to the total energy in the fluid at the end of the cycle. When the absolute change in energy of the regenerator from cycle to cycle is within a specified tolerance, shown in Eq. (2.8), steady state has been achieved. This model is implemented in MATLAB, and the MATLAB code is given in Appendix A1.

2.3. MODEL VERIFICATION

There are no general analytical solutions to the regenerator equations presented above. However, the model can also be validated in the limit of a single-blow transient passive regenerator. Shitzer and Levy (1983) present an analytical solution for fluid flow through a porous solid medium given the following assumptions:

- the properties of the fluid and solid materials are constant,
- there are no internal temperature gradients in the solid material,
- there is no axial conduction or axial dispersion in the bed,
- the solid material and the fluid initially entrained in the porous medium are at a uniform initial temperature (the reference temperature of the problem, taken to be 0 K),
- the bed geometry is uniform; no spatial gradients exist in the bed characteristics such as heat transfer coefficient, porosity, etc.,
- fluid enters the bed at a constant temperature, T_H, at x=0 starting at t=0, and
- the fluid flow is one-dimensional; flow maldistribution effects are neglected and the heat transfer coefficient is constant.

Under these conditions, the temperatures of the fluid and solid (T_r and T_f) are given by the following expressions.

$$T_r = T_H \exp(-y-z) \sum_{n=1}^{\infty} \sum_{m=0}^{\infty} \frac{y^m z^{m+n}}{m!(m+n)!} \tag{2.28}$$

$$T_f = T_H \exp(-y-z) \sum_{n=0}^{\infty} \sum_{m=0}^{\infty} \frac{y^m z^{m+n}}{m!(m+n)!} \tag{2.29}$$

where the parameters y and z are defined as

$$y = \frac{h_v \, A_c \, x}{\rho_f \, c_f \, \dot{m}_f} \tag{2.30}$$

$$z = \frac{h_V}{\rho_r \, c_r \, (1-\varepsilon)} \left(t - \frac{\varepsilon \, A_c \, x}{\dot{m}_f} \right) \tag{2.31}$$

where h_V is the heat transfer coefficient expressed on a per volume of regenerator basis, ε is the porosity of the bed, t is time, $\dot{m}_f$ is the fluid mass flow rate, A_c is the cross sectional area of the regenerator, ρ_r and ρ_f are the density of the solid regenerator material and fluid, c_r and c_f are the specific heat of the solid regenerator material and fluid, m and n are counters used for the summation process, and x is the position in the bed. This set of equations is known as the Schumann solution and is used here to verify the predicted fluid and solid temperatures from the explicit AMRR model. The Schumann solution provides valuable verification as the heat capacity, an important effect in an AMRR system, is accurately considered. The modeling parameters used for the comparison are given in Table 2.1. The material properties used for the comparison are similar to those of water and stainless steel.

Table 2.1. Parameters used for model comparison with the Schumann solution.

Parameter	Value	Parameter	Value
inlet fluid temperature, T_H	30 K	NTU	50
density of fluid, ρ_f	1000 kg/m^3	density of solid, ρ_r	8900 kg/m^3
heat capacity of fluid, c_f	4200 J/kg-K	heat capacity of solid, c_r	500 J/kg-K
length of bed, L	1 m	flow period	100 s
total bed volume	8 L	fluid mass flow rate, $\dot{m}_f$	0.005 kg/s
bed cross-sectional area, A_c	0.001 m^2	bed porosity, ε	0.36

The temperatures of the fluid and regenerator are given as infinite sums in Eqs. (2.28) and (2.29); the infinite sums are approximated by summing the first 160 terms of these equations. The magnitude of the 161st term in the sum is less than 1x10^{-9} K, so the first 160 terms is an excellent approximation of the infinite series. The number of thermal transfer units, *NTU*, is defined as

$$NTU = \frac{h_V\, A_c\, L}{\dot{m}\, c_f} \tag{2.32}$$

The initial conditions and fluid flow functions of the AMRR model were modified to agree with the system described above. The fluid and regenerator relative temperatures were set to a uniform value of 0 K. At t=0, fluid enters the bed at x=0 at a temperature T_H. The model predictions were compared to the Schumann solution for several values of the number of time steps, *Nt*, and number of spatial nodes, *Nx*. The results were found to be a weak function of the number of spatial nodes for the passive case and therefore all results presented in this section are for *Nx*=80. The characteristic fluid length, *CFL*, is defined as the ratio of the distance the fluid travels in one time step to the length of each spatial node.

$$CFL = \frac{\dot{m}_f\, Nt}{\rho_f\, A_c\, \varepsilon\, t_{final}} \frac{Nx}{L} \tag{2.33}$$

where t_{final} is the time at the end of the simulation. The results for the fluid temperature are shown in Figure 2.5 and the results for the regenerator temperature show similar results.

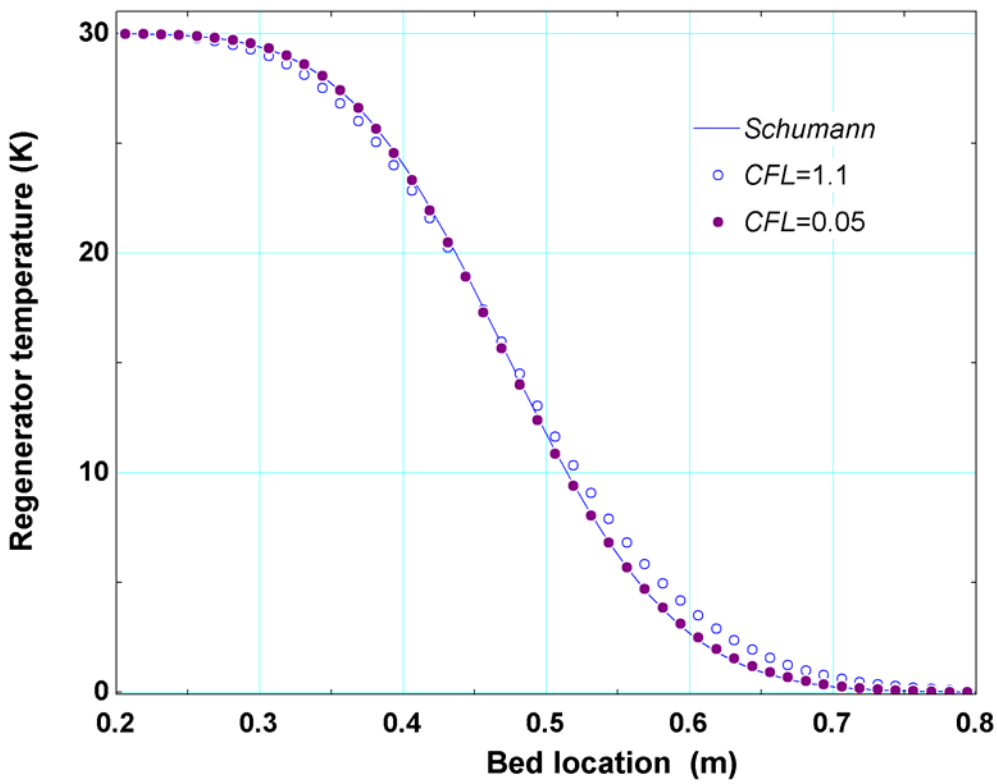

Figure 2.5. Fluid temperature predicted by the AMRR model and Schumann solution for the conditions in Table 2.1

Figure 2.5 shows good agreement between the model and the Schumann solution, provided that the number of time steps is sufficiently high. The maximum difference between the Schumann solution and the model predictions using a *CFL* of 0.05, or 2000 time steps, is 0.0661 K for the fluid and 0.0664 K for the regenerator.

The model was also verified against the solution for an oscillating passive regenerator in the limit of constant properties, no entrained fluid heat capacity and no axial conduction. A

published solution for the thermal effectiveness (ε_t) of a conventional, passive regenerator (i.e., one with no magnetocaloric effect) subjected to a stepwise mass flow rate variation (with the shape shown in Figure 2.6) is available.

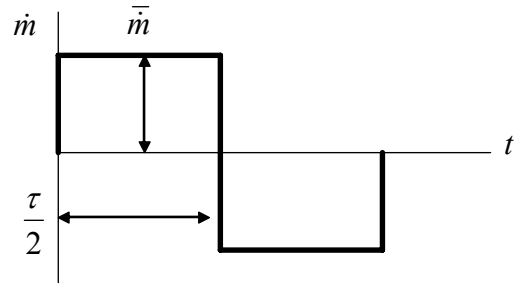

Figure 2.6. Mass flow rate variation for an idealized regenerator

According to Rohsenow et al. (1998), the thermal effectiveness (ε_t) for a regenerator with constant material properties is defined as:

$$\varepsilon_t \equiv \frac{\bar{\dot{m}}\, c_f \int_0^{\tau/2} \left(T_H - T_f\left(x = L, t\right)\right) dt}{\bar{\dot{m}}\, c_f \left(T_H - T_C\right)} \tag{2.34}$$

where $\bar{\dot{m}}$ is the magnitude of the mass flow rate function. The typical dimensionless parameters that are used to characterize this problem are the number of transfer units (*NTU*, sometimes also referred to as the reduced length of the regenerator) and the utilization ratio (*U*, the inverse of the matrix capacity rate ratio, Ackermann (1997)).

$$NTU \equiv \frac{Nu\, k_f\, a_s\, L\, A_c}{d_p\, \bar{\dot{m}}\, c_f} \tag{2.35}$$

$$U = \frac{\bar{\dot{m}}\, c_f\, \tau}{2\, A_c\, L\left(1-\varepsilon\right)\rho_r\, c_{\mu_o H}} \tag{2.36}$$

Dragutinovic and Baclic (1998) present tables for ε_t as a function of *NTU* and *U* in this limit. The numerical model can be verified against this solution by:

1. setting all fluid properties (c_f, k_f, ρ_f, and μ_f) equal to constants,
2. setting the partial derivative of entropy with respect to magnetic field equal to zero,
3. setting the remaining regenerator properties ($c_{\mu_o H}$ and ρ_r) equal to constants,
4. setting the effective thermal conductivity of the matrix (k_{eff}) and dispersion (k_{disp}) equal to zero,
5. setting the friction factor (f) equal to zero,
6. setting the specific surface area of the regenerator (a_s), particle diameter (d_p) and bed size (A_c and L) equal to constants,
7. applying the functional form of the mass flow rate shown in Figure 2.6 for a fixed cycle duration $\left(\tau\right)$,

$$\dot{m}\left(t\right) = sign\left(\frac{\tau}{2} - t\right)\bar{\dot{m}} \tag{2.37}$$

8. and setting the porosity (ε) to zero in order to specify zero entrained fluid heat capacity.

By varying the Nusselt number (Nu_f) and mass flow rate ($\bar{\dot{m}}$), it is possible to vary *NTU* and *U*. The numerical model was implemented under these conditions using a grid with 100 spatial control volumes (Nx = 100) and 3000 time steps (Nt = 3000). The results are illustrated in Figure 2.7. Notice the excellent agreement between the published and predicted results, verifying the

accuracy of the numerical model in this limit. The results in Figure 2.7 are plotted in the region were effectiveness is greater than 0.9 in Figure 2.8.

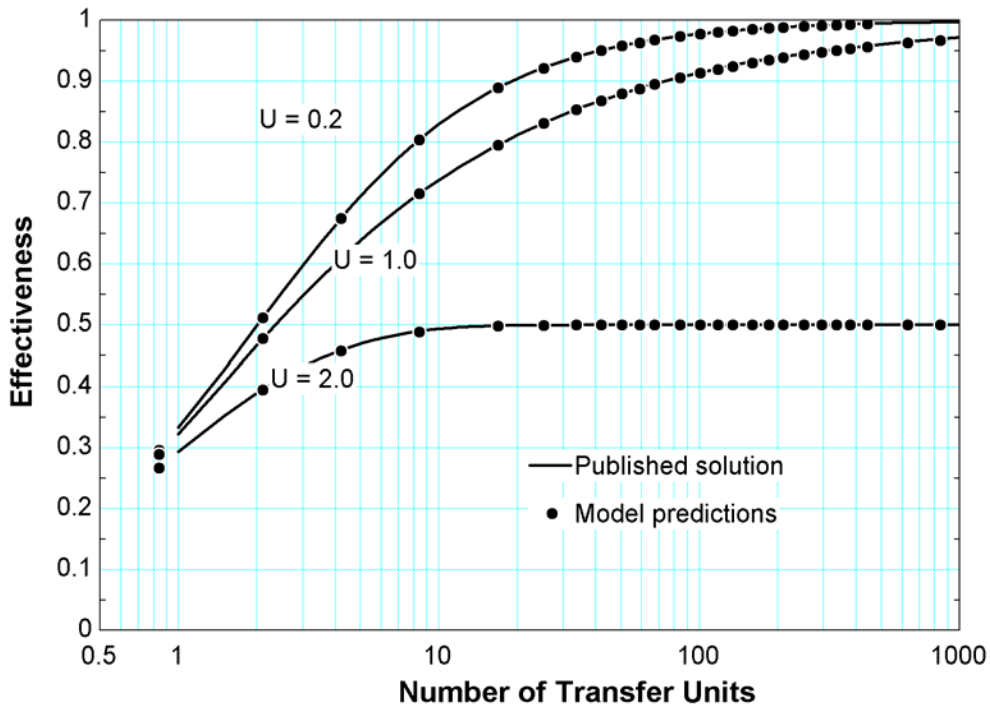

Figure 2.7. Numerical model predictions and published results for ε_t as a function of *NTU* and various values of *U* in the ideal regenerator limit

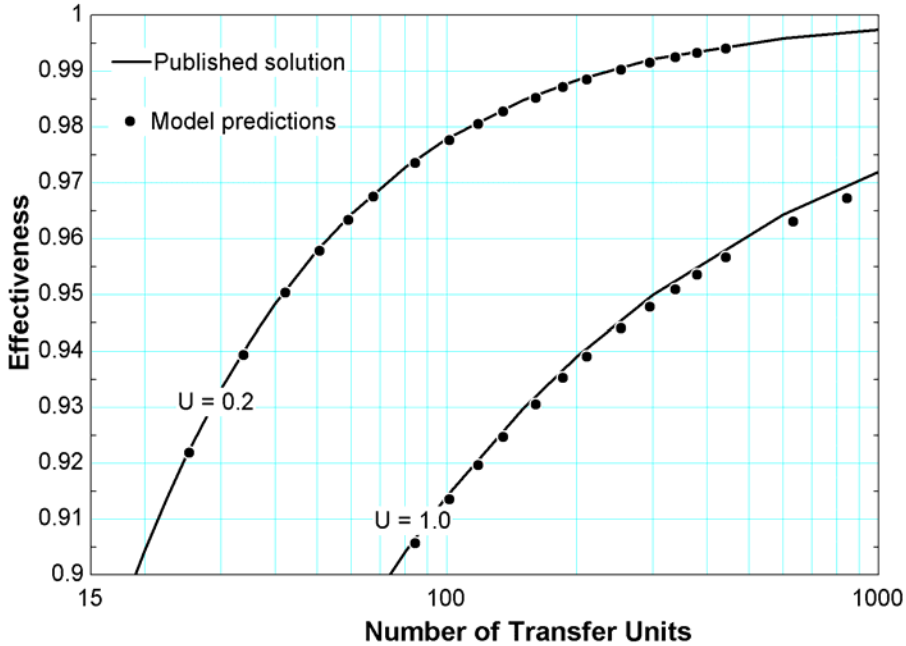

Figure 2.8. Numerical model predictions and published results from Figure 2.7 in the region $\varepsilon_t > 0.9$

2.3.1 Validation of the Magnetic Work Interaction

In order to check that the magnetic work term is correctly implemented in the regenerator governing equations, the adiabatic temperature difference predicted by the numerical model is compared to the adiabatic temperature change calculated from the magnetocaloric material properties. This comparison verifies that the material properties are self-consistent and that the numerical grid used to model the adiabatic magnetization is sufficient.

To simulate an adiabatic magnetization of the regenerator material, the Nusselt number and thermal conductivity in the AMRR model are set to zero, and the magnetic field is ramped linearly from 0 to the final value in the absence of any fluid flow rate. To determine the adiabatic temperature change at a given temperature, the entire regenerator is set to an initial temperature, the magnetic field is ramped to the final value, and the resulting temperature is

recorded. During magnetization, the magnetic field increases by a value of 0.007 Tesla per time step. Figure 2.9 shows the adiabatic temperature change calculated by the AMRR model as well as the adiabatic change when magnetized from 0 to 1 Tesla. The material properties are determined using the mean field model for pure gadolinium. Figure 2.9 shows excellent agreement between the adiabatic temperature predicted by the model and determined from material properties.

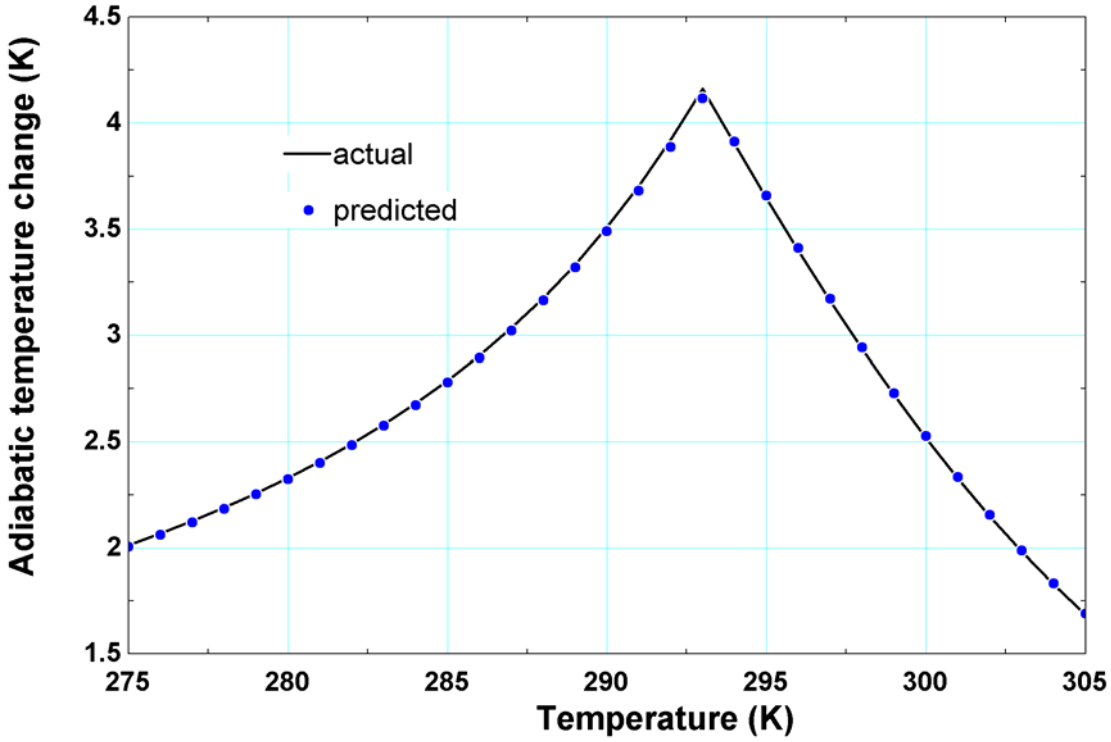

Figure 2.9. Adiabatic temperature change of gadolinium vs. temperature when magnetized from 0 to 1 Tesla determined from AMRR model and property values

2.4 MAGNETOCALORIC MATERIAL PROPERTIES

The two most important modeling inputs associated with regenerator material are the constant field specific heat capacity, $c_{\mu_0 H}$, and the partial derivative of entropy with respect to magnetic field, $\left(\partial s / \partial \mu_0 H \right)_T$. The magnetocaloric properties are an important modeling input for active magnetic regenerators; however, property data that are sufficiently smooth, resolved, and thermodynamically consistent can be difficult to obtain. There are currently no widely accepted equations of state for magnetocaloric materials and experimental uncertainty can cause empirical property values to be thermodynamically inconsistent and lead to numerical instabilities. As shown in Eq. (2.6), the magnetic work term is calculated using the partial differential of entropy with respect to magnetic field, which means that the entropy data must be well-behaved to ensure that the simulation prediction obeys the 2nd law of thermodynamics. Other models avoid this difficulty by assuming the magnetization and demagnetization of the regenerator are adiabatic processes. However, the assumption of an adiabatic magnetization and demagnetization of the regenerator severely limits the usefulness and accuracy of the model because it neglects the heat transfer between the solid regenerator and heat transfer fluid during zero-flow periods. Also, it may be desirable (or unavoidable) to have simultaneous magnetization and fluid flow. Assuming adiabatic magnetization can cause modeling error for some regenerator geometries or cycle configurations.

In order to obtain a thermodynamically consistent set of property data for any magnetocaloric material, the specific heat at constant magnetic field and the differential of entropy with respect

to magnetic field are calculated by numerically differentiating entropy data for the material. Therefore the entropy for a range of magnetic fields and temperatures must be known for any material that is to be modeled. Three methods of determining the entropy of the material are used in this project: interpolation of empirical data, the mean field model of a ferromagnet, and fitting curves to empirical data. Each method has its own advantages and difficulties; the three methods are discussed below.

2.4.1 Interpolation of Empirical Data

Experimental property data can be acquired using several methods, but the most common is to measure the material's specific heat over a range of temperatures at several values of applied magnetic fields. This data can be used to generate entropy curves by setting a 0 entropy reference temperature, T_{ref}, that is much less than the Curie temperature. Because the magnetocaloric effect is only substantial near the Curie temperature of the material, it is assumed that there is no entropy change with magnetization at the reference temperature given that T_{ref} provided that it is well below the Curie temperature. Therefore, the entropy at each magnetic field can be calculated according to:

$$s = \int_{T_{ref}}^{T} c_{\mu_0 H} \frac{dT}{T} \tag{2.38}$$

The integral in Eq. (2.38) is performed at constant magnetic field. It is possible for experimental uncertainty to cause a negative magnetocaloric effect at certain temperatures and magnetic fields. For this reason care must be taken when dealing with experimental data. The technique that is generally used for experimental data is to inspect the specific heat curves and delete any points that are clearly outliers.

The reference temperature is generally chosen as the lowest temperature for which there is specific heat data at every magnetic field available. The specific heat data is then interpolated to a uniform temperature scale. The interpolated temperature scale is chosen to have approximately the same temperature range as the experimental data but with temperature increments that are approximately half the size of experimental values. The finer temperature grid used for interpolation ensures that the shape of the specific heat curves is retained. The experimental specific is interpolated using a spline technique in MATLAB. The spline interpolation tends to smooth out uncertainty in the data and generally results in specific heat curves that are acceptably smooth. The interpolated specific heat data is then integrated to generate entropy values for each magnetic field for which data is available. This technique has been applied to commercial grade gadolinium, a 94% gadolinium 6% erbium alloy, $Gd_{0.94}Er_{0.06}$, and several advanced materials that are being considered for advanced AMRR systems by companies including Astronautics.

Interpolating experimental data has the advantage that empirical data can be used as an input to the model with small amounts of manipulation. However, the technique can be sensitive to experimental uncertainty. This technique can also be problematic because experimental data for newly developed materials is generally only available at magnetic fields in 0.5 Tesla or larger increments. When calculating $\left(\partial s / \partial \mu_0 H \right)_T$ numerically, the relatively coarse magnetic field grid can cause modeling difficulties. If the interpolation technique used to determine the entropy at

intermediate magnetic fields for a given material, the coarse magnetic field mesh can result in property values that are not thermodynamically consistent.

2.4.2 Mean Field Model of the Magnetocaloric Effect

The mean field theory describes the thermodynamic properties of a ferromagnetic material, and it has been used by Valiev (2007) to calculate the magnetocaloric properties of gadolinium with acceptable accuracy. According to Valiev, the mean field model is able to predict the magnitude of the entropy change with magnetization and adiabatic temperature change of gadolinium, as well as iron and nickel, but the predicted properties near the Curie point deviate from experimental measurements. However, the mean field model is useful for AMRR modeling because it can quickly generate thermodynamically consistent property values for a wide range of temperatures and magnetic fields. Although there are discrepancies between the model and experimental data neat the Curie point, the mean field model is able to capture general trends for the properties of gadolinium and other magnetocaloric materials.

According to Dinesen (2004), the constant field specific heat capacity of a magnetocaloric material at any temperature and magnetic field can be written as a combination of the lattice heat capacity (c_{lat}), the conduction electron heat capacity (c_{el}), and magnetic heat capacity (c_{mag}) as shown below.

$$c_{\mu_0 H} = c_{lat} + c_{el} + c_{mag} \tag{2.39}$$

where $c_{\mu_0 H}$ is the total constant field heat capacity. The first term on the right hand side of Eq. (2.39) is calculated using the Debye model given by Dinesen (2004).

$$c_{lat} = 9\,n\,k_B \left(\frac{T}{T_D}\right)^3 \int_0^{T_D/T} \frac{x^4 \exp(x)}{\left(\exp(x)-1\right)^2} dx \tag{2.40}$$

where x is an integration variable, n is the number of atoms per unit mass, k_B is the Boltzmann constant, and T_D is the Debye temperature of the material. The portion of the heat capacity contributed by the free electron is given by the Sommerfeld theory.

$$c_{el} = \gamma_{el}\, n_{el}\, T \tag{2.41}$$

where γ_{el} is a material-dependent constant that is proportional to the density of electronic levels at the Fermi level and n_{el} is the number of conduction electrons per unit mass. The magnetic portion of the constant field heat capacity is calculated using the mean field magnetic theory. The mean field theory is discussed in detail by Smart (1966) and is based on the Weiss model of magnetization of a ferromagnetic material with some modification. The mean field model applies to materials that undergo a second order magnetic phase transition. According to the mean field theory, the magnetization (M) is given in Eq. (2.42) as a function of temperature and applied field. Equation (2.42) is equivalent to the thermodynamic equation of state for the ferromagnetic portion of the material properties.

$$M\left(T, \mu_o H\right) = n_s\, g_L\, J\, B_J\left(\alpha\right) \tag{2.42}$$

where n_s is the number of magnetic spins per mass, g_L is the Lande factor which is material dependent, J is the total molecular angular momentum number which depends on orbit and spin of electrons in the material, and $B_J(\alpha)$ is the Brillouin function, which is defined as

$$B_J\left(\alpha\right) = \frac{2J+1}{2J}\coth\left(\frac{2J+1}{2J}\alpha\right) - \frac{1}{2J}\coth\left(\frac{1}{2J}\alpha\right) \tag{2.43}$$

The argument to the Brillouin function, α, is the solution to the two simultaneous equations, (2.44) and (2.45).

$$\psi = B(\alpha) \tag{2.44}$$

$$\alpha = \frac{g_L \, \mu_B \, \mu_0 H}{k_B \, T} + \frac{3 T_{Curie} \, J}{T(J+1)} \psi \tag{2.45}$$

where μ_B is the Bohr magneton, a fixed physical constant, and T_{Curie} is the Curie temperature of the material. The magnetic contribution to the total internal energy, U_{mag}, is the integration of the differential magnetic work, given by:

$$U_{mag} = -\int \mu_0 H_{tot} \, dM \tag{2.46}$$

where $\mu_0 H_{tot}$ is the total magnetic field, which is a sum of the external magnetic field and the internal field, $\mu_0 H_{int}$.

$$\mu_0 H_{int} = \frac{3 k_B \, T}{n_s \, g_L^2 \, \mu_B^2 \, J(J+1)} M \tag{2.47}$$

Using the definition of the constant field specific heat capacity, $(\partial U / \partial T)_{\mu_0 H}$, the magnetic portion of the heat capacity is

$$c_{mag} = -\mu_0 H \frac{\partial M}{\partial T} - \frac{1}{2} \frac{3 k_B \, T}{n_s \, g_L^2 \mu_B^2 \, J(J+1)} \frac{\partial M^2}{\partial T} \tag{2.48}$$

Subsituting Eqs. (2.40), (2.41), into (2.48) allow us to calculate the total constant field specific heat using the mean field theory with Eq. (2.39). The entropy can then be calculated from the specific heat.

$$S = \int_0^T \frac{c_{\mu_0 H}}{T} dT \tag{2.49}$$

A routine that calculates the entropy of a magnetic material for a given temperature and magnetic field has been implemented in MATLAB, and the code was provided by Petersen (2007). The integral for the Debye model given in Eq. (2.40) is evaluated numerically using Simpson's method. The simultaneous Eqs. (2.43), (2.44), and (2.45) are solved using the fzero function in MATLAB. There are several inputs to the mean field theory that are specific to each material, the Debye temperature, the Lande factor, the total angular momentum number, the number of magnetic spins per mass, and the Curie temperature. For pure gadolinium the inputs to the mean field model are given by Valiev (2007) and are shown in Table 2.2.

Table 2.2. Inputs used in the mean field magnetic model to calculate the material properties of pure gadolinium

Parameter	Value
Debye temperature, T_D	169 K
Lande factor, g_L	2
total angular momentum number, J	3.5
number of magnetic spins per mass, n_e	2.88e-24 kg^{-1}
Curie temperature, T_{Curie}	293 K
molar mass	0.15725 kg/mol
Sommerfeld constant, γ_{el}	0.0109 J/mol-K^2

Using the inputs from Table 2.2, the properties of pure gadolinium can be computed. Figure 2.10 shows the calculated value for the isothermal entropy change with magnetization for pure gadolinium when it is magnetized from 0 to 1.5 Tesla. Figure 2.10 also shows the entropy change for commercial grade gadolinium measured experimentally (Zimm and Gschneidner, 2005). Because of impurities in commercial grade gadolinium, the isothermal entropy change is noticeably lower than pure gadolinium; however, the shape of the entropy change curve is similar. Examination of the shape of the experimental data curve and the mean field model reveals there are some discrepancies between the two. The mean field model predicts that there is a sharp spike in entropy change at the Curie point while the experimental curve is smooth.

The mean field theory tends to over-predict the entropy change at temperatures below the Curie point and tends to under-predict the entropy change at temperatures above the Curie point. The mean field curve has a shallower curve below the Curie temperature than the experimental curve and has a steeper curve above the Curie point. Although there are discrepancies between the mean field theory and experimental data, it can be an effective tool for AMRR modeling because it generates smooth property values over very large ranges of temperature and magnetic field and eliminates difficulties that can arise when dealing with uncertainty in experimental data. It is possible to modify some of the material parameters listed in Table 2.2 in order to create a better fit to experimental data, and further discussion is given in later chapters.

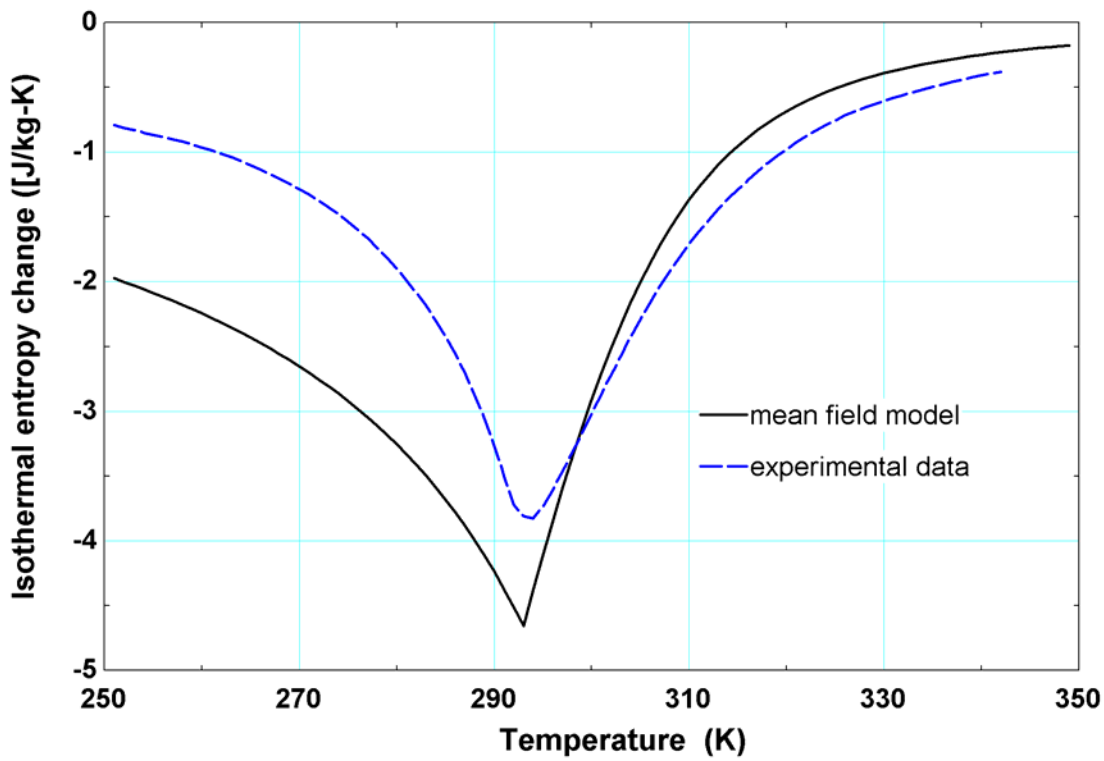

Figure 2.10. Isothermal entropy change of pure gadolinium when magnetized from 0 to 1.5 Tesla predicted by the mean field model and based on experimental data.

The mean field model is advantageous because it can generate thermodynamically consistent property data at any practical magnetic field and temperature. The inputs in Table 2.2 can be modified to build artificial material properties that can be used in parametric studies or used to model the effects of varying the magnetocaloric effect. The mean field model was developed for a second order magnetic transitions material (SOMT) and is not directly applicable to first order (FOMT) materials. The disadvantage of the mean field model is that the governing equations do not lend themselves to fitting experimental data with high accuracy. If the property values used in the model must be very close to experimental values, the mean field model is not a good method to generate entropy curves.

2.4.3 Curve Fitting Specific Heat Curves

A method that is conceptually similar to interpolating experimental data directly, discussed in Section 2.4.1, is to fit curves to the specific heat at each magnetic field. For the AMRR model to produce accurate performance predictions, the magnetocaloric material properties should be smooth and thermodynamically consistent. Therefore, experimental data generally has to be smoothed before it can be used by the model; this procedure accomplishes this smoothing by curve fitting which has the additional benefit of providing a computationally efficient, analytical model of the entropy.

The first step in obtaining a curve for heat capacity as a function of temperature is to separate the lattice portion of the data from the magnetic portion of the data. Figure 2.11 illustrates the difference between the lattice portion of the data and the magnetic portion for $HoCo_2$, which is representative of an FOMT material.

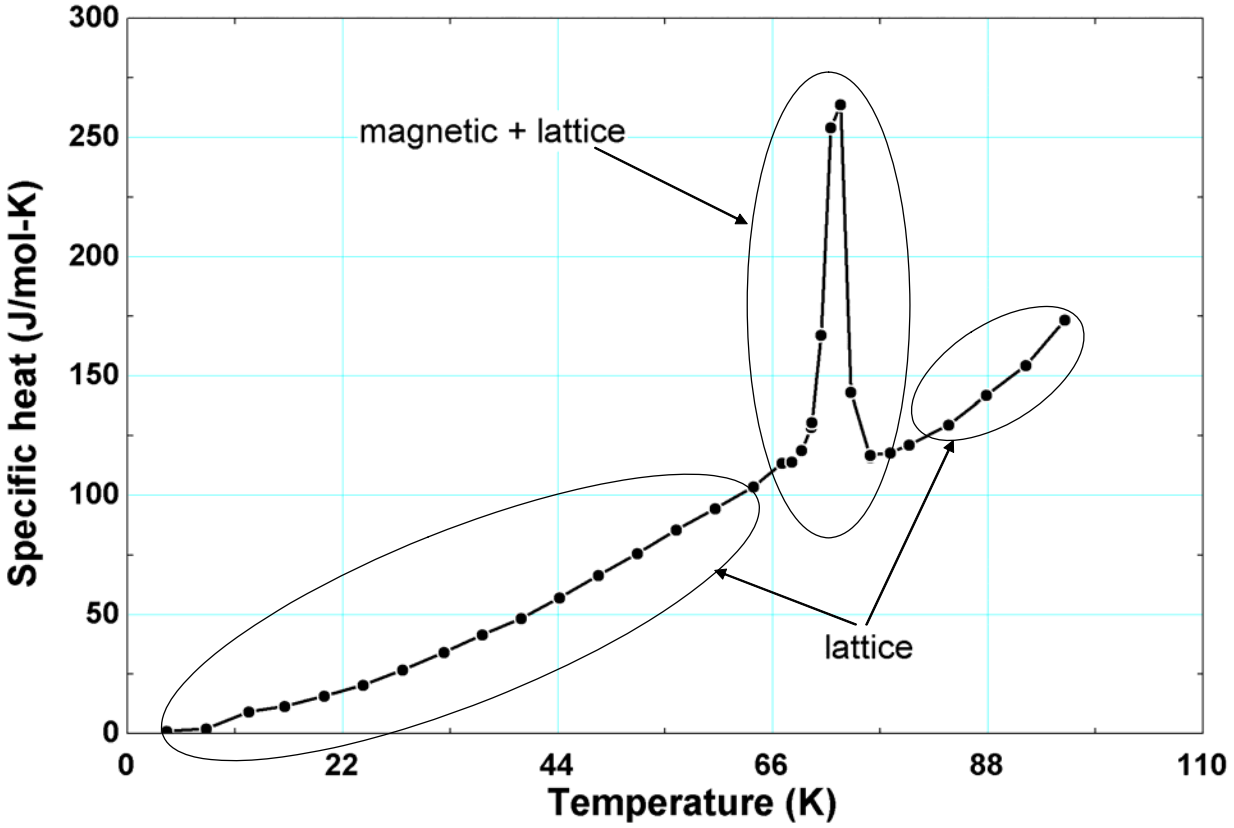

Figure 2.11. Plot of heat capacity vs. temperature with the lattice and magnetic portions indicated.

The data at very low and very high temperatures are related only to the lattice entropy and are isolated and curve fit. The appropriate temperature ranges that are used to isolate the lattice-only heat capacity data is chosen manually; the temperatures at which the magnetic heat capacity causes the specific heat curves to deviate and the temperature where the heat capacity rejoins the lattice curve are determined by inspection. These two temperatures are used as the bounds for the curve fit of the magnetic portion of the heat capacity. After lattice and magnetic specific heat capacity data sets are created, the lattice-only data can be fit with a simple polynomial. Because the magnetocaloric effect is zero for the lattice portion of the specific heat, the curve is assumed

to be the same at every magnetic field. Therefore the lattice specific heat can be fit to data from a single magnetic field or an average of specific heat data at a number of magnetic fields can be used.

In order to fit a curve to the lattice+magnetic specific heat capacity data, first the lattice specific heat capacity is subtracted using the curve fit; leaving only the magnetic specific heat capacity data. The resulting magnetic data can be fit using a curve fitting tool, such as cftool in MATLAB. Initial experience indicates that a compound Gaussian curve provides a good fit for most materials. The curve fit tool cftool will generate a set of fitting coefficients at each magnetic field. If there is a good correlation between the fitting coefficients and the magnetic field, a polynomial can be fit to these coefficients in order to obtain a completely analytical expression. For several magnetocaloric materials studied in this project, it is possible to obtain a good fit to the coefficients of the compound Gaussian curve as a function of magnetic field. If a function for specific heat fitting coefficients for magnetic field can be determined, then material properties based on experimental data can be generated for magnetic fields where no experimental data is available. The magnetic curve (c_{mag}) and the lattice curve ($c_{lattice}$) are added together in order to obtain the total curve for the heat capacity, $c_{\mu oH}$.

$$c_{\mu_o H} = c_{lattice} + c_{mag} \tag{2.50}$$

Once the curve for heat capacity was obtained, it is possible to calculate the entropy by integrating the specific heat curves. As discussed in Section 2.4.1, a zero-entropy temperature, T_{ref}, is chosen and the integral in Eq. (2.49) is evaluated numerically using the quad function in MATLAB to obtain the material's entropy as a function of temperature and magnetic field.

Curve fitting empirical magnetocaloric material property data is advantageous because it uses data to generate smooth, thermodynamically consistent data over a range of temperatures for each magnetic field for which data exists. For some materials, it is reasonable to obtain a curve-fit of specific heat capacity as a function of temperature and magnetic field, allowing the calculation of entropy for a fine mesh of temperature and magnetic field. Generating regenerator material properties at intermediate magnetic fields avoids problems with thermodynamics properties that arise from numerically differentiating experimental data over a relatively large change in magnetic field. This technique does not work for all sets of experimental data because there may not exist a simple relationship between the specific heat fitting coefficients and magnetic field.

2.5 HEAT TRANSFER FLUID PROPERTIES

The fluid properties μ_f, c_f, h_f and k_f are determined within the model assuming that the fluid is incompressible. The properties are calculated within a MATLAB function that takes the fluid temperature as its only input. Interpolation from a fluid property data table requires significant computational time given the iterative nature of the program. Therefore, the fluid properties are curve fit to a polynomial function of temperature. The property correlations built into EES were used to generate property data over a relevant range of temperatures. EES (Engineering Equation Solver) is a software package developed at the University of Wisconsin that has a large library of thermodynamic properties and is used to solve systems of algebraic equations. For water, the data was generated by EES between 273.3 K to 372.6 K and then imported into MATLAB where a polynomial function was fit to each fluid property in terms of a

dimensionless temperature, T_f/T_{ref}, where T_{ref} is an arbitrarily chosen reference temperature. For water, T_{ref} was chosen as 273.3 K. The order of the polynomial was determined by using the lowest order fit that resulted in a maximum discrepancy of less than 0.5% between the fit data and the data obtained from EES. The equation for conductivity of the heat transfer fluid is

$$k_f\left(T_f\right)=\sum_{i=0}^{N} a_i\left(\frac{T_f}{T_{ref}}\right)^i \tag{2.51}$$

where a_i is the ith curve-fit coefficient and N is the order of the curve fit used. The equations for specific heat and viscosity are identical in form to equation (2.51). The curve-fit coefficients determined by fitting properties of pure water, the freezing point of water, and the reference temperature of water are shown in Table 2.3. Sets of coefficients such as the set shown in Table 2.3 were also generated for several concentrations of propylene glycol mixed with water and for a 50% ethylene glycol and water solution.

Table 2.3. Coefficients of property functions for water

fluid	water		
T_{solid}	273.15 K		
T_{ref}	273.3 K		
	k_f	c_f	μ_f
a_0	-0.774277	7526.83	1.803302
a_1	2.055221	-7522.49	-7.216117
a_2	-0.733619	5491.12	11.58833
a_3		-1288.18	-9.32406
a_4			3.756011
a_5			-0.605683

Where T_{solid} is the freezing point of the fluid. Figure 2.12 shows a curve fit of k_f as a function of the reduced temperature for water.

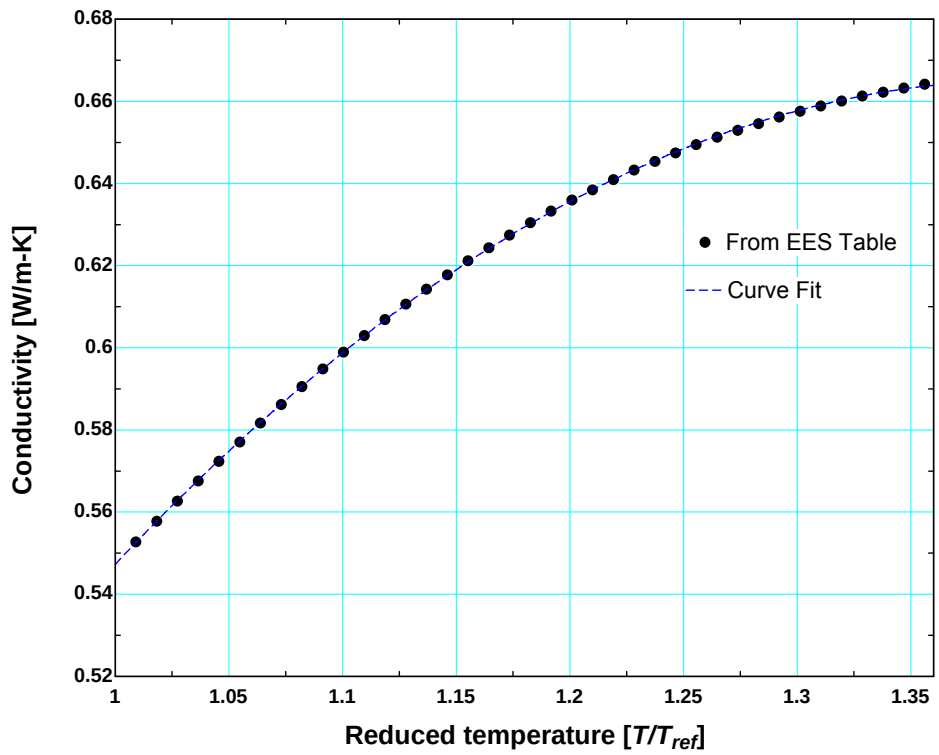

Figure 2.12. Actual and Curve Fit Data for k_f vs. T/T_{ref}

The enthalpy for each fluid is determined by integrating the $c_f(T)$ function with respect to temperature. The fluid is assumed to be incompressible and the integral is shown in Eq. (2.52). The zero reference enthalpy is chosen at T_{ref}, where T_{ref} may be different for each fluid.

$$h_f(T) = \int_{T_{ref}}^{T} c_f(T)\,dT \tag{2.52}$$

Figure 2.13 illustrates $c_f(T)$ for the different fluids considered for the AMRR application.

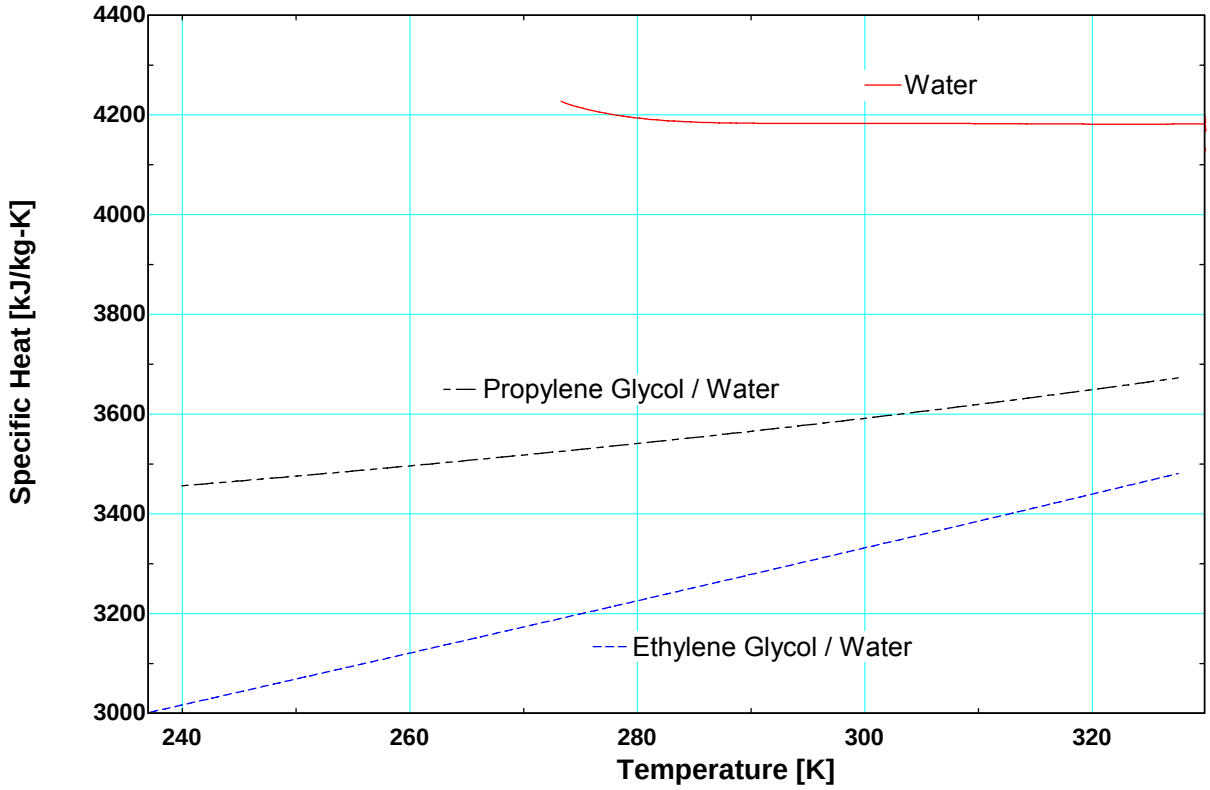

Figure 2.13. Specific heat as a function of temperature for some possible working fluids

2.6 REGENERATOR CORRELATIONS

In order to maintain modeling flexibility with regard to matrix geometry, the regenerator is characterized in the simulation in terms of general parameters such as cross-sectional area, porosity, and hydraulic diameter. The heat transfer, pressure drop, and thermal conductivity of the regenerator are determined using published correlations consistent with the particular type of matrix (e.g., packed bed of spheres) being considered. The regenerator is characterized by parameters that specify the overall size, the length (L) and cross-sectional area (A_c), as well as the local geometry of the regenerator matrix, hydraulic diameter (d_h), volume-specific surface

area (a_s) and porosity (ε). Currently, correlations have been implemented for a packed sphere regenerator and a parallel plate regenerator; these correlations are described below.

2.6.1 Packed Sphere Regenerator Correlations

Packed sphere regenerators are generally randomly packed and the porosity must be measured experimentally. The hydraulic diameter is defined as

$$d_h = \frac{2}{3}\frac{\varepsilon}{1-\varepsilon} d_p \tag{2.53}$$

where d_p is the particle, or sphere, diameter. The volume-specific surface area (i.e., the surface area of the spheres available for heat transfer per unit volume of the regenerator) is determined using Eq. (2.54), which assumes uniform diameter spheres.

$$a_s = 6\frac{(1-\varepsilon)}{d_p} \tag{2.54}$$

The Reynolds number for a packed sphere regenerator is based on the hydraulic diameter

$$Re_f = \frac{\rho_f v d_h}{\mu_f} \tag{2.55}$$

where v is the open area fluid velocity (i.e., the velocity that would be present if the regenerator were empty of any matrix material). However, many correlations for packed sphere regenerators are presented in terms of the Reynolds number based on particle diameter rather than hydraulic diameter. The particle Reynolds number for a packed sphere regenerator is

$$Re_p = \frac{\rho_f v d_p}{\mu_f} \tag{2.56}$$

Pressure Drop

The Ergun (1952) equation is used to predict pressure drop in a packed particle porous media. The equation calculates the absolute value of the pressure gradient according to:

$$\frac{dP}{dx} = \left(\frac{A\,\alpha\,\mu_f}{d_p^2} \right) v + \left(\frac{B\,\beta\,\rho_f}{d_p} \right) v^2$$
$$\alpha = \frac{(1-\varepsilon)^2}{\varepsilon^2} \quad \text{and} \quad \beta = \frac{1-\varepsilon}{\varepsilon^3} \tag{2.57}$$

Kaviany (1995) suggests that A = 180 and B = 1.8 for smooth particles. The pressure gradient from Equation (2.57) is converted to a friction factor for use in the governing equations presented in Section 2.1 and rearranged in terms of the Reynolds number based on hydraulic diameter.

$$f_f = 240 \frac{(1-\varepsilon)}{\varepsilon^2\, Re_f} + 3.6 \frac{(1-\varepsilon)}{\varepsilon^3} \tag{2.58}$$

Heat Transfer

Wakao and Kaguei (1982) have fit data from experiments with air and other gases flowing through a range of matrix geometries (cylinders, spheres, sintered spheroids) made from a number of materials (Celite, steel, bronze, glass, alumina) in order to develop the following empirical correlation for the Nusselt number in a packed sphere bed

$$Nu_f = 2 + 1.1\,\mathrm{Re}_p^{0.6}\,\mathrm{Pr}_f^{1/3} \tag{2.59}$$

Note that Eq. (2.59) uses the Reynolds number based on particle diameter and not hydraulic diameter.

Axial Conduction

Dispersion in the regenerator acts to mix fluid along the bed in the direction of flow and can be treated as an axial conduction term. Therefore, the total axial conductivity of a regenerator bed is related to both dispersion, $k_f D_d$, and static effective thermal conductivity, k_{static}; the parameter D_d is a unitless dispersion coefficient that is typically expressed as a function of the Peclet number of the fluid. From Kaviany (1995), the total effective conductivity, k_{eff}, can be expressed as the sum of the dispersive and static components:

$$k_{eff} = k_{static} + k_f D_d \tag{2.60}$$

where k_{static} is the effective conductivity of the regenerator bed when there is no flow. Hadley (1986) presents a correlation for the static fluid conductivity in a periodic porous structure

$$k_{static} = k_f \left[(1-\alpha_0) \frac{\varepsilon f_0 + k_r / k_f (1-\varepsilon f_0)}{1-\varepsilon(1-f_0) + k_r / k_f \varepsilon (1-f_0)} + \alpha_0 \frac{2(k_r / k_f)^2 (1-\varepsilon) + (1+2\varepsilon) k_r / k_f}{(2+\varepsilon) k_r / k_f + 1 - \varepsilon} \right] \tag{2.61}$$

where

$$f_0 = 0.8 + 0.1\varepsilon \tag{2.62}$$

$$\begin{aligned} \log \alpha_0 &= -4.898\varepsilon, & 0 \le \varepsilon \le 0.0827 \\ \log \alpha_0 &= -0.405 - 3.154(\varepsilon - 0.0827), & 0.0827 \le \varepsilon \le 0.298 \\ \log \alpha_0 &= -1.084 - 6.778(\varepsilon - 0.298), & 0.298 \le \varepsilon \le 0.580 \end{aligned} \tag{2.63}$$

for $\varepsilon < 0.58$.

A theoretical model of dispersion in a uniformly packed bed of spheres is presented by Kaviany and is given in Equation (2.64).

$$D_d = \varepsilon \frac{3}{4} Pe_f, \qquad Pe_f \gg 1 \tag{2.64}$$

where Pe is the Peclet number of the flow, defined as $Pe_f = Re_f Pr_f$. The dispersion correlation in Eq. (2.64) is only applicable when the Peclet number is much greater than 1, but this is not the case during the dwell periods when the Reynolds number is 0. During the dwell periods, axial dispersion is ignored.

2.6.2 Parallel Plate Regenerator Correlations

The parallel plate regenerator is assumed to consist of flat plates with uniform spacing and uniform thickness. A parallel plate regenerator can be characterized by the thickness of the plate (D_y) and the spacing between the centers of the plates (P_y). A schematic of a parallel plate regenerator is shown in Fig. 2.14.

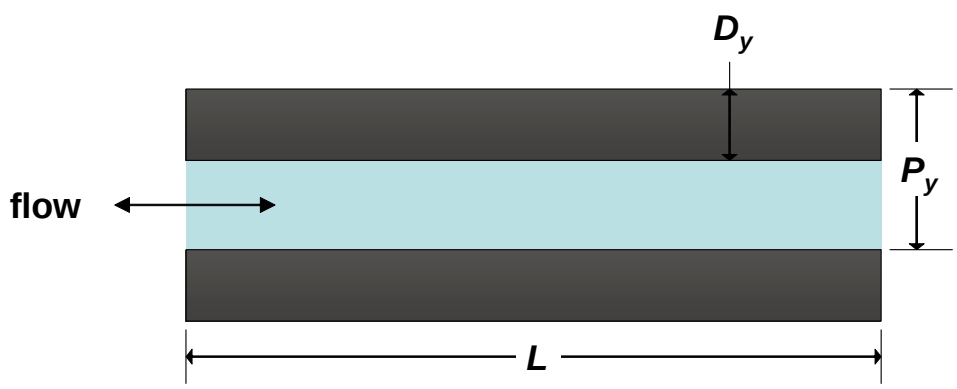

Figure 2.14. Schematic of a simple parallel plate regenerator with characteristic dimensions shown.

The porosity of the system shown in Fig. 2.14 is determined by inspection of the geometry.

$$\varepsilon = 1 - \frac{D_y}{P_y} \tag{2.65}$$

The volume-specific surface area can also be determined by inspection

$$a_s = \frac{2}{P_y} \tag{2.66}$$

Provided that the plates are very wide relative to the thickness of the gap between plates, the hydraulic diameter of the flow channel formed between adjacent plates is twice its height or

$$d_h = 2\left(P_y - D_y\right) \tag{2.67}$$

Using the hydraulic diameter, the Reynolds number for a parallel plate regenerator has the same definition as a packed sphere regenerator given by Eq. (2.56)

Pressure Drop

For a parallel plate regenerator, the spacing between plates is assumed small. This assumption implies that the flow in a parallel plate regenerator is always laminar, which is a valid assumption for practical regenerators used in AMRR systems. In this limit, the friction factor is based on the analytical solution for fully developed flow between parallel plates that are infinitely wide. For short plates or plates with spacers that break up the flow channel in the direction of flow, a friction factor that includes the viscous developing region of the flow should be used.

$$f_f = \frac{24}{\mathrm{Re}_f} \tag{2.68}$$

Heat Transfer

For laminar heat transfer associated with flow between infinitely wide parallel plates, a correlation for the local Nusselt number assuming a constant temperature boundary condition suggested by Nickolay and Martin (2002) is used.

$$Nu_1 = \left(7.541 + \left(1.841\,Gz^{1/3}\right)^{3.592}\right)^{1/3.592} \tag{2.69}$$

$$Nu_f = Nu_1 - \frac{1}{3}1.841\,Gz^{1/3}\left(\frac{1.841\,Gz^{1/3}}{Nu_1}\right)^{2.592} \tag{2.70}$$

where Gz is the Graetz number in the regenerator, which is defined as

$$Gz = Re_f\,Pr_f\,\frac{d_H}{x_f} \tag{2.71}$$

where the position, x_f, is measured from the fluid inlet. Therefore, the position of the fluid is different for the cold blow period than for the hot blow. Inspection of Eq. (2.69) shows that the Nusselt number limits to a value of 7.541 for fully developed heat transfer. Assuming a constant heat flux boundary condition, the Nusselt number limits to a value of 8.235 (Kays and London, 1984).

Axial Conduction

For a parallel plate regenerator, the static conduction can be determined by calculating the equivalent thermal conduction through parallel paths of fluid and solid.

$$k_{static} = k_r\left(1-\varepsilon\right) + k_f\,\varepsilon \tag{2.72}$$

The axial dispersion for a fluid flowing between two infinite plates is given by Beard (2001).

$$D_d = \frac{Pe_f^2}{210} \tag{2.73}$$

2.7 CORRECTION FOR INTERNAL TEMPERATURE GRADIENTS IN A PACKED SPHERE REGENERATOR

Regenerator models often neglect the temperature gradients that occur locally within the regenerator material and treat the solid as a lumped capacitance; the governing equations derived in Section 2.1 make this assumption implicitly by assigning a single temperature to the material at any axial location and time. The lumped capacitance assumption is often justified by the relatively large thermal conductivity and the small spatial extent of most regenerator matrices. For example, a regenerator for a Stirling cycle may consist of 500 mesh metal screens exposed to an oscillatory flow of helium. In this situation, any local temperature gradients within the screen material (i.e. temperature gradients between the center and surface of a wire at any position within the regenerator) will be much smaller than the temperature difference between the surface of the regenerator and the surrounding gas. However, this is not always the case; the magnetocaloric materials that are required for AMRR systems may have relatively low conductivity. Also, near room temperature AMRR systems generally use liquid working fluids that result in high fluid-to-particle heat transfer coefficients and therefore internal temperature gradients may be more significant in comparison with the resulting surface to fluid temperature gradients. Furthermore, AMRR systems become more economically competitive (i.e., smaller) as the cycle frequency increases. As a result, the thermal penetration depth associated with a cycle may become comparable to the spatial extent of the matrix geometry; therefore, the performance that is predicted by a lumped capacitance model may be significantly in error in these situations. This topic is discussed in further detail in Engelbrecht et al. (2006a).

Explicitly accounting for internal temperature gradients that exist locally within the regenerator matrix will result in a two-dimensional transient problem that will greatly increase the required computation time and the complexity of the model. Therefore, an approximate correction technique that may be used in the context of a one-dimensional regenerator model in order to account for internal temperature gradients without explicitly including them in the solution algorithm has been developed.

Jeffreson (1972) presents a Biot number based correction that can be used to correct the heat transfer coefficient in order to reflect the additional resistance associated with conduction within the regenerator matrix. However, this correction is based on a fictitious steady-state condition in which a uniformly distributed volumetric generation throughout the regenerator matrix is considered in order to predict the temperature gradients within the material; therefore, the impact that the cycle frequency and the associated thermal penetration depth have on the participation of the regenerator medium is not considered. Hausen (1983) suggests a correction factor based on an analytical model that is dependent on Biot number, cycle time, and the diffusivity of the solid material; this correction factor is derived based on a square-wave variation in the heat flux that is applied to the regenerator matrix.

2.7.1 Governing Equations for the Internal Temperature Gradient Study

The governing equations for sphere in contact with a heat transfer fluid are derived here for both a passive and active process. The active material is assumed to have a constant partial derivative of entropy with respect to magnetic field at constant temperature ($\left(\frac{\partial s}{\partial \mu_o H}\right)_T$). This property

results in a time dependent volumetric generation (actually, this is a magnetic work transfer to the material) when the material is exposed to a time-varying magnetic field. Both the active and passive materials are assumed to have a constant specific heat capacity (c) and thermal conductivity (k) and the sphere-to-fluid heat transfer coefficient (h) is assumed to be constant throughout the cycle. A single sphere in a regenerator packing is considered here; this technique can be extended to other regenerator geometries (e.g., cylinders, which might be used to consider a regenerator of stacked screens). The temperature distribution within the sphere is assumed to be one-dimensional.

The governing equation for a sphere composed of a magnetically active material is derived from a differential energy balance which balances conduction and magnetic work transfer against the storage of energy:

$$k\frac{\partial}{\partial r}\left[r^2\frac{\partial T}{\partial r}\right]-T\,r^2\rho\left(\frac{\partial s}{\partial \mu_o H}\right)_T\frac{d\,\mu_o H}{dt}=\rho\,c\,r^2\frac{\partial T}{\partial t} \tag{2.74}$$

where r is the radial position, T is the temperature, ρ is density, and t is time. The second term in Eq. (2.74) is consistent with a time-dependent but spatially-uniform variation of the applied field, which results in a volumetric heating effect that is either positive or negative, depending on the whether the magnetic field ($\mu_o H$) is increasing or decreasing, respectively. The magnetic field is assumed to vary sinusoidally from 0 to a maximum value, $\mu_o H_{max}$,:

$$\mu_o H=\frac{\mu_o H_{max}}{2}\left[1-\cos\left(\frac{2\pi t}{\tau}\right)\right] \tag{2.75}$$

where τ is the total duration of the cycle. The rate of change of the magnetic field is:

$$\frac{d\mu_o H}{dt} = \frac{\pi \mu_o H_{max}}{\tau} \sin\left(\frac{2\pi t}{\tau}\right) \tag{2.76}$$

Substituting Eq. (2.76) into Eq. (2.74) leads to:

$$k\frac{\partial}{\partial r}\left[r^2 \frac{\partial T}{\partial r}\right] - T r^2 \rho \left(\frac{\partial s}{\partial \mu_o H}\right)_T \frac{\pi \mu_o H_{max}}{\tau} \sin\left(\frac{2\pi t}{\tau}\right) = \rho c r^2 \frac{\partial T}{\partial t} \tag{2.77}$$

In the limit of a near room temperature system, the absolute temperature that multiplies the second term in Eq. (2.77) can be assumed to be nearly constant (the fluctuation in temperature is small relative to the absolute temperature); therefore, Eq. (2.77) may be rewritten approximately as:

$$k\frac{\partial}{\partial r}\left[r^2 \frac{\partial T}{\partial r}\right] - \overline{T}_f r^2 \rho \left(\frac{\partial s}{\partial \mu_o H}\right)_T \frac{\pi \mu_o H_{max}}{\tau} \sin\left(\frac{2\pi t}{\tau}\right) = \rho c r^2 \frac{\partial T}{\partial t} \tag{2.78}$$

where $\overline{T}_f$ is the average fluid temperature. In this same limit, the amplitude of the adiabatic temperature change (ΔT_a) induced by the change in the applied field is approximately equal to:

$$\Delta T_a = \left(\frac{\partial s}{\partial \mu_o H}\right)_T \frac{\mu_o H_{max} \overline{T}_f}{2c} \tag{2.79}$$

Equation (5) can be rewritten in terms of the adiabatic temperature change, which is the characteristic temperature difference associated with an active, magnetocaloric process:

$$k\frac{\partial}{\partial r}\left[r^2 \frac{\partial T}{\partial r}\right] - \Delta T_a \rho c r^2 \frac{2\pi}{\tau} \sin\left(\frac{2\pi t}{\tau}\right) = \rho c r^2 \frac{\partial T}{\partial t} \tag{2.80}$$

For a passive process, the magnetocaloric term drops out:

$$k\frac{\partial}{\partial r}\left[r^2 \frac{\partial T}{\partial r}\right] = \rho c r^2 \frac{\partial T_s}{\partial t} \tag{2.81}$$

The boundary condition at the outer radius of the sphere ($r = R$) balances conduction with convection:

$$-k\left.\frac{\partial T}{\partial r}\right|_{r=R,t}=h\left[T\left(r=R,t\right)-T_f\right] \tag{2.82}$$

where T_f is the temperature of the fluid. To simulate a passive process, the temperature of the fluid is allowed to vary sinusoidally according to:

$$T_f\left(t\right)=\overline{T}_f+\Delta T_f\sin\left(\frac{2\pi t}{\tau}\right) \tag{2.83}$$

where ΔT_f , the amplitude of the fluid temperature oscillation, is the characteristic temperature difference associated with the passive regenerator process. For an active process, the fluid temperature is assumed to be constant:

$$T_f\left(t\right)=\overline{T}_f \tag{2.84}$$

Note that these two boundary conditions reflect the fundamental difference between a passive process, where the energy exchange between the matrix and the fluid is driven the variations in the local fluid temperature, and an active process, where the energy exchange between the matrix and the fluid is driven by the local magnetocaloric effect.

The temperature gradient at the center of the sphere must be zero:

$$\left.\frac{\partial T}{\partial r}\right|_{r=0,t}=0 \tag{2.85}$$

Finally, the sphere must undergo a steady-state cycle so that:

$$T\left(r,t=0\right)=T\left(r,t=\tau\right) \tag{2.86}$$

These equations are made dimensionless by defining a reduced position ($\tilde{r}$) and reduced time ($\tilde{t}$):

$$\tilde{r} = \frac{r}{R} \tag{2.87}$$

$$\tilde{t} = \frac{t}{\tau} \tag{2.88}$$

The reduced temperature difference (θ) is defined based either on the adiabatic temperature change or the magnitude of the fluid temperature oscillation, depending on whether an active or passive process is being considered:

$$\theta = \frac{T_s - \overline{T}_f}{\Delta T_a} \quad \text{or } \theta = \frac{T_s - \overline{T}_f}{\Delta T_f} \tag{2.89}$$

The Fourier number (Fo) is defined according to:

$$Fo = \frac{k\,\tau}{\rho\, c\, R^2} \tag{2.90}$$

The Biot number (Bi) is defined according to:

$$Bi = \frac{h\,R}{k} \tag{2.91}$$

The non-dimensional governing equation for the active process becomes:

$$\frac{Fo}{\tilde{r}^2}\frac{\partial}{\partial \tilde{r}}\left[\tilde{r}^2 \frac{\partial \theta}{\partial \tilde{r}}\right] - 2\,\pi \sin\left(2\,\pi\,\tilde{t}\right) = \frac{\partial \theta}{\partial \tilde{t}} \tag{2.92}$$

with the outer surface boundary condition:

$$-\left.\frac{\partial \theta}{\partial \tilde{r}}\right|_{\tilde{r}=1,\tilde{t}} = Bi\,\theta\left(\tilde{r}=1,\tilde{t}\right) \tag{2.93}$$

The non-dimensional governing equation for the passive process becomes:

$$\frac{Fo}{\tilde{r}^2}\frac{\partial}{\partial \tilde{r}}\left[\tilde{r}^2 \frac{\partial \theta}{\partial \tilde{r}}\right] = \frac{\partial \theta}{\partial \tilde{t}} \tag{2.94}$$

with the outer surface boundary condition:

$$-\left.\frac{\partial\theta}{\partial\tilde{r}}\right|_{\tilde{r}=1,\tilde{t}} = Bi\left[\theta\left(\tilde{r}=1,\tilde{t}\right)-\sin\left(2\pi\tilde{t}\right)\right] \tag{2.95}$$

In either case, the remaining boundary conditions are:

$$\left.\frac{\partial\theta}{\partial\tilde{r}}\right|_{\tilde{r}=0,\tilde{t}} = 0 \tag{2.96}$$

and

$$\theta_s\left(\tilde{r},\tilde{t}=0\right)=\theta_s\left(\tilde{r},\tilde{t}=1\right) \tag{2.97}$$

2.7.2 Numerical Solution for the Internal Temperature Gradient Model

The solution to the governing equations is obtained over a grid that extends from 0 to 1 in reduced position with *m* spatial steps and from 0 to 1 in reduced time with *n* time steps:

$$\tilde{r}_i = \frac{\left(i-1\right)}{\left(m-1\right)} \quad i=1..m \tag{2.98}$$

$$\tilde{t}_j = \frac{\left(j-1\right)}{\left(n-1\right)} \quad j=1..n \tag{2.99}$$

The reduced spatial and temporal step size ($\Delta\tilde{r}$ and $\Delta\tilde{t}$, respectively) are given by:

$$\Delta\tilde{r} = \frac{1}{\left(m-1\right)} \tag{2.100}$$

$$\Delta\tilde{t} = \frac{1}{\left(n-1\right)} \tag{2.101}$$

The discretized form of the dimensionless governing equation for the active case is:

$$Fo\left[\frac{\theta_{i+1,j}+\theta_{i-1,j}-2\theta_{i,j}}{\Delta\tilde{r}^2}+\frac{1}{\tilde{r}_i}\frac{\left(\theta_{i+1,j}-\theta_{i-1,j}\right)}{\Delta\tilde{r}}\right]-2\pi\sin\left(2\pi\tilde{t}\right)=\frac{\left(\theta_{i,j}+\theta_{i,j-1}\right)}{\Delta\tilde{t}} \tag{2.102}$$

$$\text{for } i=2...\left(m-1\right) \text{ and } j=2...n$$

and the boundary condition at the surface for the active process leads to:

$$-\frac{\left(\theta_{m,j}-\theta_{m-1,j}\right)}{\Delta\tilde{r}}=Bi\,\theta_{m,j}\quad \text{for } j=2...n \tag{2.103}$$

For the passive case, the discretized governing equation and external surface boundary condition are:

$$Fo\left[\frac{\theta_{i+1,j}+\theta_{i-1,j}-2\theta_{i,j}}{\Delta\tilde{r}^2}+\frac{1}{\tilde{r}_i}\frac{\left(\theta_{i+1,j}-\theta_{i-1,j}\right)}{\Delta\tilde{r}}\right]=\frac{\left(\theta_{i,j}+\theta_{i,j-1}\right)}{\Delta\tilde{t}} \tag{2.104}$$

$$\text{for } i=2...\left(m-1\right) \text{ and } j=2...n$$

$$-\frac{\left(\theta_{m,j}-\theta_{m-1,j}\right)}{\Delta\tilde{r}}=Bi\,\theta_{m,j}-Bi\sin\left(2\pi\tilde{t}_j\right)\quad \text{for } j=2...n \tag{2.105}$$

The temperature gradient at the center of the sphere is zero, which leads to:

$$\theta_{1,j}-\theta_{2,j}=0\ \text{ for } j=2...n \tag{2.106}$$

Steady state is specified by:

$$\theta_{i,1}=\theta_{i,n}\qquad i=1...m \tag{2.107}$$

Equations (29) through (34) are solved using a sparse matrix decomposition algorithm implemented in MATLAB.

2.7.3 Verification of Internal Temperature Gradients Model

The numerical model can be verified in the passive limit by comparison with the analytical solution presented by Carslaw and Jaeger (1959) for a sphere subjected to a sinusoidal fluid temperature. Neglecting the terms in the analytical solution that disappear at long times (i.e., the non-cyclic terms):

$$\theta = \frac{Bi}{\tilde{r}} \frac{A_1}{A_2} \sin\left(2\pi\tilde{t} + \phi_1 - \phi_2\right) \tag{2.108}$$

where

$$A_1 \exp\left(i\phi_1\right) = \sinh\left[\sqrt{\frac{\pi}{Fo}}\tilde{r}\right]\cos\left[\sqrt{\frac{\pi}{Fo}}\tilde{r}\right] + i\cosh\left[\sqrt{\frac{\pi}{Fo}}\tilde{r}\right]\sin\left[\sqrt{\frac{\pi}{Fo}}\tilde{r}\right] \tag{2.109}$$

$$A_2 \exp\left(i\phi_2\right) = \sqrt{\frac{\pi}{Fo}}\left(1+i\right)\cosh\left[\sqrt{\frac{\pi}{Fo}}\left(1+i\right)\right] + \left(Bi-1\right)\sinh\left[\sqrt{\frac{\pi}{Fo}}\left(1+i\right)\right] \tag{2.110}$$

Figure 2.15 illustrates the dimensionless temperature as a function of $\tilde{t}$ for various values of $\tilde{r}$ at Bi = 2.5 and Fo = 0.25 predicted by the numerical model and by Eqs. (2.108) through (2.110).

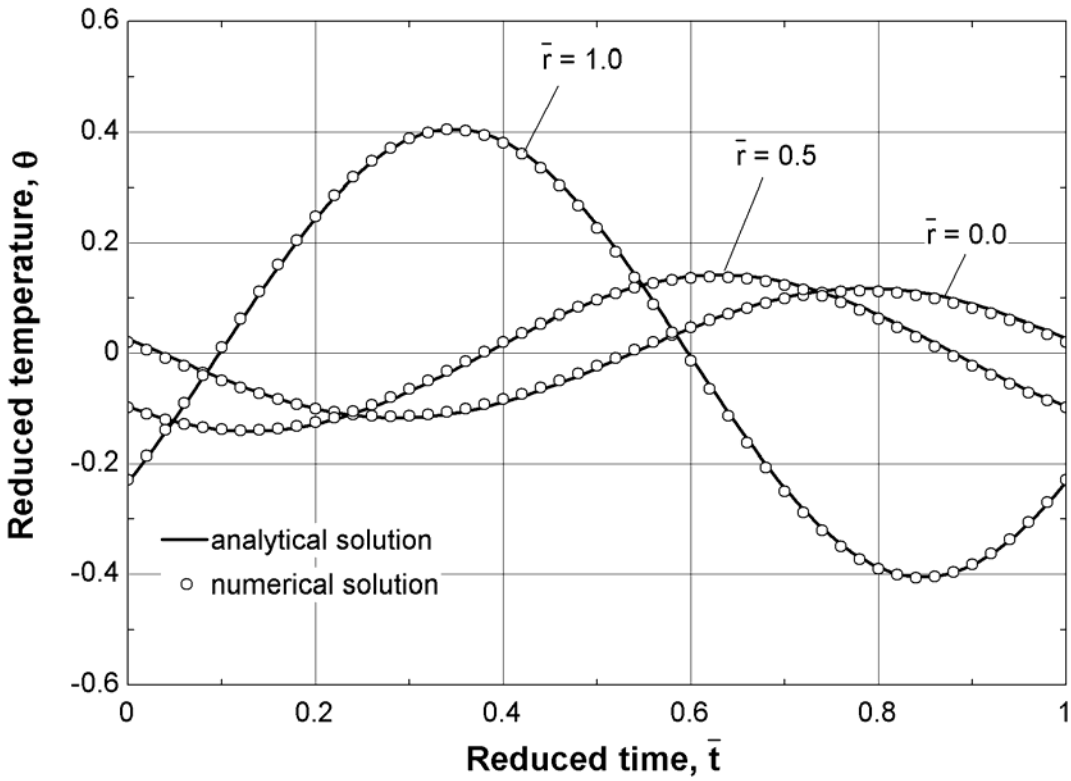

Figure 2.15. Reduced temperature as a function of reduced time for various values of reduced radius with Bi = 2.5 and Fo = 0.25.

The analytical and numerical results converge to within 0.01% for all *m* greater than 200 and *n* greater than 100 under the conditions shown in Fig. 2.15. The results presented in Fig. 2.15 use 250 spatial steps and 150 temporal steps.

2.7.4 Results for a Passive Regenerator

The energy stored in the sphere (*U*) in the passive limit is given by:

$$U(t) = \rho c \int_0^R 4\pi r^2 \left[T(r,t) - \overline{T}_f \right] dr \tag{2.111}$$

The maximum possible energy that can be stored in the sphere during one cycle (ΔU_{max}) occurs if the sphere temperature is spatially uniform and varies from $-\Delta T_f$ to $+\Delta T_f$. This is the limiting case for a perfect regenerator in which the conductivity and heat transfer coefficient are large ($h \rightarrow \infty$ and $k \rightarrow \infty$). This limit occurs when *Fo* and the *Fo Bi* product are both large.

$$\Delta U_{max} = \rho c \frac{8}{3} \pi R^3 \Delta T_f \tag{2.112}$$

The dimensionless stored energy ($\tilde{U}$) is the ratio of the instantaneous stored energy to the maximum possible stored energy and given by:

$$\tilde{U}(\tilde{t}) = \frac{3}{2} \int_0^1 \tilde{r}^2 \, \theta(\tilde{r},\tilde{t}) \, d\tilde{r} \tag{2.113}$$

The performance of the regenerator relative to this maximum possible limit is referred to as the total efficiency of the sphere (η) and is given by:

$$\eta = \max\left[\tilde{U}(\tilde{t})\right] - \min\left[\tilde{U}(\tilde{t})\right] \quad \text{for} \quad 0 \le \tilde{t} \le 1 \tag{2.114}$$

Figure 2.13 illustrates the total sphere efficiency as a function of the product of the Biot number and Fourier number for various values of the Fourier number. Note that the Biot Fourier number product:

$$Bi\,Fo = \frac{\tau\,h}{\rho\,c\,R} \tag{2.115}$$

is proportional to the ratio of the cycle period to the time constant associated with the sphere if it were spatially uniform in temperature (i.e., if it were treated as a lumped capacitance). The lumped capacitance limit is consistent with the sphere having an infinite thermal conductivity and therefore, this limit represents the typical modeling assumption for a one-dimensional regenerator model (i.e., the regenerator matrix is assumed locally to be at a uniform temperature); the impact of the surface to fluid temperature difference associated with a finite heat transfer coefficient is considered, but the temperature gradients internal to the sphere (induced by the finite thermal conductivity of the sphere) are ignored in this limit. The temperature of the sphere in this infinite conductivity limit ($\theta_{k\to\infty}$) is given by:

$$\theta_{k\to\infty}\left(\tilde{t}\right) = \frac{\sin\left(2\pi\tilde{t} - \phi\right)}{\sqrt{1 + \left(\dfrac{2\pi}{3\,Bi\,Fo}\right)^2}} \tag{2.116}$$

where

$$\phi = \tan^{-1}\left[\frac{2\pi}{Bi\,Fo}\right] \tag{2.117}$$

Substituting Eq. (2.116) into Eq. (2.113) leads to:

$$\tilde{U}_{k\to\infty}\left(\tilde{t}\right) = \frac{\sin\left(2\pi\tilde{t} - \phi\right)}{2\sqrt{1 + \left(\dfrac{2\pi}{3\,Bi\,Fo}\right)^2}} \tag{2.118}$$

and therefore the total efficiency of the infinite conductivity particle ($\eta_{k\to\infty}$) is:

$$\eta_{k\to\infty} = \frac{1}{\sqrt{1+\left(\frac{2\pi}{3\,Bi\,Fo}\right)^2}} \tag{2.119}$$

The total efficiency of the infinite conductivity particle is also shown in Fig. 2.16; note that the results for large Fourier number approach this infinite conductivity limit. The Fourier number is approximately equal to the ratio of the cycle period to the time required for a thermal wave to penetrate to the center of the sphere. When the Fourier number is large, therefore, the conductivity is sufficiently high such that the entire particle participates in the energy storage process and the efficiency is not affected by the thermal conductivity. On the other hand, when the Fourier number is small, the thermal wave does not penetrate significantly into the sphere and only the outer surface participates in the process. This behavior is shown in Fig. 2.17, which illustrates the reduced temperature as a function of reduced position at various values of reduced time for a small Fourier number (Fo= 0.1) and $Fo\ Bi$ = 1.0.

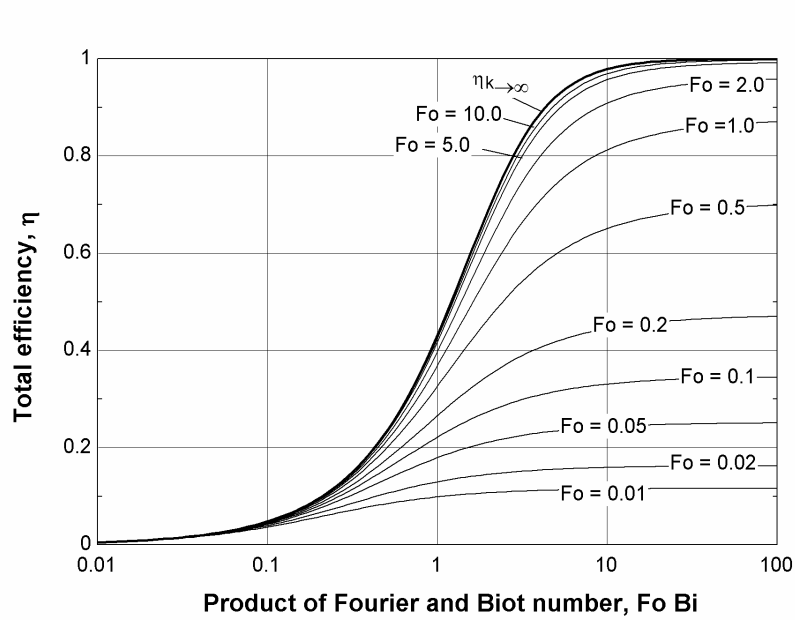

Figure 2.16. Total efficiency as a function of *Fo Bi* for various values of *Fo*. Also shown is the efficiency in the limit of infinite thermal conductivity.

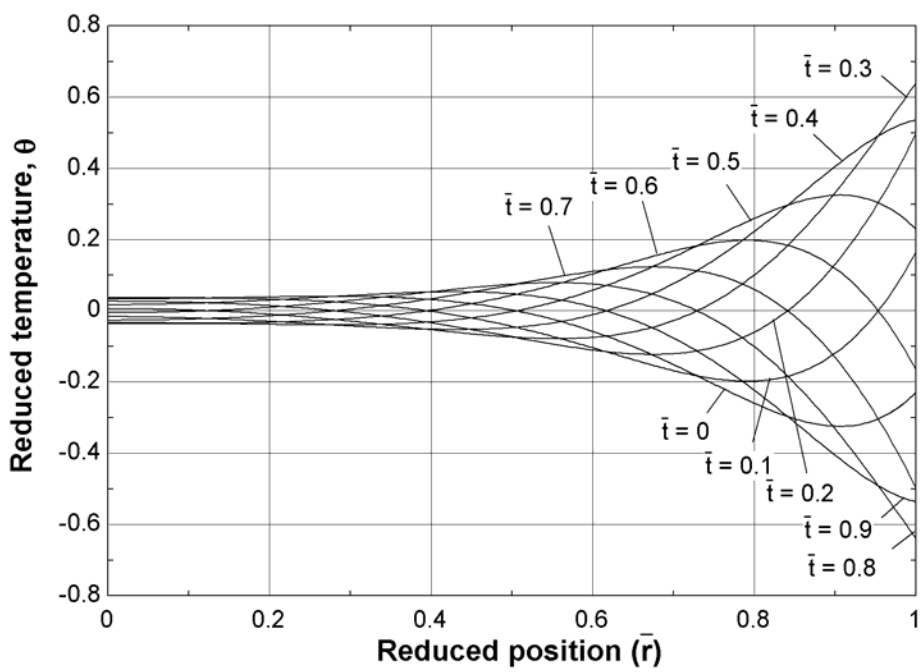

Figure 2.17. Reduced temperature as a function of $\tilde{r}$ for various values of $\tilde{t}$ for $Fo = 0.1$ and $Fo\ Bi = 1.0$. Note that the cycle time is insufficient to allow the entire sphere to participate in the energy storage process and so only the outer edge temperature is affected by the fluid.

One method that has been suggested and widely used to approximately correct for the finite conductivity of regenerator material is presented by Jeffreson (1972); the heat transfer coefficient is modified based on the Biot number, which represents the ratio of the resistance to conduction to the resistance to convection from the surface. The Jeffreson correction factor is derived by assuming a uniform and steady volumetric generation throughout the material in order to determine the temperature distribution. The temperature distribution is subsequently integrated in order to determine the elevation of the volume-weighted average temperature relative to the surface temperature. Finally, the reduction in the heat transfer coefficient that would be required to achieve the same increase in temperature in the limit of a perfectly conducting sphere is determined. The fractional reduction in the heat transfer coefficient is referred to here as a degradation factor (*DF*)

$$h^* = DF\, h \tag{2.120}$$

where h^* is the corrected heat transfer coefficient. The degradation factor derived by Jeffreson for a spherical particle is:

$$DF_J = \frac{1}{1 + \frac{Bi}{5}} \tag{2.121}$$

Hausen (1983) presents a degradation factor for a balanced-flow regenerator that is based on Biot number and Fourier number and can be expressed as

$$DF_H = \frac{1}{1 + \frac{Bi}{5}\phi_H} \tag{2.122}$$

where

$$\phi_H = 1 - \frac{4}{35Fo} \qquad Fo \geq 0.4$$
$$\phi_H = \frac{5\pi}{\sqrt{27 + \frac{72}{Fo}}} \qquad Fo < 0.4 \tag{2.123}$$

The corrected heat transfer coefficient using either the Jeffreson or Hausen degradation factor is therefore less than the actual heat transfer coefficient h by an amount that grows with increasing Biot number and (for the Hausen degradation factor) decreasing Fourier number. Applying the degradation factor to the infinite conductivity efficiency, Eq. (2.119), leads to a corrected efficiency (η_c):

$$\eta_c = \frac{1}{\sqrt{1 + \left[\frac{2\pi}{3\,Bi\,Fo\,DF}\right]^2}} \tag{2.124}$$

The corrected efficiency based on the Jeffreson correlation (η_J) is obtained by substituting Eq. (2.121) into Eq. (2.124):

$$\eta_J = \frac{1}{\sqrt{1 + \left[\frac{2\pi}{3\,Bi\,Fo}\left(1 + \frac{Bi\,Fo}{5\,Fo}\right)\right]^2}} \tag{2.125}$$

and the corrected efficiency based on the Hausen correction factor is

$$\eta_H = \frac{1}{\sqrt{1 + \left[\frac{2\pi}{3\,Bi\,Fo}\left(1 + \frac{Bi\,Fo}{5\,Fo}\phi_H\right)\right]^2}} \tag{2.126}$$

The corrected efficiency based on the Jeffreson and Hausen correlations and the actual efficiency are shown in Fig. 2.18 as a function of *Fo Bi* for various values of *Fo*. Note that both the Jeffreson and Hausen corrections provide significantly improved predictions relative to the

infinite conductivity limit. However, the corrected efficiency using the Jeffreson correction does not match the efficiency predicted by the numerical model because it does not depend on *Fo* and the efficiency using the Hausen correction does not match numerical model because it is only an approximate correction that was developed based on a particular operating condition.

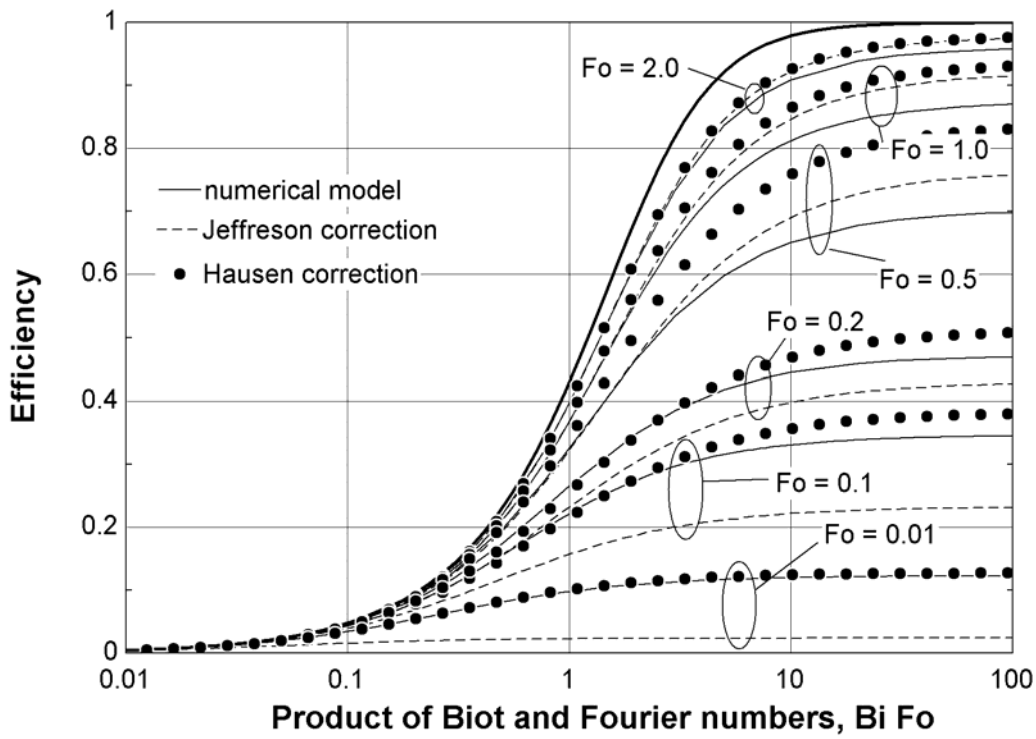

Figure 2.18. Efficiency predicted by the numerical model and using lumped capacitance model corrected with the Jeffreson and Hausen degradation factor. Efficiency is shown as a function of the product of the Biot and Fourier number for various values of the Fourier number.

It is not surprising that the Jeffreson correction factor, which is based on a steady state concept, does not completely represent the transient phenomena that are occurring in a regenerator. The correction factor was implicitly based on the assumption that the entire sphere participates in the energy storage process whereas Fig. 2.17 shows that as *Fo* decreases, only the outer layer participates. However, a degradation correction factor provides a technique that may be used to

easily and quickly modify the heat transfer coefficient used in a one-dimensional model and therefore, this concept is very valuable. Eq. (2.124) may be solved for the degradation factor that forces the corrected efficiency to exactly match the actual efficiency predicted by the numerical model:

$$DF = \frac{\left(\dfrac{2\pi}{3\,Bi\,Fo}\right)}{\sqrt{\dfrac{1}{\eta^2} - 1}} \tag{2.127}$$

Figure 2.19 illustrates the degradation factor as a function of the Biot number and Fourier number product for various values of the Fourier number. The information presented in Fig. 2.19 is sufficient to correct a one-dimensional passive regenerator model for internal temperature gradients; the Fourier number and Biot number that characterize the bed and operating conditions should be calculated and used to determine the degradation factor that may subsequently be applied to the heat transfer coefficient.

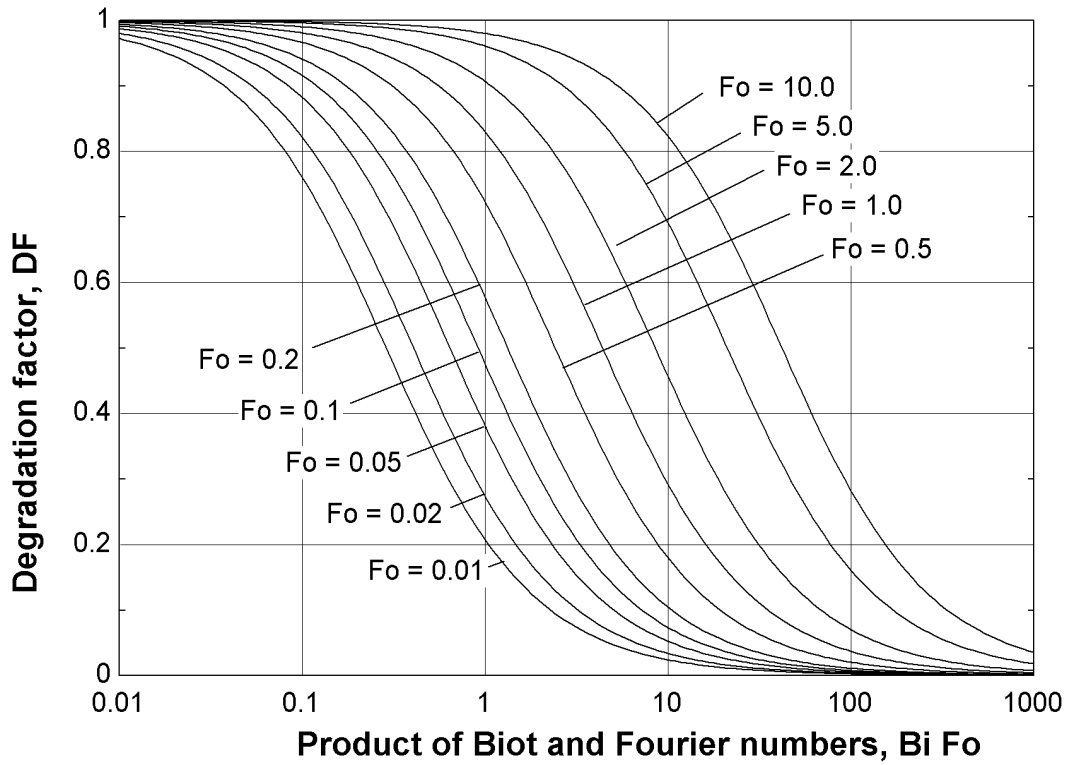

Figure 2.19. Degradation factor predicted by the numerical model as a function of the product of the Biot and Fourier number for various values of the Fourier number.

Using a degradation factor that has the same form suggested by Hausen leads to:

$$DF = \frac{1}{1 + \frac{Bi}{5}\chi\left(Fo\right)} \tag{2.128}$$

where χ is a function of the Fourier number that is obtained by empirically fitting the data shown in Figure 2.19:

$$\chi\left(Fo\right) = Fo\exp\left[0.246196 - 0.84878\ln\left(Fo\right) - 0.05639\left(\ln\left(Fo\right)\right)^2\right] \tag{2.129}$$

The efficiency based on the corrected degradation factor and the efficiency calculated by the numerical model are both shown in Fig. 2.20. Note the good agreement over a wide range of Fourier number and Biot number.

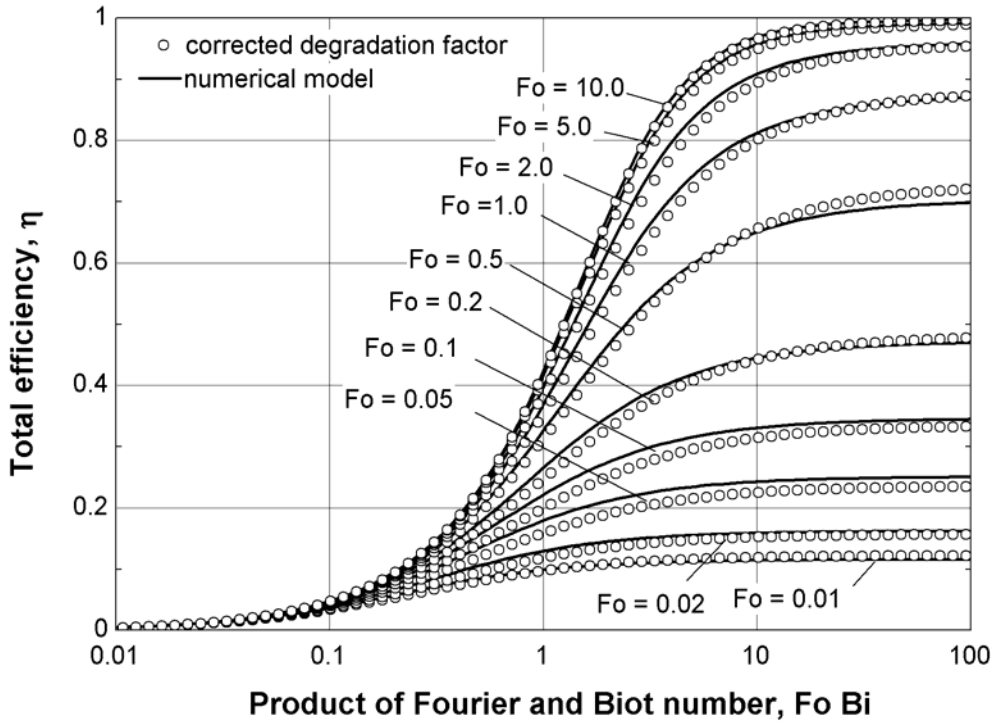

Figure 2.20. Total efficiency computed using the corrected degradation factor presented in Eqs. (2.128) and (2.129) and predicted by the numerical model as a function of the product of the Biot and Fourier number for various values of the Fourier number.

2.7.5 Temperature Gradient Results for an Active Magnetic Regenerator

The sphere in a magnetic regenerator is subjected to a volumetric process that is driven by the variation in the magnetic field. In the absence of any communication with the environment, the sphere temperature will fluctuate with an amplitude that is determined by the adiabatic magnetization temperature difference. Fig. 2.21(a) illustrates the reduced temperature in the sphere as a function of reduced time for a situation in which the sphere experiences relatively poor thermal communication with its surroundings but high internal conductivity (Bi = 0.2 and Fo = 5.0). Note that the sphere is at a nearly spatially uniform dimensionless temperature which oscillates between -1.0 and 1.0 during the cycle. Figure 2.21(b) illustrates the situation when the communication with the environment is improved and the internal conductivity is still high

($Bi = 5.0$ and $Fo = 5.0$); note that the sphere remains at essentially a spatially uniform temperature but the amplitude of the oscillations is reduced as the material is able to transfer more energy to and from its surroundings. Finally, Fig. 2.21(c) illustrates the situation when the communication with the environment is high but the internal conductivity is poor ($Bi = 5.0$ and $Fo = 0.2$) so that the material very near the surface remains near the surrounding fluid temperature (a reduced temperature of 0.0) whereas the temperature near the center internally fluctuates between -1.0 and 1.0 as in Figure 2.21(a).

The efficiency of the sphere undergoing a magnetic process must be defined differently than in the passive case. The objective of a magnetic refrigeration process is to convert the magnetically driven volumetric heating/cooling into a heat transfer to/from the fluid; Figs. 2.21(a) and 2.21(c) show that this process is inhibited by either a low convection coefficient or poor internal conduction. The figure of merit that is most appropriate for this process is the average rate of heat transfer between the fluid and the particle during a cycle ($\bar{\dot{Q}}$):

$$\bar{\dot{Q}} = \frac{4\pi h R^2}{\tau}\int_0^{\tau}\left|T\left(r=R,t\right)-\bar{T}_f\right|dt \tag{2.130}$$

The maximum heat transfer rate occurs if the sphere is infinitely conductive and the heat transfer coefficient is infinite, in which case the temperature of the material is always at the fluid temperature. The heat transfer rate in this limit ($\dot{Q}_{max}$) is:

$$\dot{Q}_{max} = \bar{T}_f\left(\frac{\partial s}{\partial \mu_o H}\right)_T \frac{4\pi R^3}{3}\rho\frac{\pi\mu_o H_{max}}{\tau}\sin\left(\frac{2\pi t}{\tau}\right) \tag{2.131}$$

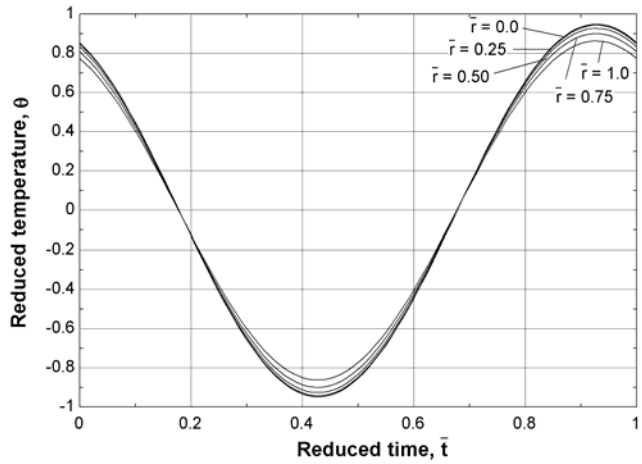

(a) Bi = 0.2, Fo = 5.0

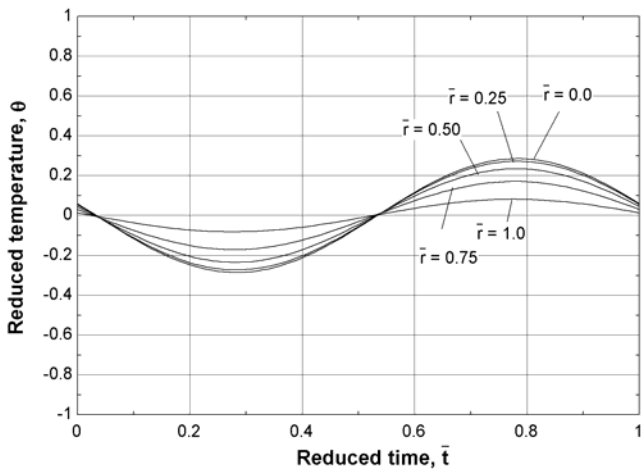

(b) Bi = 5.0, Fo = 5.0

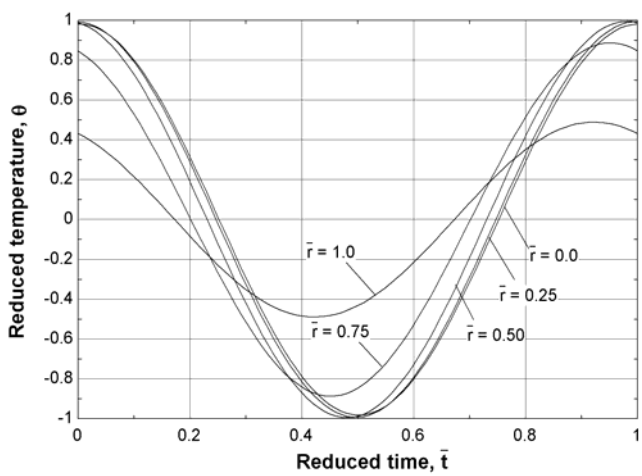

(c) Bi = 5.0., Fo = 0.2

Figure 2.21. Reduced temperature as a function of reduced time for various values of reduced radius for a sphere with (a) Bi = 0.2, Fo = 5.0, (b) Bi = 5.0, Fo = 5.0, and (c) Bi = 5.0, Fo = 0.2.

Substituting the definition of the adiabatic temperature change into Eq. (2.131) leads to:

$$\dot{Q}_{max} = \frac{8\pi R^3}{3}\rho c \frac{\pi}{\tau}\Delta T_a \sin\left(\frac{2\pi t}{\tau}\right) \tag{2.132}$$

The maximum, average rate of heat transfer is obtained by integrating Eq. (2.132) over a half-cycle:

$$\bar{\dot{Q}}_{max} = \frac{16\pi R^3}{3\tau}\rho c \frac{\pi}{\tau}\Delta T_a \int_0^{\tau/2} \sin\left(\frac{2\pi t}{\tau}\right) dt \tag{2.133}$$

or

$$\bar{\dot{Q}}_{max} = \frac{16\pi R^3}{3\tau}\rho c \Delta T_a \tag{2.134}$$

The efficiency for the active process is defined as the ratio of the actual to the maximum possible average heat transfer (η):

$$\eta = \frac{\bar{\dot{Q}}}{\bar{\dot{Q}}_{max}} \tag{2.135}$$

Substituting Eqs. (2.130) and (2.134) into Eq. (2.135) leads to:

$$\eta = \frac{3h\tau}{4R\rho c}\int_0^1 \left|\theta\left(\tilde{r}=1,\tilde{t}\right)\right| d\tilde{t} = \frac{3}{4} Bi\, Fo \int_0^1 \left|\theta\left(\tilde{r}=1,\tilde{t}\right)\right| d\tilde{t} \tag{2.136}$$

Figure 2.22 illustrates the efficiency as a function of the Fourier Biot number product for various values of the Fourier number. Notice that Fig. 2.22 is very similar to Fig. 2.16, which shows efficiency of the passive process; overlaid on Fig. 2.22 are the efficiency curves for the passive case which shows the mathematical similarity that underlies these two processes. The degradation factor derived for the passive case and presented in Eqs. (2.128) and (2.129) can therefore be applied to the active case without modification.

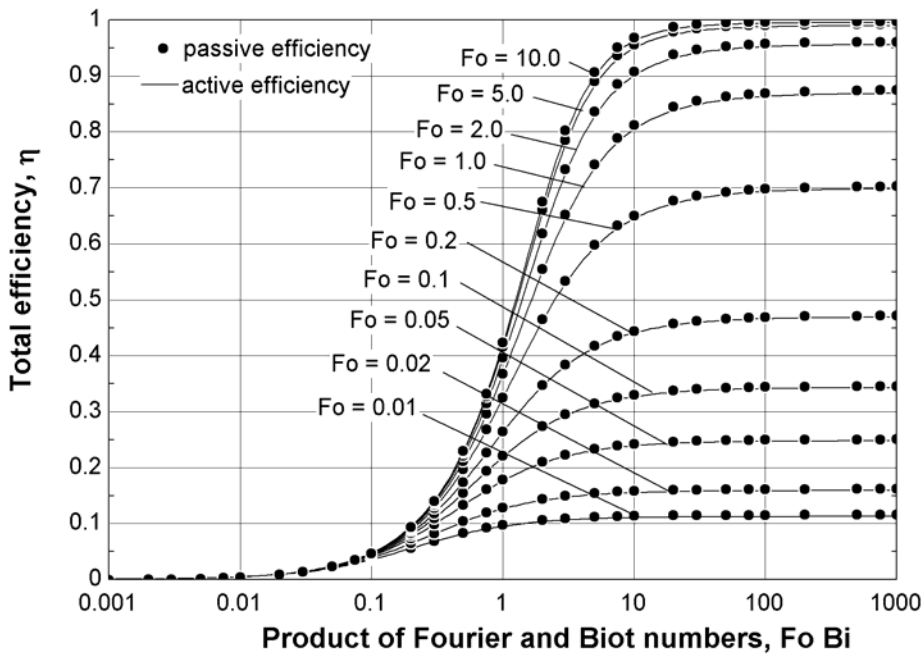

Figure 2.22: Total efficiency for the active and passive processes as a function of the product of the Biot and Fourier number for various values of the Fourier number. Note that the behavior of these processes is identical when normalized in this manner.

The correction factor from Eq. (2.128) and (2.129) has been implemented in the model for a packed sphere regenerator. However, the same analysis in this section has not been applied to a parallel plate regenerator, although the method would be the same.

2.8 CORRECTION FOR INTERNAL TEMPERATURE GRADIENTS IN A PARALLEL PLATE REGENERATOR

For a parallel plate regenerator the degradation factor is determined using the method suggested by Jeffreson (1972). In the case of a parallel plate regenerator, each plate is modeled as having a uniform internal heat generation per unit volume, $\dot{g}'''$, and each plate has a thickness D_y. The

temperature profile of each plate is assumed to be symmetric about the centerline, therefore only half of the plate thickness is modeled. Half the thickness of the plate is defined as *b*.

$$b = \frac{D_y}{2} \tag{2.137}$$

The Biot number for this case is defined as

$$Bi = \frac{b\,h}{k} = \frac{D_y\,h}{2\,k} \tag{2.138}$$

where *k* is the thermal conductivity of the regenerator material. The governing equation for uniform heat generation in a plate is:

$$\dot{g}''' = \frac{d}{dy}\left(-k\frac{dT}{dy}\right) \tag{2.139}$$

Rearranging terms yields:

$$d\left[\frac{dT}{dy}\right] = -\frac{\dot{g}'''}{k}dy \tag{2.140}$$

Integrating twice leads to:

$$T = -\frac{\dot{g}'''}{2\,k}y^2 - C_1\,y + C_2 \tag{2.141}$$

The boundary conditions are:

$$\left.\frac{dT}{dy}\right|_{y=0} = 0$$
$$T(y=b) = T_s \tag{2.142}$$

where *b* is half the thickness of plate and T_s is the surface temperature. C_1 must be zero in order to satisfy the first boundary condition. The second boundary condition allows C_2 to be solved in terms of T_s in order to obtain the temperature profile through the plate.

$$T(y) = T_s + \frac{b^2\,\dot{g}'''}{2k} - \frac{y^2\dot{g}'''}{2k} \tag{2.143}$$

The volumetric average temperature of the material can be determined by integrating the temperature distribution.

$$\overline{T} = \frac{1}{b}\int_0^b \left[T_s + \frac{b^2\,\dot{g}'''}{2k} - \frac{y^2\,\dot{g}'''}{2k} \right] dy \tag{2.144}$$

Carrying out the integration, the average temperature is:

$$\overline{T} = \frac{1}{3}\frac{\dot{g}'''b^2}{k} + T_s \tag{2.145}$$

Equation (2.145) can be written in terms of the heat flux from the wall, $\dot{q}''$ where $\dot{q}'' = D_y\,\dot{g}'''$.

$$\overline{T} = T_s + \frac{1}{3}\frac{\dot{q}''b}{k} \tag{2.146}$$

The temperature of the surface of the plate can be related to the temperature of the fluid to which it is convecting according to:

$$T_s = T_f + \frac{\dot{q}''}{h} \tag{2.147}$$

where h is the heat transfer coefficient. Substituting (2.147) into Eq. (2.146) and solving for $\overline{T}$ yields:

$$\overline{T} = T_f + \frac{\dot{q}''}{h} + \frac{\dot{q}''b}{3\,k_r} \tag{2.148}$$

which simplifies to:

$$\overline{T} - T_f = \frac{\dot{q}''}{h}\left(1 + \frac{b\,h}{3k_r}\right) \tag{2.149}$$

Substituting the definition of the Biot number ($Bi = b\,h/k$) into Eq. (2.149) yields

$$\overline{T} - T_f = \frac{\dot{q}''}{h}\left(1 + \frac{Bi}{3}\right) \tag{2.150}$$

which suggests the degradation factor for a parallel plate regenerator is:

$$DF = \frac{1}{1 + \frac{Bi}{3}} \tag{2.151}$$

Chapter 3 Active Magnetic Regenerative Refrigeration System Modeling Results

3.1. MODELING TRANSIENT AMRR OPERATION

The AMRR model described in Chapter 2 is used here to model a simple residential AMRR cooling system. The system consists of a regenerator and hot heat exchanger mounted outside and a cold heat exchanger mounted inside. In order to model the transient operation of the AMRR system, the AMRR model is coupled with simple models of the hot and cold heat exchangers. The AMRR system uses a liquid heat transfer fluid and therefore the heat capacity of the fluid in the pipes connecting the regenerator and heat exchanger is significant relative to the heat capacity of the heat exchangers and the bed, and it must be considered. For this analysis, the total heat capacity of the heat exchangers, heat transfer fluid, and tubing are broken into three parts corresponding to the upstream reservoir (the pipe and fluid upstream of the heat exchanger), the heat exchanger itself and the associated entrained fluid, and the downstream reservoir (the pipe and fluid downstream of the heat exchanger). A schematic of the fluid in the connecting piping and the heat exchanger that are modeled is shown in Fig 3.1. The model shown in Fig 3.1 is adopted for both the hot and cold heat exchanger circuits so that a total of six thermal masses (exclusive of the bed itself) are considered.

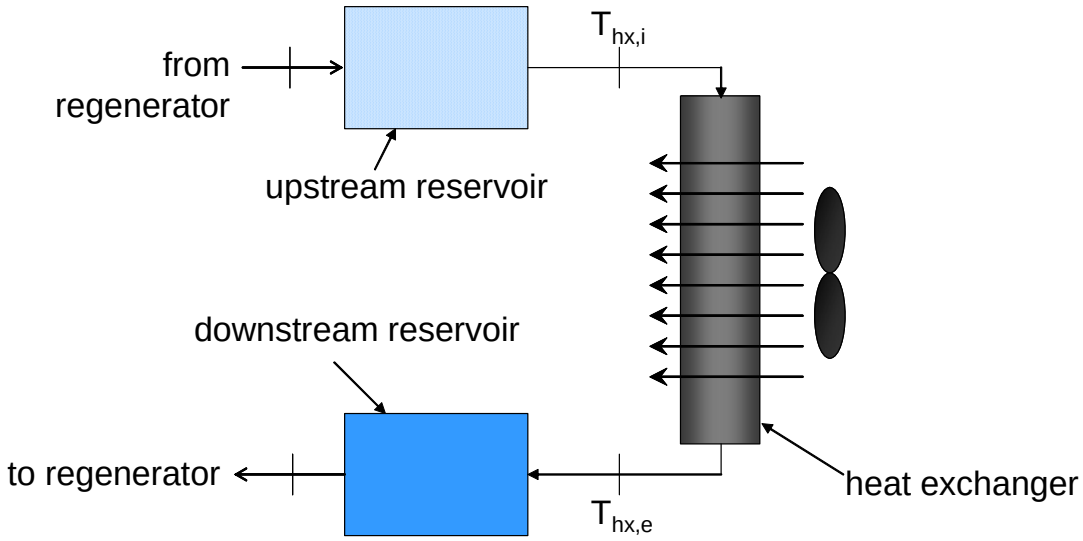

Figure 3.1. Schematic of heat exchanger modeled in transient operation

In order to determine the size of each thermal mass, the size of the heat exchangers and the length of pipe connecting them to the active regenerator bed must be specified. These pipes were sized by running the DOE/ORNL Heat Pump Design Model developed by Rice (2005) using its default inputs, which correspond to a domestic air conditioning system with a capacity of 2.5 ton (8.8 kW). The use of the DOE/ORNL model ensures that the AMRR system that is considered has external hardware that is nominally equivalent to a comparably sized vapor compression system. A unique design aspect of an AMRR system is that there is no phase change associated with the passage of the heat transfer fluid through either the hot or cold heat exchangers (which are analogous to the condenser and evaporator in the vapor compression system). In addition, the temperature rise/fall of the heat transfer fluid exiting the regenerator compared to the reservoir temperature is less than 5 K in any practical system using a practical magnetic field and magnetocaloric materials that are currently available. If the system is configured such that the fluid flow rate through the heat exchangers is the same as the flow rate through the regenerator, the fluid mass flow rate in the AMRR system must be substantially

larger than in a vapor compression cycle with comparable capacity. The approximate ratio of mass flow rates for an AMRR system ($\dot{m}_{AMRR}$) to the mass flow rate for a vapor compression system ($\dot{m}_{vc}$) is given by:

$$\frac{\dot{m}_{AMRR}}{\dot{m}_{vc}} \sim \frac{\Delta h_{v,ref}}{c_f \Delta T_{mc}} \tag{3.1}$$

where $\Delta h_{v,ref}$ is the latent heat of vaporization of the refrigerant and ΔT_{mc} is the adiabatic temperature change of the regenerator material. A typical value of the temperature rise due to the magnetocaloric effect, ΔT_{mc}, is 2 K when water is used as the heat transfer fluid; Eq. (3.1) suggests that the required AMRR mass flow rate will be approximately 20 times the mass flow rate of R22 required by an equivalent vapor compression system. To avoid large pumping losses due to the increased fluid flow, the diameter of the connecting tube is increased from 6.4 mm (the DOE/ORNL model value) to 37 mm for this analysis. Alternative configurations of an AMRR system can be implemented to reduce the mass flow rate through the heat exchangers, but the reduction in pumping power through the heat exchangers would most likely be offset by a reduction in efficiency of the regenerator. For this analysis, a high fluid flow rate through the heat exchangers was assumed and the connecting piping diameter was increased to 37 mm to reduce pumping power. Otherwise, the outputs from the DOE/ORNL model were used to determine the total heat capacity of the heat exchangers and connecting tubing. The total length of tubing is 14.6 m to the cold heat exchanger and 0.6 m to the hot heat exchanger (consistent with an air-conditioning compressor unit that is placed out-of-doors near the hot heat exchanger). The increased tube size and high heat capacity of water make the total heat capacity of the upstream and downstream reservoirs associated with the cold heat exchanger circuit quite large. The heat capacities of the reservoirs that are modeled in this analysis are summarized in Table

3.1; all values in Table 3.1 include the heat capacity of the fluid, tubing, and fins, if applicable.

Table 3.1. Calculated system heat capacities

Component	Hot Side Heat Capacity	Cold Side Heat Capacity
upstream reservoir	30200 J/K	724300 J/K
heat exchanger	15300 J/K	11200 J/K
downstream reservoir	30200 J/K	724300 J/K

The numerical model was used to predict the transient performance of an AMRR system for several conditions. In order to simulate transient operation, the regenerator is started from a specified initial temperature distribution and the model is stepped forward in time for one cycle to reach a new regenerator temperature distribution. The temperature of the fluid entering the regenerator from the hot and cold downstream reservoirs is assumed constant during the cycle. The temperature of fluid exiting the regenerator is assumed to mix perfectly in the upstream reservoir and therefore enters the heat exchanger at a uniform temperature. The hot heat exchanger is modeled as a cross-flow, air-to-liquid heat exchanger using an ε-*NTU* method. Analysis of the cold heat exchanger considers the water condensation that takes place if air is cooled below its dewpoint temperature; heat transfer and moisture removal for the cold heat exchanger are modeled using a heat transfer analogy that is similar to the ε-*NTU* method presented by Braun et al. (1989). The heat transfer accepted or rejected by the heat exchanger is determined and the fluid exiting the heat exchanger is assumed to mix perfectly in the downstream reservoir and the new temperature provided to the AMRR for the following cycle is calculated with an energy balance. The system parameters used in this study are given in Table 3.2 and correspond to an optimally designed AMRR system for domestic air conditioning, as discussed in Engelbrecht et al. (2006b).

Table 3.2. System parameters used for transient study

Parameter	Value	Parameter	Value
maximum applied field	1.5 Tesla	heat transfer fluid	Water
cold air flow rate	0.57 kg/s	fluid mass flow rate	1.4 kg/s
hot air flow rate	1.42 kg/s	Period	0.2 sec (5 Hz)
cold heat exchanger UA	880 W/K	sphere size for packing	0.2 mm
hot heat exchanger UA	1430 W/K	motor efficiency	0.9
regenerator volume	10 L	pump efficiency	0.7
regenerator type	packed sphere	cycle time (τ)	0.5 s

The startup response of an AMRR system that is entirely at a uniform temperature of 300 K (~80ºF) was simulated and the response, presented in terms of refrigeration capacity as a function of time, is shown in Fig. 3.2. Note that the temperature of the air entering the hot and cold heat exchangers is assumed to be constant and equal to 300 K.

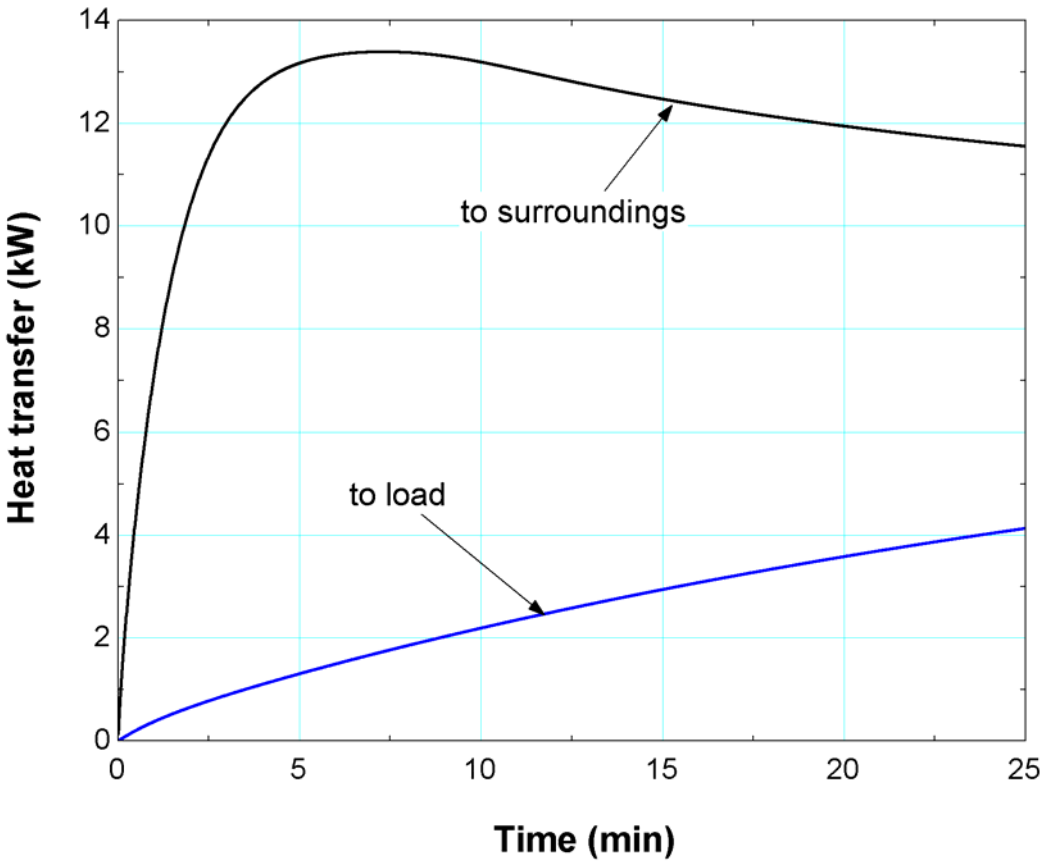

Figure 3.2. Refrigeration capacity of a system started from a uniform temperature of 300 K

Another transient condition of interest corresponds to a system that has reached steady state and is then shut off for a short period and restarted. This situation corresponds to modulation of the capacity through on/off control; the subsequent section shows that there are more efficient control strategies for an AMRR system; however, the transient response under these conditions is still of interest. Kim and Bullard (2001) measured the dynamic response of a vapor compression air-conditioning system using R-410A under this type of transient operation. In order to compare the transient performance of an AMRR system directly to a vapor compression system, the test conditions reported by Kim and Bullard were used to simulate the transient performance

of an AMRR system. The regenerator and hot heat exchanger circuit are assumed to start from a uniform temperature of 308 K (corresponding to being placed in a warm, outdoor environment) while the cold circuit starts at a uniform temperature of 300 K (corresponding to its placement in a previously conditioned, indoor environment). The temperature of the air entering the heat exchangers is assumed to be constant and equal to the temperature of either the surroundings or cooled space. The temperatures of the upstream reservoirs, which are the temperatures of the fluid that enters the regenerator during each cycle, are shown in Fig. 3.3 as a function of time.

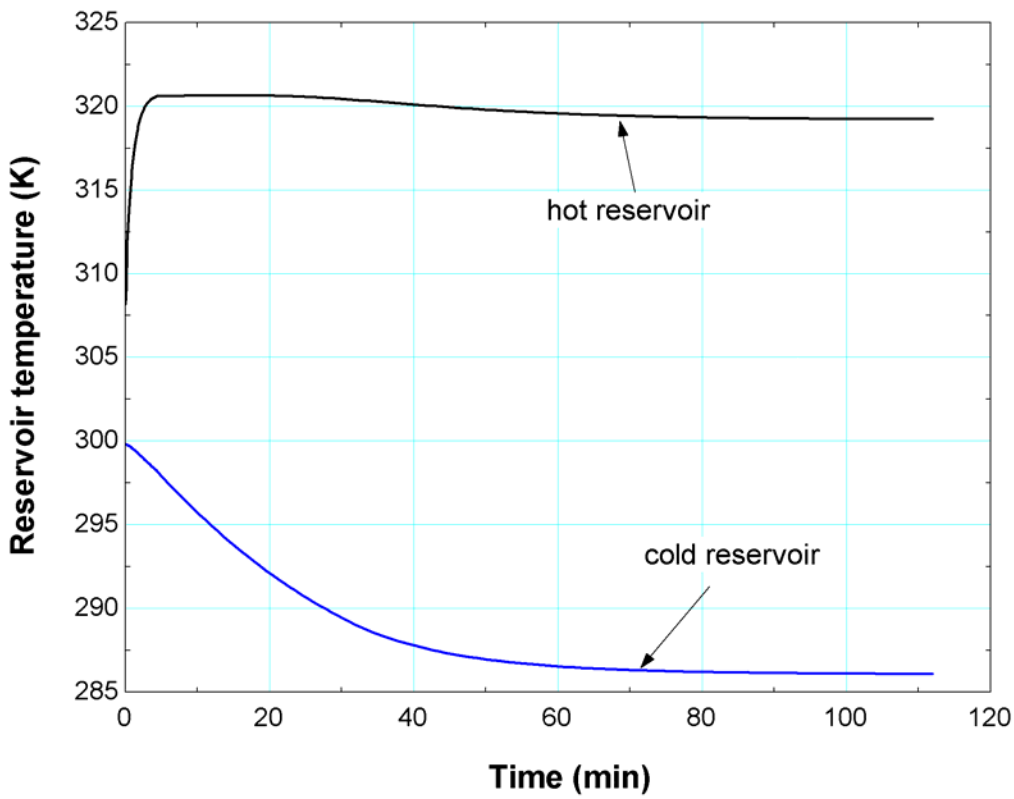

Figure 3.3. Reservoir temperature as a function of time for the system that is shut off and restarted

Figure 3.2 shows that the heat transfer in the hot heat exchanger increases much more rapidly

than the heat transfer in the cold heat exchanger, and Fig. 3.3 shows that the hot reservoir temperature also exhibits a much faster response than the cold circuit because the tubing to the cold heat exchanger is much longer than to the hot heat exchanger and therefore the cold circuit heat capacity is much higher. Kim and Bullard reported that the vapor compression system took approximately 15 min to reach steady state after it was restarted and Fig. 3.3 shows that the AMRR system took approximately 120 min under the same conditions. However, the relatively fast response of the hot reservoir shows that if the length of the connecting tubing to the cold heat exchanger were reduced, the transient response time of the AMRR system would also be significantly reduced.

3.2. PART LOAD PERFORMANCE

The cooling capacity of AMRR systems may be varied by changing the flow rate of the heat transfer fluid, the cycle time, or both. This analysis compares system performance for three methods of controlling the cooling power produced by an AMRR system: varying the cycle time, varying the fluid mass flow rate, and varying the cycle time and flow rate simultaneously. To investigate the dependence of efficiency on cycle time and mass flow rate, the performance of a single system was predicted over a range of fluid mass flow rates and cycle times (corresponding to varying the pump and motor speeds). The system parameters are summarized in Table 3.3; note that the AMRR model alone was used to predict the performance and the heat exchangers were not considered.

Table 3.3. Parameters used for space cooling part load performance.

Parameter	Value	Parameter	Value
heat rejection temp.	310 K	sphere size for packing	0.2 mm
load temperature	287 K	number of beds	6
dwell ratio	0.5	pump efficiency	0.7
maximum applied field	1.5 Tesla	motor efficiency	0.9
total regenerator volume	8 L	heat transfer fluid	Water
regenerator aspect ratio	0.25	regenerator type	packed sphere

The dwell ratio listed in Table 3.3 is the portion of the cycle time when there is no fluid flow and the aspect ratio is the ratio of the regenerator length to diameter. The results of the parametric study are presented in terms of the coefficient of performance as a function of cooling power provided by the system for constant values of the heat transfer fluid mass flow rate, $\dot{m}$, and cycle time, τ. The refrigeration capacity and coefficient of performance are complicated functions of cycle time and mass flow rate, and the results are summarized in Figure 3.4.

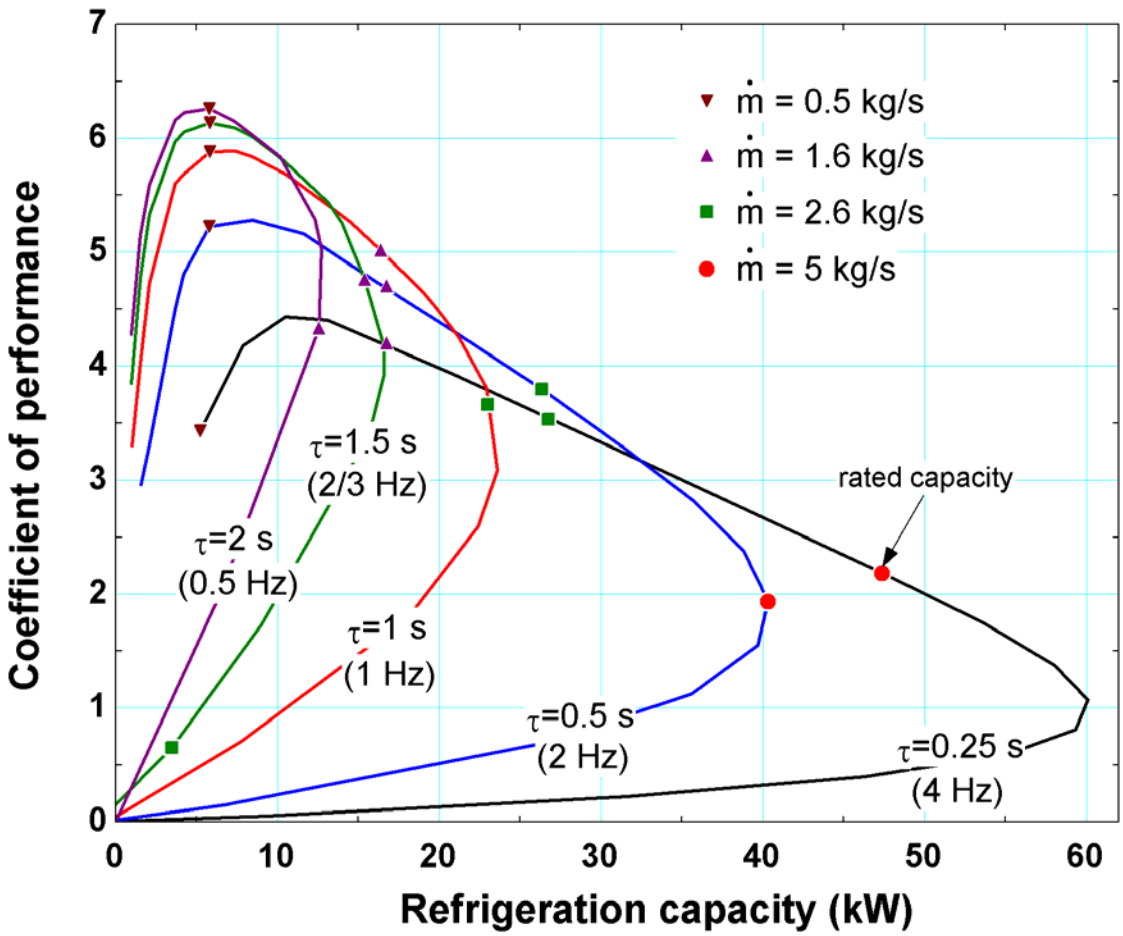

Figure 3.4. *COP* as a function of cooling power for various values of cycle time and fluid mass flow rate

Figure 3.4 can be used to determine the optimum cycle time and mass flow rate for a given refrigeration capacity. The best operating condition is the curve that results in the highest *COP* for the desired cooling capacity. Studying curves of constant cycle time reveals that the system is capable of producing the same cooling power with two unique coefficients of performance. The lower *COP* corresponds to operation at a fluid flow rate that is too large for the regenerator. At high cycle times (i.e., low frequency), the number of times the material is magnetized and

demagnetized per unit time decreases and therefore maximum attainable cooling power decreases; for example, at τ=0.5 s, the maximum cooling power is approximately 40 kW whereas τ=2 s would provide at most 13 kW. However, at low cycle times (i.e., high frequency) there is not sufficient time for heat transfer and therefore *COP* decreases.

Lines of constant mass flow rate are harder to study in Figure 3.4 because some mass flow rates are not at all appropriate for certain frequencies and therefore these operating conditions do not appear on the figure. However, the cooling capacity initially increases with increasing flow rate but the regenerator eventually becomes overwhelmed and the cooling capacity begins to decrease and can become negative; this trend is especially evident by examining those points that correspond to $\dot{m}$=2.6 kg/s where the refrigeration capacity is approximately equal for cycle time of 0.25 – 1 s but then decreases dramatically for a cycle time of 1.5 s.

The optimum fluid flow rate and cycle time combinations correspond to traversing the apex of the curves shown in Figure 3.4 and provide the highest system COP at a given cooling capacity. The optimum operating points were estimated for several refrigeration capacities and the results are shown in Figure 3.5. The optimal modulation strategy shown in Fig. 3.5 requires simultaneous control of the pump and the motor. A simpler control strategy would vary only one of these control parameters. The *COP* and refrigeration capacity were calculated when the cycle time was held constant and the fluid mass flow rate varied (pump modulation) and also when the fluid flow was held constant while the cycle time varied (frequency modulation) and the results are also shown in Fig. 3.5. Notice that when the desired refrigeration capacity is near the design point, modulation of only the fluid mass flow rate (or pump speed) is effective and yields

efficiencies that are very near the optimum control scheme. However, as the desired cooling rate becomes relatively small, it becomes beneficial to vary the cycle time as well. When only the cycle time is modulated, the bed quickly becomes overwhelmed by the fluid flow and the efficiency decreases quickly; clearly for the design considered here modulating the fluid flow rate is more attractive than modulating the cycle time, especially near the design point.

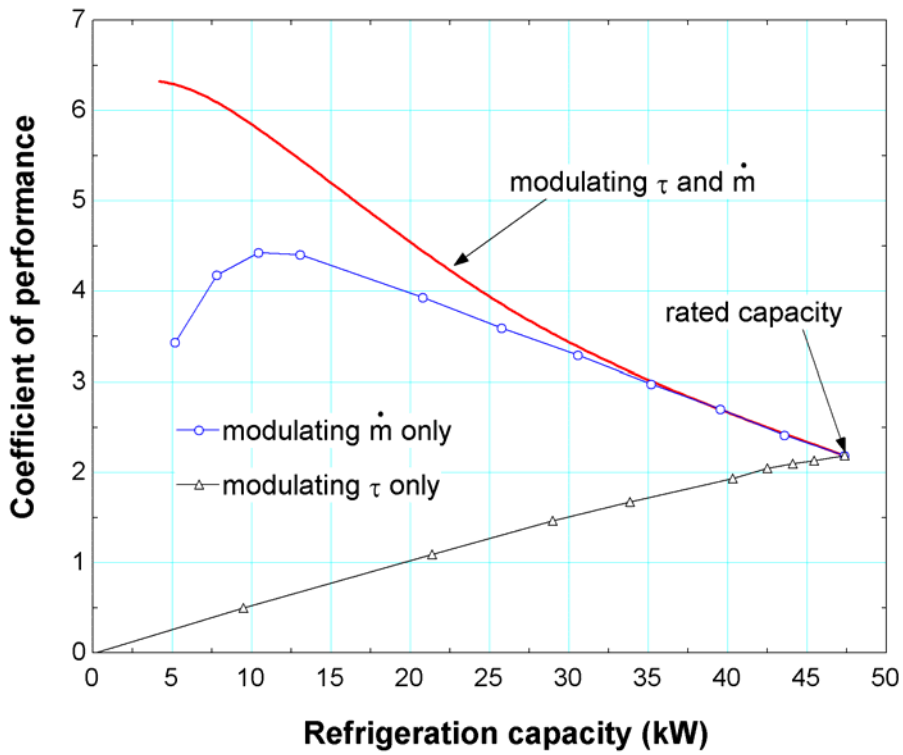

Figure 3.5. Optimum fluid flow rate and cycle time as a function of refrigeration capacity

Figure 3.6 shows the necessary fluid flow rate and cycle time corresponding to the optimum operating conditions as a function of cooling capacity.

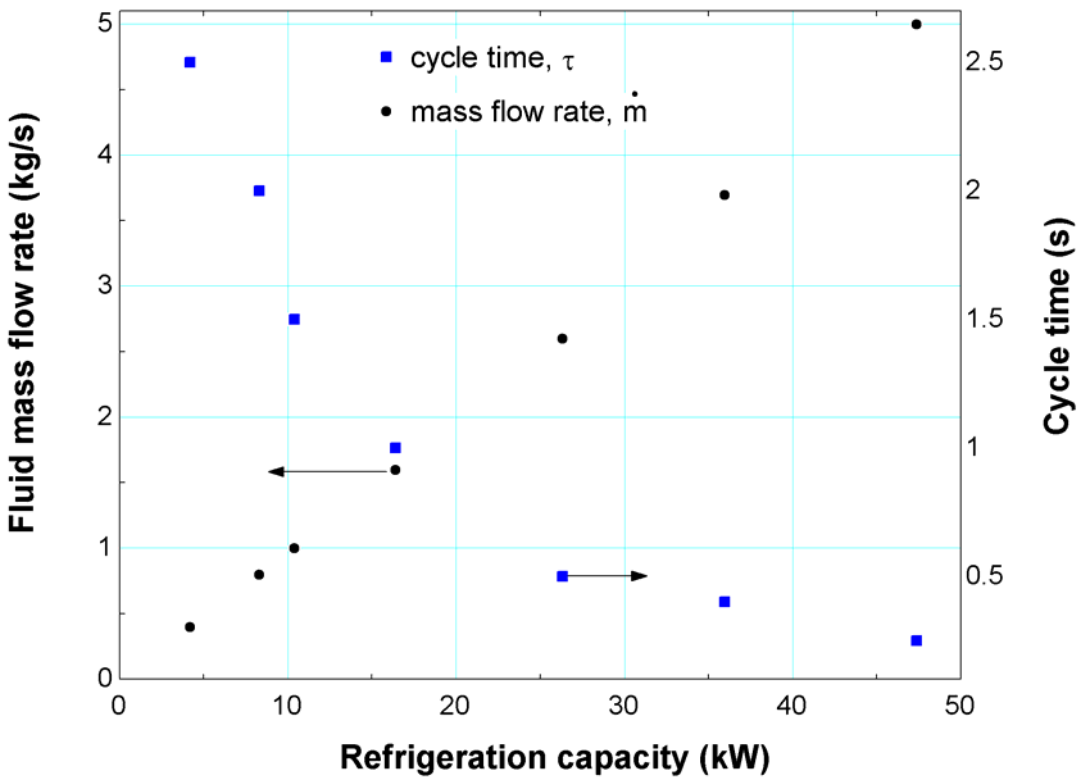

Figure 3.6. Fluid flow rate and cycle time corresponding to the optimum control strategy shown in Fig. 3.5 for a desired cooling power

Figure 3.3 shows that the transient response of an AMRR system was found to be significantly slower than a comparable vapor compression system; this is mostly to the high heat capacity of the liquid heat transfer fluid in the connecting tubing from the regenerator to the cold heat exchanger. However, the cooling capacity of AMRR systems can be controlled when a variable speed pump is used and therefore the cooling capacity of the system could be controlled to match the load. Controlling the pump speed to match the cooling power demanded by the load would decrease the importance of the transient response of the system that was presented in Section 3.1.

3.3. COMPARISON TO A 2D NUMERICAL AMRR MODEL

The 1D numerical model described in this thesis was compared to a 2D finite element AMRR model developed at Risø National Laboratories in Denmark and described by Petersen et al. (2007). The 2D model solves the laminar Navier-Stokes equations and therefore does not need to assume a flow profile in the regenerator. The 2D model can also solve the governing equations for modeling parameters such as the Nusselt number, axial conduction, and friction factor as well as explicitly account for temperature gradients perpendicular to the fluid flow in the fluid and solid. However, the increased capability of the 2D model comes at the expense of increased computation time over the 1D model. The two models are compared here for a flat plate regenerator composed of gadolinium using water as a heat transfer fluid.

3.3.1 Cycle Characteristics for the Model Comparison

The 2D model was developed specifically to model a flat plate regenerator that has a flow channel height that is half the thickness of each plate. The constraint on the flow channel dimensions results in a regenerator with a constant porosity of 0.33. A simple drawing of the regenerator modeled in this comparison is shown in Fig. 3.7. The mass flux of the heat transfer fluid was set to a constant value of 2.42 kg/m^2, which corresponds to a regenerator utilization of 0.27. The regenerator utilization (Φ) for the system modeled here is defined as

$$\Phi = \frac{\dot{m}_f c_f \lambda}{\rho_r \left(1-\varepsilon\right) L A_c c_{\mu_0 H}} \tag{3.2}$$

where λ is the period of the hot or cold blow.

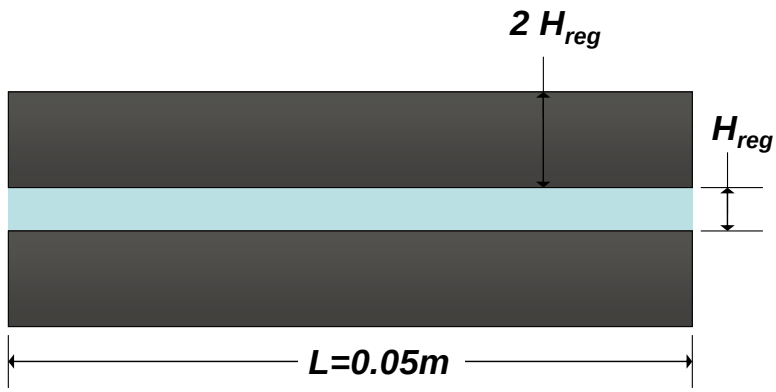

Figure 3.7. Schematic of regenerator geometry used for the 1D and 2D model comparison

In Fig. 3.7, H_{reg} is the height of the flow channel or half the thickness of the plates. A regenerator made of pure gadolinium using water as the heat transfer fluid was modeled. The properties of gadolinium were determined using the mean field model described in Section 2.4.2 and the properties of water were assumed constant. The cycle time for this comparison was set to a constant value of 6 s and the maximum effective magnetic field was 1 Tesla. A summary of the modeling parameters used for the 1D and 2D model comparison is given in Table 3.4. The mass flow and magnetic field profile used in the comparison are shown in Fig. 3.8.

Table 3.4. Modeling parameters used to compare the 1D model described in this thesis to a 2D model developed by Petersen et al. (2007)

Parameter	Value	Parameter	Value
cycle time	6 s	dwell ratio	0.2
fluid mass flux	2.42 kg/m^2	regenerator utilization	0.27
max magnetic field	1 Tesla	regenerator type	flat plate
heat transfer fluid	water	regenerator material	Gd
porosity	0.33	number of time steps	2000
regenerator length	0.05 m	number space steps	90
hot reservoir temperature	298 K	convergence tolerance	0.0002
cold reservoir temperature	288 K	plate thickness	0.1-3 mm

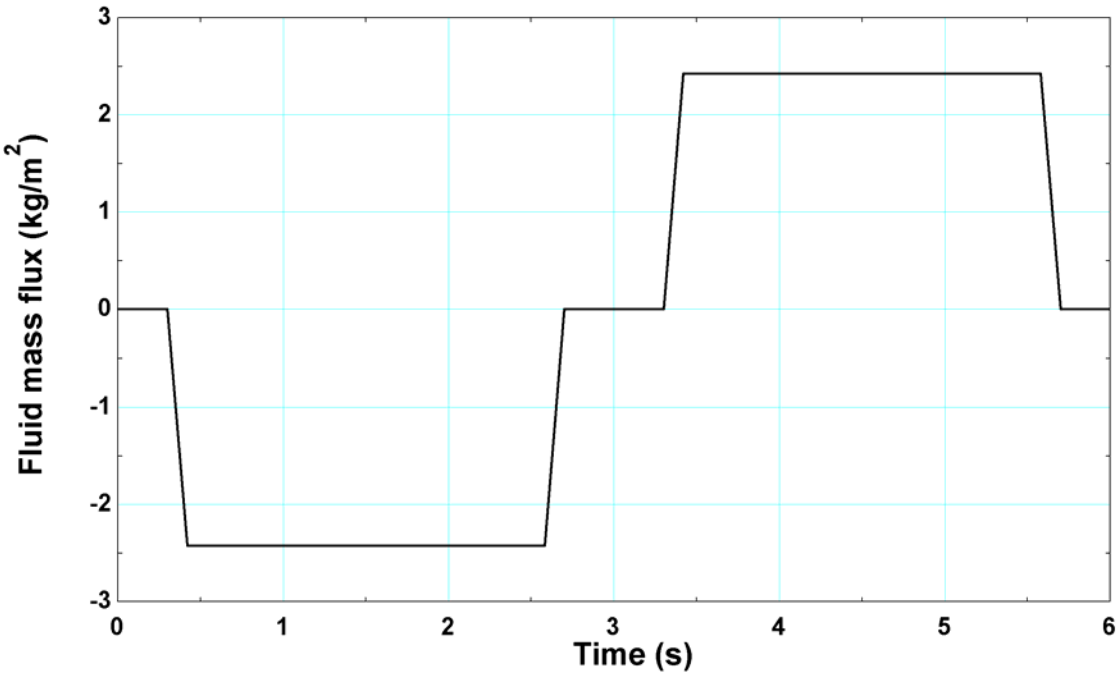

(a)

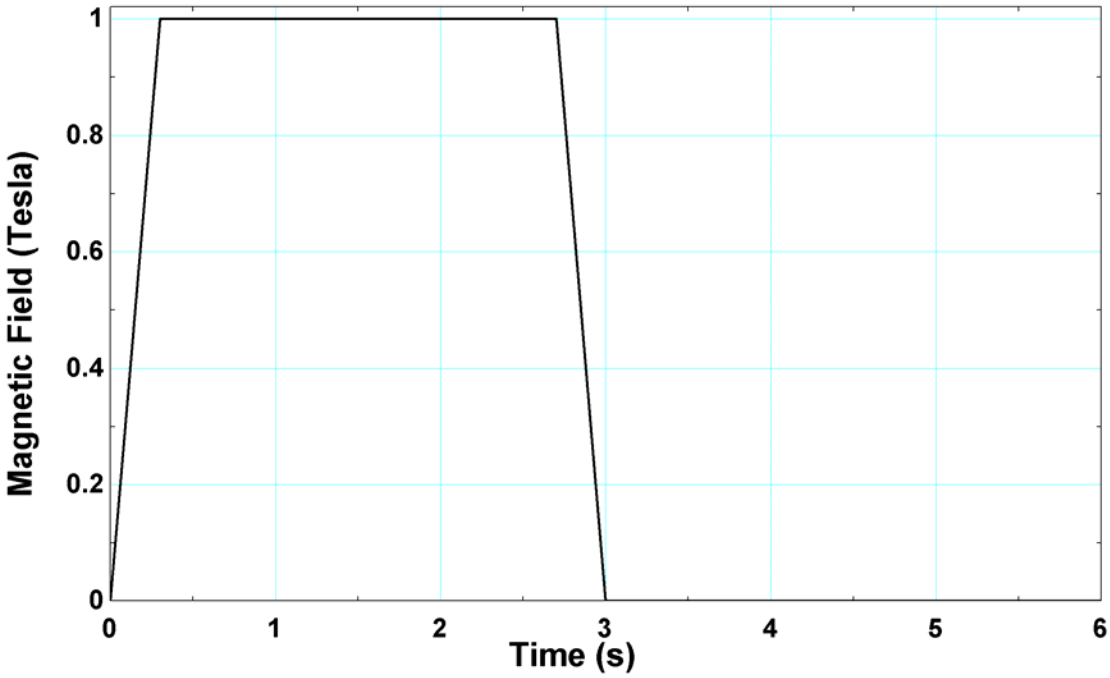

(b)

Figure 3.8. Profile of (a) mass flow rate as a function of time and (b) magnetic field as a function of time for the model comparison

3.3.2 2D Model Description and Governing Equations

In the 2D model, the velocity distribution in the fluid flow channel is determined by solving the momentum (3.3) and continuity equations (3.4) for an incompressible fluid with constant (temperature independent) properties.

$$\rho_f \left(\frac{\partial U}{\partial t} + \left(U \cdot \nabla \right) U \right) - \mu_f \nabla^2 U + \nabla p = 0 \tag{3.3}$$

$$\nabla \cdot U = 0 \tag{3.4}$$

where U is the velocity vector. The governing equations for the fluid entrained in the regenerator are

$$\rho_f c_f \left(\frac{\partial T_f}{\partial t} + \left(U \cdot \nabla T_f \right) \right) + \nabla \cdot \left(k_f \nabla T_f \right) = 0 \tag{3.5}$$

$$\rho_r c_r \frac{\partial T_r}{\partial t} + \nabla \cdot \left(-k_r \nabla T_r \right) = 0 \tag{3.6}$$

The solid and fluid governing equations are coupled with the following boundary condition

$$k_f \left(\frac{\partial T_f}{\partial y} \right)_{y=H_{reg}} = k_r \left(\frac{\partial T_r}{\partial y} \right)_{y=H_{reg}} \tag{3.7}$$

The solid regenerator material is assumed to magnetize and demagnetize adiabatically and the magnetic work input is implemented as an instantaneous temperature change (ΔT_{ad}) in the regenerator:

$$T_{r,i}^{+} = T_{r,i} + \Delta T_{ad} \left(T_{r,i}, \mu_0 H_i, \mu_0 H_i^{+} \right) \tag{3.8}$$

where $T_{r,i}$ is the temperature of the regenerator at spatial step i before the change in magnetic field, $T_{r,i}^{+}$ is the regenerator temperature at spatial step i after the change in magnetic field, and $\Delta T_{ad}\left(T_{r,i}, \mu_0 H_i, \mu_0 H_i^{+}\right)$ is the adiabatic temperature change of the regenerator material when the magnetic field changes from $\mu_0 H_i$ to $\mu_0 H_i^{+}$. The 2D model assumes symmetry in the regenerator and considers only half the thickness of one plate and the half height of one flow channel. The 2D model was developed specifically for a flat plate regenerator and modeling other regenerator geometries would require major modifications to the model. The model starts from a uniform initial temperature in the regenerator and flow channels and then takes steps forward in time until cyclical steady-state is obtained. Steady-state occurs when the difference between the temperature profiles after two subsequent cycles is below a specified tolerance. The 2D model has been implemented in COMSOL. The 2D model calculates the magnetic work input, W_{mag}, from the calculated cooling load accepted by the cold reservoir and the heat rejected to the ambient.

$$W_{mag} = Q_{rej} - Q_{ref} \tag{3.9}$$

where Q_{rej} is the heat rejected to the ambient and Q_{ref} is the energy transferred from the load to the cold reservoir. A notable difference between the two models is the implementation of the magnetic work interaction of the regenerator material. The 2D model treats the magnetocaloric effect as an instantaneous temperature change based on the adiabatic temperature change, ΔT_{ad}, whereas the 1D model treats the magnetocaloric effect as an energy input to the regenerator governing equations based on the isothermal entropy change, Δs_{mag}. To ensure the two methods yield the same results for an adiabatic magnetization of the regenerator material, a test was performed where the 1D model was used to simulate an adiabatic magnetization by setting the

Nusselt number and the conduction in the regenerator to zero and ramping the magnetic field from 0 to 1 Tesla as was done in Section 2.3.1. The resulting temperature change was compared to the ΔT_{ad} obtained directly from the mean field model. The ramping of the magnetic field was performed for a range of time steps from 50 to 200. The results are shown in Figure 3.9, which show that using the isothermal entropy change, Δs_{mag}, to model an adiabatic magnetization results in temperature changes virtually identical to the reference value of ΔT_{ad}. For this comparison, it was deemed sufficient to use 100 time steps during magnetization, which requires a total of 2000 time steps for the full AMRR cycle.

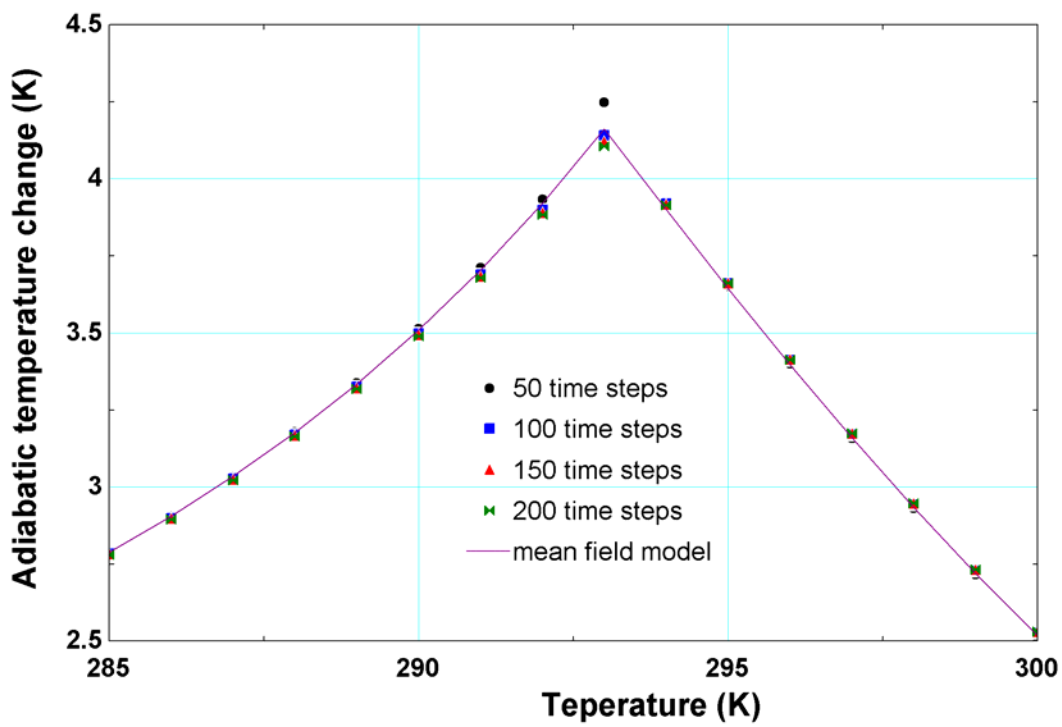

Figure 3.9. Predicted adiabatic temperature change using the 1D model compared to the adiabatic change from Gd material properties

3.3.3 Model Comparison Results

The predicted refrigeration capacity, the rejected heat, the magnetic work, the coefficient of performance and the temperature profiles during the refrigeration cycle are used to compare the two models. To obtain a meaningful comparison of the predicted temperature profiles of the two models, the results from the 2D model were averaged in the direction perpendicular to flow. The resulting average temperature profiles then correspond to the temperature profiles obtained from the 1D model.

The 1D and 2D models were compared for a constant mass flow rate for a range of plate thicknesses in the regenerator. The plate thickness was varied from 0.1 mm to 3 mm, while the height of the flow channel remained at a factor of half the plate thickness. The utilization was held constant (assuming a constant heat capacity of Gd) by using a constant fluid flow rate and regenerator volume during the model comparison. The refrigeration capacity predicted by the two models as a function of plate thickness is shown in Fig 3.10 and the rejected heat is shown in Fig 3.11.

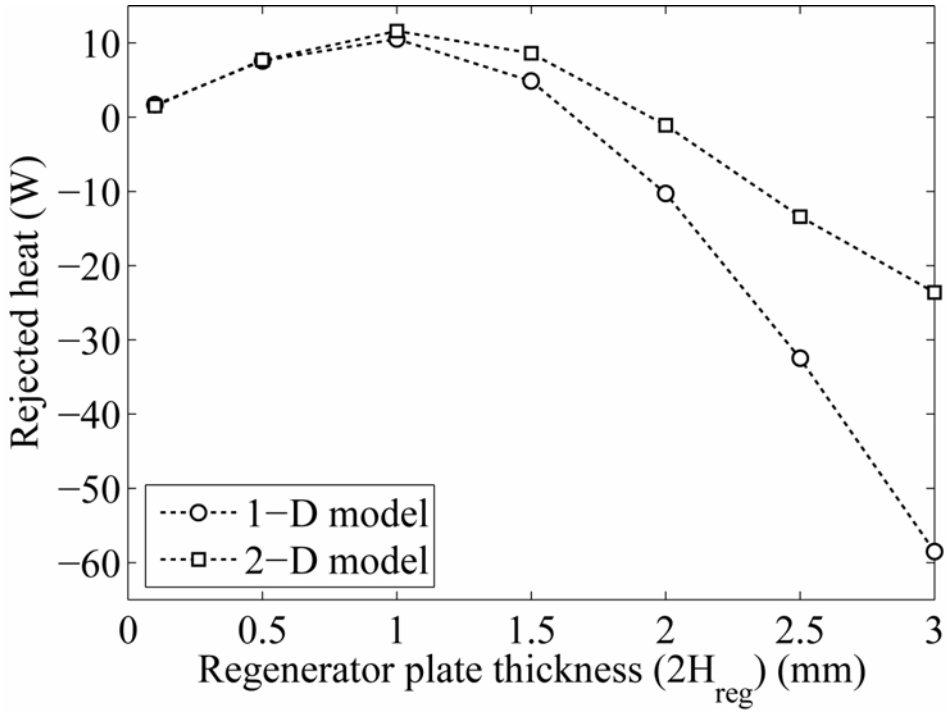

Figure 3.10. Predicted refrigeration capacity of the 1D and 2D models as a function of regenerator plate thickness

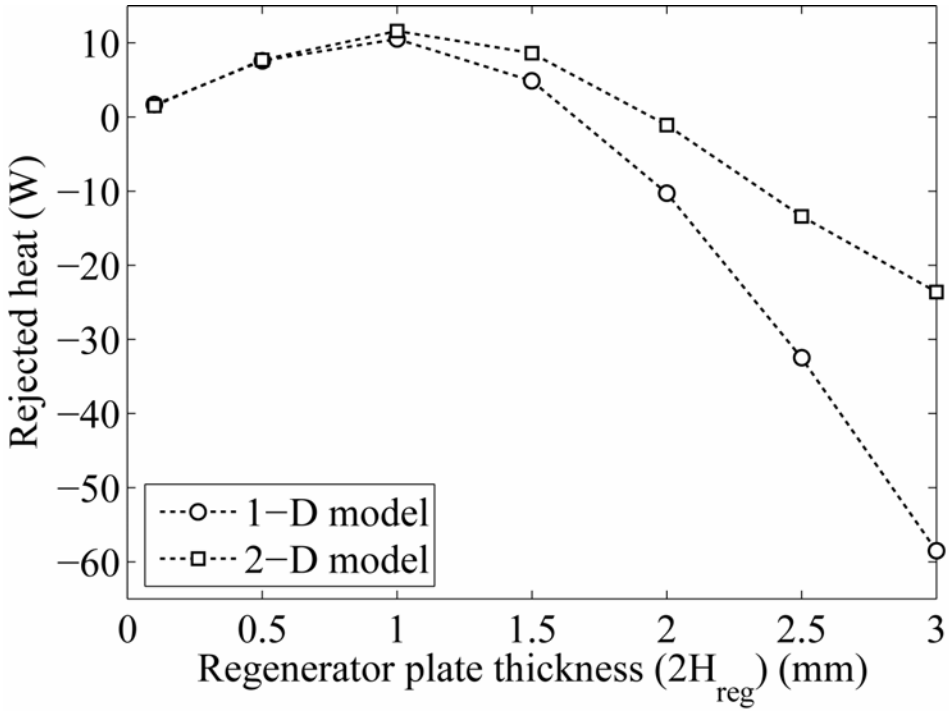

Figure 3.11. Predicted heat rejection to ambient of the 1D and 2D models as a function of regenerator plate thickness

The two models predict virtually identical results for the refrigeration capacity and the rejected heat for plate thicknesses equal to and below 1 mm. For plates thicker than 1 mm, the results of the two models start to diverge and the 1D model consistently predicts lower refrigeration capacity and lower rejected heat than the 2D model. Note that both models predict a negative cooling capacity for plate thicknesses greater than approximately 2 mm. A negative cooling power shows that regenerators with thick plates are a poor design and are probably not important design points for AMRR systems. The general trends regarding the refrigeration capacity and the rejected heat predicted by both models are approximately the same. The agreement between the two models decreases as the plate thickness increases but the 1D model still shows the same trends as the 2D model. The agreement between the two models despite their significantly different numerical implementations adds credibility to the predicted results of each model for AMRR systems. The magnetic work predicted by both models is shown in Fig 3.12 and the corresponding COP as a function of plate thickness is shown in Fig 3.13.

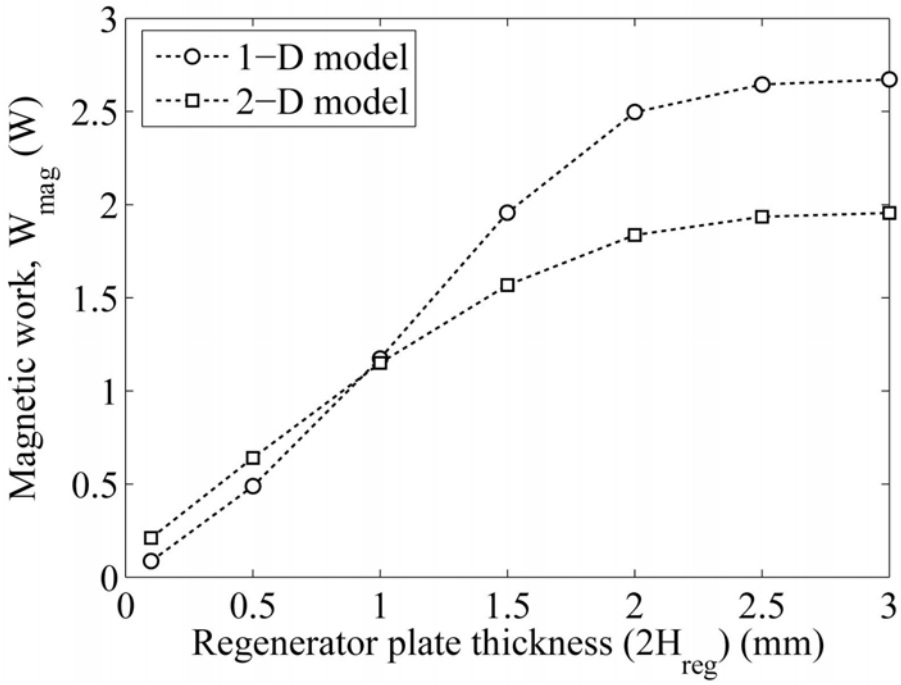

Figure 3.12. Predicted magnetic work input of the 1D and 2D models as a function of regenerator plate thickness

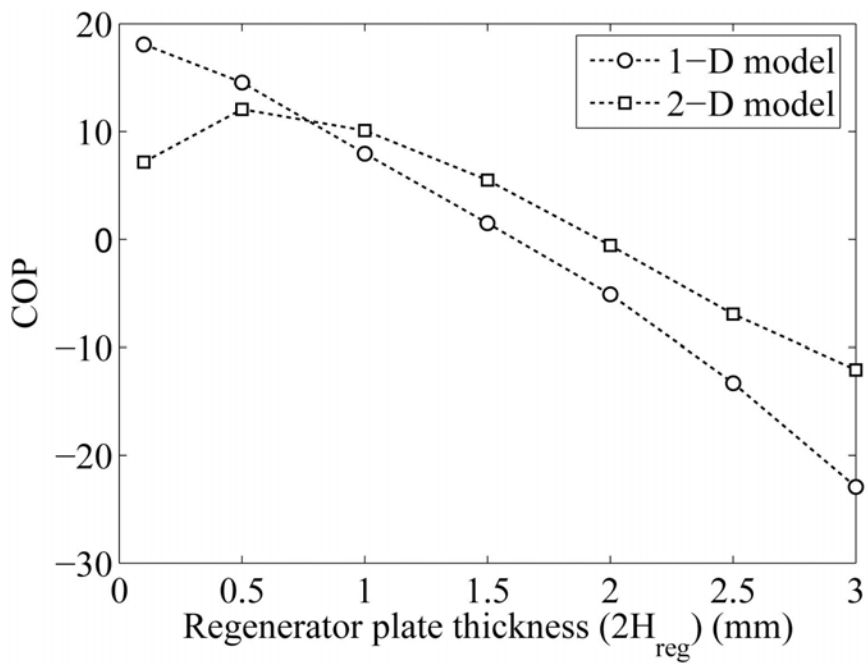

Figure 3.13. Predicted COP of the 1D and 2D models as a function of regenerator plate thickness

Compared to the 2D model, the 1D model predicts a higher magnetic work for plates thinner than 1 mm and predicts a lower magnetic work for plates thicker than 1 mm but shows no obvious trend towards better agreement between the two models appears. Figure 3.13 shows that the two models obtain similar values of the COP for regenerator plates between 0.5 mm and 1.5 mm but the COP diverges at both thinner and thicker regenerator plates. The trends of the COP predicted by the two models are also different. The 2D model shows a parabolic shape the COP, which has a maximum for a plate thickness of 0.5 mm. Figure 3.13 shows that the 1D model predicts an increasing COP for a decreasing plate thickness and with no optimum value above a plate thickness of 0.1 mm. These results can be explained from the results of the magnetic work. Since the magnetic work of the 1D model decreases below that of the 2D model for plates thinner than 1 mm, but the refrigeration capacity of the two models is almost equal, the COP of the 1D model must be higher compared to the 2D model. These results are somewhat surprising given the good agreement of both the refrigeration capacity and the rejected heat. However, the magnetic work is a derived value determined from the difference in refrigeration capacity and the rejected heat and small differences between the two models can lead to large differences in both the magnetic work and the COP. Because of the numerical formulation of the 1D model, it cannot directly account for temperature gradients perpendicular to the direction of flow ($\partial T / \partial y$). An explanation of the increasing agreement of the two models for decreasing thickness of the regenerator plates is that the smaller dimensions of the plates and channels results in smaller $\partial T / \partial y$. As a result, the 2D model should approach 1D conditions as the plate thickness and flow channel height decrease. To study the influence of temperature gradients on

predicted results, $\partial T / \partial y$ predicted by the 2D model is plotted. Figure 3.14 shows the shows the average temperature gradient in the plate and the heat transfer fluid during an AMRR cycle.

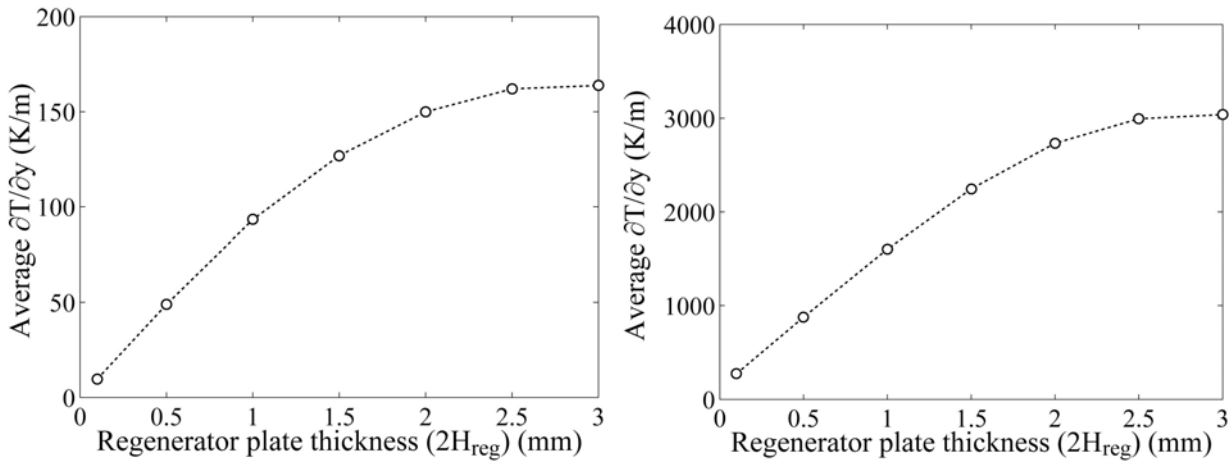

(a) (b)

Figure 3.14. Average temperature gradient in (a) the regenerator and (b) the heat transfer fluid

The results shown in Fig. 3.14 show a likely cause of the increasing discrepancy between the 1D and 2D models as the plate thickness increases. Because the 1D model cannot directly account for temperature gradients in the fluid or regenerator, the agreement between the 1D and 2D models should decrease as the plate thickness, and therefore temperature gradient in the fluid and solid, increases.

The predicted temperature profiles of the 1D and 2D models were also compared. The temperature profile of the fluid in the flow channel before the cold and before the hot blow periods affects the refrigeration capacity and the rejected heat and therefore theses two points in the AMRR cycle were chosen to compare the two models. Figure 3.15 shows the temperature profiles in the flow channel before the cold and hot blow obtained by the 1D model and the 2D

models for a plate thickness of 0.1 mm. Figure 3.15 shows an excellent agreement between the temperature profiles predicted by the two models for a plate thickness of 0.1 mm with virtually no difference between the temperature profiles. There is also a good qualitative and quantitative agreement between the two models and both predict the same shape of the temperature profile in the flow channel.

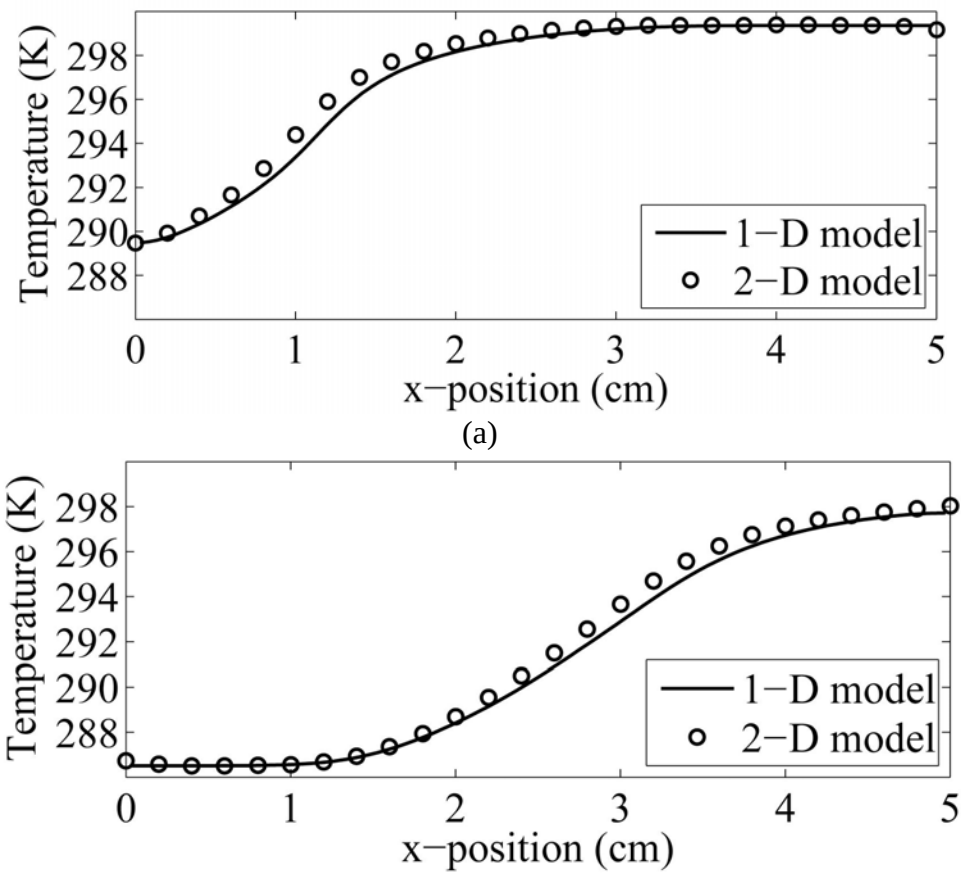

Figure 3.15. Fluid temperature as a function of regenerator location (a) before the cold blow and (b) before the hot blow for a 0.1 mm plate thickness and 0.05 mm flow channel height

Figure 3.16 shows the temperature profiles predicted by the two models for a plate thickness of 3 mm. Figure 3.16 shows that for a larger plate thickness, the 2D model predicts a higher fluid

temperature before the cold blow and a lower fluid temperature before the hot blow. These results can explain the deviations of the refrigeration capacity and the rejected heat observed at thicker regenerator plates. The lower temperatures before the cold blow predicted by the 1D model result in a lower amount of heat that is rejected during the cold blow and likewise, the higher temperatures before the hot blow mean that a lower amount of heat is absorbed from the load during the hot blow. These temperature profiles agree with the results shown in Fig. 3.10 and 3.11.

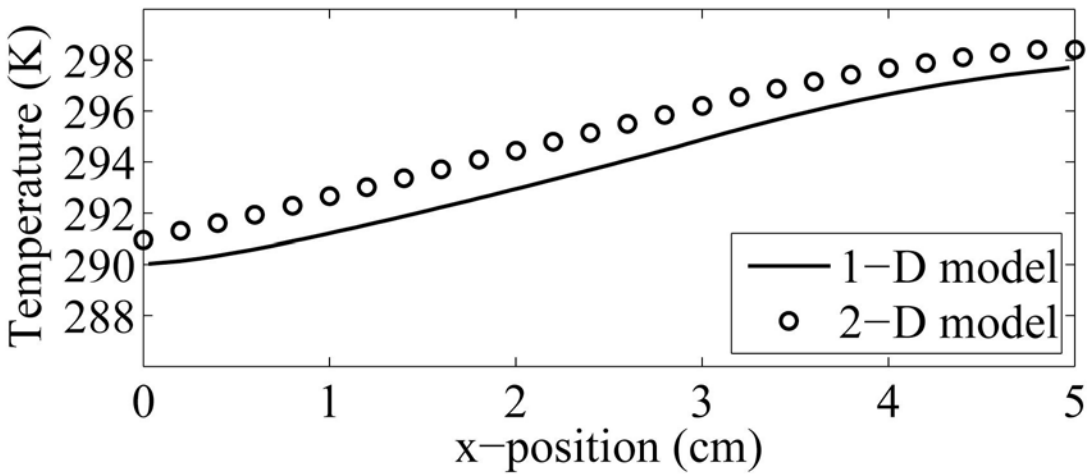

(a)

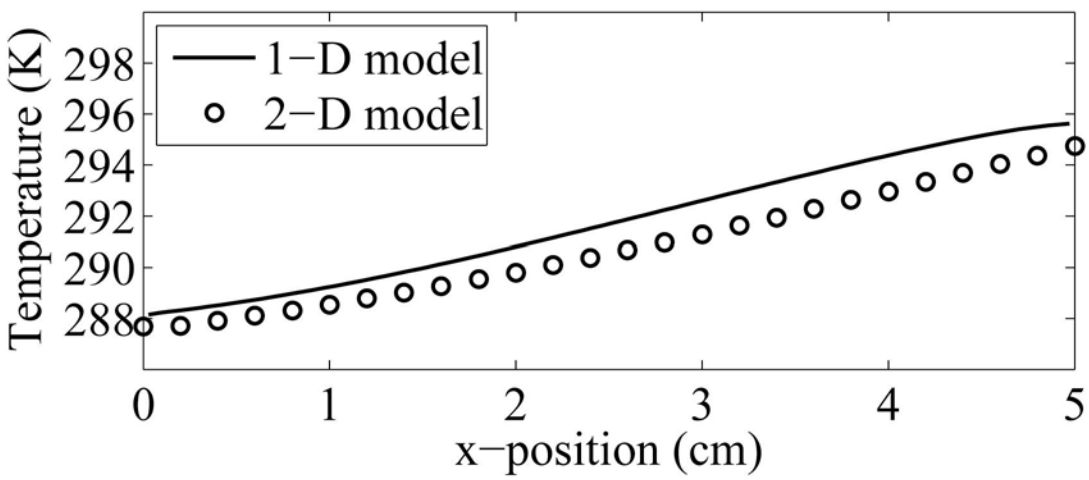

(b)

Figure 3.16. Fluid temperature as a function of regenerator location (a) before the cold blow and (b) before the hot blow for a 3 mm plate thickness and 1.5 mm flow channel height

The comparison between the 1-D and 2-D AMR models showed excellent qualitative and quantitative agreement between the refrigeration capacity and the rejected heat for thin regenerator plates (1 mm or less). However the results of the two models diverged as the thickness of the regenerator plates increased. There was also reasonable quantitative agreement between the magnetic work and the COP for thin plates. However, the qualitative agreement of the COP and the magnetic work did not show the same good agreement. This discrepancy was

attributed to the fact that the magnetic work and the COP are both derived from the refrigeration capacity and the rejected heat and small differences in either can result in large deviations between the models. The temperature profiles in the flow channel predicted by the two models also showed excellent qualitative and good quantitative agreement, especially for thin regenerator plates. However, the temperature profile agreement between the two models decreases as the plate thickness increases. The cause of the discrepancy is likely due to the effect of the temperature gradients in the solid and fluid, which increases with the plate thickness but is not explicitly accounted for in the 1D model. On the same computer, the 1D model took approximately 1 hour to converge for the modeling parameters listed in this section while the 2D model took approximately 500 hours to converge. The conclusion to the comparison of the 1D and the 2D AMRR models is that for an AMRR with a parallel-plate regenerator with sufficiently small dimensions, the additional computation time associated with the 2D model is not necessary and good results can be achieved with a 1D model provided that the main results are the refrigeration capacity and the temperature profiles. Results from this study showed that regenerators using relatively thick plates (2 mm or more) produced significantly lower refrigeration capacity and COP, which shows that these designs are probably not practical for AMRR systems. Therefore, this comparison shows that the 1D approximation used by the model described in this thesis is justified for flat plate regenerators using practical dimensions.

Chapter 4 Description of the Passive Regenerator Experiment and Experimental Results

A single-blow passive regenerator experiment has been constructed and used to test the heat transfer characteristics of a packed sphere regenerator using a liquid heat transfer fluid. The single blow regenerator experiment consists of bringing the regenerator to a uniform temperature (i.e., soaking it) and then subjecting it to a step change in fluid flow rate and inlet fluid temperature. The heat transfer characteristics of the regenerator can be inferred by measuring the temperature of the fluid exiting the regenerator as a function of time. This chapter describes the design of the single blow experiment and discusses the experimental results and data analysis techniques.

4.1 EXPERIMENT DESIGN

A flow schematic of the experimental setup is shown in Fig. 4.1. The flow loop is designed such that the regenerator can be cooled to a uniform temperature by circulating fluid through the regenerator followed by a heat exchanger that is interfaced with fluid in a cold temperature bath. In order to initiate a test, a solenoid valve is activated causing warm liquid to be pumped from the hot temperature bath through the regenerator. The inlet and outlet fluid temperatures are measured as well as the fluid volumetric flow rate and the pressure drop across the regenerator. Operating instructions for the experiment are given in Appendix A2, and a list of the experimental components used is given in Table 4.1

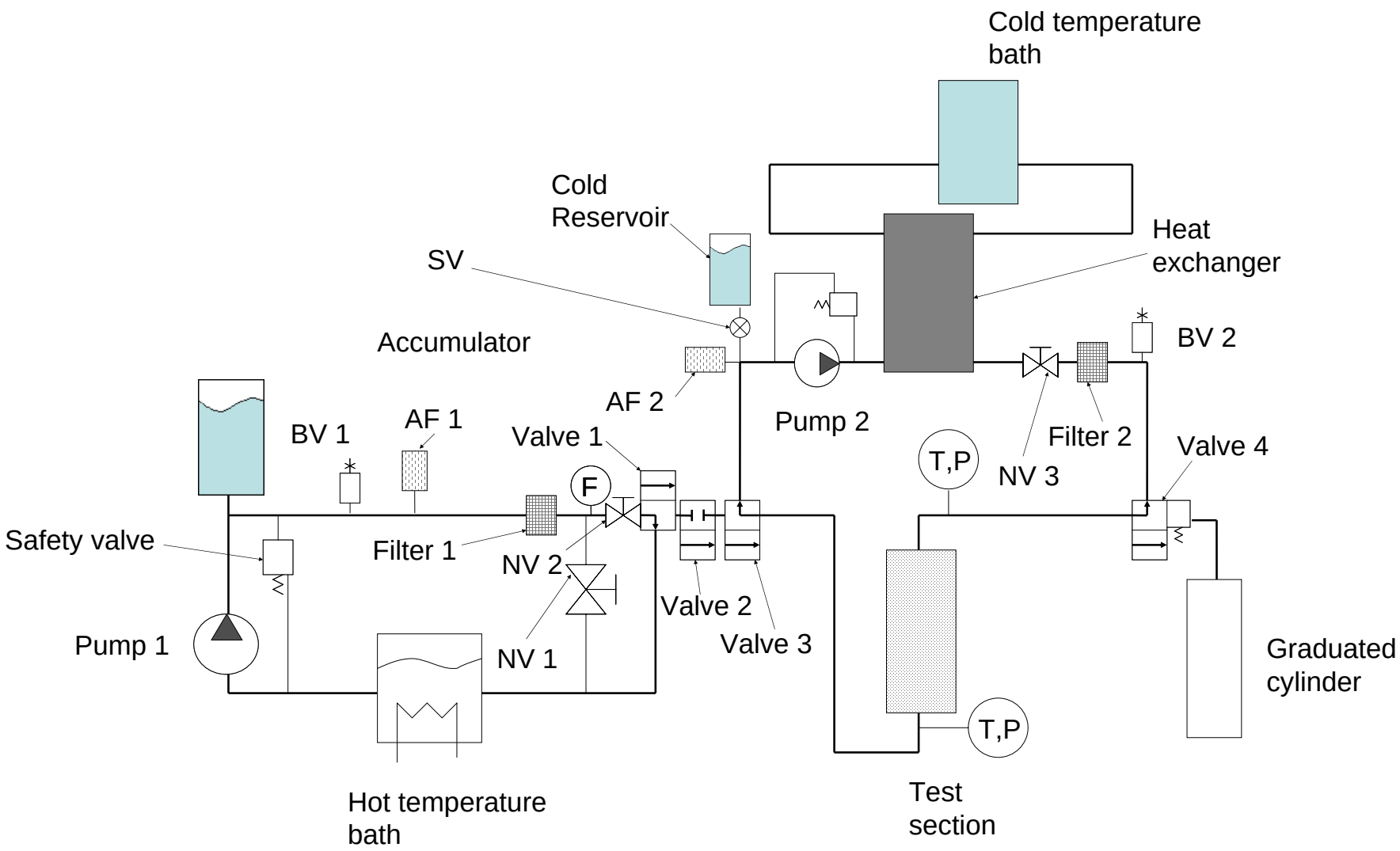

Figure 4.1. Flow schematic of the single blow passive regenerator test stand

Table 4.1. Experimental equipment list

Item	Desription	Part Number
Fluid flow meter	4 liter/min max magnetic flow meter	Omega FMG200
Differential pressure sensor	10 psi max transducer	Omega PX2300
Hot temperature bath	Temperature controlled heated bath	Blue M Magniwhirl
Cold temperature bath	Temperature controlled chiller bath	Polyscience 575
Main Pump	7.6 liter/min bronze rotary gear pump w/ 1/4 HP motor	Oberdorfer N61K10G
Cold soak pump	General purpose centrifugal pump w/ 1/3 HP motor	Sta-Rite JHB-61
Solenoid valve	Normally closed, 2 psi crack brass solenoid valve	Granzow 21EN 1/2"
Filters	15 liter/min filter with 10 micron element	Keystone 3/4" Water Filter
Data acquisition system	Computer PCI card	NI PCI 6034E
	Multiplexer	National Instruments SCXCI 1000
	Thermocouple module and input board	NI SCXI 1102 w/ SCXI 1303
	General voltage module and input board	NI SCXI 1100 w/ SCXI 1300

The test section is a packed sphere regenerator consisting of spheres that are approximately 4 mm in diameter and made of type 304 stainless steel. A detailed description of the regenerator design is given by Marconnet (2007). The regenerator is broken into 7 sections or ‘pucks’ and the temperature of the fluid between each regenerator puck is measured as a function of time by redundant thermocouples embedded in the flow stream between adjacent pucks. The regenerator is mounted such that fluid flows vertically against gravity through the test section in order to reduce flow channeling and flow maldistribution that may be caused by gravitational forces. Flow straighteners are placed at the entrance and exit of the regenerator in order to make the

fluid flow profile and temperature profile more uniform. A photograph of the regenerator and the rest of the experimental setup is shown in Figure 4.2.

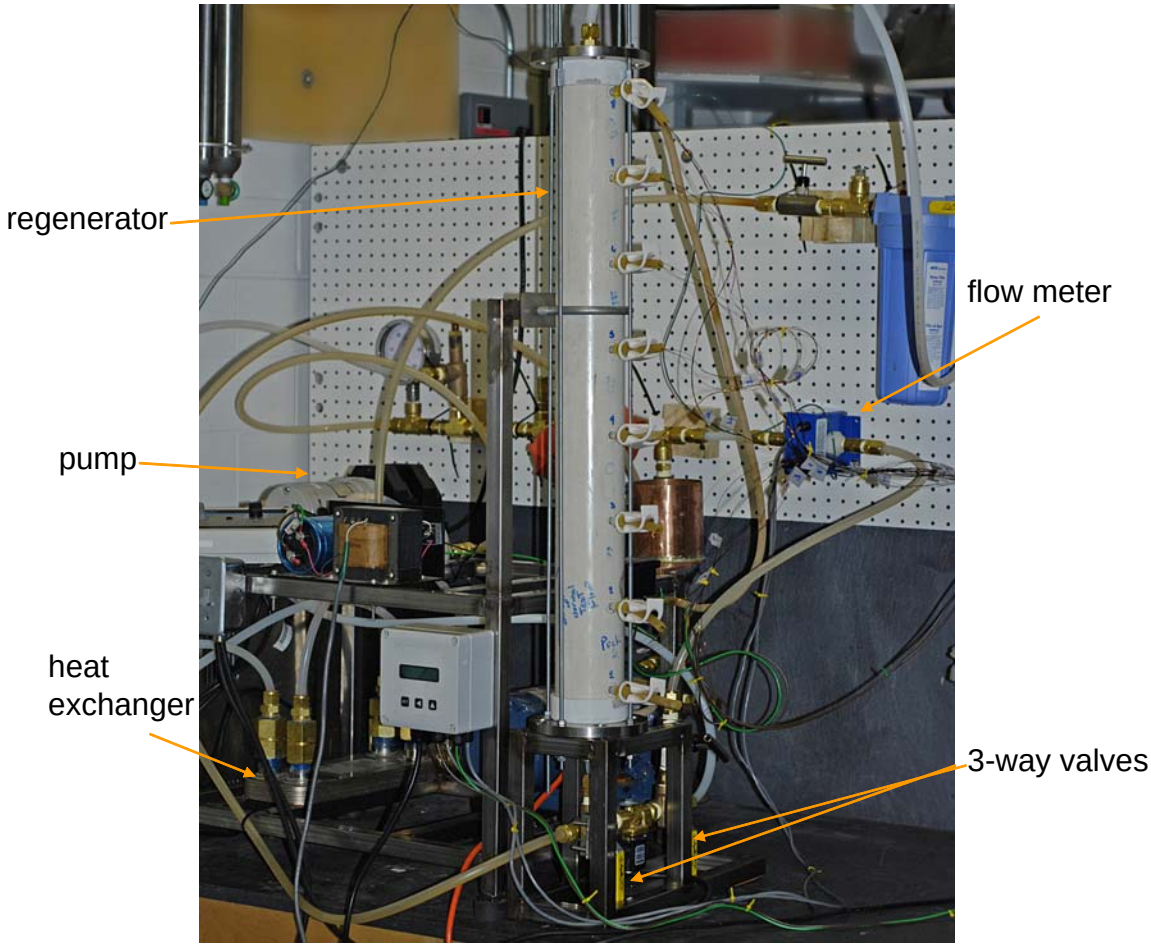

Figure 4.2. Photograph of the single blow experimental apparatus

In order to approximate a step change in fluid flow at the beginning of the experiment, the start of the fluid flow is controlled by the activation of a solenoid valve. Because the flow profile cannot be a true step change, it is important to measure the actual time variation in the fluid flow rate. A magnetic flow meter was selected for this purpose. The magnetic flow meter is a non-contacting flow meter that is compatible with a range of heat transfer fluids and has a response

time of 50 ms; these characteristics allow the flow meter to time resolve the transient behavior of the fluid flow at the initiation of the experiment. The flow meter was calibrated using a graduated cylinder and a stopwatch.

The fluid temperature at each location of interest is measured using type E thermocouples made from 30 gauge wire. A small thermocouple wire diameter is used in order to reduce the time constant of each thermocouple in order to to accurately measure transient behavior of the fluid temperature. Marconnet (2007) found that the time constant of each of the thermocouples that were used was below 140 ms. The thermocouples were calibrated using an ice bath and boiling water.

Fluid flow for the system shown in Figure 4.1 is provided by two pumps – one for the cold soak period before the experiment begins and one that provides flow during the experiment. The main pump (Pump 1) is a fixed flow rate gear pump. The flow rate through the regenerator is controlled by adjusting a bypass needle valve (NV 1 in Fig. 4.1) that diverts a portion of the pump flow back to the hot temperature bath. Using the bypass flow configuration reduces the flow spike that occurs when the solenoid valve opens because the change in flow restriction experienced by the system at the beginning of the experiment is reduced when using the bypass valve. The cold soak loop uses a centrifugal pump (Pump 2). The flow rate provided by the centrifugal pump can be controlled by adjusting the needle valve upstream of the cold soak filter. The flow rate in the cold soak loop is not important provided it is sufficiently high to transfer energy between the cold temperature bath and regenerator and is not so high that the regenerator is over-pressurized. Both pumps have adjustable crack pressure one-way check valves at the

outlet to prevent over-pressurization of the system. Both of these check valves were set to a cracking pressure of approximately 140 kPa (20 psi). To prevent contamination of the regenerator, the instrumentation, and other system components, 10 micron filters were placed near the outlet of each pump.

The direction of flow through the regenerator is controlled by a solenoid valve and three manual three-way valves. Figure 4.3 shows a photograph of two of the three-way valves, a needle valve, and the solenoid valve that are installed upstream of the regenerator. These valves are labeled Valve 1, Valve 2, Valve 3, and NV 2 in Fig. 4.1, and they must be manually switched to control the flow direction of the heat transfer fluid.

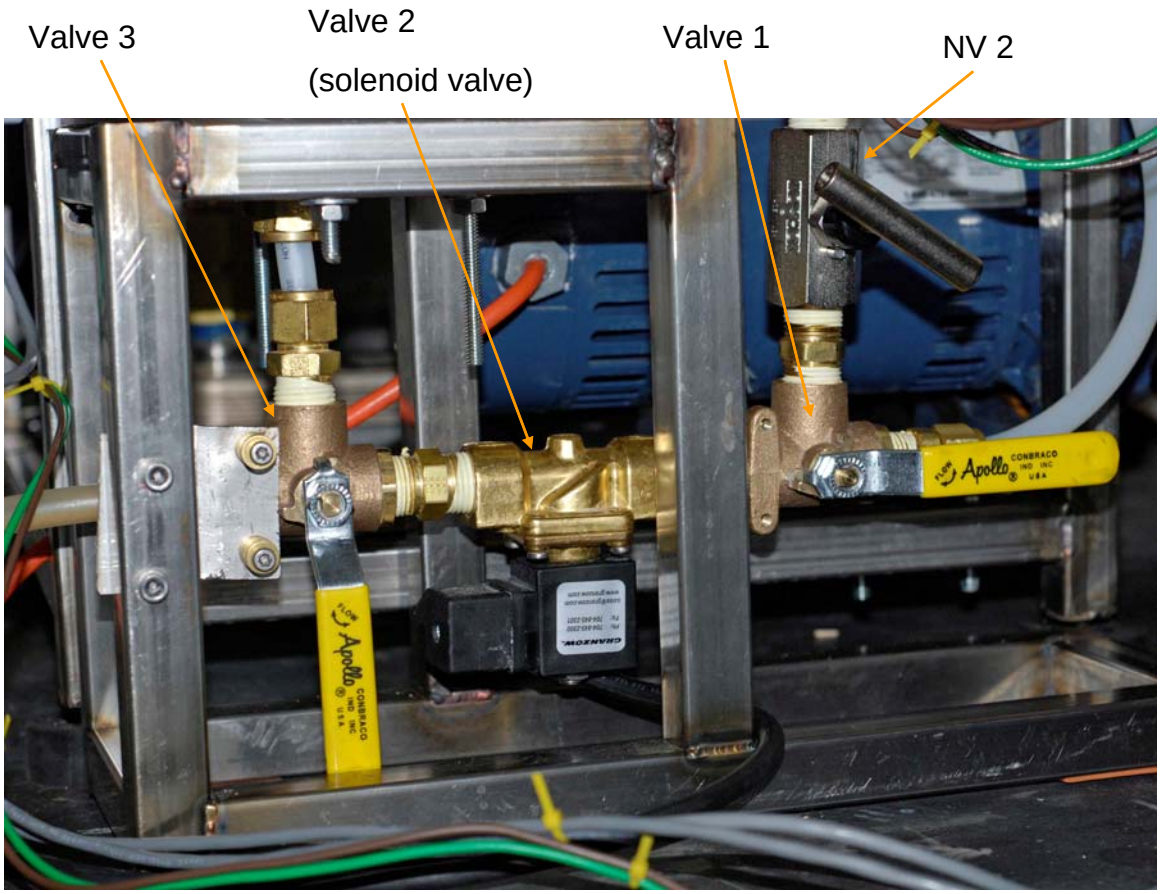

Figure 4.3. Photograph of the manual three-way valves and solenoid valve mounted near the inlet of the regenerator

The flow loop is designed to be an open circuit during the experiment; this configuration allows a constant inlet temperature to be achieved more easily than a closed circuit. Because each experiment lasts only a few minutes, the temperature of the hot bath, which has a volume of approximately 20 L, changes very little during the experiment and requires little or no temperature control. If the cold fluid exiting the regenerator were fed back to the hot bath then a large heating load would be placed on the hot temperature bath which would therefore require a fast and accurate method of controlling the hot bath temperature. Using an open flow loop avoids these difficulties and is possible due to the relatively large volume of fluid that can be contained in the hot bath.

The experiment is compatible with a range of operating fluids and the system was designed to facilitate easy fluid change, allowing the plumbing to be purged of air after each fluid change. In order to allow easy fluid changes, the fluid in the cold temperature bath is isolated from the rest of the system and communicates with the regenerator via a counterflow plate heat exchanger. Two bleeder valves are installed, one on the cold soak loop and one on the hot loop, to allow air bubbles to be eliminated from the system. The separate reservoir for the cold soak provides makeup liquid for the cold soak flow loop as well as a means of filling the system after it has been drained.

4.2 EXPERIMENTAL MEASUREMENTS

The single blow experiment was run over a range of fluid flow rates, with a corresponding range of Reynolds numbers, for pure water and mixtures of 20%, 30% and 40% propylene glycol and water solutions by mass. The operating conditions associated with these tests are shown in Table 4.2. Because the regenerator model is flexible with regard to operating temperature, the experimentally measured temperatures can be used as a modeling input. Therefore, it is not necessary to control the initial regenerator temperature distribution and the fluid inlet temperature with high accuracy.

Table 4.2. Experimental operating conditions for the single blow regenerator

Water		**20% Propylene Glycol**	
Temperature Range (K)	Flow Rates(L/min)	Temperature Range (K)	Flow Rates(L/min)
295 - 315	1.5	298 -313	0.5
	2.0		1.0
	2.7		1.5
	4.0		2.0
283 - 297	0.25		2.5
	0.5		3.0
	1.0		4.0
	1.5		
	2.5		
	3.4		
30% Propylene Glycol		**40% Propylene Glycol**	
298 -313	0.5	298 -313	0.5
	1.0		1.0
	1.5		1.5
	2.0		2.0
	2.5		2.5
	3.0		3.0
	4.0		4.0

The fluid flow at the beginning of the experiment is initiated by activating the solenoid valve. When the valve opens, there is an abrupt change in the flow restriction seen by the pump and there is a corresponding spike in the flow rate at the beginning of the experiment. Figure 4.4 shows a representative fluid flow profile during an experiment. The data in Fig. 4.4 were obtained for a 40% propylene glycol and 60% water mixture. There is a small but noticeable increase in flow rate at the beginning of the experiment that is quickly damped out; the fluid flow rate is subsequently nearly constant during the remainder of the experiment. The model uses the experimentally measured fluid flow rate as an input and therefore it can capture effects due to variations in the flow rate with time.

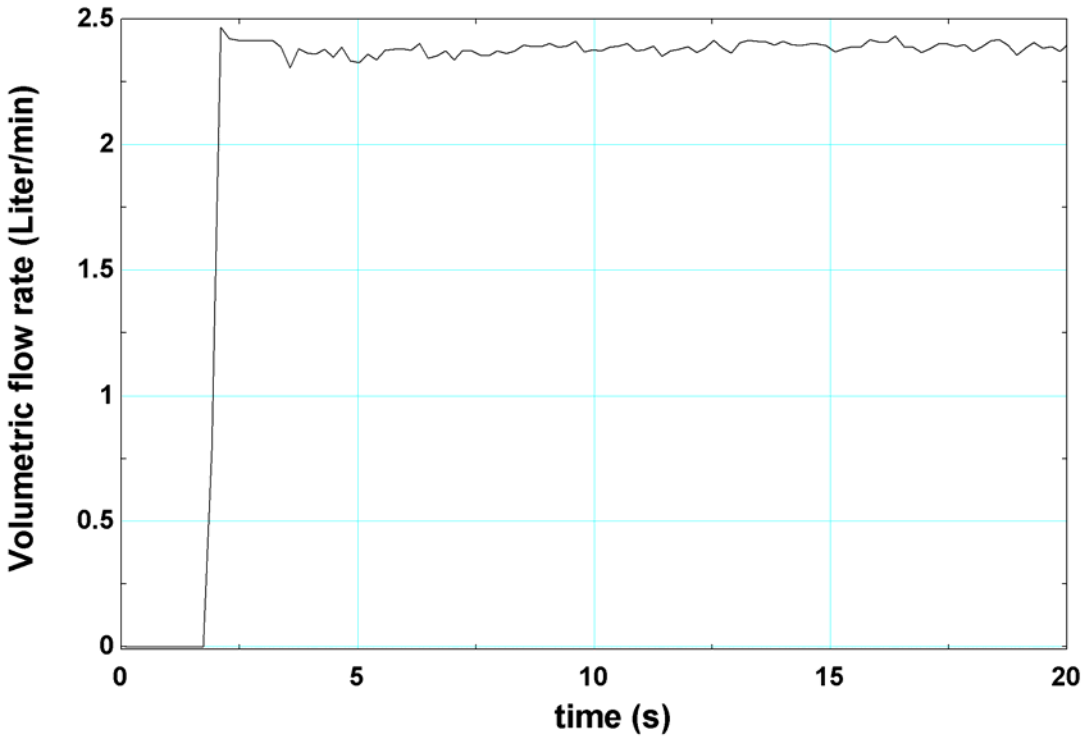

Figure 4.4. Single blow experimental volumetric flow rate as a function of time

The fluid temperature is measured at eight locations along the regenerator – at the inlet of each regenerator puck and the outlet of the final regenerator puck. Figure 4.5 shows the locations of the temperature measurements along the regenerator. A more detailed description of the regenerator test section is given by Marconnet (2007). Three thermocouples are inserted in the flow stream at different radial positions at each temperature measurement location in the regenerator.

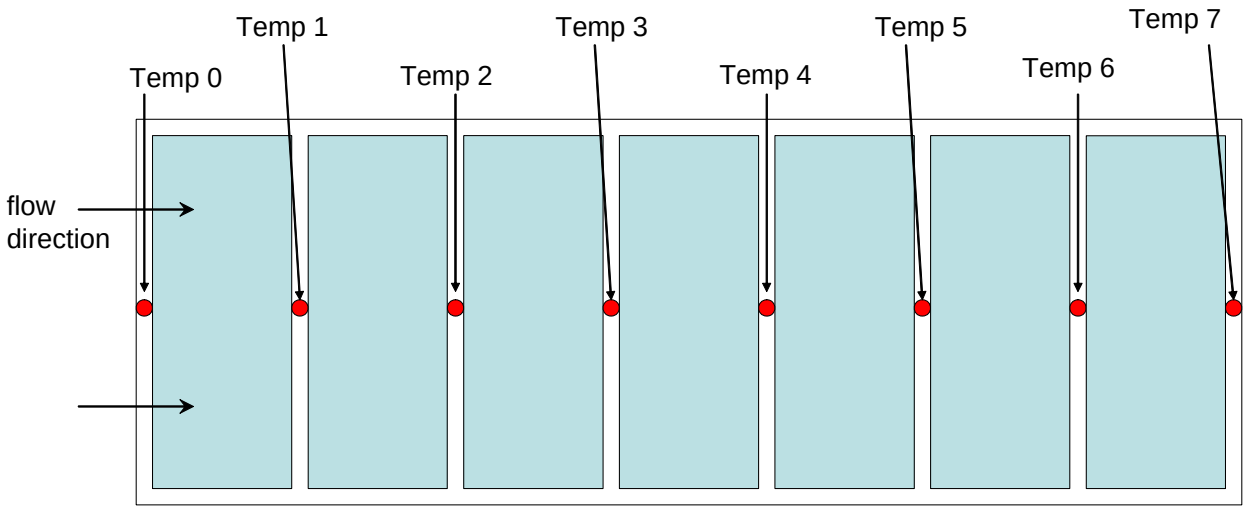

Figure 4.5. Schematic of temperature sensors in the regenerator test section

Figure 4.6 shows the temperature measured by all 24 thermocouples in the test setup, 8 groups of 3 thermocouples, as a function of time. The data in Fig. 4.6 are for a 1 L/min flow rate of water. The data were collected at a rate of 20 Hz. The shapes of the temperature profiles give an indication of the regenerator effectiveness. However, the temperature variation itself is not a direct measurement of the heat transfer inside the regenerator. A regenerator model must be used to infer the heat transfer coefficients inside the bed based on the inlet and outlet temperature profiles. Figures 4.4 and 4.6 show that there is no true step change in fluid flow rate or inlet temperature, and therefore the model must use the measured values for inlet temperature and mass flow rate as a function of time.

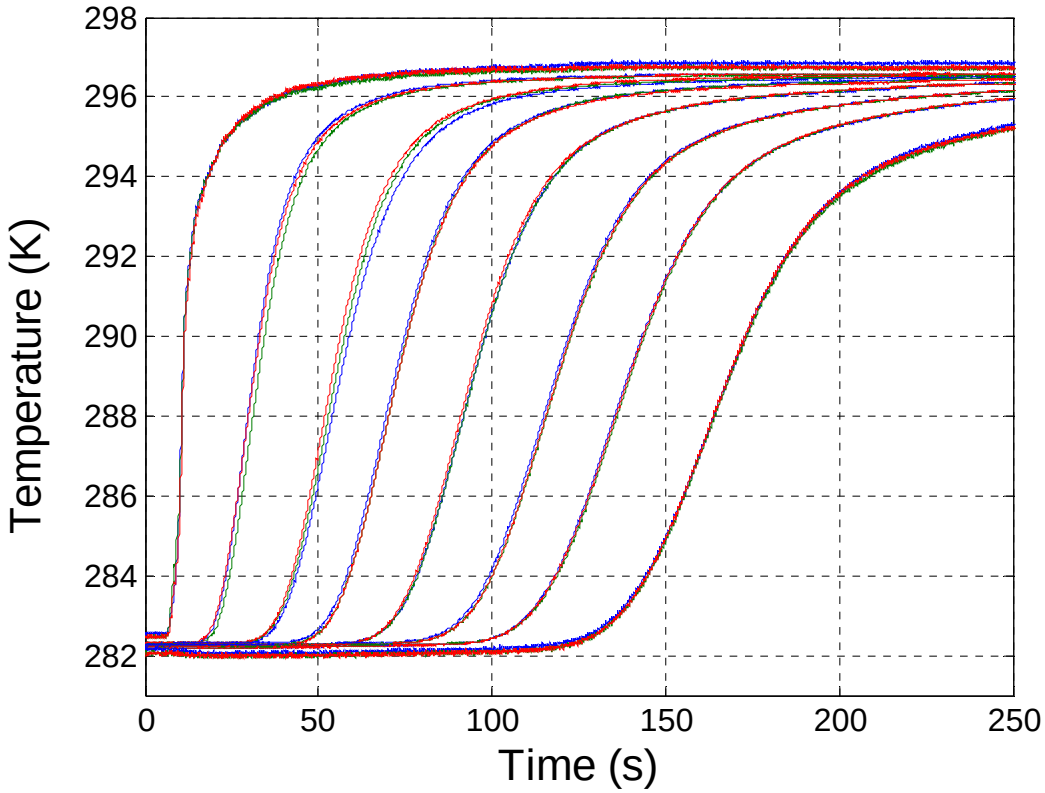

Figure 4.6. Schematic of temperature sensors in the regenerator test section

Temperature profiles were obtained at the inlet and outlet of each regenerator puck for the range of experimental conditions shown in Table 4.2. The temperature/time data, such as that shown in Fig. 4.6, provides an indication of the heat transfer coefficient - in general, the greater the slope of the temperature rise after breakthrough, the higher the heat transfer coefficient in the regenerator. An example of this can be demonstrated by comparing the temperature profile of an experiment using water to the temperature profile of an experiment using a propylene glycol and water mixture. Mixtures of propylene glycol and water mixtures are characterized lower thermal conductivity and higher viscosity than pure water, which results in lower heat transfer coefficients in the regenerator. Experimental results for the inlet and outlet temperatures of pure water as well as a 20% propylene glycol and water mixture with a volumetric flow rate of

approximately 2 L/min are overlaid in Fig. 4.7 and demonstrate the effect of the reduced heat transfer coefficient associated with the propylene glycol mixture on the temperature/time data. The temperature of the water results were shifted slightly in the time and temperature scales to match the propylene glycol temperature. Comparing the outlet temperature profiles for water and the propylene glycol mixture shows that the outlet temperature profile for water has a greater slope, indicating a higher heat transfer coefficient in the regenerator. Results for other flow rates are similar.

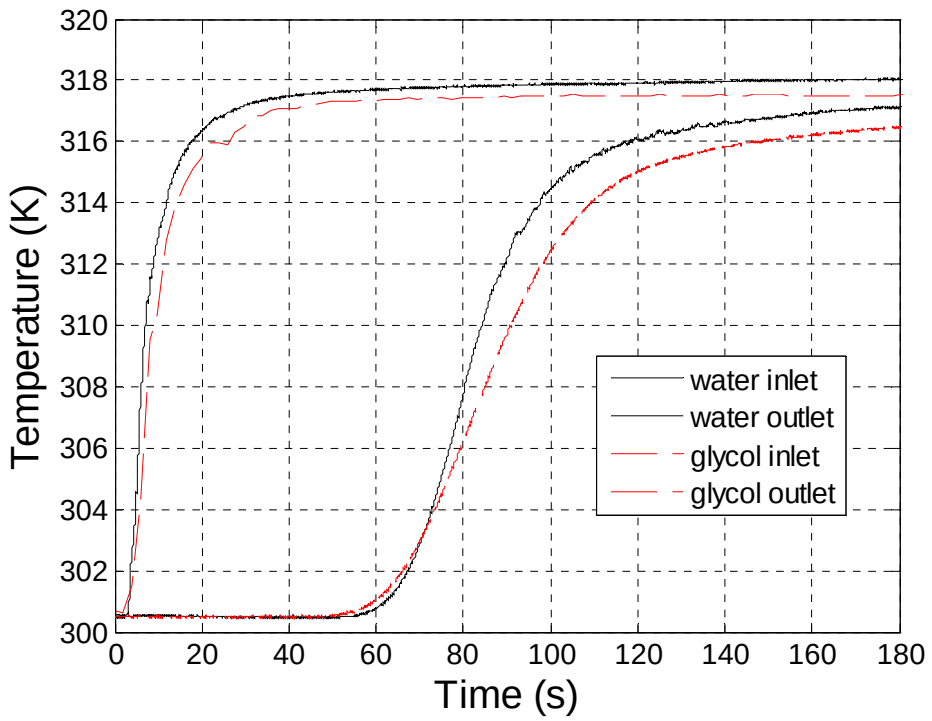

Figure 4.7. Experimental inlet and outlet temperature profiles for both pure water and a mixture of 20% propylene glycol and water at a flow rate of 2 L/min.

4.3 MODIFICATIONS TO THE NUMERICAL AMRR MODEL FOR SINGLE BLOW DATA ANALYSIS

The AMRR model can be used to model a passive, single blow regenerator (i.e., to simulate the test facility described in this chapter) by making several modifications. The magnetic work term is removed from the governing equations of the solid material by setting the partial differential of entropy with respect to magnetic field to zero for the materials used in the regenerator. The model operation and boundary conditions were modified to simulate a continuous, transient regenerator operation rather than calculate cyclical steady state temperature profiles.

The model was modified so that it accepts a data file containing the experimentally measured mass flow rate and inlet fluid temperature as a function of time for a particular run. Although the goal of the single blow experiment is to subject the regenerator to a step change in fluid flow rate and temperature, a real experiment cannot produce a true step change. Therefore, when modeling single blow experiments, it is important to account for the variation of the inlet fluid temperature and fluid flow rate (Heggs and Burns, 1988). The fluid inlet temperature at each time in the simulation is obtained by interpolation from the experimental data file used in that simulation.

The initial conditions of the fluid and solid were modified to be a uniform temperature. The initial temperatures of the regenerator and fluid are assumed to be the average temperature in the regenerator before the fluid flow begins. The average temperature was used rather than the measured temperature because the regenerator is at a nearly uniform temperature at the beginning of the experiment and spatial differences in temperature are most likely due to uncertainty in the temperature measurement. The simulation starts at time = 0 and is run until the end of the experiment, t_{final}. The main output of the model is the temperature of the fluid exiting the regenerator at the right end of the bed ($x=L$).

4.4 EXPERIMENTAL DATA ANALYSIS

One of the objectives of the passive regenerator experiments is to develop a Nusselt number correlation that can be easily integrated with the AMRR model in order to predict a liquid heat transfer coefficient in a packed sphere regenerator. A Nusselt number correlation should, at a minimum, be a function of the Reynolds number and the Prandtl number. Several correlations for heat transfer in a packed sphere regenerator have been developed using different techniques. Currently, the AMRR model uses a correlation suggested by Wakao and Kaguei (1982) that was developed using data obtained mostly for gaseous heat transfer fluids and is given in Eq. (4.1).

$$Nu_f = 2 + 1.1 Re_f^{0.6} Pr_f^{1/3} \tag{4.1}$$

Macias-Machin et al. (1991) measured the heat transfer from an immersed wire in a packed sphere regenerator with a liquid heat transfer fluid and developed the correlation is shown in Eq. (4.2).

$$Nu_{Macias} = 1.27 + \frac{2.66}{\varepsilon} \mathrm{Re}_f^{1/2} \, \mathrm{Pr}_f^{-0.41} \left(\frac{1-\varepsilon}{\varepsilon} \right)^{0.29} \tag{4.2}$$

The correlation presented by Kunii and Levenspiel (1969) also give a correlation based on data, which is given in Eq. (4.3).

$$Nu_{Kunii} = 2 + \frac{1.8}{\varepsilon} \mathrm{Re}_f^{1/2} \, \mathrm{Pr}_f^{1/3} \tag{4.3}$$

The Nusselt number correlations in Eq. (4.1)-(4.3) have similar forms, but predict significantly different Nusselt numbers. The Nusselt numbers predicted by these three established correlations are shown in Fig. 4.8 as a function of Reynolds number for a constant Prandtl number of 6.8 (corresponding to water at room temperature) and a porosity of 0.36. One interesting difference between the correlation presented by Macias-Machin et al. and the other two correlations is that the Prandtl number has a negative exponent, while the correlations presented by Wakao and Kaguei both use a positive exponent of 1/3; therefore the curves in Fig. 4.8 would look different for other fluid Prandtl numbers; at very high Prandtl number, the Macias-Machin correlation will actually drop below the other two. Experimental data collected on the single blow regenerator test were used to generate a new Nusselt number correlation that has a functional form similar to the three correlations shown above.

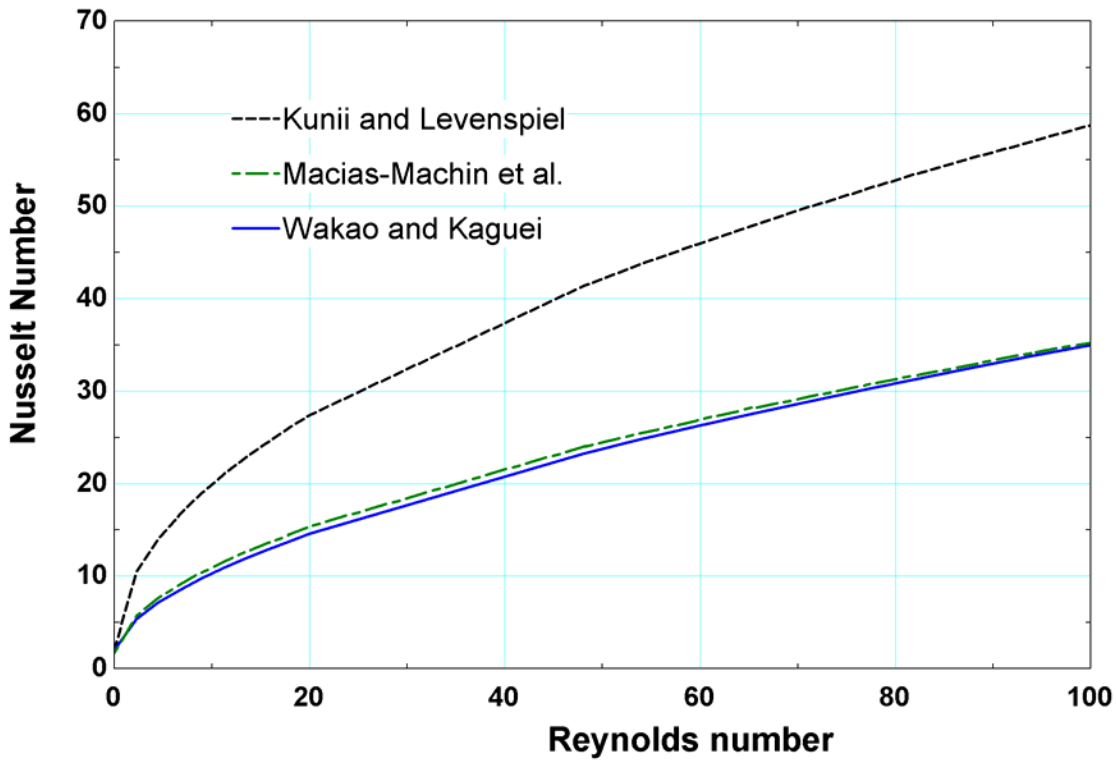

Figure 4.8. Nusselt number as a function of Reynolds number for a regenerator with a porosity of 0.36

According to Heggs and Burns (1988), the most effective method of determining the heat transfer in a single blow regenerator experiment is to match the shape of the predicted outlet fluid temperature with the experimental data. Shape matching of experimental data can be done by varying the Nusselt number used by the model in order to identify the value of the Nusselt number that produces a predicted outlet temperature that best matches the measured outlet temperature. The quality of the fit of the predicted fluid outlet temperature to the measured data is determined by the calculating the root mean squared error (*RMSE*) between the predicted and measured fluid temperature profile between the measured 20% and 80% temperature breakthrough times, as suggested by Heggs and Burns (1988).

$$RMSE = \frac{1}{N_{exp}} \sqrt{\sum_{i=1}^{N_{exp}} \left(T_{exp,i} - T_{pre,i} \right)^2} \tag{4.4}$$

where T_{exp} is the experimentally measured fluid outlet temperature, T_{pre} is the predicted fluid outlet temperature, and N_{exp} is the number of experimental measurements over the period of the 20% to 80% breakthrough times. To simplify modeling efforts for the single blow regenerator and reduce computational time, the entire regenerator (which is comprised of the seven regenerator pucks) was initially modeled as a single, continuous regenerator. Because the void volume between the regenerator pucks is not modeled using this method, the predicted 20% breakthrough time is shorter than the measured breakthrough time. Rather than modeling the void volume, the predicted outlet fluid temperature is shifted in time so that the 20% breakthrough time predicted by the model coincides with the measured 20% breakthrough time. Notice in Figure 4.7 that the breakthrough time is only a weak function of the heat transfer characteristics (the water and propylene glycol results are nearly the same until a time of approximately 60 s) and the shape of the breakthrough curve is the main indicator of heat transfer coefficient in the regenerator. When calculating the *RMSE* from Eq. (4.4), the predicted outlet temperature data points are interpolated over the experimental time scale to facilitate calculation.

The inlet temperature used by the model is the average of the three thermocouples at the regenerator inlet, and the modeled temperature values are interpolated over the modeling time mesh using a cubic interpolation technique in MATLAB. The model uses measured fluid mass flow rates and inlet temperature profiles. For each modeling run, the model assumes the Nusselt number in the regenerator is a constant value and calculates the corresponding outlet temperature

profile in order to calculate the *RMSE* associated with that Nusselt number. The *RMSE* is calculated for a range of Nusselt numbers and the experimentally determined Nusselt number is the one that minimizes the *RMSE*, producing the best fit to experimental data. The *RMSE* as a function of Nusselt number used by the model for the data point with water as a heat transfer fluid at a flow rate of 1 L/min when all seven pucks in the regenerator are considered is shown in Fig 4.9.

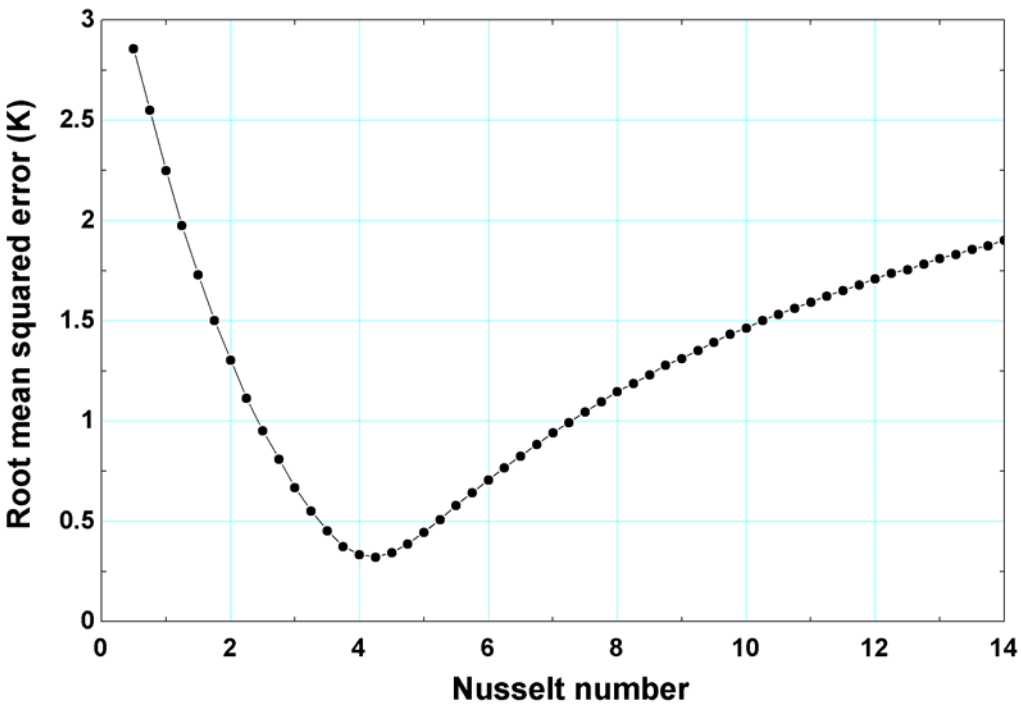

Figure 4.9. Root mean squared error between the predicted and measured temperature profile for the single blow regenerator experiment for water at a 1 L/min flow rate when the entire regenerator is considered.

The Nusselt number that produces the best fit for the 1 L/min water data is 4.25 and the corresponding predicted temperature profile is shown in Fig. 4.10. Examination of Fig. 4.10 shows that the predicted temperature profile captures the shape of the measured outlet

temperature well during up to approximately 180 s, but shows a relatively large discrepancy afterward. The shape of the outlet curve suggests that there is a heat leak that prevents the fluid at the outlet from reaching the inlet temperature as quickly as the model predicts.

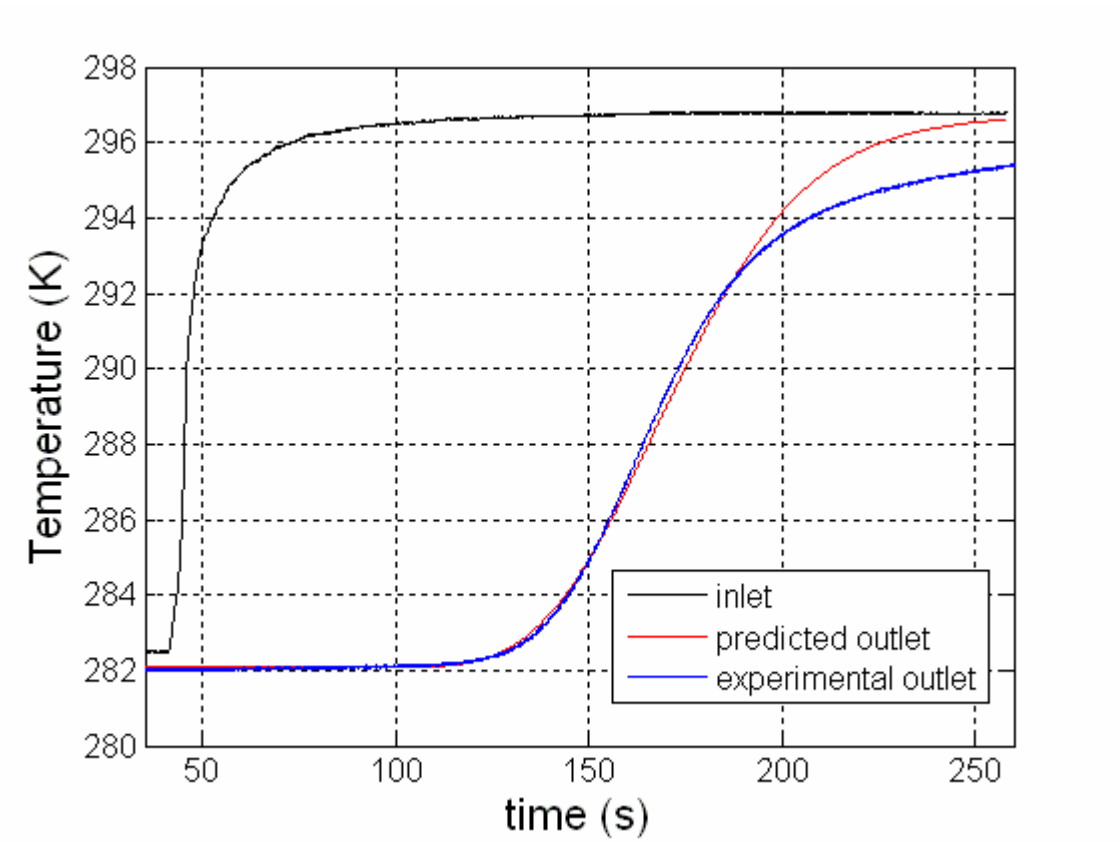

Figure 4.10. Experimental inlet and outlet temperatures as a function of time as well as the best-fit predicted outlet temperature when all seven regenerator pucks are considered

One possible source of a heat leak is convection from the outside walls of the regenerator to the room. To test the effects of the heat transfer from the regenerator to the room, the experiment was operated for a long time with the inlet fluid temperature set to a higher value than was used for the experiments presented in this chapter in order to artificially increase convection to the room. Once the transients in the regenerator die out, any observed temperature drop from the

inlet to the outlet of the regenerator can only be attributed to heat losses from the regenerator walls to the room. The results are shown in Fig 4.11 and show that the steady-state temperature drop across the regenerator is low.

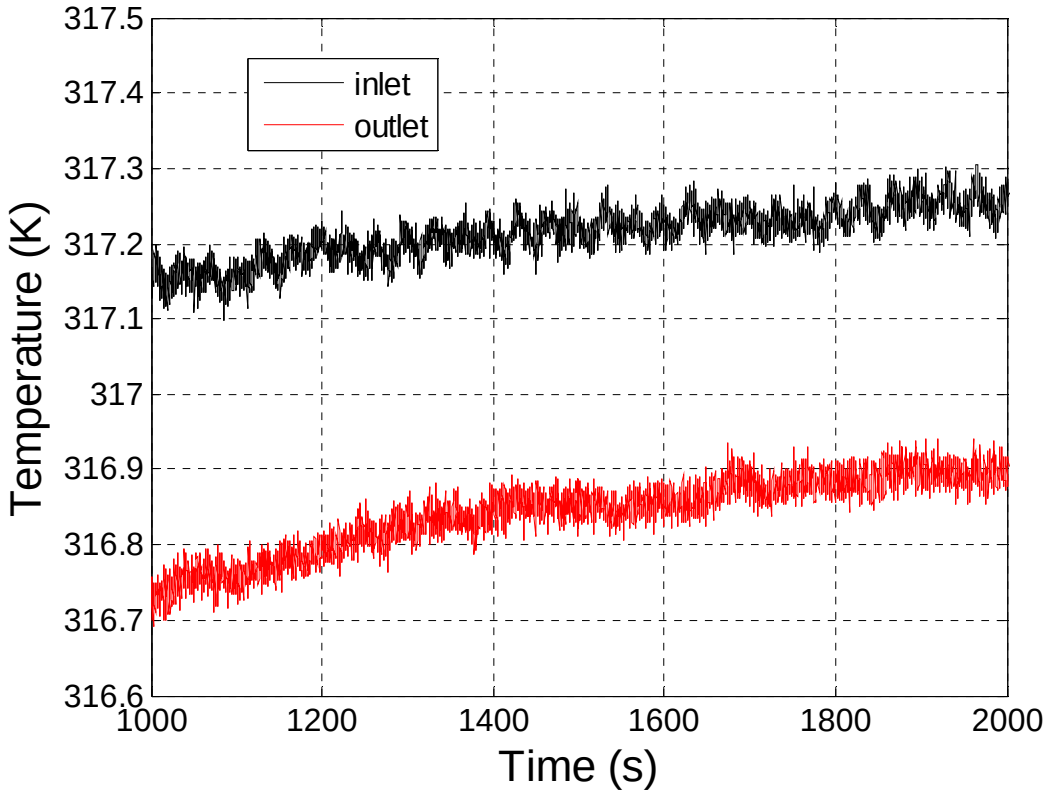

Figure 4.11. Temperature in the regenerator after a long flow time. The temperature drop across the regenerator is an indicator of the heat loss to the room.

The temperature drop seen across the regenerator shown in Fig. 4.11 is approximately 0.3 K for an inlet temperature of 317 K. The temperature drop across the regenerator would be lower for an inlet temperature of 297 K, as shown in Fig. 4.10, and therefore heat loss to the room are not large enough to explain the 1-2 K temperature discrepancy observed between the predicted and measured temperature profiles in Fig. 4.10.

Another possible explanation of the apparent heat leak is energy transfer from the heat transfer fluid to the regenerator wall that occurs on a different time scale than the heat transfer between the fluid and the stainless steel particles in the regenerator. A CAD drawing of the passive regenerator test section is given in Fig. 4.12 (Marconnet 2007).

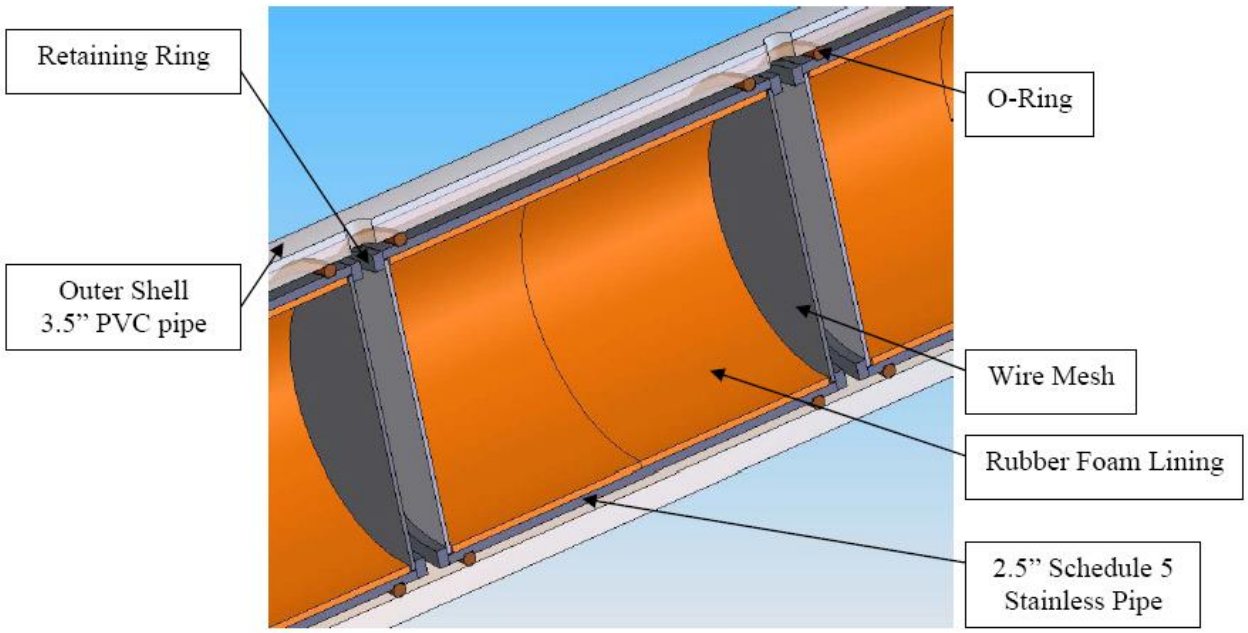

Figure 4.12. Drawing of the single blow regenerator test section showing the regenerator puck construction and flow area between pucks

Figure 4.12 shows that there are O-ring seals at the ends of each regenerator, but there is still a gap between each puck that is filled with fluid in direct contact with the PVC outer shell. Because the fluid is in direct contact with the PVC shell between regenerator pucks, most of the effective heat leak to the shell likely occurs in the open flow area between the pucks. To assess the heat loss to the regenerator wall during an experiment, the thermal properties of the regenerator housing have been calculated and the parameters used for the analysis are given in

Table 4.3. The regenerator housing is made of a commercial grade PVC so the properties listed in the table are approximate values take from Callister (1997).

Table 4.3. Properties of the regenerator housing

Parameter	Value	Parameter	Value
shell specific heat	1200 J/kg-K	shell length	0.838 m
shell density	1400 kg/m3	shell inner diameter	0.0762 m
shell thermal conductivity	0.18 W/m-K	shell outer diameter	0.0889 m
shell thermal diffusivity	1.07e-7 m2/s		

To estimate what portion of the volume of the regenerator shell participates thermally during the experiment, the shell was modeled as a semi-infinite solid. For a semi-infinite solid, the thermal penetration depth is (Incropera and DeWitt, 1996)

$$d_{thermal} = \sqrt{4\alpha_{shell}\, t_{exp}} \tag{4.5}$$

where $d_{thermal}$ is the thermal penetration depth into the PVC shell, α_{shell} is the thermal diffusivity of the shell, and t_{exp} is the total time that the experiment was run. For an experiment that lasts 200 s to reach the 80% breakthrough time, the thermal wave can penetrate 9.3 mm into the PVC wall. Assuming the thermal penetration depth is 9.3 mm for the entire length of the regenerator, the heat capacity of the participating PVC shell can be up to 40% of the heat capacity of the stainless steel particles depending on the heat transfer fluid and experiment time. Because the shell interacts thermally with the heat transfer fluid in a less direct and more complex manner than the packing, the effective heat capacity of the shell cannot be easily accounted for in the model. Rather than modifying the regenerator section or the model, the effect of the heat loss to the PVC shell is minimized by treating each puck as a separate test section. This can be done easily by using temperature measurements from all eight locations shown in Fig. 4.5. The outlet

temperature profile is used as the inlet temperature to the downstream puck; therefore, there are effectively seven simultaneous experiments being carried out on the 7 different test sections for each experimental run.

The data used to generate Fig. 4.9 and 4.10 (water with a flow rate of 1 L/min) were used to analyze each regenerator puck individually. As when considering the entire regenerator, the Nusselt number used by the model was varied and the *RMSE* was calculated for each value. The results for the 1st regenerator puck in the test section are shown in Fig. 4.13.

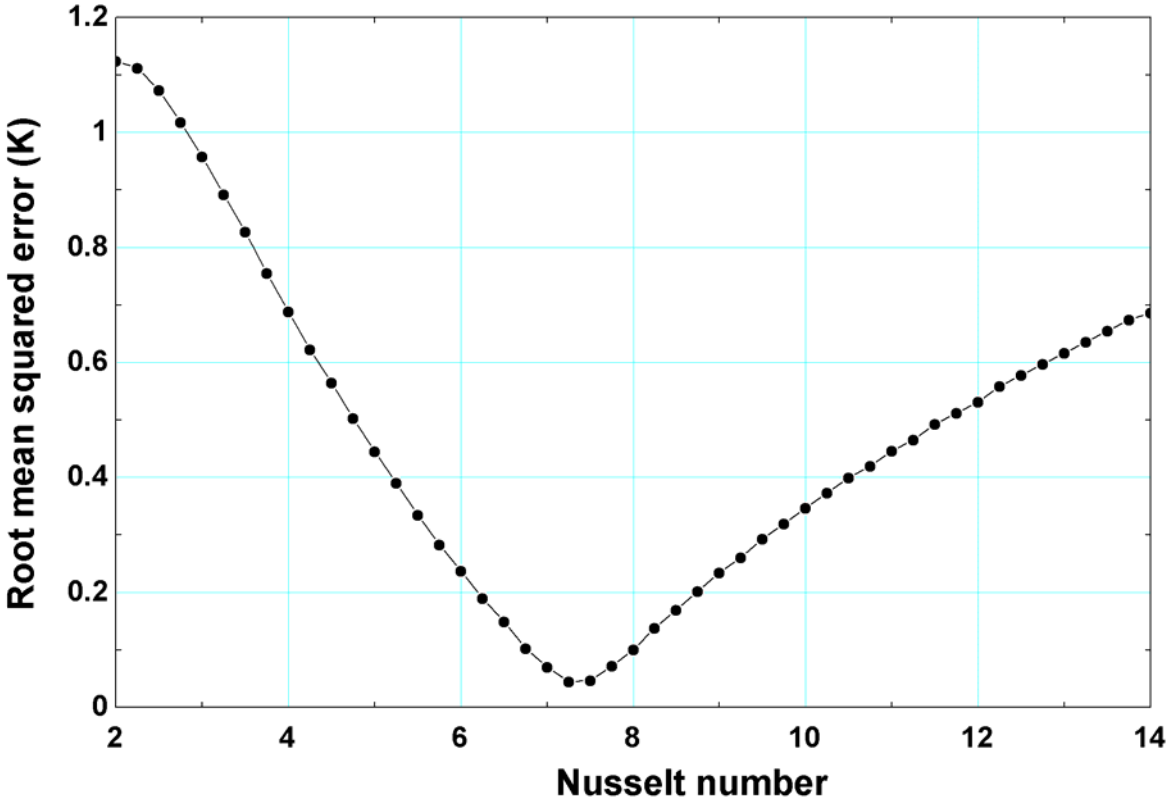

Figure 4.13. Root mean squared error between the predicted and measured temperature profile for the single blow regenerator experiment for water at a 1 L/min flow rate when the only puck 1 in the regenerator is considered.

The results shown in Fig 4.13 show approximately the same shape as the *RMSE* for the entire regenerator shown in Fig. 4.9, but the minimum value of the *RMSE* occurs at a higher Nusselt number. The measured inlet and outlet temperatures and the outlet temperature predicted by the model using the best-fit Nusselt number of 7.25 are shown in Fig. 4.14. The shape of the predicted outlet curve in Fig. 4.14 shows better agreement with the measured outlet curve than the predicted outlet curve for the entire regenerator shown in Fig. 4.9.

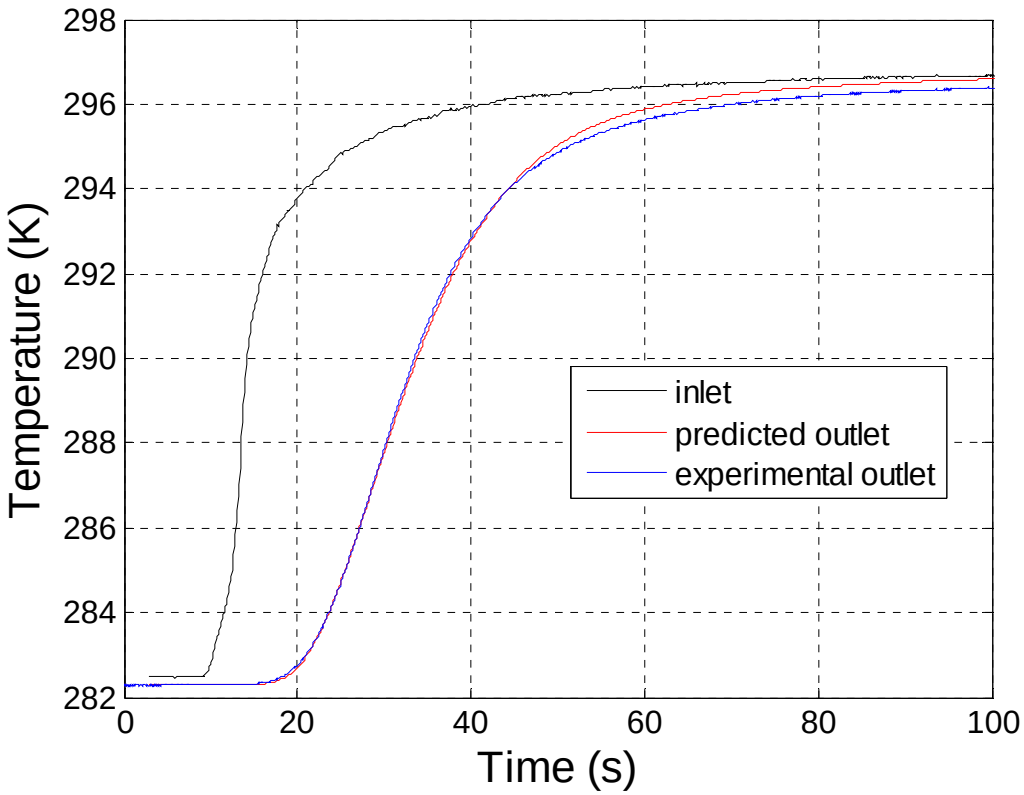

Figure 4.14. Experimental inlet and outlet temperatures as a function of time as well as the best-fit predicted outlet temperature when only puck 1 is considered

Note that the time associated with the single-puck experiment in Fig. 4.14 is significantly lower than the time shown in Fig. 4.10 because the time to reach the 80% breakthrough temperature is much shorter when only one regenerator puck is considered. Comparing Fig. 4.14 to the Fig.

4.10 (the corresponding inlet and outlet temperature profiles when considering all seven pucks) reveals that the predicted outlet temperature achieves a much better fit for only one puck than when all seven pucks are used. The improved outlet temperature fit indicates that considering each puck individually does decrease the effects of the apparent heat leak to the PVC shell that becomes significant when all seven pucks are considered. Therefore each puck is considered individually when experimental data is used to determine the Nusselt number in the regenerator.

4.5 EXPERIMENTAL DATA ANALYSIS FOR INDIVIDUAL REGNERATOR PUCKS

Because treating each regenerator puck separately reduces the heat leak from the heat transfer fluid to the PVC shell, all data that were used to develop the Nusselt number correlation were analyzed considering each regenerator puck individually. When each puck is considered individually, every experiment contains data for seven test sections (and therefore seven independent measurements of the Nusselt number). Using the measured Nusselt number from all seven pucks gives seven replicates that can be used to determine and minimize the experimental uncertainty.

A numerical grid sensitivity analysis was performed to determine the number of time steps and spatial steps required by the numerical model in order to analyze the single blow regenerator data; the 4 L/min experimental data was used for the grid sensitivity analysis. For the 4 L/min experiment, the model predicted that the 3rd puck had the highest Nusselt number. Puck 3 was therefore used to conduct the grid sensitivity analysis because it should experience the highest heat transfer rate and therefore be the most sensitive to the numerical grid used by the model. First, the sensitivity to the number of time steps used by the model was studied by setting the

number of spatial steps to a relatively high value of 60 and varying the number of time steps. The Nusselt number that minimizes the *RMSE* predicted by the model as a function of the number of time steps is estimated using a Richardson approximation as described in Jaluria (2002). The data are fit to an equation with the following form.

$$Nu_{pred} = a_0 + \frac{a_1}{Nt} \tag{4.6}$$

where a_0 and a_1 are fitting parameters. The coefficient a_0 represents the predicted Nusselt number when an infinite number of time steps is used or $Nu_{Richardson}$. The predicted Nusselt number as a function of time steps used by the model is shown in Fig 4.15. The Richardson extrapolation predicts the Nusselt number for an infinite number time steps is 21.45. From Fig. 4.15, the model predicts a Nusselt number of 21.25 using 4000 time steps. 4000 times steps corresponds to a time step of 0.0287 s and a characteristic fluid length, *CFL*, of 0.091.

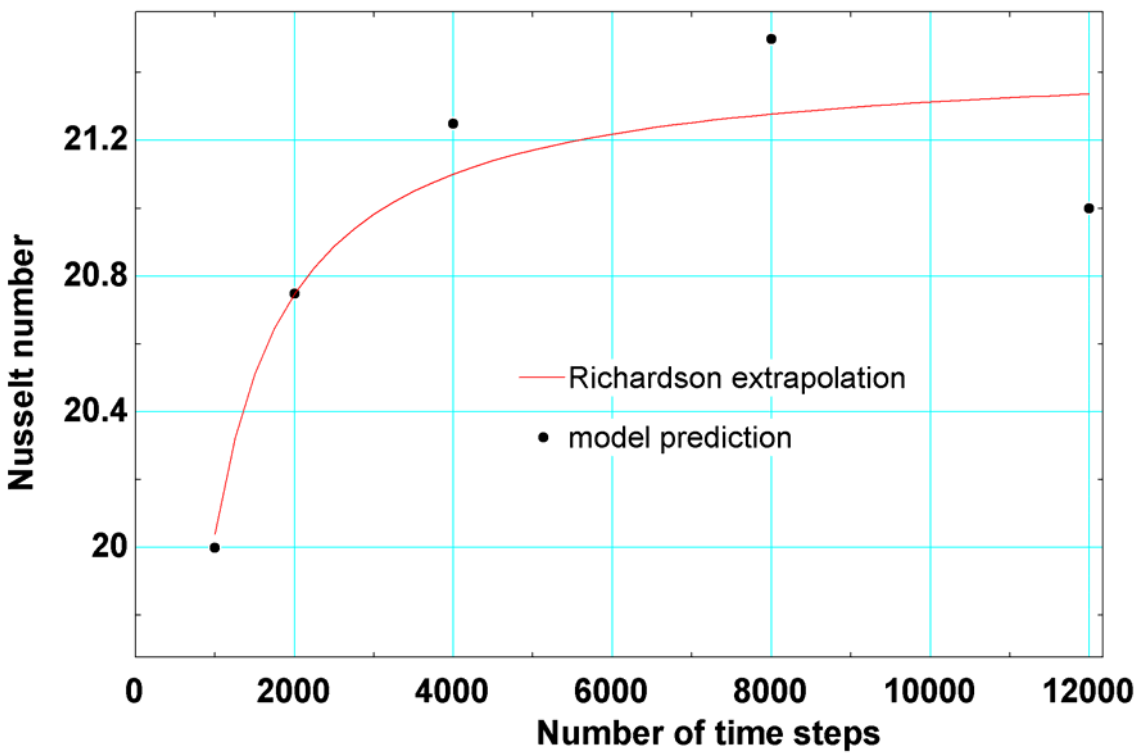

Figure 4.15. Nusselt number predicted by the numerical model for 4 L/min flow rate of water as a function of number of time steps. Also shown is the Richardson extrapolation curve.

Figure 4.15 shows that the model is sensitive to the numerical time step used. Therefore it is desirable to limit the time of the experiment that is considered by the model in order to keep the number of necessary time steps to a relatively low value. Studying the inlet and outlet temperatures measured for each regenerator puck shown Fig. 4.6 shows that although the entire experiment runs for over 250 s, a majority of the heat transfer for each puck happens over a period of approximately 100 s. Therefore, when each separate regenerator puck is analyzed, the time scale of the experiment is shifted so that only the portion of the experiment that is important to that puck is considered. The starting time for each analysis is a user-defined time based on the each experiment and the final time used in the model is 10 s after the experimentally observed

80% breakthrough time. For the data presented in Fig. 4.6, the start time is 0 s and the final time used by the numerical model is approximately 60 s. For the 4th puck, the breakthrough curve does not start near the beginning of the experiment so the start time is set to 30 s and the end time determined by the model is approximately 140 s.

The model's sensitivity to the number of spatial steps was then studied. Using 2000 time steps and only analyzing the important portion of the experiment for puck 3, the number of spatial steps was varied and the best-fit Nusselt number was calculated by the model for each value of number of spatial steps. Because the model was considering a shorter time span than was used to generate Fig. 4.15, the time step was reduced to 0.0448 s with Nt=2000. The predicted Nusselt number as a function of spatial steps, Nx, is shown in Fig. 4.16.

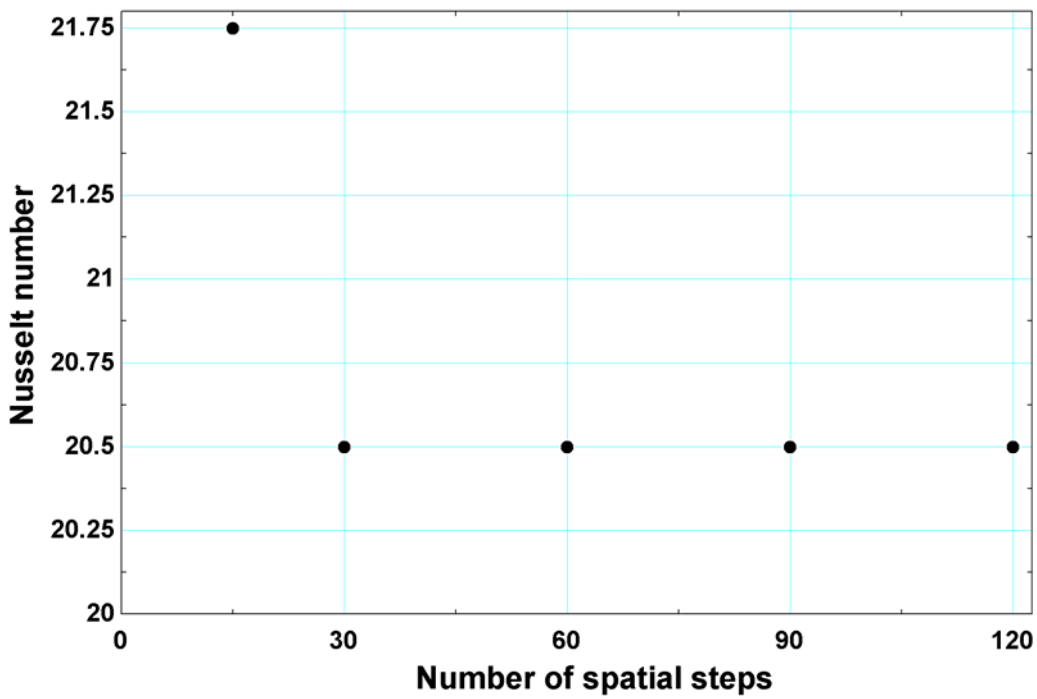

Figure 4.16. Nusselt number predicted by the numerical model for 4 L/min flow rate of water as a function of number of the number of spatial steps

Figure 4.16 shows that the predicted Nusselt number is independent of the number of spatial steps used by the model, provided there are 30 or more spatial steps. For all single blow regenerator data presented here, the model uses 30 spatial steps and 4000 time steps.

4.5.1 Reynolds Number and Prandtl Number Used for the Nusselt Number Correlation

Because the difference between the cold soak temperature and the regenerator inlet temperature is greater than 10 K, the Reynolds number and Prandtl number in the regenerator can vary due to the temperature-dependence of the heat transfer fluid's viscosity. An example of how the Reynolds number changes during an experiment is shown in Fig 4.17. Figure 4.17 shows the Reynolds number calculated by the model for the 1st puck in the experiment shown in Fig. 4.6 (water with a flow rate of 1 L/min).

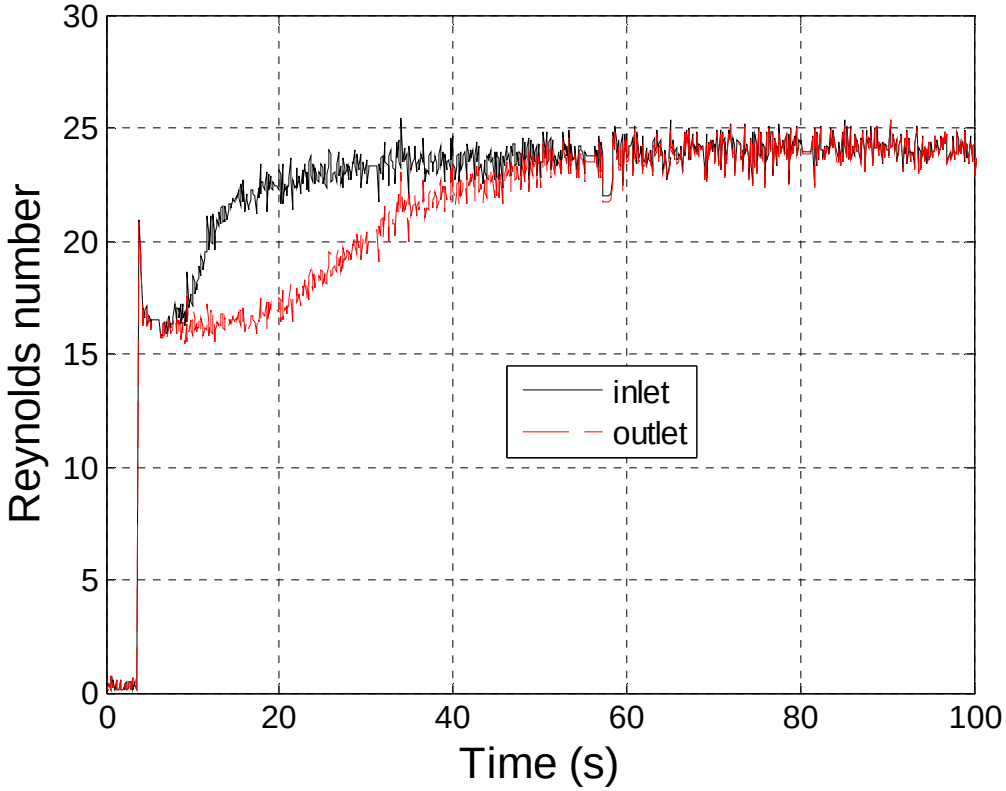

Figure 4.17. Reynolds number calculated by the model for a 1 L/min flow of water for puck 1 in the regenerator.

Initially the Reynolds number is 0 because there is no fluid flow through the regenerator. Once the solenoid valve opens there is a flow spike, which causes the spike in Reynolds number at approximately 4 s. After the flow spike the fluid flow rate becomes nearly constant and the change in Reynolds number is due mainly to the change in fluid temperature. The Prandtl number for the same experimental condition is shown in Fig 4.18.

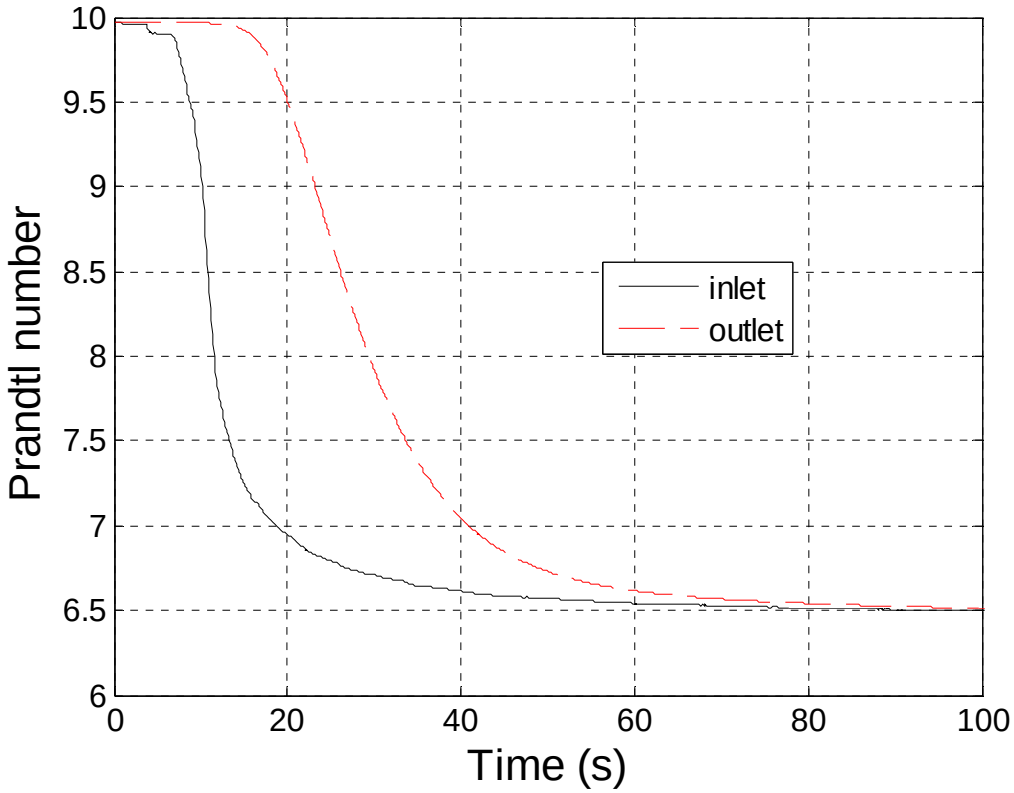

Figure 4.18. Prandtl number calculated by the model for a 1 L/min flow of water for puck 1 in the regenerator.

Figures 4.17 and 4.18 show that there is a change in both the Reynolds number and Prandtl number during the experiment. However, Fig. 4.14 shows that excellent agreement can be achieved between the measured and predicted outlet temperatures using a constant (independent of Reynolds number and Prandtl number) Nusselt number. The experimental data do not contain enough information to determine the effects of the varying Prandtl and Reynolds number that occur during each experiment on the Nusselt number. Therefore, there is an uncertainty in the both the Prandtl number and Reynolds number that should be assigned to the Nusselt number evaluated for any particular experiment. The nominal value for each number is the average between the Reynolds number and Prandtl number at the 20% breakthrough temperature and 80% breakthrough temperature.

4.6 EXPERIMENTAL RESULTS

For each experimental run, there are seven Nusselt number measurements – one for each regenerator puck in the entire regenerator. The measured Nusselt number for each regenerator puck for a 1 L/min flow rate of water are shown in Fig 4.19. The Reynolds number range for the experiment shown in Fig. 4.19 is 17.5-24.5 and the Prandtl number range is 6.6-9.0. The average Nusselt number for the seven regenerator pucks is 6.57, which is also shown in Fig. 4.19. The variation in measured Nusselt number with puck number is typical for this single blow experiment.

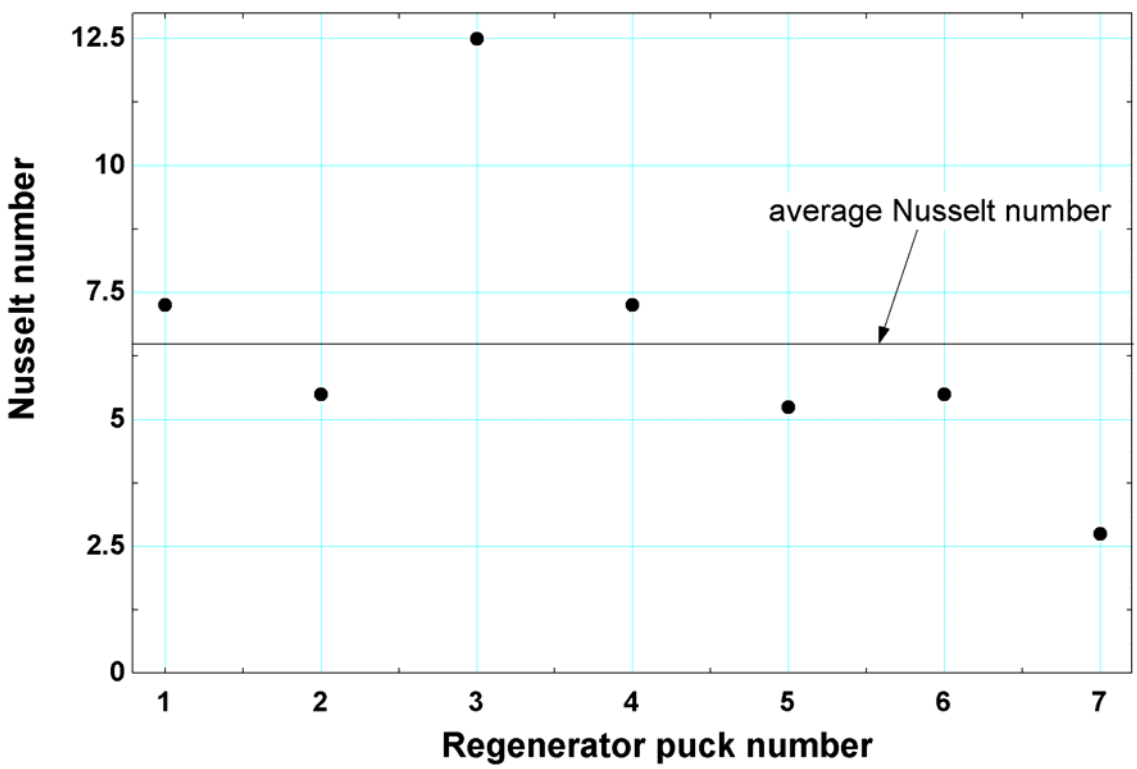

Figure 4.19. Measured Nusselt number for each regenerator puck for water at a flow rate of 1 L/min. Also shown is the average Nusselt number for the seven regenerator pucks.

Figure 4.19 shows that there is a relatively large variation in the Nusselt number from puck to puck. The variation may be caused by several factors such as uncertainty in temperature measurements or a heat leak to the PVC shell. However, the uncertainty is reduced by taking multiple measurements for each experiment (i.e. measuring the Nusselt number for multiple regenerator pucks for each experiment). Some experiments were replicated to test the repeatability of the experiment. When the Nusselt number for any experiment reported here, it is the average Nusselt number across all the regenerator pucks and for all of the replicates. The uncertainty of the average Nusselt number for an experiment is defined as:

$$e_{Nu} = \frac{\sigma}{\sqrt{N_{meas}}} \tag{4.7}$$

where e_{Nu} is the uncertainty in the Nusselt number, σ is the standard deviation of the measured Nusselt numbers, and N_{meas} is the number of Nusselt number measurements. For each experiment there will be seven measurements and some experiments were repeated a total of four times, so that in some cases are as many as 28 measurements.

The repeatability of the test apparatus was checked by calculating the average Nusselt number and uncertainty for several tests and comparing the repeated measurements. A comparison of the measured Nusselt number for an experiment that was repeated a total of four times is shown in Fig. 4.20. The data in Fig. 4.20 are for a 40% propylene glycol and water mixture with a flow rate of approximately 3.0 L/min.

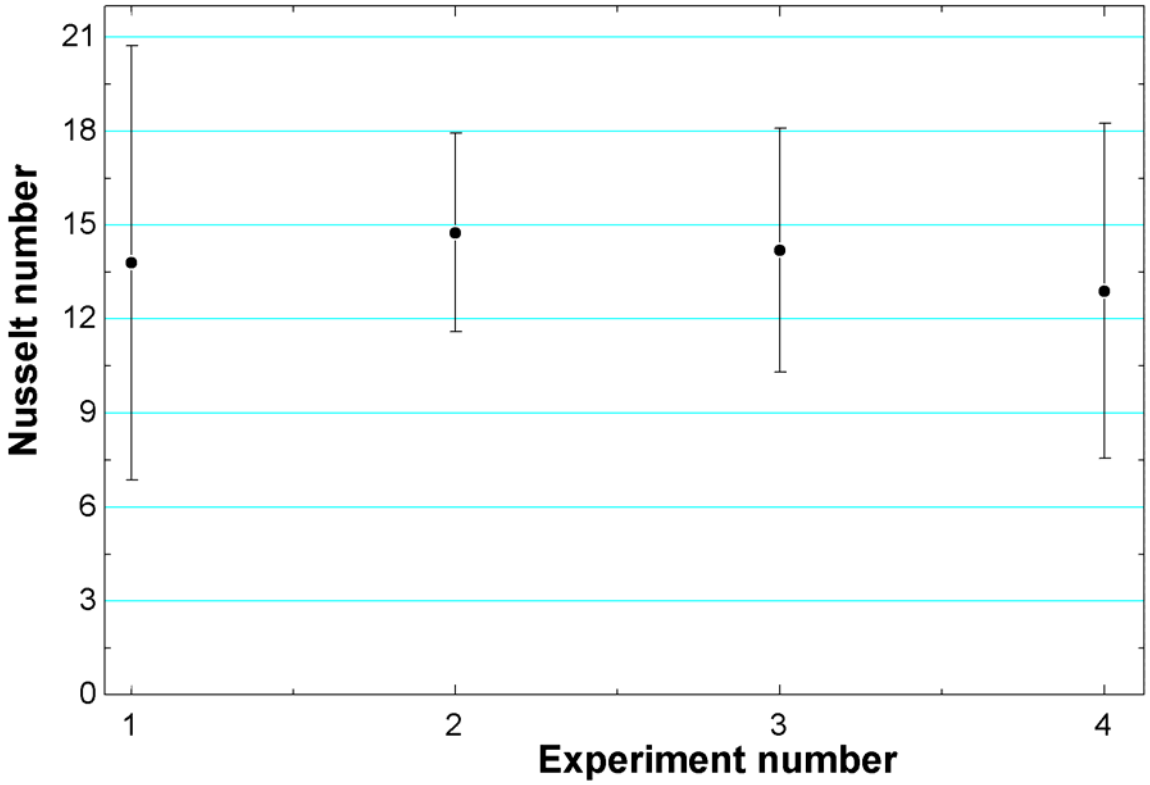

Figure 4.20. Measured average Nusselt number and uncertainty for four repeated experiments using a 40% propylene glycol and water mixture with a flow rate of 3 L/min

Figure 4.20 shows that the average Nusselt number for each of the four repeated experiments falls within the range of uncertainty of the others, and the experiment is repeatable within an acceptable limit. The uncertainty for each experiment is relatively high, but the uncertainty of the average Nusselt number for a flow rate of 3 L/min is relatively low because there are four replicated experiments. Using data from Fig. 4.20, the measured Nusselt number is 13.9±2.3 for a Reynolds number span of 18.6-26.9 and a Prandtl number range of 22.7-32.2. The Nusselt number as a function of Reynolds number for experiments using pure water as a heat transfer fluid is shown in Fig. 4.21. In order to achieve a larger Reynolds number span, some experiments were run with a higher inlet temperature. The higher inlet temperature lowers the

fluid viscosity and therefore raises the Reynolds number for the same flow rate, but it also changes the Prandtl number for the experiments. In Fig 4.21, some of the data points seem to be in disagreement with others, but the difference is due in large part to the different Prandtl numbers for the experiments.

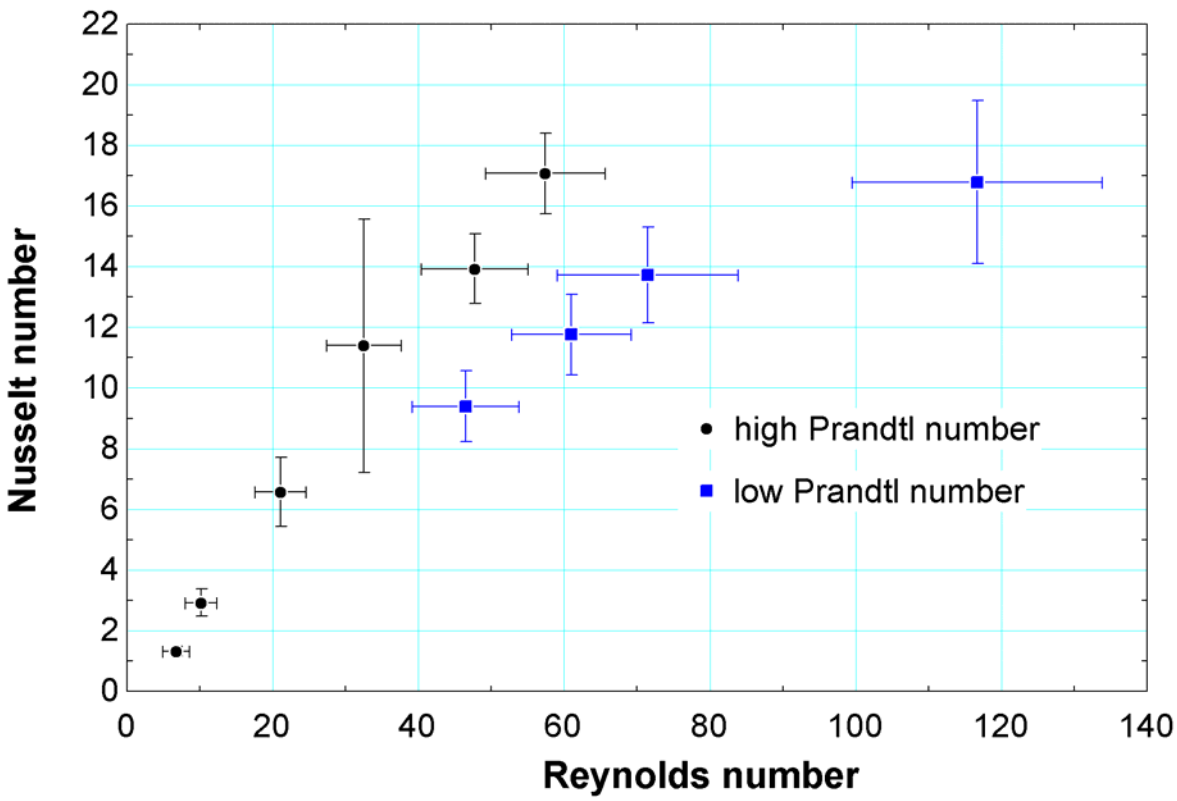

Figure 4.21. Measured average Nusselt number as a function of Reynolds number for experiments using water as a heat transfer fluid

The data from Fig. 4.21 can be better represented as function of both Reynolds number and Prandtl number as shown in Fig. 4.22. Heat transfer for each experiment takes place over a range of Reynolds numbers and Prandtl number. Each data point is represented as an ellipsoid

that covers a range of Reynolds number and Prandtl number as well as the Nusselt number measurement uncertainty for each point.

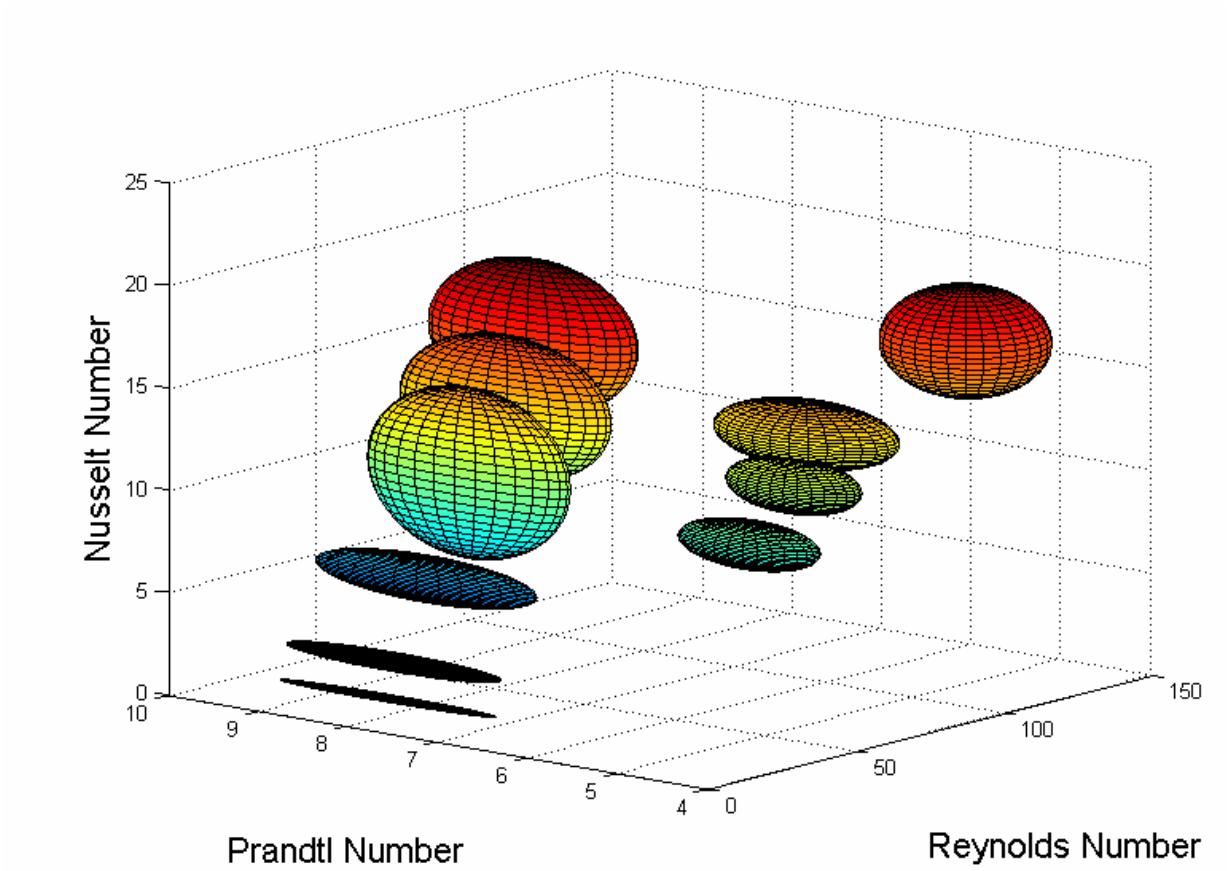

Figure 4.22. Measured average Nusselt number as a function of Reynolds number and Prandtl number for experiments using water as a heat transfer fluid

The Nusselt number as a function of Reynolds number for a 20% propylene glycol and water heat transfer fluid is shown in Fig. 4.23. The Prandtl number for the experiments shown in Fig. 4.23 has a range of approximately 8.5-12.5 across the experimental range.

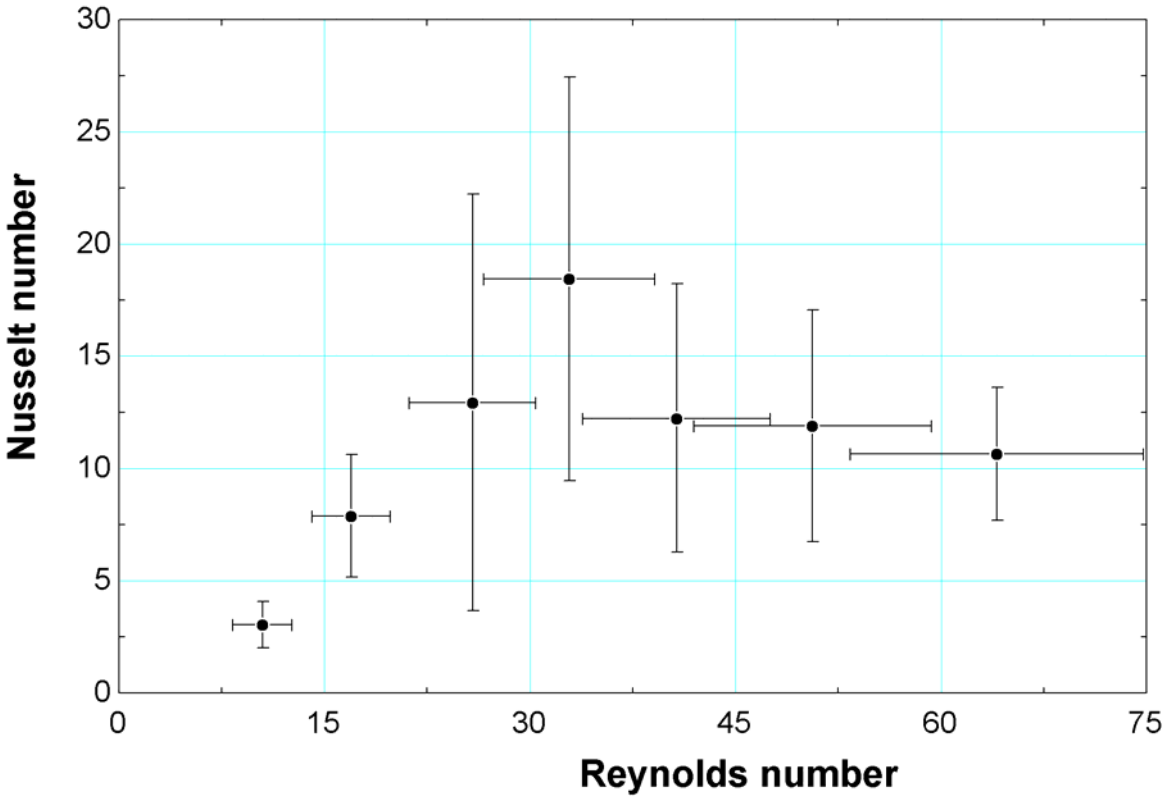

Figure 4.23. Measured average Nusselt number as a function of Reynolds number and Prandtl number for experiments using a mixture of 20% propylene glycol and water as a heat transfer fluid

The Nusselt number as a function of Reynolds number for a 30% propylene glycol and water heat transfer fluid is shown in Fig. 4.24. The Prandtl number for the experiments shown in Fig. 4.24 has a range of approximately 12.5-20 across the experimental range.

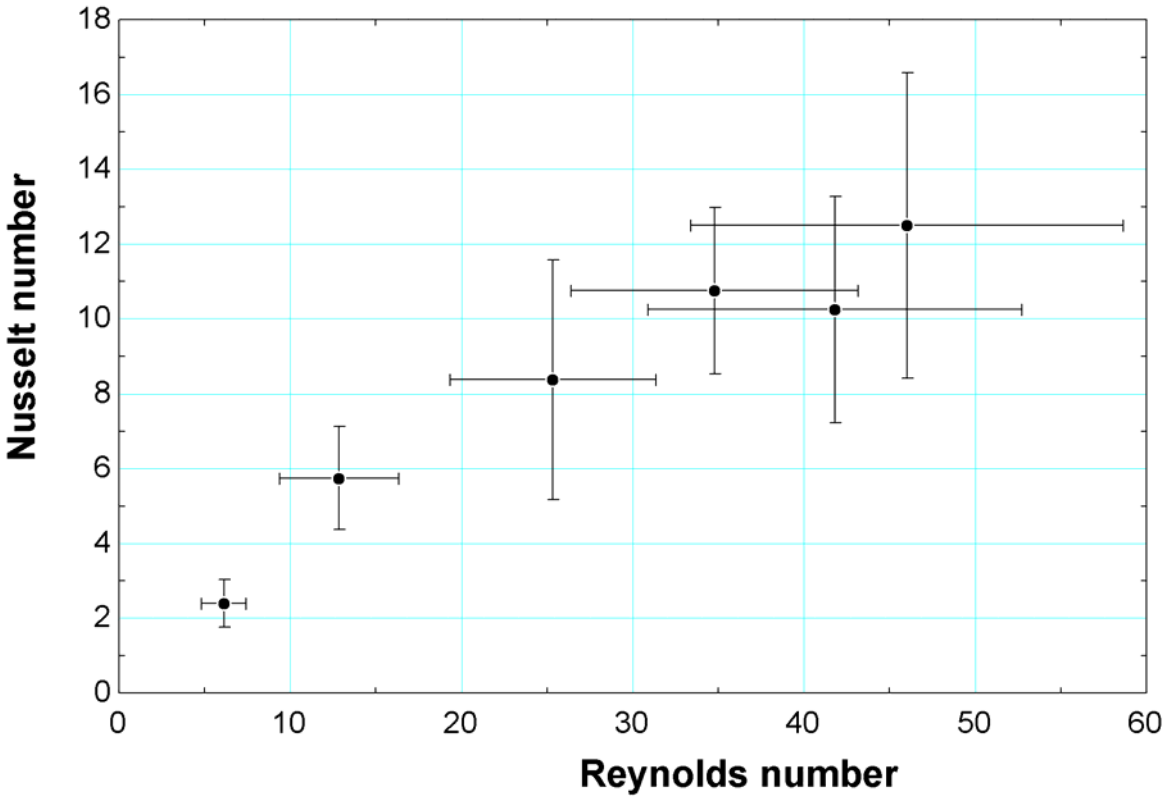

Figure 4.24. Measured average Nusselt number as a function of Reynolds number for experiments using 30% propylene glycol and water as a heat transfer fluid

Finally, the Nusselt number as a function of Reynolds number for a 40% propylene glycol and water heat transfer fluid is shown in Fig. 4.25. The Prandtl number for the experiments shown in Fig. 4.25 has a range of approximately 18.5-33.5 across the experimental range. The uncertainty in the Nusselt number in Fig. 4.25 is lower than for other concentrations of propylene glycol because all experiments for the 40% concentration were repeated a total of 3-4 times.

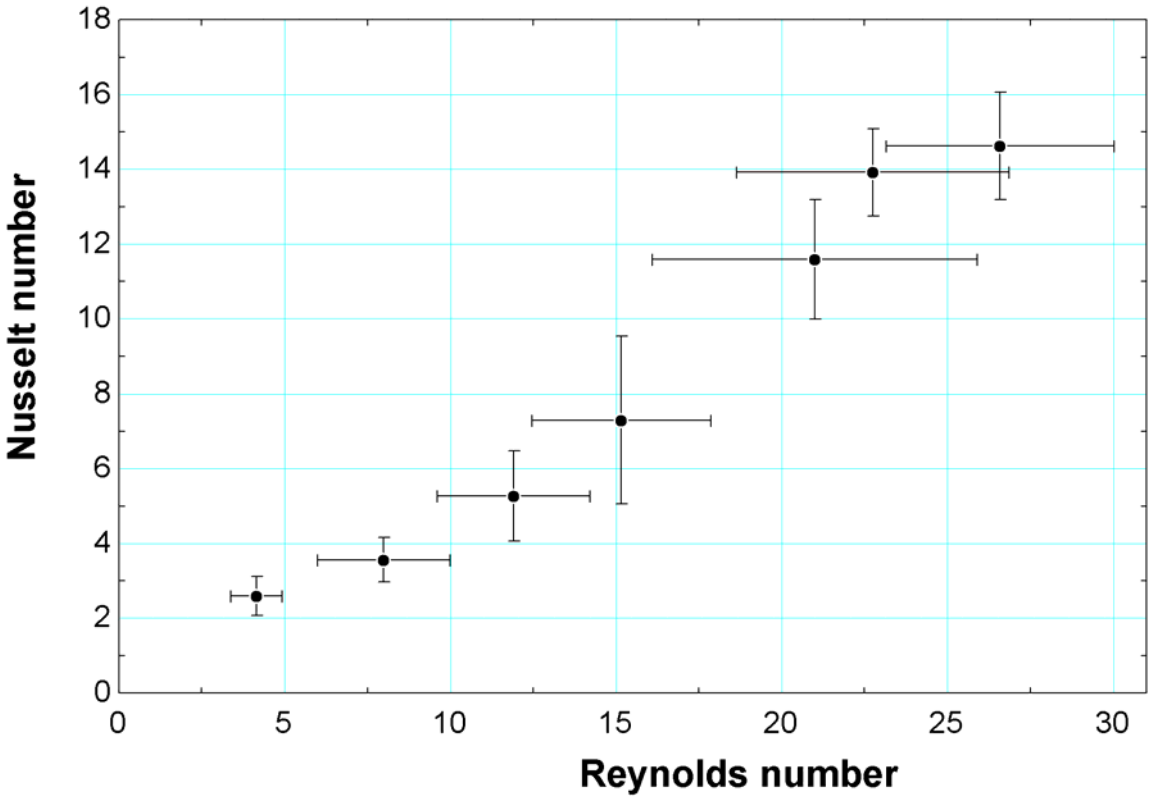

Figure 4.25. Measured average Nusselt number as a function of Reynolds number for experiments using 40% propylene glycol and water as a heat transfer fluid

4.6.1 Fitting Curve Fitting of Experimental Measurements

The experimental data were fit to a Nusselt number correlation with the form

$$Nu = A + B\left(Re^{C} Pr^{D}\right) \tag{4.8}$$

where A, B, C, and D are fitting coefficients. The fitting coefficients were determined by minimizing the root sum squared of the error between the curve fit values and experimental Nusselt number measurements. The RSS error was minimized using the Nelder-Mead simplex method in EES. The resulting correlation is shown in Eq. (4.9).

$$Nu_{UW} = 0 + 0.70\, Re^{0.60} Pr^{0.23} \tag{4.9}$$

The new Nusselt number correlation from Eq. (4.9) is plotted against other existing correlations for a Prandtl number of 6.8 in Fig. 4.26.

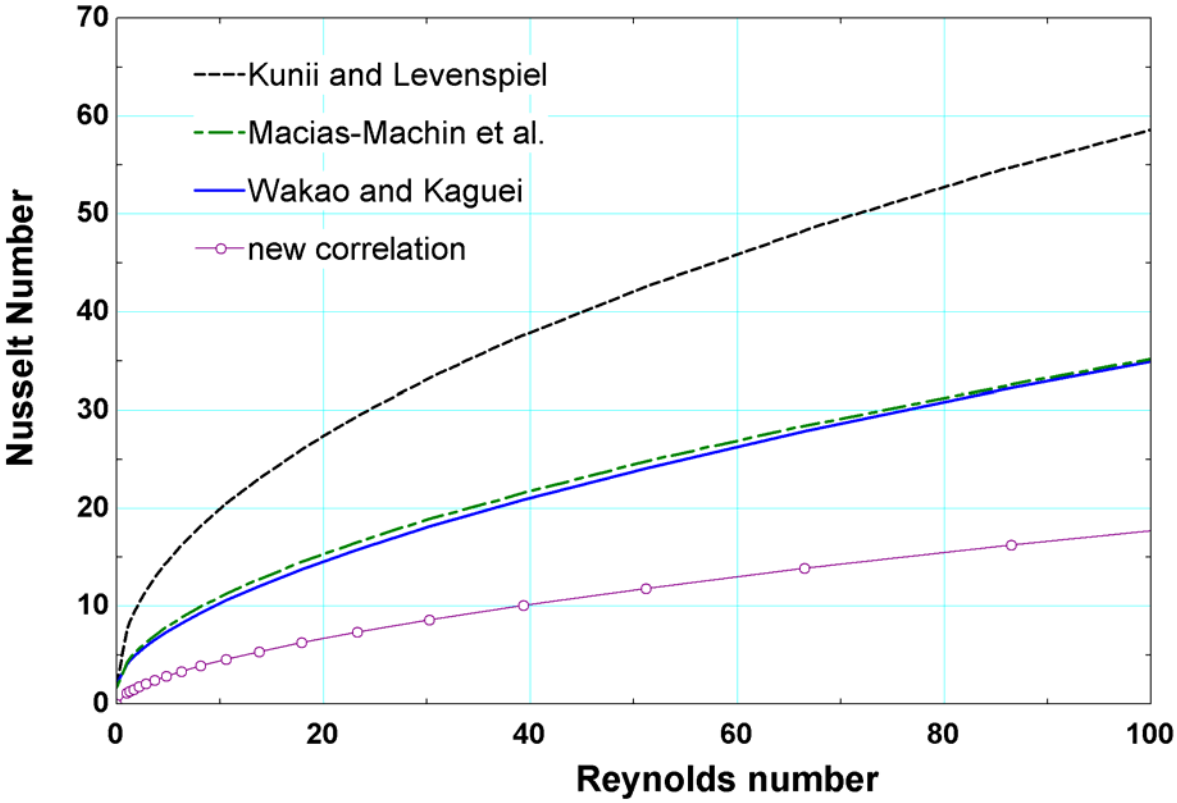

Figure 4.26. Nusselt number as a function of Reynolds number for a Prandtl number of 6.8 and a regenerator with a porosity of 0.36

Figure 4.26 shows that the new correlation predicts a significantly lower Nusselt number for all Reynolds numbers for a Prandtl number of 6.8. However, when the Prandtl number is increased to 30, the new correlation predicts a higher Nusselt number than the correlation presented by Macias-Machin et al. when the Reynolds number is greater than 15. The Nusselt number predicted by the correlations for a Prandtl number of 30 is shown in Fig. 4.27.

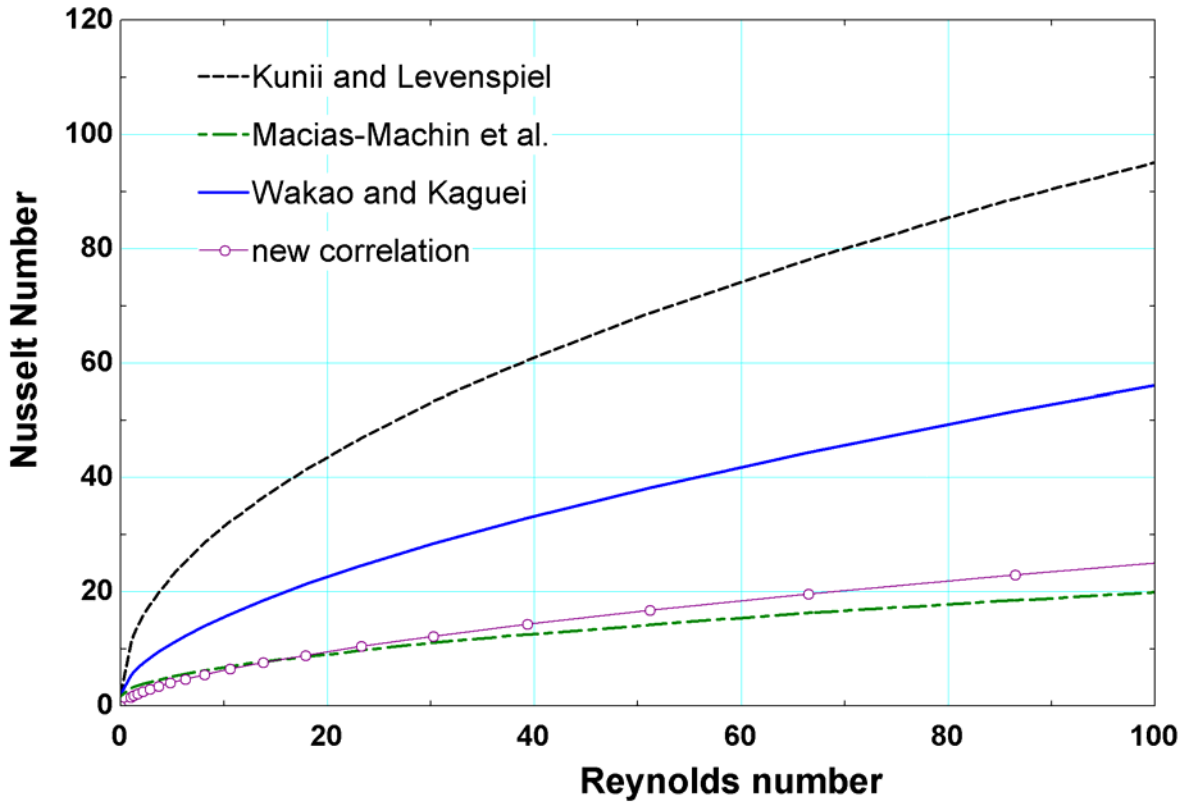

Figure 4.27. Nusselt number as a function of Reynolds number for a Prandtl number of 30 and a regenerator with a porosity of 0.36

It is encouraging that the new correlation developed here predicts Nusselt number values that are near values predicted by Macias-Machin et al because that is the only other correlation presented here that was developed specifically for liquid heat transfer fluids. The Nusselt number predicted by the curve fit is plotted against the experimental Nusselt number in Fig. 4.28.

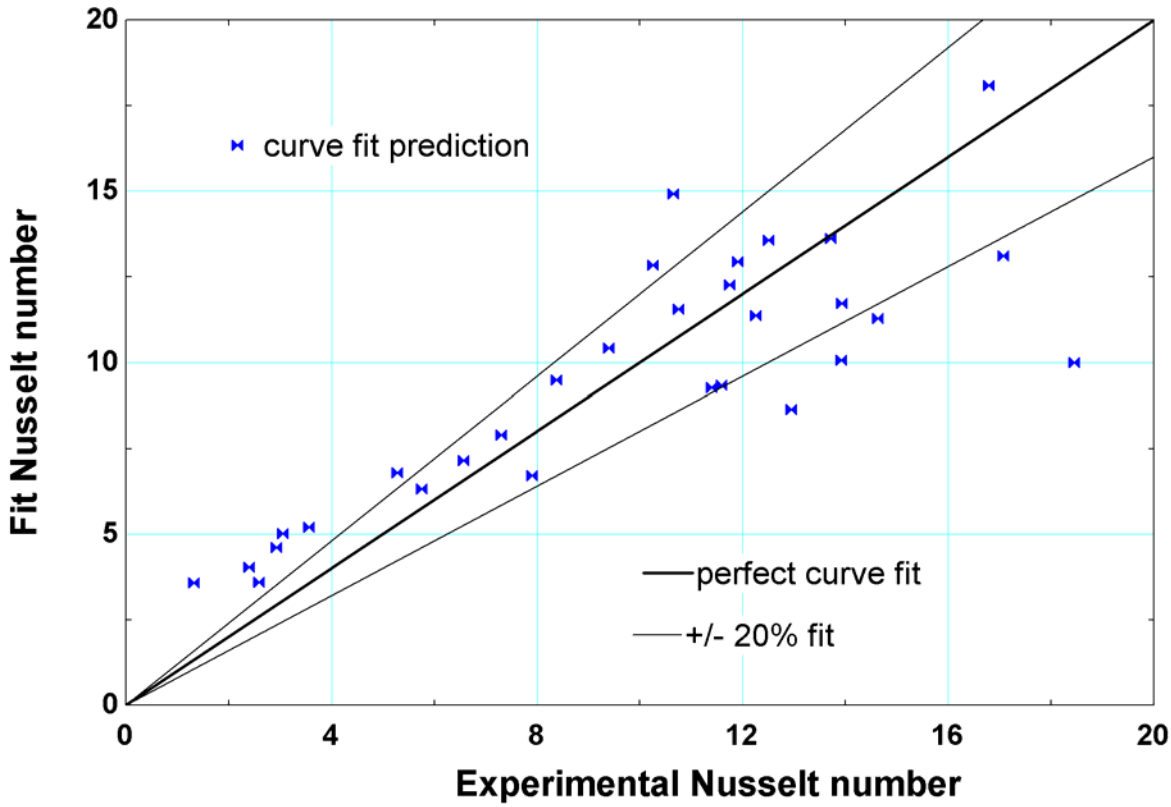

Figure 4.28. Nusselt number predicted by Eq. (4.9) as a function of measured Nusselt number. Also shown is a line indicating a perfect curve fit and lines indicating ±20% of the measured values.

Figure 4.28 shows that the curve fit over predicts the measured values for low Nusselt numbers. The two largest outliers in Fig. 4.28 are data points taken for a mixture of 20% propylene glycol. The 20% propylene glycol solutions exhibited the highest experimental uncertainty, and it is not surprising that the correlation does not fit the 20% propylene glycol data points well. It is surprising that the best fit curve predicts a Nusselt number of 0 when there is no flow. The lower-than-expected heat transfer coefficient at low flow rates may be caused by the energy that is lost to the regenerator outer shell, and some tests were done to investigate the effect that the outer shell has on experimental results.

4.6.2 Testing the Effects of Heat Transfer to the Outer Shell

In this section, the effect of heat transfer to the outer shell on the experimentally measured Nusselt number was investigated. For all experiments in this section, the heat transfer fluid is a mixture of 40% propylene glycol and water. To check the effects of heating versus cooling the regenerator, the initial conditions of the experiment were modified such that the regenerator is initially at a relatively high temperature and fluid at a lower temperature enters the regenerator at the beginning of the experiment. A high initial regenerator temperature can be achieved easily by increasing the temperature set point of the 'cold' temperature bath to a temperature that is higher than room temperature. The main reservoir is only heated and cannot achieve a temperature lower than room temperature. The heater on the main reservoir was shut off for this experiment, and the inlet fluid temperature is therefore room temperature. A fluid flow rate of 3 L/min was chosen for this experiment because experimental results were previously obtained at this flow rate. The experiment was run with the inlet temperature set to room temperature (~292 K) and the initial regenerator temperature set to approximately 307 K, and the experiment was run twice. The inlet temperature was then set to approximately 307 K and the initial temperature was set to approximately 292 K, and the experiment was again run twice. The results are shown in Fig 4.29. In the figure, the first two experiments are for a regenerator that is initially at a high temperature (hot soaked) and the second two are for a regenerator that is at a low initial temperature (cold soaked). Figure 4.29 shows that the measured Nusselt number in the regenerator is independent of whether the regenerator is being heat or cooled during the experiment.

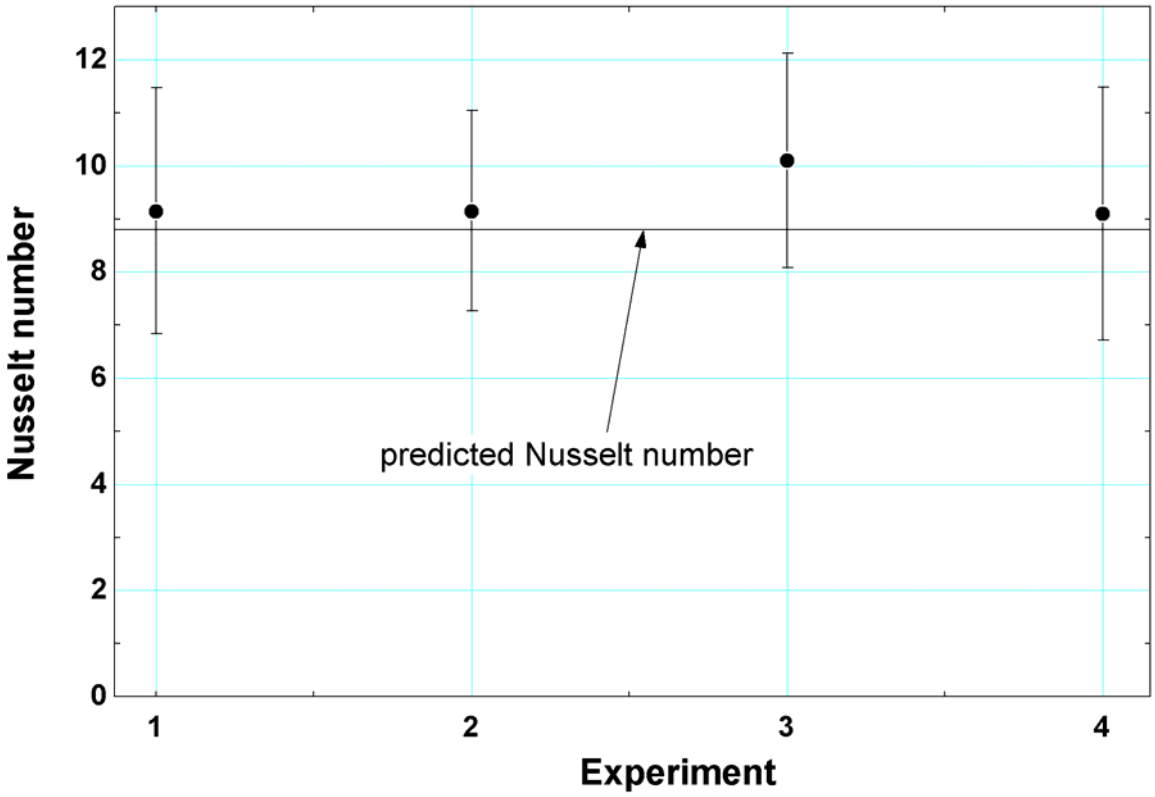

Figure 4.29. Measured Nusselt number for a hot soaked regenerator (experiments 1 and 2) and for a cold soaked regenerator (experiments 3 and 4)

The nominal Reynolds number for the experiments in Fig. 4.29 is approximately 17.5 and the nominal Prandtl number is approximately 30.5. For these values, the new Nusselt number correlation predicts a Nusselt number of 8.8, which is within the experimental uncertainty range of the experiments in Fig. 4.29.

The effect of the thermal mass of the PVC outer shell on experimental results was investigated by heating the outer shell during an experiment. A 200 W heater was applied to the outside of the PVC outer shell that completely covered the regenerator. Before the experiment was run, the heater was turned on for a long time in order to allow the outer shell to reach steady state. For

the first experiment, the regenerator was cold soaked to a uniform temperature and then experienced no fluid flow for 10 minutes while the shell was heated. The shell was heated for 10 minutes before the experiment began to ensure that the energy from the heat had adequate time to penetrate the shell. After 10 minutes, the solenoid valve was opened and fluid was pumped through the regenerator. For the second experiment, the regenerator was cold soaked and the experiment began just after the regenerator reached a uniform temperature. A flow rate of approximately 1 L/min was chosen for both experiments because it is a relatively low flow rate that results in a longer time period for the regenerator outlet temperature to reach a temperature near the inlet temperature. Longer tests allow more time for the outer shell to interact with the heat transfer fluid and should show the effects of the outer shell better than short tests.

The average Nusselt number was calculated for each test and they were compared to results previously reported for a flow rate of 1 L/min and to the value predicted by the new Nusselt number correlation. The results are shown below in Fig. 4.30.

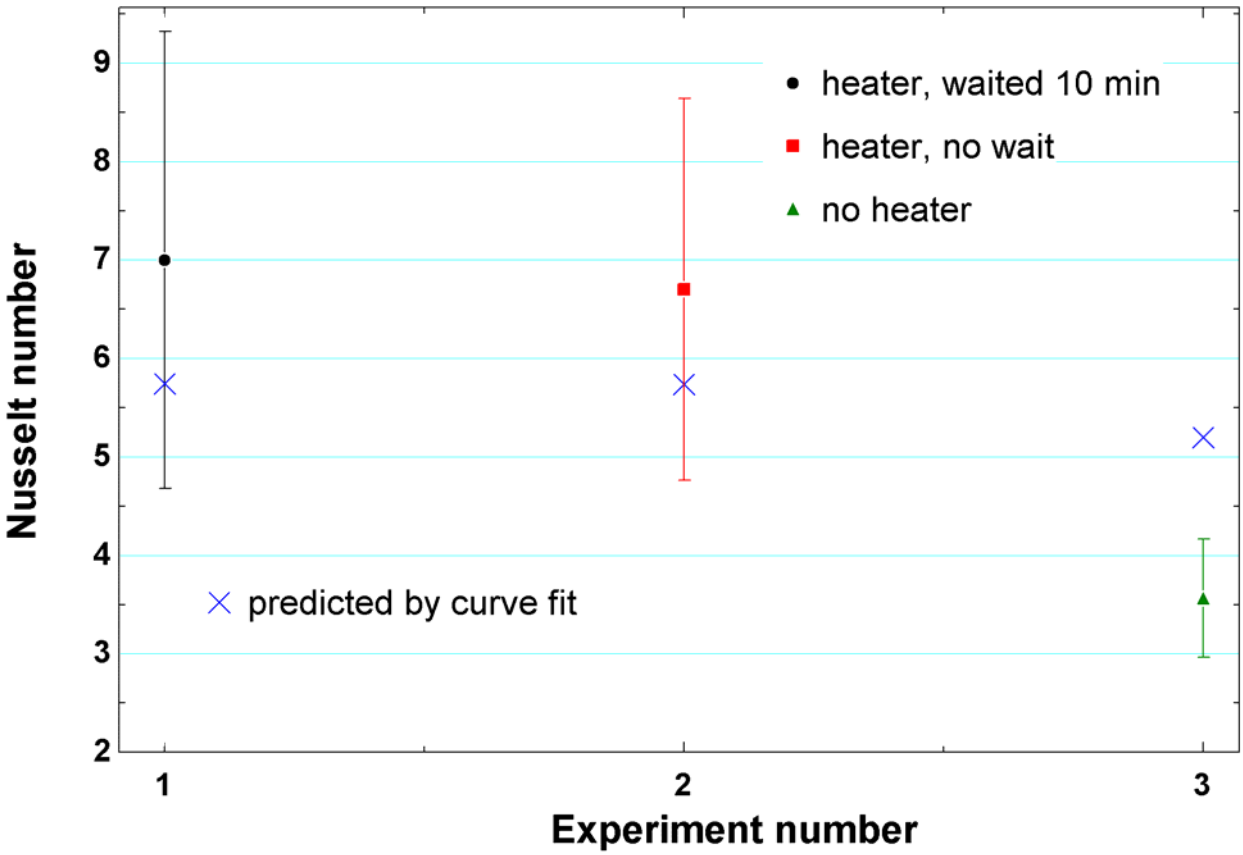

Figure 4.30. Measured Nusselt number when the PVC outer shell is heated (experiments 1 and 2) and when the outer shell is not heated (experiment 3). Also shown is the prediction from the new Nusselt number correlation.

For the experiments shown in Fig 4.30, the Wakao and Kaguei correlation predicts a value of approximately 14 and overpredicts the Nusselt number even when the outer shell is heated. Because the Wakao and Kaguei over predicts the Nusselt number for this experiment, even when the outer shell is heated shows that the heat transfer in the regenerator is significantly lower than predicted by existing correlations, even with the possible confounding factor of heat leak to the shell.

The effect of the heat leak to the wall was also studied for a flow rate of 4 L/min. The heater was allowed to run for a long time, then the regenerator was cold soaked. There was no waiting time between the end of the cold soak process and the beginning of the experiment. The results for two experiments with the shell heat and one with no heat applied to the shell are shown in Fig. 4.31.

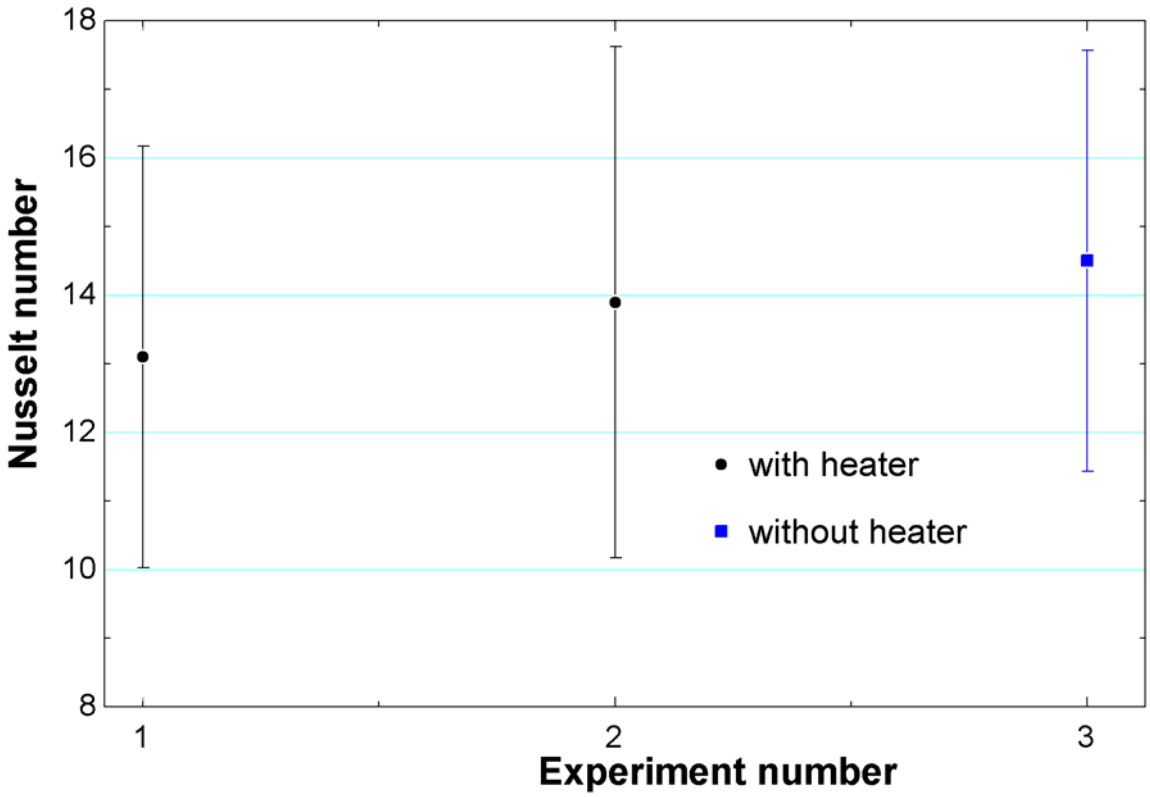

Figure 4.31. Measured Nusselt number when the PVC outer shell is heated (experiments 1 and 2) and when the outer shell is not heated (experiment 3)

Figure 4.31 shows that the measured Nusselt number was actually slightly higher when the shell was not heated. The difference the measured Nusselt number between the non-heated shell and the heated shell is most likely due to experimental uncertainty. The results shown in Fig. 4.31

shows that the effect of the apparent heat leak to the outer shell becomes negligible as the fluid flow rate increases. However, Figure 4.30 shows that, for lower flow rates, the thermal interaction with the wall is an important aspect of regenerator design and performance that has been ignored by modeling efforts thus far in this thesis. The effect of the heat transfer to the outer wall is an apparent degradation of heat transfer in the regenerator that is very difficult to isolate from heat transfer losses between the fluid and particles with the data that was taken in this thesis. The effect of heat transfer to the outer shell should be greater for tests with lower flow rates because there is more time for the shell to interact with the heat transfer fluid. Heat transfer to the shell is most likely the reason that the correlation developed in this chapter predicts a Nusselt number of 0 when there is no flow. Although the heat transfer to the outer shell did lower the Nusselt number measured in this experiment, it is not enough to explain the difference between the Nusselt numbers predicted by correlations presented by Wakao and Kaguei or Kunii and Levenspiel. The Nusselt number correlation presented in this chapter is based on data that were collected for liquid heat transfer fluids and should be more a more accurate representation of the heat transfer that is seen in a practical AMRR system than the Nusselt number correlations developed primarily from data using gas heat transfer fluids.

Chapter 5 Modeling the Astronautics Rotary AMRR Prototype

5.1. DESCRIPTION OF THE EXPERIMENTAL APPARATUS

Astronautics has built a rotary AMRR experimental apparatus, described by Zimm et al. (2006), with a magnetic field that is generated by a 1.5 Tesla $Ne_2Fe_{14}B$ permanent magnet. A photograph of the system is shown in Figure 5.1. The magnetocaloric wheel, or regenerator, is comprised of six regenerator beds that are arranged back-to-back, i.e., with the hot end of each bed sharing a separating wall with the hot end of an adjacent bed (and the cold ends also adjacent). This back-to-back configuration reduces conduction losses between individual regenerator beds as compared with the alternative configuration where the hot and cold ends of each sequential bed are adjacent. During operation, the regenerator wheel rotates while the magnet remains stationary; this configuration allows each regenerator bed to complete an AMRR cycle in one revolution of the regenerator wheel. The flow circuit is designed so that the flow through the pump and heat exchangers is approximately continuous while each regenerator bed experiences an oscillating flow as well as periods with no flow at all. Astronautics has provided experimental data from the prototype operating with regenerator beds that are packed with spherical particles of commercial grade gadolinium (Gd).

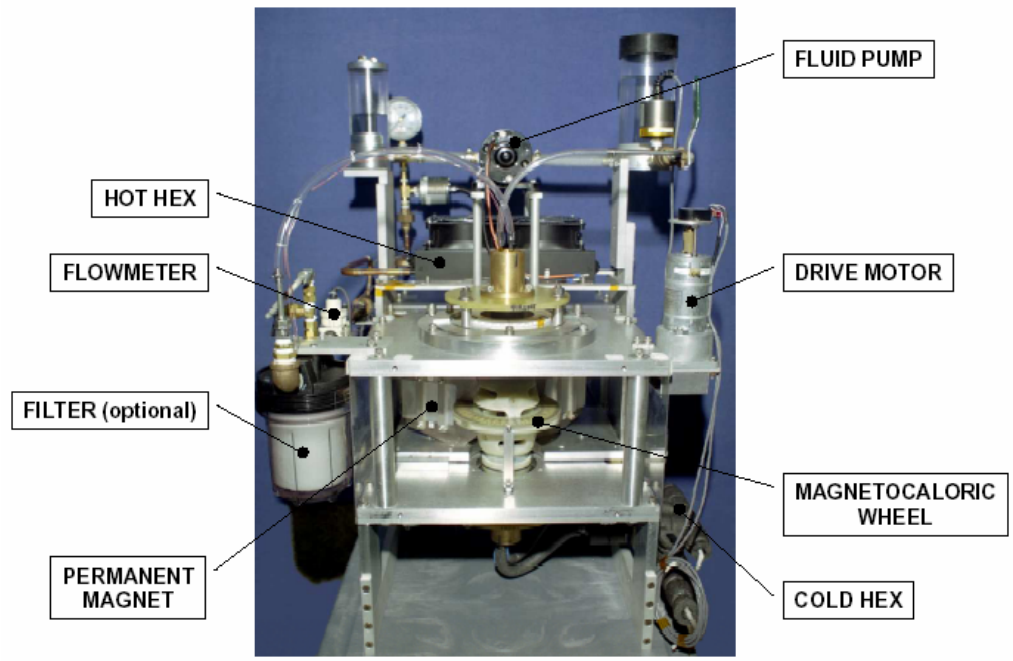

Figure 5.1. Rotary AMRR experiment at Astronautics

A simple drawing of the regenerator in the apparatus shown in Figure 5.1 is given in Figure 5.2. The dimensions in Figure 5.2 were provided by Astronautics and are used to determine modeling inputs. The flow path through each regenerator bed in the prototype system is circumferential; however, the AMRR numerical model is 1D and therefore the length of the bed at the centerline is used for the curved beds shown in Figure 5.2.

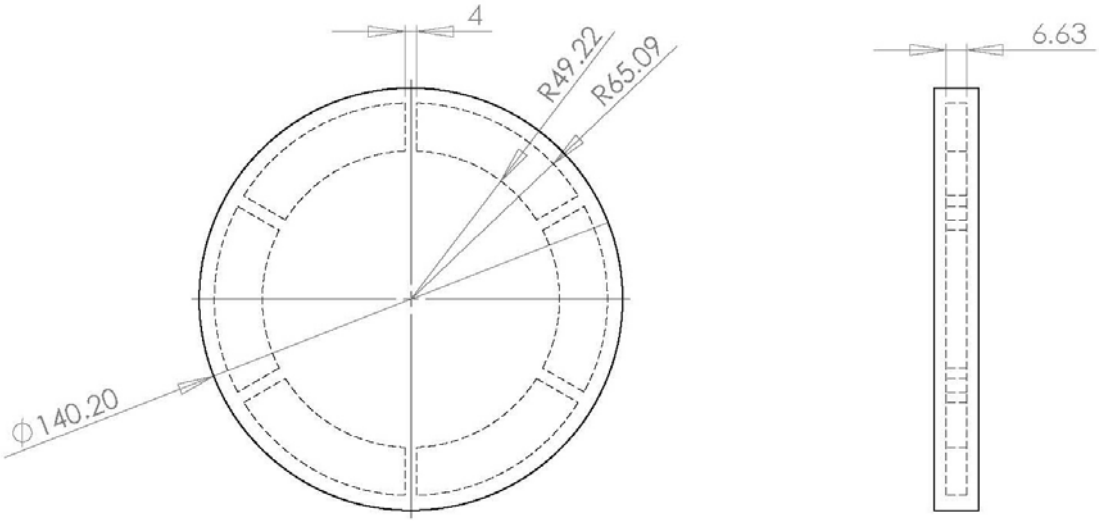

Figure 5.2. Part drawing of the regenerator wheel used in the prototype device (all dimensions in mm)

The experimental apparatus is instrumented so that the fluid flow rate at the pump outlet, the pressures at the inlet and outlet of the flow control valve, and the power input to a heater in the cold reservoir are all measured. A simple schematic of the experimental setup designed by Astronautics is shown in Fig. 5.3. Flow through the regenerator is controlled by a proprietary valve so the actual flow path through the regenerator wheel is not shown in the schematic. The cooling load produced by the system is controlled by varying the voltage supplied to a resistance heater in the cold heat exchanger. The power required to rotate the regenerator in the magnetic field is not measured in this experiment. Table 5.1 contains a summary of the measured and controlled experimental parameters for this system. The ranges given in Table 5.1 are approximately the minimum and maximum values observed in the experimental data that were provided.

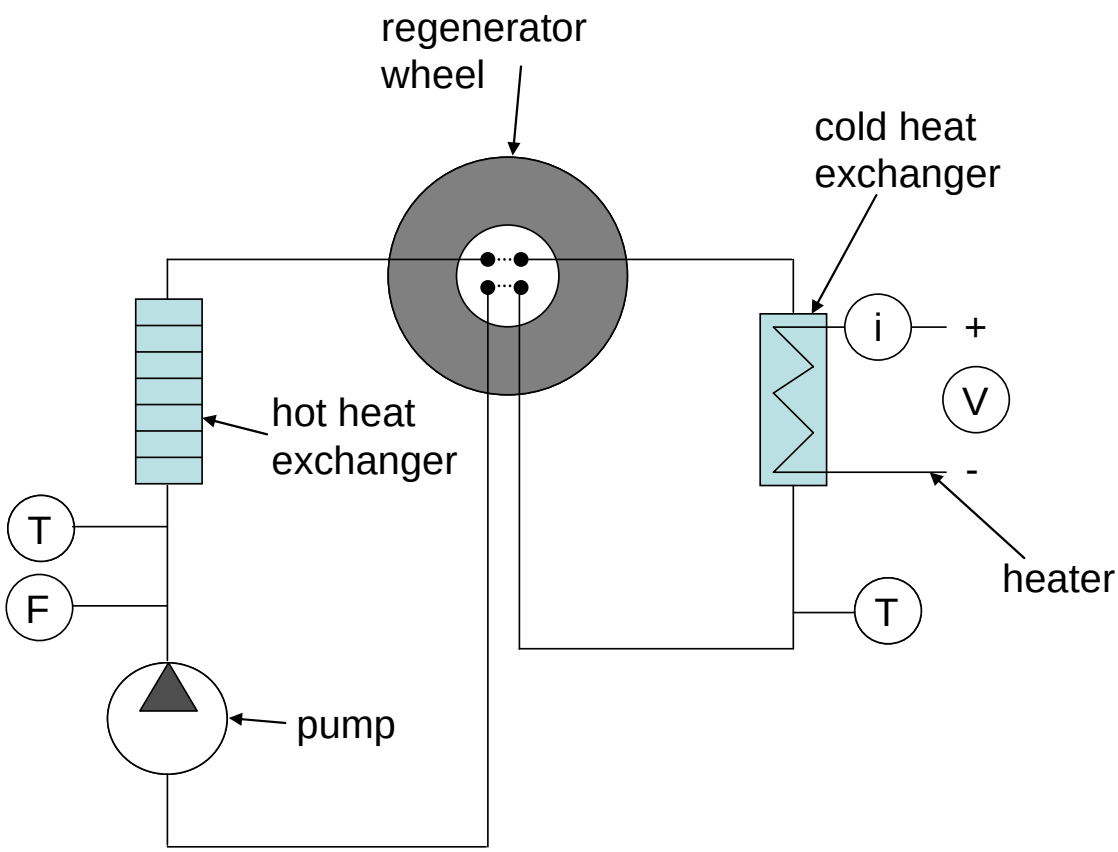

Figure 5.3. Test schematic of the rotary AMRR apparatus at Astronautics

Table 5.1. Experimentally measured and controlled parameters for experimental data provided by Astronautics

Controlled Value	Range	Measured Value	Range
regenerator rotational speed	30-240 RPM	cold reservoir temperature	~273-300 K
fluid flow rate	~0.2-0.8 L/min	hot reservoir temperature	~290-305 K
cooling load	0-75 W	pressure drop	~0-150 kPa

The cold and hot reservoir temperatures measured in this experimental setup are the average values of the reservoir temperature. The setup is incapable of measuring the time dependence of the reservoir temperature and therefore the reservoir temperatures are treated as constant values in the numerical model for the data provided by Astronautics.

5.2. PROTOTYPE AMRR MODELING PARAMETERS

The modeling parameters that are used to simulate the system shown in Figures 5.1 and 5.2 are summarized in Table 5.2; these parameters were provided by Astronautics. The details associated with the hardware controlling the flow through the device are proprietary; however, the net effect of this hardware is to impose a fixed dwell ratio of 1/3, meaning that the fluid flow is deactivated (i.e., not flowing) during 1/3 of the cycle in each regenerator bed. The Gd spheres were screened in order to obtain a specific range of sizes. The spheres that were selected for tje beds passed through a screen with nominally 0.5 mm openings but did not pass through a screen with nominally 0.425 mm openings; these spheres are randomly packed to fabricate the regenerator beds. The resulting average porosity of the regenerator is 0.362. The permanent magnet occupies a 120° arc in which the field strength is approximately constant and equal to its maximum value; the field strength is assumed to vary linearly at each end from its maximum value to 0 Tesla field over a 15° arc. The flow-control valves are designed so that the cold-to-hot blow period is 50% complete when the middle of the regenerator coincides with the middle of the arc of the magnet.

Table 5.2. Modeling parameters used to simulate the rotary AMRR device at Astronautics

Parameter	Value	Parameter	Value
regenerator type	packed sphere	maximum applied field	1.5 Tesla
regenerator material	Gd	sphere size for packing	0.425-0.5 mm
regenerator beds	6	porosity	0.362
regenerator height	6.6 mm	motor efficiency	N/S
regenerator width	15.9 mm	dwell ratio	1/3
regenerator length	51.44 mm	magnet arc	120°
regenerator volume	33 cm^3	heat transfer fluid	90% water/10% ethylene glycol

Previous analyses of AMRR systems with this type of geometry have assumed that the magnetic field is spatially uniform within each regenerator bed. However, for the prototype shown in Figure 5.1, this assumption may lead to significant modeling error. As the regenerator moves into the field of the permanent magnet, the magnetic field sweeps across the regenerator bed in this configuration. The magnetic field at any time is therefore a function of position in the bed. Using the geometry shown in Figures 5.1 and 5.2 and the information in Table 5.2, it is possible to calculate the magnetic field as a function of time and position in the regenerator; the resulting profile is shown in Figure 5.4.

The experiment is only capable of measuring the average fluid flow rate from the outlet of the pump and cannot measure the instantaneous fluid flow experienced by each bed. Therefore, it is assumed that the fluid flow is equally divided between two regenerator beds at all times (Zimm, 2006). The flow is assumed to increase from 0 to the full flow rate during the first 25% of the flow process and remain constant at this value until it returns to zero over the last 25% of the flow process; the variation in the flow during the ramped sections is represented with a cubic

spline. In order to make the mass flow through the regenerator over an entire cycle agree with the flow measured at the outlet of the pump, the amplitude of the mass flow rate is modified according to

$$\dot{m}_f = \dot{m}_0 \frac{\dot{m}_{pump}\left(t_f - t_i\right)}{\int_{t_i}^{t_f} \dot{m}_0 \, dt} \tag{5.1}$$

where $\dot{m}_{pump}$ is the mass flow rate measured at the outlet of the pump, $\dot{m}_0$ is the mass flow profile before it has been scaled, t_i is the time at the beginning of the flow period, and t_f is the time at the end of the fluid flow period. The specific valve geometry is not known and the test facility is not sufficiently instrumented to time resolve the fluid flow rate; therefore, this fluid flow distribution is a "best guess". The magnetic field and fluid mass flow rate that are initially used to model the system are shown in Figure 5.4.

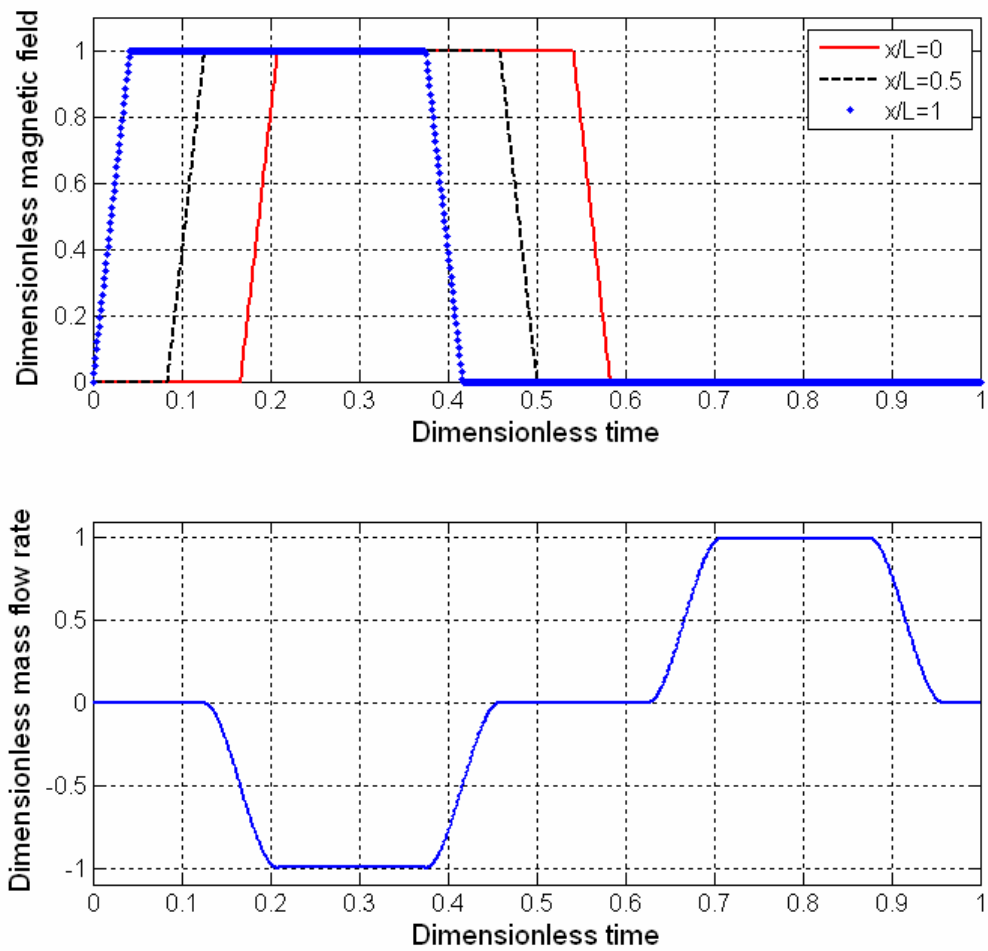

Figure 5.4. Form of the mass flow rate and magnetic field functions as a function of dimensionless time for a bed that is magnetized from the cold end (x=L) to the hot end. Positive mass flow is defined as flow from the hot reservoir to the cold reservoir.

As discussed in Section 5.1, the regenerator beds shown in Figure 5.2 are arranged back-to-back. This back-to-back arrangement implies that half of the regenerator beds will be magnetized from the hot end to the cold end (a type 2 bed) while the other half regenerators are magnetized from the cold end to the hot end (a type 1 bed). The magnetic field profile in Figure 5.4 is for a regenerator that is magnetized from the cold end (x=L) to the hot end (x=0). When the prototype

system is modeled, one of each type of regenerator bed is modeled separately and the results are averaged.

5.2.1 Thermal Capacity of the AMRR Housing

In Section 4.4, it was shown that the portion of the regenerator housing that participates in the experimental measurements can be of the same order of magnitude as the regenerator material. The properties of the regenerator housing of the rotary AMRR prototype were analyzed in order to determine whether their thermal capacity is likely to substantially affect the system performance. The regenerator housing is made of G-10 which has properties that are summarized in Table 5.3. G-10 properties were determined using CRYOCOMP.

Table 5.3. Properties of the AMRR regenerator housing

Parameter	Value
specific heat	857 J/kg-K
density	1950 kg/m3
thermal conductivity	0.77 W/m-K
thermal diffusivity	4.6×10^{-7} m2/s

The portion of the housing that participates in the heat transfer process is estimated by calculating the thermal penetration depth, as discussed in Section 4.4. For the cyclical AMRR data, the thermal penetration depth is:

$$d_{thermal} = \sqrt{4\alpha_{housing}\frac{\tau}{2}} \tag{5.2}$$

where the cycle time, τ, is divided by two because the regenerator housing is heated for half the cycle and cooled for the other half. The volume of the regenerator housing that participates can be calculated using the dimensions of the regenerator flow channel, the penetration depth, and

the cycle time. The ratio of the heat capacity of the portion of the housing that participates thermally in the process to the heat capacity of the Gd in the regenerator was calculated and the results are shown in Fig. 5.5 as a function of cycle time.

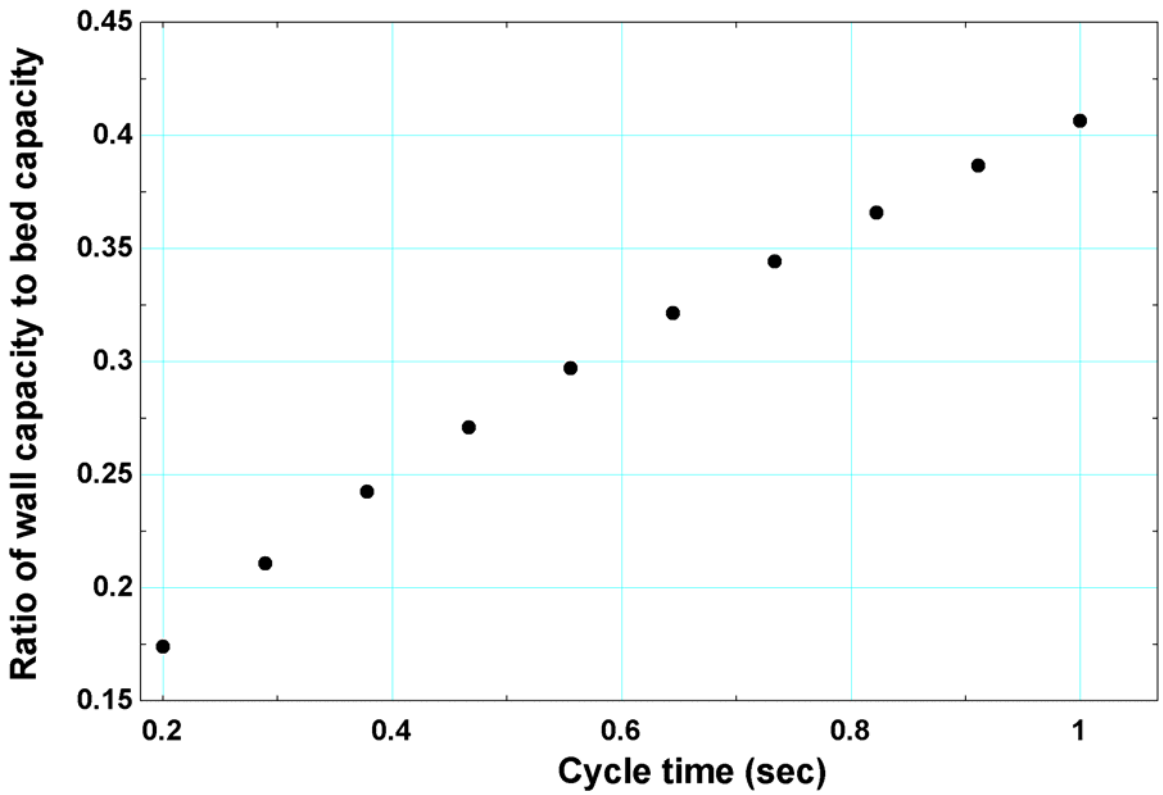

Figure 5.5. Ratio of the thermal capacity of the regenerator housing to the thermal capacity of the regenerator material as a function of cycle time

Figure 5.5 shows that the heat capacity of the regenerator housing can reach up to 40% for experimental data there were collected. As was the case with the case with the passive regenerator experiment, the thermal interaction with the regenerator housing in the prototype AMRR could affect the system performance. Because the temperature of the fluid oscillates,

there will be a frequency response of the regenerator wall. Assuming the regenerator wall acts as a first order system, the phase shift of the temperature profile in the wall is

$$\theta = \tan^{-1}\left(\omega R_{cond} C_{wall}\right) \tag{5.3}$$

where θ is the phase shift of the wall temperature compared to the fluid temperature, ω is the angular velocity of the regenerator wheel, R_{cond} is the thermal resistance associated with conduction through the wall, and C_{wall} is the heat capacity of the regenerator wall. The thermal conduction resistance is estimated as

$$R_{cond} = \frac{d_{thermal}}{k_{wall}\, A_{cond}} \tag{5.4}$$

where A_{cond} is the total area available for conduction to the regenerator wall and k_{wall} is the thermal conductivity of the regenerator wall. Examining the argument of the $\tan^{-1}$ function in Eq. (5.3) shows that the only quantities that vary in the experimental data are the angular velocity (the inverse of cycle time), the thermal penetration depth (proportional to the square root of the cycle time), and the capacity of the portion of the regenerator housing that participates thermally (proportional to the thermal penetration depth). Therefore the phase shift is proportional to

$$\theta \sim \tan^{-1}\left(\frac{d_{thermal}^2}{\tau}\right) \tag{5.5}$$

Since the thermal penetration depth scales according to the square root of the cycle time, Eq. (5.2), the phase shift is independent of cycle time. The phase shift was estimated here to be approximately 90°. If the phase shift were 0°, then the losses to the regenerator walls would be relatively small because the temperature of the wall would follow the fluid temperature. As the phase shift increases, the negative impact of the regenerator walls also increases because the heat transfer from the wall begins to coincide with the time that the fluid is being cooled and vice

versa. The estimated phase shift of 90° indicates that thermal interactions with the regenerator wall may be important.

5.3. PROTOTYPE EXPERIMENTAL RUNS

The data provided by Astronautics were collected in groups of experiments. For each group of experiments, one experimental parameter was varied while others were either measured or held constant. Table 5.4 summarizes the types of data sets that were collected by Astronautics. In Table 5.4, $\omega_{regenerator}$ is the rotation rate of the regenerator wheel, $\dot{V}_{pump}$ is the volumetric flow rate of fluid from the pump, $\dot{Q}_{heater}$ is the power supplied to the resistance heater in the cold reservoir, T_C is the cold reservoir temperature, and T_H is the hot reservoir temperature.

Table 5.4. Summary of experimental data sets

Data Set	Varied Parameter	Constant Parameter	Measured Quantity
I	$\dot{V}_{pump}$	$\dot{Q}_{heater}$, T_H, $\omega_{regenerator}$	T_C
II	$\dot{Q}_{heater}$	$\dot{V}_{pump}$, T_H, $\omega_{regenerator}$	T_C
III	$\omega_{regenerator}$	$\dot{V}_{pump}$, T_H, T_C	$\dot{Q}_{heater}$

The primary experimental measurements are the cold reservoir temperature and the cooling power of the prototype system. Generally, the other experimental parameters are varied in order to investigate their effect on either of these parameters. All of the data provided by Astronautics were acquired as part of one of the three data sets listed in Table 5.4. For data set III, the cold reservoir temperature is held approximately constant by adjusting the heater power to achieve a desired reservoir temperature. The hot reservoir temperature is regulated by a constant

temperature liquid bath. A complete list of all experimental results that are considered in this thesis is given in Appendix A3.

5.4. INITIAL MODEL PREDICTIONS COMPARED TO EXPERIMENTAL RESULTS

The numerical model was used to predict experimental results for the prototype AMRR using the inputs discussed in Section 5.2. The model was run for both a bed that is magnetized from the cold end to the hot end (type 1 bed) and a bed that is magnetized from the hot end to the cold end (type 2 bed). The profiles of the time variation of the magnetic field and fluid flow rate shown in Fig. 5.4 indicate that not all of the regenerator is magnetized during the cold-to-hot blow portion of the cycle. At the beginning of the period, the hot end of a type 1 bed and the cold end of a type 2 bed act as passive regenerators because they remain in the 0 magnetic field region. During the hot-to-cold blow period, the entire regenerator is demagnetized so a type 1 bed experiences the same process during this period of the cycle. The model predicts that a type 1 bed produces a slightly larger cooling power (1-6 W cooling or ~5-10%, depending on operating conditions) than a type 2 bed for almost every experimental condition that was studied.

Fluid flow and magnetization move from the cold end to the hot end for a type 1 bed, which may be a more effective heat rejection configuration resulting in a higher cooling power for a type 1 bed. The numerical model predicts that a regenerator bed with a spatially uniform magnetic field will produce approximately 1-4 W more cooling capacity (approximately 1-5% higher) than a type 1 bed with the sliding magnetic field profile shown in Fig. 5.4 depending on operating conditions. The model predicts that a spatially uniform magnetic field produces the highest

cooling power for the test conditions that were studied.

The experimentally determined hot and cold reservoir temperatures, fluid flow rates, and regenerator rotation rate were used to predict the cooling power produced by the prototype AMRR. A comparison of all experimentally measured cooling power and predicted cooling power is shown in Fig. 5.6 and the performance of a type 1 bed and a type 2 bed are shown in Fig 5.7.

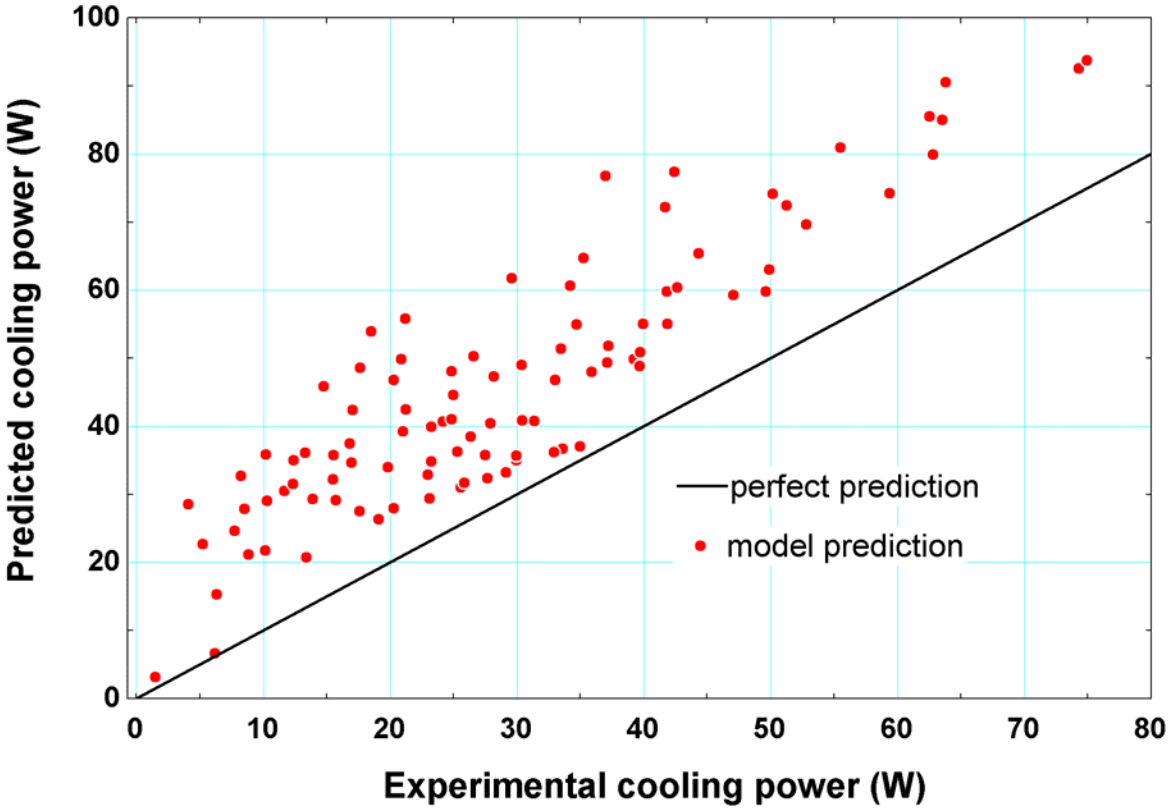

Figure 5.6. Predicted cooling power vs. experimental cooling power for a range of operating conditions. Also shown is a line indicating a perfect prediction

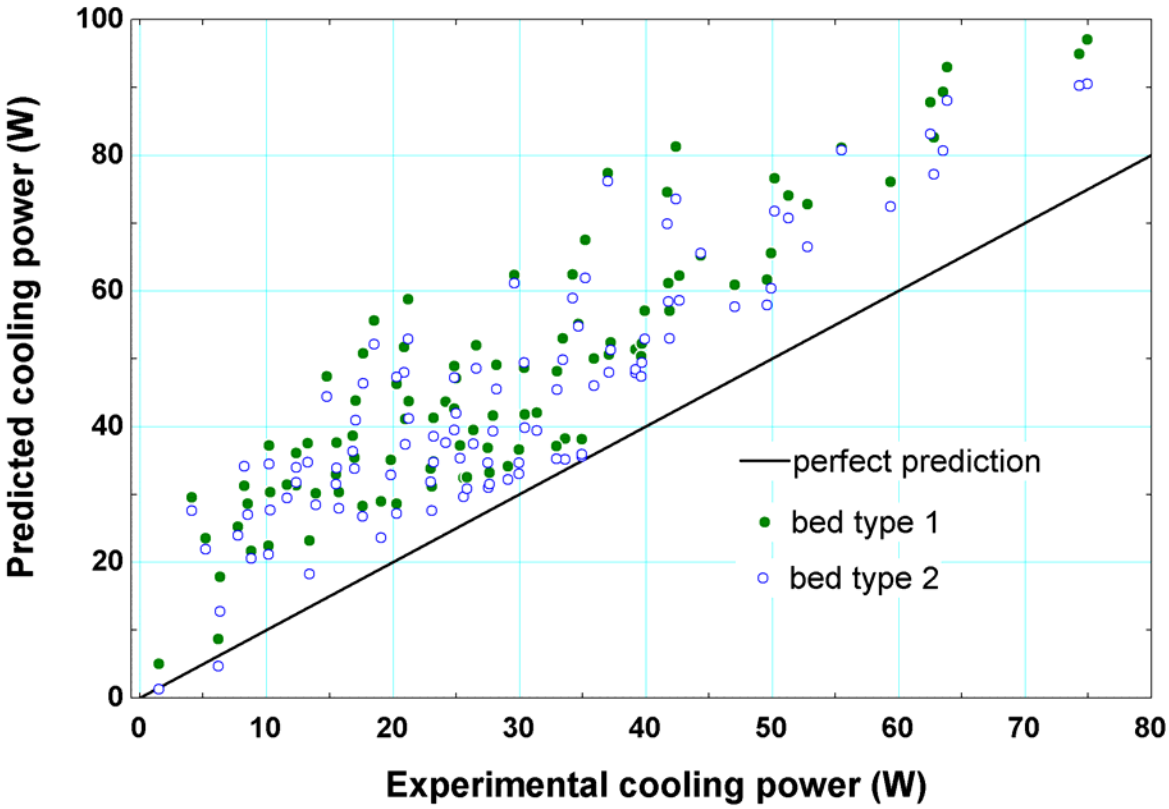

Figure 5.7. Predicted cooling power for a type 1 and type 2 bed vs. measured cooling power for a range of operating conditions

The experimental data and model predictions in Figures 5.6 and 5.7 represent a wide range of operating conditions and show that the initial modeling efforts predict that the device produces a higher cooling power than was measured experimentally for every operating condition. The predicted results show a strong correlation in predicted and measured cooling power with an offset. Thus, a small correction in modeling parameters may substantially improve the agreement between predicted and experimental results.

The experimental results and model predictions for the prototype AMRR operating with a regenerator rotation rate of approximately 120 rev/min and a hot reservoir temperature of

approximately 298 K are plotted in Fig. 5.8. For these data, the model over-predicts the cooling power, as indicated in Fig. 5.6, but is again able to capture general trends in the data.

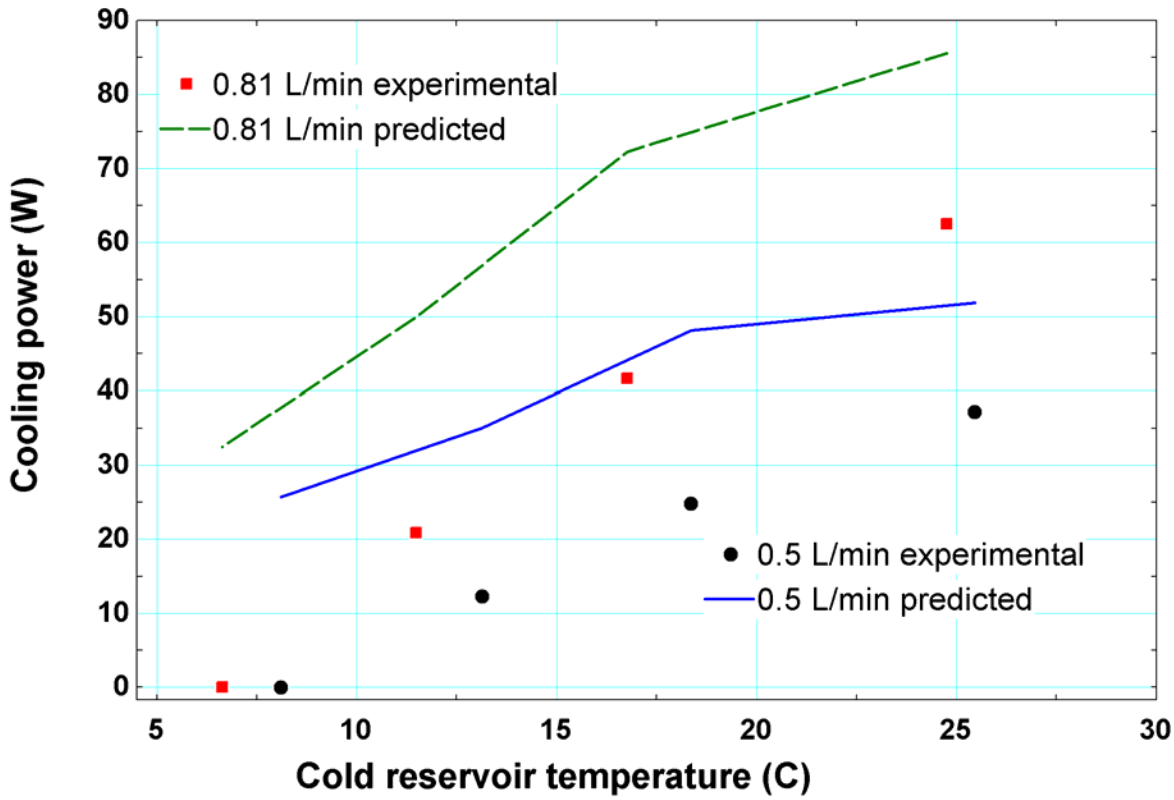

Figure 5.8. Experimental and predicted cooling power for a regenerator rotation rate of 120 rev/min, T_H = 298 K

5.5. IMPROVING MODEL AGREEMENT WITH EXPERIMENTAL RESULTS

The initial model predictions captured general trends in the experimental data. However, in order to use the numerical model for design it is necessary to attain better agreement between the predicted and experimental results and identify the reasons behind the discrepancy. Eight representative experiments were selected from the data set presented in Fig. 5.6 for closer

examination. These eight experiments were selected so that they represent the boundaries of the experimental operating conditions. The experiments were chosen such that each one contained a unique combination of high or low values of the cycle frequency, fluid flow rate, and operating temperature span. Table 5.5 summarizes the operating conditions that were considered for this study. Reducing the entire experimental set to eight operating conditions enables them to be studied in greater detail in a reasonable amount of time while still capturing the range of operating conditions that were studied in the larger data set.

Table 5.5. Summary of the representative data sets chosen to study the effects of modeling parameters on predicted values

Case	Temperature Span		Cycle Frequency		Fluid Flow Rate	
	low	high	low	high	low	high
1	x		x		x	
2	x		x			x
3	x			x	x	
4	x			x		x
5		x	x		x	
6		x	x			x
7		x		x	x	
8		x		x		x

The AMRR model was used to determine how sensitive the system at each operating condition is to the effect of the various loss mechanisms; this exercise was useful because it showed that the system at some conditions is not strongly affected by the many of the details of the model (e.g., the correlation chosen for the heat transfer coefficient, etc.) while the system at other conditions is extremely sensitive to these details. To determine the predicted loss in cooling capacity, a ‘normal’ system, a system with all losses considered (as in Section 5.4), and then a ‘lossless’ system is modeled. A lossless regenerator is approximated by setting the Biot number in the

regenerator to 0 (eliminating losses due to internal temperature gradients), setting the friction factor and axial conduction parameters to 0, and scaling the heat transfer by a factor of four. A factor of four was selected because increasing the heat transfer coefficient by more than a factor of four resulted in essentially no increase in predicted performance of the AMRR system. Subtracting the cooling power predicted for the regenerator with all losses turned on from the predicted cooling power for the lossless regenerator provides an estimate in the loss in cooling power due to all of the modeled regenerator losses. The loss in cooling power was calculated for the eight cases from Table 5.5 and the results are shown in Table 5.6.

Table 5.6. Loss of cooling power compared to a perfect regenerator due to regenerator losses for the representative experimental runs

Case	T_H	T_C	ΔT	Cycle Frequency	Fluid Flow Rate	Predicted Cooling Power	Cooling Power Loss
	K	K	K	Hz	Liter/min	W	W
1	293.8	293.9	0.2	1.0	0.34	35.7	0.4
2	298.6	298.9	0.3	1.0	0.67	53.2	0.3
3	292.6	293.4	0.8	4.0	0.35	35.4	0.2
4	298.3	298.4	0.2	4.0	0.81	67.8	0.7
5	285.3	298.4	13.1	1.0	0.35	24.6	2.4
6	287.4	298.9	11.5	1.0	0.67	44.1	7.4
7	281.6	293.4	11.8	4.0	0.34	22.4	1.3
8	281.3	298.7	17.4	4.0	0.67	39.1	6.5

The predicted cooling power column in Table 5.6 is the predicted cooling power including all loss mechanisms, or the cooling power from Fig. 5.6. Studying the first four cases in Table 5.6, experiments with approximately no temperature span, shows that the model predicts very little loss in cooling power as the temperature span approaches 0. The *COP* may be different for the 'lossless' regenerator, but the predicted cooling power is essentially unchanged as loss mechanism are turned off in the model. This result occurs because there are no axial conduction

or axial dispersion losses as the temperature span goes to 0. If viscous dissipation losses were significant, the cooling power would be higher for the lossless regenerator, but pumping power is relatively low in these experiments and viscous dissipation losses are nearly negligible. The loss of cooling due to decreased heat transfer is less intuitive. Provided that the fluid flow rate is sufficiently high, as long as the heat transfer coefficient between solid and fluid is non-zero it is possible to recover the maximum possible cooling power from the regenerator in the zero temperature span case. Because the hot and cold reservoirs are at the same temperature, it is impossible to overload the regenerator bed with fluid flow at 0 temperature span. Therefore, eventually all of the potential cooling from the material can be utilized, even if the heat transfer coefficient is low. To check if any of the cases studied in this section are near the threshold where heat transfer losses become important, the heat transfer coefficient was scaled by a factor of 0.5 relative to the normal regenerator. The results for cooling power loss of the eight cases are summarized in Table 5.7.

Table 5.7. Predicted cooling power for a normal system from Table 5.5 compared to the predicted cooling power for a regenerator with a Nusselt number scaling factor of 0.5

Case	ΔT	Cycle Frequency	Fluid Flow Rate	Predicted Cooling Power	Cooling Power 0.5xNu	Cooling Power Loss
	K	Hz	Liter/min	W	W	
1	0.2	1.0	0.34	35.7	34.9513	1.0%
2	0.3	1.0	0.67	53.2	53.15282	0.3%
3	0.8	4.0	0.35	35.4	34.96168	8.3%
4	0.2	4.0	0.81	67.8	67.82871	2.2%
5	13.1	1.0	0.35	24.6	24.57089	10.8%
6	11.5	1.0	0.67	44.1	44.0867	19.6%
7	11.8	4.0	0.34	22.4	22.37061	17.1%
8	17.4	4.0	0.67	39.1	39.07387	25.4%

Table 5.7 shows that loss of cooling power for conditions when the Nusselt number of the normal system is multiplied by a factor of 0.5 is higher for the cases with higher temperature spans, as expected. It also shows that the loss of cooling power is small for cases 1, 2 and 4; however, it is relatively high, 8%, when the cycle frequency is high and the fluid flow rate is low. In case 3, the regenerator utilization is low and therefore heat transfer loss could be a significant loss mechanism for that experiment if the actual heat transfer in the bed is less than that predicted by the model.

Because losses in cooling power approach zero as the temperature span goes to zero, any discrepancy between the measured and predicted cooling power for these cases is not related to the details of how the model predicts the various loss mechanisms. Rather, assuming that all of the input parameters discussed in Section 5.2 are correct, the discrepancy can be attributed to details related to the potential cooling power of the bed itself. Demagnetization losses, discrepancies in magnetocaloric material properties, or inaccuracies in other boundary conditions can account for the discrepancy between the model and experiment at zero temperature span. According to Rowe and Tura (2007), demagnetization losses are an observed reduction in effective magnetic field inside magnetically permeable body due its shape. Demagnetization losses are more significant for magnetic fields below 2 Tesla than they are for high magnetic fields (Rowe and Tura, 2007). For an isolated sphere with a constant magnetic permeability in the presence of a constant magnetic field $\mu_0 H^0$, the effective magnetic field in the sphere according to Shkel and Klingenberg (2001) is

$$\mu_0 H_{eff} = \mu_0 H^0 \frac{3}{2 + \frac{\mu}{\mu_0}} \tag{5.6}$$

where $\mu_0 H_{eff}$ is the effective magnetic field in the sphere, $\mu_0 H^0$ is the magnetic field in the magnet gap, μ is the magnetic permeability of the sphere, and μ_0 is the permeability of free space. Ferromagnetic materials have a permeability that is highly dependent on the effective magnetic field and is significantly higher than the permeability of free space. Eq. (5.6) shows that for a material with a permeability that is twice that of free space, the effective magnetic field is 75% of the magnetic field in the magnet gap. Demagnetization losses could be a source of significant modeling error; the model assumes that the maximum magnetic field in the permanent magnet that is measured in the absence of a bed is then experienced by the bed as it moves through the magnet gap.

The discrepancy between the predicted and measured cooling power may also occur because the actual properties of the commercial grade gadolinium used in the prototype are different than the properties assumed by the model. Because the gadolinium used in the prototype is commercial grade and not high purity, the actual properties may be different than the commercial grade Gd that was measured in order to determine the properties that are used in the model. Measurements show that the change in entropy for commercial grade Gd is approximately 10% lower than high-purity Gd (Zimm et al. 2003 and Dan'kov et al. 1998). According to Wu and Lu (2006), the amount of impurities in commercial grade Gd as well was the type of impurities vary by origin of the material and can affect the material properties of Gd. Because of the uncertainty in the amount of impurities in the Gd used in the prototype AMRR's regenerator and the effect impurities can have on Gd material properties, there is uncertainty in Gd material properties used in this analysis.

The effect of either demagnetization loss or inferior magnetocaloric materials is a reduction in the fundamental magnetocaloric potential for refrigeration that is available in the bed. In some sense, a discrepancy in many of the input parameters (e.g., the bed volume) also would lead to a fundamental reduction in the refrigeration capacity. Rather than attempt to explicitly calculate the demagnetization losses or determine the actual material properties or somehow identify which input parameter is in error (any of these would require disassembly of the prototype and equipment beyond the scope or budget of the project), the combined effect of any of these effects can be accounted for by determining an effective maximum magnetic field that leads to good agreement between the predicted and experimental results for the zero temperature span cases (cases 1,2, and 4 in Table 5.6). The ratio of the effective maximum field to the measured magnetic field represents the observed degradation in the fundamental magnetocaloric potential of the bed relative to what is expected based on the bed geometry, material, and magnetic field. The effective magnetic field assumed by the model was varied in order to optimize agreement between the predicted and experimental cooling power for the experiments in Table 5.6 that operate with nearly zero temperature span and large regenerator utilization (cases 1, 2, and 4).

The cooling power produced by the AMRR prototype was predicted for a range of maximum magnetic field from 0.9 to 1.5 Tesla and the results are shown in Fig. 5.9. Figure 5.9 shows that the predicted cooling power decreases with decreasing maximum magnetic field, and eventually the predicted cooling power is less than the experimentally measured value. The effective maximum magnetic field that is used by the model was determined by minimizing the root mean squared error (*RMSE*) between the predicted and measured cooling power for the three

experimental cases that were considered (cases 1, 2, and 4). The *RMSE* is plotted against the maximum magnetic field used in the model in Figure 5.10.

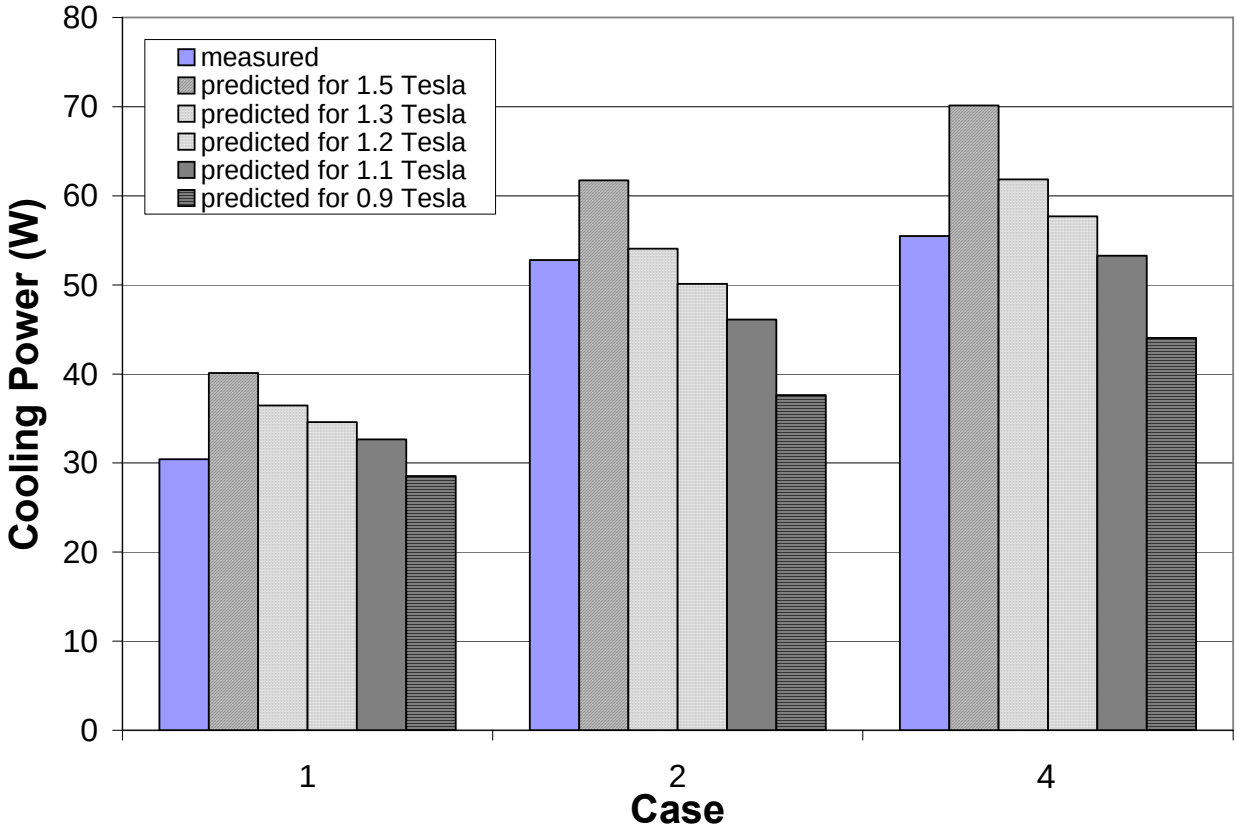

Figure 5.9. Predicted cooling power for cases 1, 2, and 4 when the maximum magnetic field is varied. Also shown are the experimental cooling powers for each case

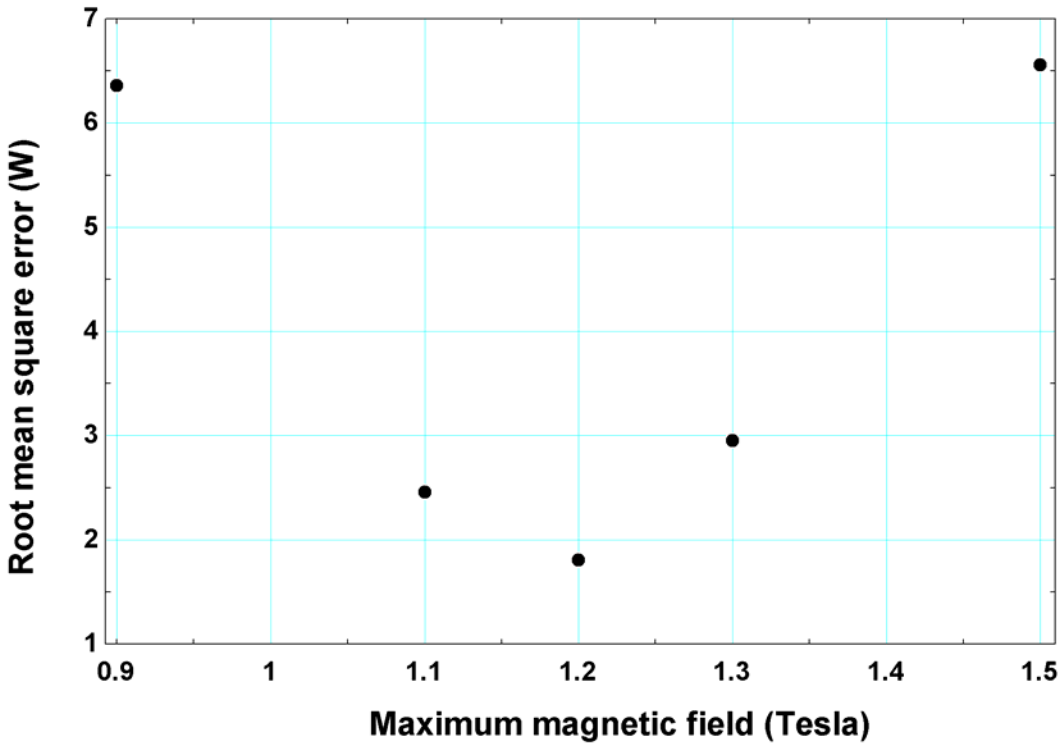

Figure 5.10. *RMSE* of the predicted cooling power for a range of maximum for varying maximum magnetic field used by the model

Based on the results shown in Fig. 5.9 and 5.10, a maximum magnetic field of 1.2 Tesla was chosen as having the best fit to the experimental data. The effective magnetic field is 20% lower than the magnetic field in the magnet gap. Rowe and Tura (2006) reported that the actual magnetic field in a regenerator bed they analyzed was approximately 12% less than the magnetic field in the magnet gap, which is in line with the results found in this analysis. The model was run for all experimental cases using a reduced magnetic field of 1.2 Tesla and the results are shown in Fig. 5.11. Reducing the maximum magnetic field used by the model from 1.5 to 1.2 Tesla (by 20%) reduces the predicted cooling power and improves the agreement between the

simulation and the experimental data over all of the cases. However, reducing the magnetic field alone does not yield excellent model agreement with experimental data.

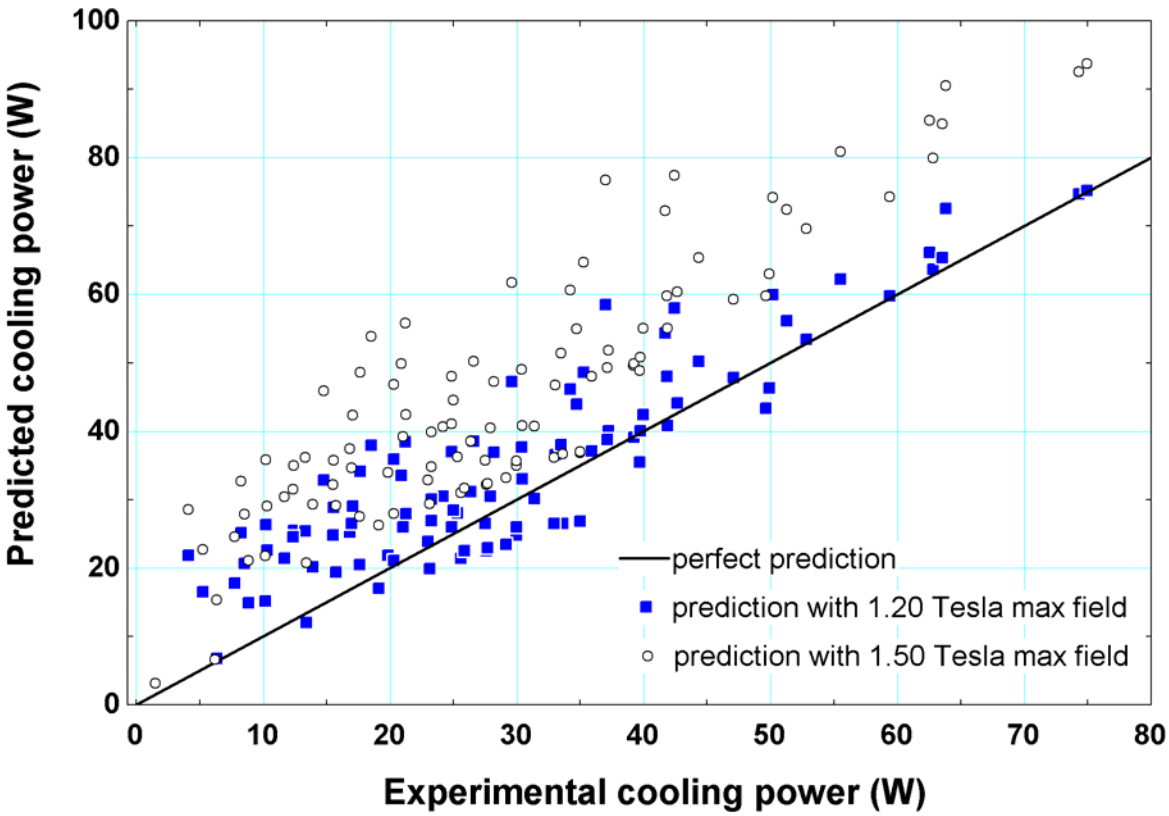

Figure 5.11. Predicted cooling power vs. experimental cooling power using a maximum effective magnetic field of 1.2 Tesla. Also shown is a line indicating a perfect prediction

As shown in Table 5.7, other loss mechanisms begin to affect the predicted cooling power as the temperature span increases and regenerator utilization decreases. Uncertainty in correlations used for other regenerator parameters such as heat transfer, static conduction, and axial dispersion also will affect the predicted cooling power for cases with larger temperature spans. For example, the Nusselt number correlation presented in Chapter 2 was developed using data

for gaseous heat transfer fluids and may not be appropriate for the mixture of water and ethylene glycol used in this experiment.

5.6. MODELING AND EXPERIMENTAL UNCERTAINTY

5.6.1 Experimental Uncertainty

It is difficult to estimate the actual experimental error because it is currently infeasible to run duplicate experiments at Astronautics' test facility. The heater power (the measured cooling capacity) is determined by measuring the voltage and current through a resistance heater and the associated uncertainty is very low. Several tests where the temperature span was near zero were duplicated and the difference in measured cooling power was within 2 W. Therefore, the experimental uncertainty is taken to be 2 W for the experimental data in this chapter.

5.6.2 Modeling Uncertainty

The experimental setup is only able to measure the fluid flow rate at the exit of the pump and is unable to measure the flow profile in each regenerator bed or the distribution of fluid flow between regenerator beds. Therefore, there is modeling uncertainty associated with the uncertainty in actual flow in each regenerator bed. The uncertainty is estimated by testing the model's sensitivity to several of the related inputs. First, the sensitivity to the flow ramp (shown in Fig 5.4) was investigated. The model assumes that the ramp in flow rate occurs over 25% of the total flow period. The model was also run with a 12.5% and 50% flow ramp for the experiments listed in Table 5.6 in order to determine the uncertainty in predicted cooling power

due to the uncertainty in the fluid flow profile (note that the peak mass flow rate was adjusted in order to achieve the same average mass flow rate). The cooling power predicted for several flow ramp periods for the eight cases that were modeled is shown in Table 5.8.

Table 5.8. Predicted cooling power for a system with a 12.5% flow compared to the predicted cooling power for a system with a 50% flow ramp

Case	ΔT	Cycle Frequency	Fluid Flow Rate	25% Ramp Cooling Power	12.5% Ramp Cooling Power	50% Ramp Cooling Power
	K	Hz	Liter/min	W	W	W
1	0.2	1	0.34	35.72	35.67	35.75
2	0.3	1	0.67	53.20	53.16	53.20
3	0.8	4	0.35	35.38	35.15	35.74
4	0.2	4	0.81	67.80	67.49	68.19
5	13.1	1	0.35	24.61	24.63	24.51
6	11.5	1	0.67	44.09	44.25	43.68
7	11.8	4	0.34	22.36	22.23	22.54
8	17.4	4	0.67	39.13	39.07	39.11

The predicted cooling power from Table 5.8 shows that the model is not highly sensitive to the length of the assumed flow ramp. The modeling uncertainty associated with the length of the fluid flow ramp is estimated to be approximately 1% of the predicted value.

The actual distribution of flow within the regenerator is not known. The amount of the total fluid through each regenerator could vary from regenerator to regenerator due to variations in the flow control valve, differences in internal plumbing, and difference in the packing of each regenerator. The effect of flow distribution on the predicted cooling power was determined by running the model with a flow rate that was reduced by 10% and a flow rate that is increased by 10% and averaging these two results (consistent with having a system in which 50% of the beds

experience a 10% reduced flow while the other 50% experience a 10% increased flow). The model predicts that the effect of a 10% difference in the fluid flow split between regenerator beds has almost no impact on the predicted cooling. Assuming that the flow rate is equal in the hot-to-cold and cold-to-hot directions, there is practically no change in predicted cooling power. It is also possible that the fluid flow in any single regenerator is not exactly the same during the hot-to-cold and cold-to-hot flow portions of the cycle (i.e., the individual beds may be slightly unbalanced). The effect of unbalanced flow was predicted by running the model with one regenerator bed experiencing a 5% higher flow rate in the positive flow direction than the negative direction while a second regenerator bed experiences a 5% higher flow rate in the negative flow direction and the positive direction. The predicted cooling powers for 5% unbalanced flow are shown in Table 5.9.

Table 5.9. Predicted cooling power for a system with a 5% flow unbalance and the predicted cooling power for a system with no flow unbalance

Case	ΔT	Cycle Frequency	Fluid Flow Rate	No Unbalance	5% Unbalance	Cooling Power Loss
	K	Hz	Liter/min	W	W	W
1	0.2	1	0.34	35.72	34.66	1.06
2	0.3	1	0.67	53.20	51.26	1.94
3	0.8	4	0.35	35.38	34.73	0.65
4	0.2	4	0.81	67.80	67.66	0.14
5	13.1	1	0.35	24.61	21.49	3.12
6	11.5	1	0.67	44.09	38.04	6.05
7	11.8	4	0.34	22.36	20.93	1.43
8	17.4	4	0.67	39.13	33.77	5.36

Table 5.9 shows that the effect of flow unbalance is complex. The cooling power loss is highly dependent on the operating temperature span and seems to be inversely proportional to the cycle frequency. Comparing the cooling power loss to the cooling power loss due to uncertainty in the

flow ramp shape from Table 5.8 shows that the possibility of flow unbalance in any single bed is the major source of modeling uncertainty that was identified here. Therefore, the total modeling uncertainty for data presented in this chapter is taken to be the uncertainty associated with a 5% flow unbalance. Because the effect of the flow unbalance is difficult to predict, the cooling loss for a 5% flow unbalance was calculated for each experimental case.

5.7. MODELING RESULTS USING THE NEW NUSSELT NUMBER CORRELATION

The model was used to analyze every experiment for which data was available using the reduced magnetic field determined in Section 5.5 and using the Nusselt number correlation for a liquid heat transfer fluid determined in Chapter 4. The inputs used to model the experiments are that same as those given in Table 5.2, except that a maximum magnetic field of 1.2 Tesla was used instead of 1.5 Tesla. The other modeling difference is that the Nusselt number correlation developed in Chapter 4 was used rather than the correlation suggested by Wakao and Kaguei. The results are shown in Fig. 5.12.

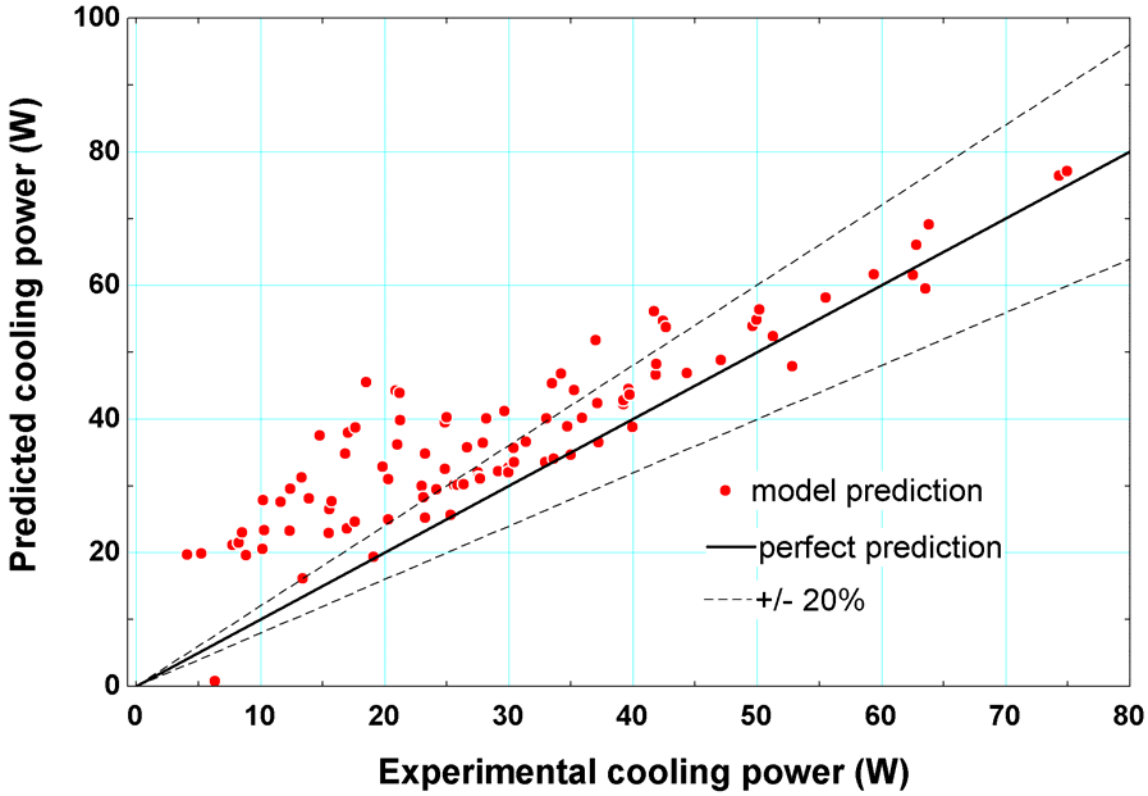

Figure 5.12. Predicted cooling power vs. experimental cooling power using the Nusselt number developed in Chapter 4 and a maximum effective magnetic field of 1.2 Tesla. Also shown is a line indicating a perfect prediction

The data from Fig. 5.12 are plotted with the modeling and experimental errors shown in Fig. 5.13. Only half of the data are shown in Fig. 5.12 to better show the uncertainty values.

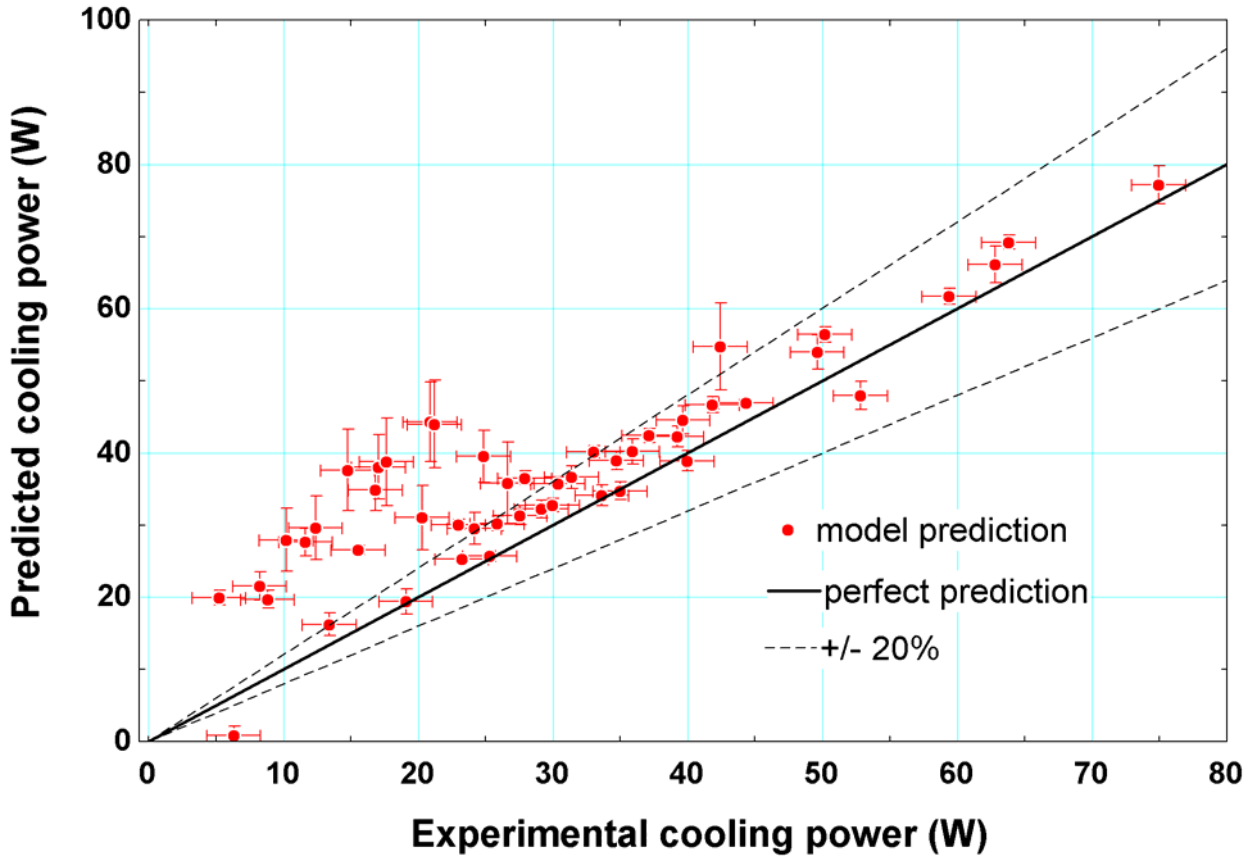

Figure 5.13. Modeling results from Fig. 5.12 with error bars shown.

It is interesting to note that a large portion of the experimental data that falls outside of the 20% error range have relatively large modeling uncertainty. The high uncertainty is caused by relatively high sensitivity of these data points to flow unbalance. To better understand the nature of the remaining modeling error, the difference between the predicted cooling power and measured cooling power is plotted as a function of temperature span in Fig. 5.14.

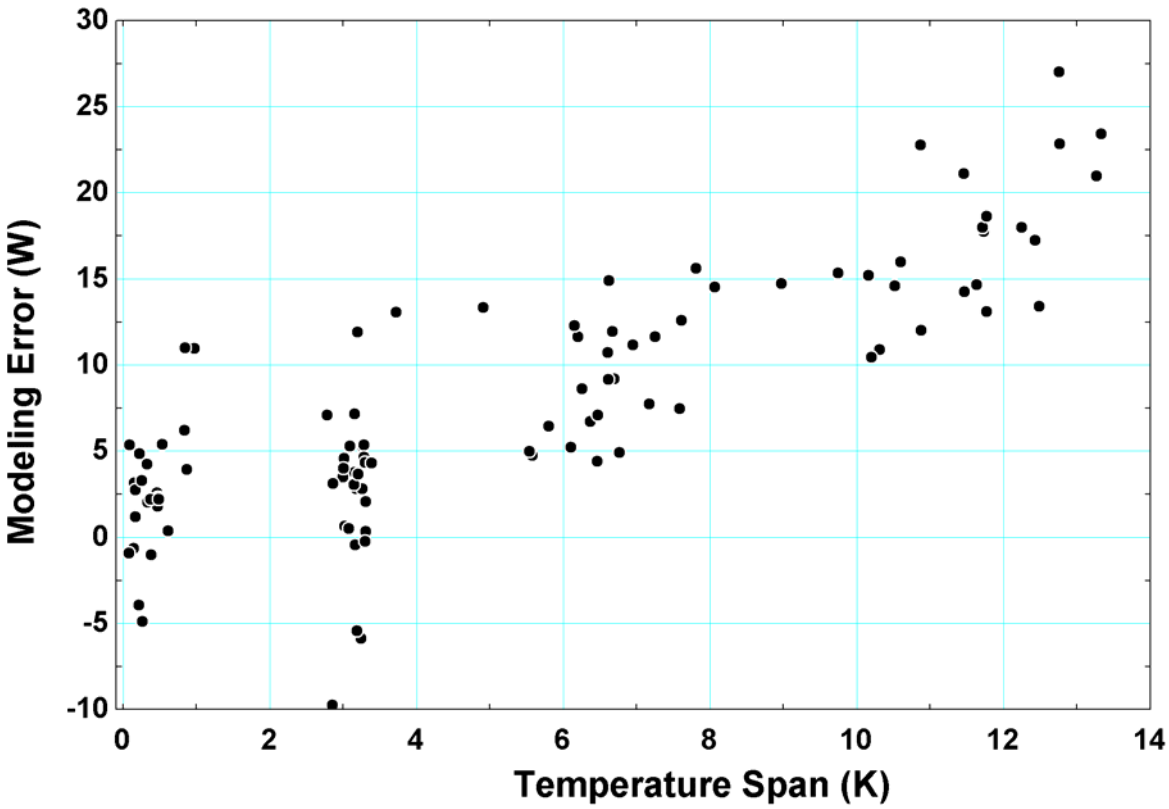

Figure 5.14. Difference between the predicted and measured cooling power as a function of operating temperature span

Figure 5.14 shows there is a correlation between modeling error and the operating temperature span. The temperature span dependence suggests there is a loss term that is being ignored or under-predicted by the model. The loss could be due to axial dispersion that is much higher than predicted by the correlation used by the model, flow unbalance in the regenerator, an axial conduction loss, or interactions with the regenerator housing that are ignored. Results in Table 5.9 suggest that a relatively low flow unbalance in the regenerator (5%) could cause significant losses in cooling power, but it is difficult to determine if flow unbalance is the cause of the modeling error with the current experimental device.

Although there is still modeling discrepancy between the predicted and measured cooling power for the rotary AMRR device, the model is able to predict the cooling power with acceptable accuracy. The model continues to be generally optimistic (predicting a cooling power higher than the measured cooling power), especially at higher temperature spans. Given the limited number of measured experimental parameters, it is difficult to achieve much better agreement between the model and experiment.

Chapter 6 Conclusions

This thesis describes a numerical model that can be used as a design tool for active magnetic regenerative refrigerator systems used for space cooling or refrigeration applications. The model was used in this thesis to analyze practical implementations of AMRR systems, a prototype AMRR device, and a passive regenerator experiment. The model has been demonstrated for transient system operation and cyclical steady state operation and has been coupled to a simple heat exchanger model. The model is flexible with regards to operating conditions, fluid flow magnetic field profiles, and regenerator geometry.

The model has been verified numerically, experimentally, and against a similar numerical AMRR model. The model was verified numerically against the Schumann solution, an analytic solution, for a passive regenerator and against steady state passive results presented by Dragutinovic and Baclic (1998). The model was verified experimentally against experimental rotary AMRR data that were provided by Astronautics. The model results were compared to results for a 2D AMRR model developed at Risø National Laboratories. The 1D model presented in this thesis produced similar results to the 2D AMRR model for practical regenerator dimensions, demonstrating that the 1D modeling assumption is justified for many practical AMRR systems. The numerical model was also shown to be flexible with regards to regenerator geometry; the model was verified experimentally against a Prototype AMRR using a packed sphere regenerator, and it was verified against the 2D numerical model for a parallel plate regenerator.

During the experimental verification phase of this thesis, it was determined that the actual magnetic field experienced by the regenerator material must be determined in order to accurately predict the system performance. The effective magnetic field experienced by the regenerator material of an AMRR system will be equal to or lower than the magnetic field in magnet gap, and the lower effective magnetic field was shown to significantly reduce the performance of the prototype AMRR system in Chapter 5. Therefore, it is important to consider how the shape of the regenerator will affect the effective magnetic field in regenerator when modeling the system. It is also important to consider the magnetic permeability of the regenerator material and how it may affect the effective magnetic field when choosing a regenerator material.

The heat transfer coefficient between the solid and fluid plays an important part in AMRR performance. Using the Nusselt developed in Chapter 4, the agreement between the predicted and measured cooling power improved compared to results using the correlation presented by Wakao and Kaguei (1982). The Nusselt number developed in this thesis is more appropriate for the AMRR system that was modeled in this thesis because it was developed for a liquid while the correlation presented by Wakao and Kaguei was developed primarily for gaseous heat transfer fluids.

In Chapter 4, it was determined that the interaction between the heat transfer fluid and the regenerator housing can affect the regenerator performance depending on the housing properties and operating conditions. Some work was done in Section 5.2.1 to determine the effect of the regenerator housing, but a detailed analysis was not performed. However, the regenerator

housing properties, such as thermal diffusivity and volumetric heat capacity, should be considered during the design of AMRR systems.

Although the flow unbalance could not be measured by the experimental apparatus, it was shown in Section 5.6.2 to have a significant effect on AMRR performance, especially when the operating temperature span is high. For high temperature span AMRR applications, it is important that the fluid flow through each regenerator bed be equal in both flow directions.

The model presented in this thesis has been shown to accurately predict the cooling power produced by a prototype AMRR device and has been used to analyze passive regenerator systems. The model has been designed to be a useful, publicly available design tool that can be used to design AMRR systems and to assess AMRR technology for cooling applications.

6.1. SUGGESTIONS FOR FUTURE WORK

Although the agreement between the model and experiment was improved by reducing the effective magnetic field and using a different Nusselt number correlation, there are still operating conditions where the model does not agree well with the experiment. In order to further improve agreement between predicted cooling power, especially at higher temperature spans, the following future work is suggested:

- Investigate a method to account for interaction with the regenerator housing in the 1D numerical model
- Research techniques to determine the actual magnetic field in the regenerator based on regenerator geometry and packing type
- Investigate the effects of edge effects and axial dispersion in a packed sphere regenerator
- Account for magnetic hysteresis of magnetocaloric materials in the 1D model

References

Ackermann, R. A., 1997, *Cryogenic Regenerative Heat Exchangers*, Plenum Press, New York.

Allab, F., A. Kedous-Lebouc, J. P. Yonnet, J. M. Fournier, 2006, A Magnetic Field Source System for Magnetic Refrigeration and Its Interaction with Magnetocaloric Material, *International Journal of Refrigeration* 29(8):1340-1347.

Braun, J. E., S. A. Klein, and J. W. Mitchell, 1989, Effectiveness Models for Cooling Towers, *ASHRAE Transactions* 95(2):164-174.

Brown, G. V., 1976, Magnetic Heat Pumping Near Room Temperature, *Journal of Applied Physics* 47:3673-3680.

Brueck, E., 2005, Developments in Magnetocaloric Refrigeration, *Journal of Physics D* 38:R381-R391.

Brueck, E., M. Ilyn, A. M. Tishin, and O. Tegus, 2005, Magnetocaloric Effects in $MnFeP_{1-x}As_x$-Based Compounds, *Journal of Magnetism and Magnetic Materials* 290-291:8-13.

Callister, W. D., 1997, *Material Science and Engineering an Introduction 4th Edition*, Wiley, New York, NY, Appendices.

Canepa, F., S. Cirafici, M. Napoletano, and F. Merlo, 2002, Magnetocaloric Properties of Gd_7Pd_3 and Related Intermetallic Compounds, *IEEE Transactions on Magnetics* 38(5):3249-3251.

Carslaw, H. S., and J. C. Jaeger, 1959, *Conduction of Heat in Solids*, 2nd Edition, Oxford University Press, New York, pp. 238, Chap. 9.

Clot, P., D. Viallet, F. Allab, A. Kedous-Lebouc, J. M. Fournier, and J. P. Yonnet, 2003, A Magnet-Based Device for Active Magnetic Regenerative Refrigeration, *IEEE Transactions on Magnetics* 39(5):3349-3351.

Dagula, W., O. Tegus, B. Fuquan, L. Zhang, P. Z. Si, M. Zhang, W. S. Zhang, E. Brueck, F. R. de Boer, and K. H. Buschow, 2005, Magnetic-Entropy Change in $Mn_{1.1}Fe_{0.9}P_{1-x}Ge_x$ Compounds, *IEEE Transactions of Magnetics* 41(10):2778-2780.

Dai, W., B. G. Shen, D. X. Li, and Z. X. Gao, New Magnetic Refrigeration Materials for Temperature from 165 K to 235 K, *Journal of Alloys and Compounds* 311(1):22-25.

Dan'kov, S. Y., A. M. Tishin, V. K. Pecharsky, and K. A. Gschneidner, 1998, Magnetic Phase Transitions and the Magnetothermal Properties of Gadolinium, *Physical Review B* 57(6):3478-3490.

DeGregoria, A. J., J. A. Barclay, P. J. Claybaker, S. R. Jaeger, S. F. Kral, R. A. Pax, J. R. Rowe, and C. B. Zimm, 1990, Preliminary Design of a 100 W 1.8 K to 4.7 K Regenerative Magnetic Refrigerator, *Adv. Cryogenic Eng*. vol. 35:1125-1131.

DeGregoria A. J., L. J. Feuling, J. F. Laatsch, J. R. Rowe, J. R. Trueblood, and A. A. Wang, 1991a, Test results of an active magnetic regenerator, *Adv. Cryogenic Eng*., vol. 37:875-882.

DeGregoria, A. J., 1991b, Modeling the active magnetic regenerator, *Adv. Cryogenic Eng*. vol. 37:867-873.

Dinesen, A. R., Magnetocaloric and Magnetoresistive Properties of $La_{0.67}Ca_{0.33x}Sr_xMnO_3$, Ph.D. thesis, Risoe National Laboratory – Technical University of Denmark (2004).

Dinesen, A. R., L. Linderoth, S. Morup, 2005, Direct and Indirect Measurement of the Magnetocaloric Effect in $La_{0.67}Ca_{0.33-x}Sr_xMnO_{3\pm\delta}$, *Journal of Physics: Condensed Matter* 17:6257-6269.

Dragutinovic, G. D., and B. S. Baclic, 1998, *Operation of Counterflow Regenerators*, Computational Mechanics Inc., Billerica, MA.

Engelbrecht, K., 2005, *A Numerical Model of an Active Magnetic Regenerator Refrigeration System*, M.S. Thesis, University of Wisconsin Madison.

Engelbrecht, K. L., G. F. Nellis, and S. A. Klein, 2006a, The Effect of Internal Temperature Gradients on Regenerator Matrix Performance, *Journal of Heat Transfer* 12:1060-1069.

Engelbrecht, K. L., G. F. Nellis, and S. A. Klein, 2006b, Predicting the Performance of an Active Magnetic Regenerator Refrigerator Used for Space Cooling and Refrigeration, *HVAC&R Research* 12(4).

S. Ergun, 1952, Fluid Flow through Packed Column, *Chemical Engineering Progress*, 48(2):125-127.

Fujieda, S., A. Fujita, and K. Fukamichi, 2002, Large Magnetocaloric Effect in $La(Fe_xSi_{1-x})_{13}$ Itinerant-electron Metamagnetic Compounds, *Applied Physics Letters* 81(7):1276-1278

Fujieda, S., A. Fujita, and K. Fukamichi, 2004, Enhancements of Magnetocaloric Effects in $La(Fe_{0.90}Si_{0.10})_{13}$ and Its Hydride by Partial Substitution of Ce for La, *Materials Transactions* 45(11):3228-3231.

Fujieda, S., A. Fujita, and K. Fukamichi, 2006, Control of Large Magnetocaloric Effects in $La_{1-z}Pr_z(Fe_xSi_{1-x})_{13}H_y$ Magnetic Refrigerants Working around Room Temperature, *International Journal of Refrigeration* 29(8):1302-1306.

Fujieda, S., Y. Hasegawa, A. Fujita, and K. Fukamichi, 2004, Thermal Transport Properties of Magnetic Refrigerants $La(Fe_xSi_{1-x})_{13}$ and their hydrides, and $Gd_5Si_2Ge_2$ and MnAs, *Journal of Applied Physics* 95(5):2429-2431.

Fujita, A, S. Fujieda, Y. Hasegawa, and K. Fukamichi, 2003, Itinerant-electron Metamagnetic Transition and Large Magnetocaloric Effects in $La(Fe_xSi_{1-x})_{13}$, Compounds and Their Hydrides *Physical Review B* 67(104416):1-11.

Giauque, W. F. and D. P. MacDougall, 1933, Attainment of temperatures below 1º absolute by demagnetization of $Gd_2(SO_4)_3$ $8H_2O$, *Phys. Rev.* 43:7768.

Green, G., G. Patton, J. Stevens, and J. Humphrey, 1986, Reciprocating Magnetic Refrigerator, *Proceedings of the Fourth International Cryocoolers Conference*, Easton MD:65-77

Gschneidner, K. A. and V. K. Pecharsky, 2000, Influence of Magnetic Field on the Thermal Properties of Solids, *Material Science and Eng. A* 287(2):301-310.

Gschneidner, K. A., V. K. Pecharsky, and A. O. Tsokol, 2005, Recent Developments in Magnetocaloric Materials, *Rep. Prog. Phys.* 68:1479-1539.

Guggenheim, E. A., 1967, Thermodynamics, an Advanced Treatment for Chemists and Physicists, *North Holland, Amsterdam.*

Hadley, G.R., 1986, Thermal Conductivity of Packed Metal Powders, *International Journal of Heat and Mass Transfer* 29(6):909-919.

Hausen, H., 1983, *Heat Trasfer in Counterflow, Parallel-Flow and Cross-Flow*, McGraw-Hill Co., New York.

He, J., J. Chen, and C. Wu, 2003, The influence of heat-transfer laws on the performance of a magnetic Stirling refrigeration cycle, *Int. J. Ambient Energy* vol. 24(2):75-82.

Heggs, P. J. and D. Burns, 1988, Single-Blow Experimental Prediction of Heat Transfer Coefficients, Experimental Thermal and Fluid Science 1:243-251.

Hirano, N., S. Nagaya, M. Takahashi, T. Kuriyama, K. Ito, and S. Nomura, 2002, Development of Magnetic Refrigerator for Room Temperature Application, *Advances in Cryogenic Engineeering* 47:1027-1034.

Hooijkaas, H. W. G. and A. A. J. Benschop, 1999, Pulse Tube Development using Harmonic Simulations, *Proc. 10th Int. Cryocooler Conf*. R. G. Ross, Jr., ed., Kluwer Academic/Plenum Publishers, New York, NY, pp. 359-367.

Hu, J. C. and J. H. Xiao, 1995, New method for analysis of active magnetic regenerator in magnetic refrigeration at room temperature, *Cryogenics* vol. 35:101-104.

Incropera, F. P., and D. P. DeWitt, *Fundamentals of Heat and Mass Transfer*, John Wiley & Sons, New York (1996).

Jaluria, Y., and K. Torrance, 2002, *Computational Heat Transfer, 2nd Edition*, Taylor and Francis, New York.

Janda, D., A. J. DeGregoria, J. Johnson, and S. Kral, 1989, Design of an active magnetic regenerative hydrogen liquefier, *Adv. Cryogenic Eng*. vol. 37:891-898.

Jeffreson, C. P., 1972, Prediction of Breakthrough Curves in Packed Beds: I. Applicability of Single Parameter Models, *AIChE Journal,* 18:409-416.

Johnson, J. W. and C. B. Zimm, 1996, Performance modeling of a 4 K active magnetic regenerative refrigerator, *J. Appl. Phys*., vol. 79(5):2171-2175.

Kaviany, M., 1995, *Principles of Heat Transfer in Porous Media*, Springer, New York, NY, p. 33, 46-47, 130, 228-229.

Kays, W. M. and A. L. London, *Compact Heat Exchangers 3rd Edition*, Krieger Publishing Company, Malibar, Florida (1984).

Kim, H., and C. W. Bullard, 2001, Dynamic Characteristics of a R-410A Split Air-Conditioning System, *Int. J. Refrigeration* 24:652-659.

Kirol, L. D. and J. I. Mills, 1984, Numerical Analysis of Thermomagnetic Generators, *J. Appl. Phys*. vol. 56(3):824-828.

Kunii, D. and O Levenspiel, 1969, *Fluidization Engineering*, Wiley, New York, NY.

Lu, D. W., X. N. Xu, H. B Wu, and X. Jin, 2005, A Permanent Magnet Magneto-Refrigerator Study on Using Gd/Gd-Si-Ge/Gd-Si-Ge-Ga Alloys, *1st International Conference on Magnetic Refrigeration at Room Temperature* Montreux, Switzerland.

Macias-Machin, A., Oufer, L., and N. Wannenmacher, 1991, Heat Transfer between an Immersed Wire and a Liquid Fluidized Bed, *Powder Technology* 66:281-284.

Marconnet A., 2007, *Predicting Regenerator Performance with a Single-Blow Experiment*, M.S. Thesis, University of Wisconsin Madison.

Nickolay, M. and H. Martin, 2002, Improved Approximation for the Nusselt Number for Hydrodynamically Developed Laminar Flow Between Parallel Plates, Intl Journal of Heat and Mass Transfer 45:3263-3266.

Nikitin, S. A., A. A. Andreyenko, A. M. Tishin, A. M. Arkharov, and A. A. Zherdev, 1985, Magnetocaloric Effect in Rare-Earth Alloys Gd-Ho and Gd-Er, *Physics of Metals and Metallography* 59(2):104-108.

Okamura, T., K. Yamada, N. Hirano, S. Nagaya, 2006, Performance of a Room-Temperature Rotary Magnetic Refrigerator, *International Journal of Refrigeration* 29(8):1327-1331..

Okamura, T., R. Rachi, N. Hirano, S. Nagaya, 2007, Improvements of 100W Class Room Temperature Magnetic Refrigerator, *2nd International Conference on Magnetic Refrigeration at Room Temperature* Portoroz, Slovenia.

Pawlik, K., I Skorvanek, J. Kovac, P. Pawlik, J. Wyslocki, and O. I. Bodak, 2006, Phase Structure and Magnetocaloric Effect in Binary Pr-Fe Alloys, *Journal of Magnetism and Magnetic Materials* 304:e510-e512.

Pecharsky, A. O., Gschneidner, K. A. and V. K. Pecharsky, 2003, The Giant Magnetocaloric Effect of Optimally Prepared $Gd_5Si_2Ge_2$, *Journal of Applied Physics* 93(8):4722-4728.

Pecharsky, V. K. and K. A. Gschneidner, 1997, Giant Magnetocaloric Effect in $Gd_5(Si_2Ge_2)$, *Physical Review Letters* 78(23):4494-4497.

Pecharsky, V. K. and K. A. Gschneidner, 1997a, Tunable Magnetic Regenerator Alloys with a Giant Magnetocaloric Effect for Magnetic Refrigeration from ~20 to ~290 K), *App. Phys. Lett.* 70(24):3299-3301.

Pecharsky, V. K. and K. A. Gschneidner, Jr., 1997b, Effect of Alloying on the Giant Magnetocaloric Effect in $Gd_5(Si_2Ge_2)$, *Journal of Magnetism and Magnetic Materials,* 167:L179-184.

Petersen, T. F., 2007, Risoe National Laboratory, Roskilde, Denmark, personal communication.

Petersen, T. F., N. Pryds, A. Smith, J. Hattel, H. S., and H. J. H. Knudsen, 2007, Two Dimensional Mathematical Model of a Reciprocating Room-Temperature Active Magnetic Regenerator, Accepted by the Int. J. Refrig.

Rice, K., DOE/ORNL Heat Pump Design Model, Mark VI Version, http://www.ornl.gov/~wlj/hpdm/MarkVI.shtml

Rohsenow, W. M., J. P. Hartnett and Y. I. Cho, 1998, *Handbook of Heat Transfer*, McGraw-Hill, New York, NY.

Rowe, A. and A. Tura, 2007, Active Magnetic Regenerator Performance Enhancement Using Passive Magnetic Materials, *2nd International Conference on Magnetic Refrigeration at Room Temperature* Portoroz, Slovenia.

Rowe, A. and A. Tura, 2006, Experimental Studies of Near Room-Temperature Magnetic Refrigeration, *International Journal of Refrigeration* 29(8):1286-1293.

Rowe A., A. Tura, M. A. Richard, R. Chahine, and J. Barclay, 2004, An Overview of Operating Experience Using the AMR Test Apparatus, *Advances in Cryogenic Engineering* 49:1721-1728.

Russek, S. L. and C. B. Zimm, 2006, Potential for Cost-Effective Magnetocaloric Air-Conditioning Systems, *International Journal of Refrigeration* 29(8):1366-1373.

Shir, F., L. Yanik, L. H. Bennet, E. D. Torre, and R. D. Shull, 2003, Room temperature active regenerative magnetic refrigeration: Magnetic nanocomposites, *J. Appl. Phys*. vol. 93(10):8295-8297.

Shitzer, A. and M. Levy, 1983, Transient Behavior of a Rock-Bed Thermal Storage System Subjected to Variable Inlet Air Temperatures: Analysis and Experimentation, *Journal of Solar Engineering* 105:200-206.

Shkel, Y. M. and D. J. Klingenberg, 2001, Magnetorheology and Magnetostriction of Isolated Chains of Nonlinear Magnetizable Spheres, *Journal of Rheology* 45(2):351-368.

Shull, R. D., V. Provenzano, A. J. Shapiro, A. Fu, M. W. Lufaso, J. Karapetrova, G. Kletetschka, and V. Mikula, 2006, The Effects of Small Metal Additions (Co, Cu, Ga, Mn, Al, Bi, Sn) on the Magnetocalric Properties of the $Gd_5Si_2Ge_2$ Alloy, *Journal of Applied Physics* 99(08K908):1-3.

Smart, J. S., 1966, *Effective Field Theories of Magnetism*. Philadelphia: W. B. Saunders Co.

Strassle, T. and A Furrer, 2005, Replacing the Magnetic Field by Pressure – the Barocaloric Effect for Magnetic Refrigeration, *1st International Conference on Magnetic Refrigeration at Room Temperature* Montreux, Switzerland.

Tegus, O. E. Brueck, X. W. Li, L. Zhang, W. Dagula, F. R. de Boer, K. H. J. Buschow, Tuning of the Magnetoc-Caloric Effects in MnFe(P,As) by Substitution of Elements, *Journal of Magnetism and Magnetic Materials* 272-276:2389-2390.

Tishin, A. M., 2005, Physical Mechanisms of Large Magnetocaloric Effect, *1st International Conference on Magnetic Refrigeration at Room Temperature* Montreux, Switzerland.

Utaki, T., K. Kamiya, T. Nakagawa, T. A. Yamamoto, and T. Numazawa, 2007, Research on a Magnetic Refrigeration Cycle for Hydrogen Liquefaction, *Proc. 14th Int. Cryocooler Conf.*, S. D. Miller and R. G. Ross, Jr, ed. Kluwer Academic/Plenum Publishers, New York, NY, p. 645-653.

Valiev, E. Z., 2007, "Entropy and Magnetocaloric Effect in Ferromagnets and Antiferrormagnets," *The Physics of Metal and Metallography* 104(1):8-12.

Vasile, C. and C. Muller, 2006, Innovative Design of a Magnetocaloric System, *International Journal of Refrigeration* 29(8):1318-1326.

Wada, H., Ch. Funaba, T. Asano, M. Ilyn, and A. M. Tishin, 2005, Recent Progress of Magnetocaloric Effect of $MnAs_{1-x}Sb_x$, *1st International Conference on Magnetic Refrigeration at Room Temperature* Montreux, Switzerland.

Wada, H. and Y. Tanabe, 2001, Giant Magnetocaloric Effect of $MnAs_{1-x}Sb_x$, *Applied Physics Letters* 79(20):3302-3304.

Wakao, N. and S. Kaguei, 1982, *Heat and Mass Transfer in Packed Beds*, Gordon and Breach Science Publishers, New York, NY, chapter 8.

Wu, W. 2003. Room Temperature Magnetic Refrigerator using a 1.4 T Permanent Magnet Field *Source Abstract K7.004, American Physical Society Conference* Austin, TX.

Wu, W. and D. W. Lu, 2005, Study on Gd-Si-Ge Alloys Using Chinese Gd, *1st International Conference on Magnetic Refrigeration at Room Temperature* Montreux, Switzerland.

Yan, Z. and J. Chen, 1991, The characteristics of polytropic magnetic refrigeration cycles, *J. Appl. Phys.* vol. 70(4):1911-1914.

Yan, Z. and J. Chen, 1992, The effect of field-dependent heat capacity on the characteristics of the ferromagnetic Ericsson refrigeration cycle, *J. Appl. Phys*. vol. 72(1):1-5.

Yan, A., K. H. Mueller, L. Schultz, and O. Gutfleisch, 2006, Magnetic Entropy Change in Melt-spun MnFePGe, *Journal of Applied Physics* 99(08K903):1-3.

Yu, B. F., Q. Gao, C. F. Wang, B. Zhang, D. X. Yang, and Y. Zhang, 2006, Experimental Investigation on Refrigeration Performance of a Reciprocating Active Magnetic Regenerator of Room Temperature Magnetic Refrigeration, *International Journal of Refrigeration* 29(8):1274-1285..

Yu, B. F., Q. Gao, B. Zhang, X. Z. Meng, and Z. Chen, 2003, Review on Research of Room Temperature Magnetic Refrigeration, *International Journal of Refrigeration* 26:622-636.

Zhang, L., S. A. Sherif, T. N. Veziroglu, and J. W. Sheffield, 1993, Second law analysis of active magnetic regenerative hydrogen liquefiers, *Cryogenics* vol. 33(7):667-674.

Zhang, L., S. A. Sherif, A. J. DeGregoria, C. B. Zimm, and T. N. Veziroglu, 2000, Design optimization of a 0.1 ton/day active magnetic regenerative hydrogen liquefier, *Cryogenics* vol. 40:269-278.

Zhang, Z. Y., Y. Long, R. C. Ye, Y. Q. Chang, and W. Wu, 2005, Corrosion Resistance of Magnetic Refrigerant Gadolinium in Water, *1st International Conference on Magnetic Refrigeration at Room Temperature* Montreux, Switzerland.

Zhou, K. W., Y. H. Zhang, J. Q. Li, J. Q. Deng, and Q. M. Zhu, 2006, Magnetocaloric Effects in $(Gd_{1-x}Tb_x)Co_2$, *Solid State Communications* 137:275-277.

Zimm, C., A. Boeder, J. Chell, A. Sternberg, A. Fujita, S. Fujieda, and K. Fukamichi, 2006, Design and Performance of a Permanent Magnet Rotary Refrigerator, *International Journal of Refrigeration* 29(8):1302-1306..

Zimm, C., J. Auringer, A. Boeder, J. Chell, S. Russek, and A. Sternberg, 2007, Design and Initial Performance of Magnetic Refrigerator with a Rotating Permanent Magnet, *2nd International Conference on Magnetic Refrigeration at Room Temperature* Portoroz, Slovenia.

Zimm C. B., K. A. Gschneidner Jr, S. A. Nikitin, and A. M. Tishin, 2003, Personal communication with Astronautics Inc., Madison, WI and Ames Laboratory, Ames, IA.

Zimm C. B. 2006, Personal communication with Astronautics Inc., Madison, WI.

Appendix A1 Numerical Model

Regenerator Model

```
%% This is the main regenerator model developed at UW.  This function takes
%% inputs that define the system and forcing functions, such as mass flow
%% profile, and calculates the regenerator performance.  This model does
%% not account for heat exchangers.  The main outputs of the model are the
%% cyclical steady state temperatures of the fluid and solid over an entire
%% cycle and the heat rejection, cooling power, and pumping power of the
%% system.  This model is described in Progress Report #1.
%%
%% 3_2 changes the indexing slighttly so that the number of rows in the
%% temperature matrices as the time array.
%% 3_3 uses the heat transfer degradation factor from the Journal of Heat
%% Transfer paper and fixed bug in calculation of t_node
%% 3_4 the inputs to this function are modified to allow more flexibility
%% in the text input file.  The call to the magnetic field function has
%% been modified to be more flexible.
%% 3_5 accepts the mass flow rate and magnetic field as inputs to the
%% function.  These values are no longer calculated inside the function as
%% previous functions did.
%% 3_6 added additional outputs from the function, removed some unused
%% lines of code and other housekeeping.
%% 3_7 calls updated versions of pack_geom and bedcorrfunction.  The way
%% the regenerator material is specified has been corrected.
%% 3_8 changes the velocity arrary 'v' that is passed to the bedcorrfun.
%% Added function outputs.
%% 3_9 changes some of the model outputs.
%% 3_10 fixes a bug that caused the viscous dissipation to be calculated
%% incorrectly.  The problem was related to the calculation of dP.

function[Qpump,ref_cap,heat_rej,COP,Tr,Tf,t_conv]=AMRregen_3_10(L,Ac,tau,TC,TH
…,Nx,Nt,n_beds,tol,mdot_amp,dwell,cnk,cNu,cff,pacRAW,magpropfun,fluidfun,
…bedcorrfun,modelcheck,mdot,muoH,numlayer,mcm_inp,mcmfun);

%%Bed paramters

tic %start timer to determine clock time needed to achieve convergence
dby=0; %m, bypass flow pipe diameter

[dh,eps,as]=pack_geom(pacRAW,bedcorrfun);
n_motor=1; %electric motor efficiency
n_pump=1; %pump efficiency
imp=1; %1=run implicit to generate guess values, 0=don't run implicit

%%Conditions
% cnk=1; %axial conduction scaling factor
% cff=1; %friction factor scaling factor
```

```
% cNu=1; %Nusselt number scaling factor
layer=0; %0 not layered 1=layered

extrapnum=5; %number of cycles between extrapolations
extlin=9; %linear number of cycles to extrapolate
order=1; %polynomial fit order
wt=1;

dt=tau/Nt; %time step in s

%% Allocate the sparse matrices A and B.
N=2*Nx;
A=spalloc(N,N,8*N);
B=spalloc(N,1,N);
%%

i=1:Nx;
xf=L*(i'-1/2)/Nx; %fluid spatial grid
xr=xf; %regenerator spatial grid
j=0:Nt;
t=j'*tau/(Nt);
t_node=(j(1:Nt)'+0.5)/Nt*tau; %time grid at center of time step
dt=t(2)-t(1);
TCurie=292*ones(Nx,1);

if imp==0

    %% start model with a ramp temperature profile

    pacCOOKED=[pacRAW,as,eps,dh,cNu,cff,cnk,L];
    Tr(:,1)=TH-xr*(TH-TC)/L; %initial regenerator temp
    Tf(:,1)=TH-xf*(TH-TC)/L;  %initial fluid temp
else

    %% call implicit UW model to generate initial guess values and speed
    %% model convergence

    pacCOOKED=[pacRAW,as,eps,dh,cNu,cff,cnk,L]; %inputs to the bed correlation
function

[Trg,Tfg,tf,tr]=AMR_impguessT_6(magpropfun,fluidfun,bedcorrfun,pacCOOKED,L,tau
,Ac,Nx,mdot_amp,t_node,TH,TC,TCurie,n_beds,mdot,muoH);
    Tr(:,1)=Trg(:,1);
    Tf(:,1)=Tfg(:,1);
end

%% inputs for new mcmprops

magpropfun=@mcmprops;

%calculate energy difference between fluid at TH and TC.  These properties
%are also used to calculated heat flux at the hot and cold reservoirs.
[mufC,kfC,cfC,rhofC,hfC,sfC]=fluidfun(TC);
```

```
[mufH,kfH,cfH,rhofH,hfH,sfH]=fluidfun(TH);
deltaUf=hfH-hfC;

% initialize variables before beginning the main loop.  These variables are
% used to check for co
done=0;
j=0;
ref_load=[-500 -500];
Er=[0 0]; %this matrix stores the total energy in the fluid for this past two
cycles
Ef=[0 0];%this matrix stores the total energy in the solid material for this
past two cycles
Etot=[0 0];%this matrix stores the total energy in the fluid and solid for
this past two cycles
count=0;
count2=0;
iteration(1)=1;
deltaE=zeros(extrapnum,1);

while(done==0)
    j=j+1;
    time=t(j);
    [muf(:,j),kf(:,j),cf(:,j),rhof,hf(:,j),sf(:,j)]=fluidfun(Tf(:,j));
    v=-mdot/(Ac*rhof);
    Prf(:,j)=cf(:,j).*muf(:,j)./(kf(:,j)); %Prandtl number
    Ref(:,j)=4*abs(v(j))*rhof./(as*muf(:,j)); %Reynolds number based on
hydraulic diameter

[cmuoH(:,j),dsdmuoH(:,j),rhor,kr(:,j),sr(:,j),hr(:,j)]=magpropfun(xr,L,Tr(:,j)
,muoH(:,j),numlayer,mcm_inp,mcmfun);
    cf_av=mean(mean(cf)); %average fluid specific heat over the entire cycle
    muf_av=mean(mean(muf)); %average fluid viscosity over the entire cycle
    cmuoH_av=mean(mean(cmuoH)); %average solid specific heat over the entire
cycle


[Nuf(:,j),ff(:,j),kstat(:,j),kdisp(:,j)]=bedcorrfun(pacCOOKED,Ref(:,j),Prf(:,j
),kf(:,j), kr(:,j),v(j),muf(:,j),rhof,cf(:,j),tau);
    dP(:,j)=ff(:,j).*(v(j)).^2/(2*dh)*rhof*L/Nx; %Pressure drop in Pa, based
on hydraulic diameter
%    f*rhof*v^2/2*L/dh;
%
dP(:,j)=ff(:,j).*(Ref(:,j)).^2*2/dh^3.*(muf(:,j)/rhof).^2*rhof*L/Nx; %Pressure
drop in Pa, based on hydraulic diameter

    %% Fill the A and B matrices according to the system governing
    %% equations.  A and B are used to solve for the temperature of every
    %% node in the regenerator at each time step in the cycle.

    if(mdot(j)>=0)
        %hot-to-cold flow
        % fluid energy equations
        for i=2:Nx-1;
            h(i,j)=Nuf(i,j).*kf(i,j)/dh; %convection coefficient in node i,j
```

```
A(i,i)=eps*rhof*Ac*L/Nx*cf(i,j)/dt+h(i,j)*as*Ac*L/Nx+2*kdisp(i,j)*Ac*Nx/L;
…%energy balance for center node
            A(i,i-1)=-kdisp(i,j)*Ac*Nx/L-mdot(j)*cf(i,j)/2;
…%energy balance for left node
            A(i,i+1)=-kdisp(i,j)*Ac*Nx/L+mdot(j)*cf(i,j)/2;
…%energy balance for right node
            A(i,Nx+i)=-h(i,j)*as*Ac*L/Nx;
…%energy balance for regenerator

B(i)=Tf(i,j)*eps*rhof*Ac*L/Nx*cf(i,j)/dt+dP(i,j)*abs(mdot(j))/rhof;
…%right hand side of energy balance
        end
        i=1; %hot end
        h(i,j)=Nuf(i,j).*kf(i,j)/dh;

A(i,i)=eps*rhof*Ac*L/Nx*cf(i,j)/dt+cf(i,j)*mdot(j)/2+h(i,j)*as*Ac*L/Nx+1*kdisp
(i,j)*Ac*Nx/L;
        A(i,i+1)=-kdisp(i,j)*Ac*Nx/L+mdot(j)*cf(i,j)/2;
        A(i,Nx+i)=-h(i,j)*as*Ac*L/Nx;

B(i)=Tf(i,j)*eps*rhof*Ac*L/Nx*cf(i,j)/dt+dP(i,j)*abs(mdot(j))/rhof+TH*cf(i,j)*
mdot(j);
        i=Nx; %cold end
        h(i,j)=Nuf(i,j).*kf(i,j)/dh;

A(i,i)=eps*rhof*Ac*L/Nx*cf(i,j)/dt+cf(i,j)*mdot(j)+h(i,j)*as*Ac*L/Nx+1*kdisp(i
,j)*Ac*Nx/L;
        A(i,i-1)=-kdisp(i,j)*Ac*Nx/L-mdot(j)*cf(i,j);
        A(i,Nx+i)=-h(i,j)*as*Ac*L/Nx;
        B(i)=Tf(i,j)*eps*rhof*Ac*L/Nx*cf(i,j)/dt+dP(i,j)*abs(mdot(j))/rhof;

    else
        if(mdot(j)<0)
            %cold-to-hot flow
            % fluid energy equations
            for i=2:Nx-1;
                h(i,j)=Nuf(i,j).*kf(i,j)/dh; %convection coefficient in node
i,j

A(i,i)=eps*rhof*Ac*L/Nx*cf(i,j)/dt+h(i,j)*as*Ac*L/Nx+2*kdisp(i,j)*Ac*Nx/L;
…%energy balance for center node
                A(i,i-1)=-kdisp(i,j)*Ac*Nx/L-mdot(j)*cf(i,j)/2;
…%energy balance for right node
                A(i,i+1)=-kdisp(i,j)*Ac*Nx/L+mdot(j)*cf(i,j)/2;
…%energy balance for right node
                A(i,Nx+i)=-h(i,j)*as*Ac*L/Nx; %energy balance for regenerator

B(i)=Tf(i,j)*eps*rhof*Ac*L/Nx*cf(i,j)/dt+dP(i,j)*abs(mdot(j))/rhof;
…%right hand side of energy balance
            end
            i=1; %hot end
            h(i,j)=Nuf(i,j).*kf(i,j)/dh;
            A(i,i)=eps*rhof*Ac*L/Nx*cf(i,j)/dt-
cf(i,j)*mdot(j)+h(i,j)*as*Ac*L/Nx+1*kdisp(i,j)*Ac*Nx/L;
```

```
            A(i,i+1)=-kdisp(i,j)*Ac*Nx/L+mdot(j)*cf(i,j);
            A(i,Nx+i)=-h(i,j)*as*Ac*L/Nx;

B(i)=Tf(i,j)*eps*rhof*Ac*L/Nx*cf(i,j)/dt+dP(i,j)*abs(mdot(j))/rhof;
            i=Nx; %cold end
            h(i,j)=Nuf(i,j).*kf(i,j)/dh;
            A(i,i)=eps*rhof*Ac*L/Nx*cf(i,j)/dt-
cf(i,j)*mdot(j)/2+h(i,j)*as*Ac*L/Nx+1*kdisp(i,j)*Ac*Nx/L;
            A(i,i-1)=-kdisp(i,j)*Ac*Nx/L-mdot(j)*cf(i,j)/2;
            A(i,Nx+i)=-h(i,j)*as*Ac*L/Nx;

B(i)=Tf(i,j)*eps*rhof*Ac*L/Nx*cf(i,j)/dt+dP(i,j)*abs(mdot(j))/rhof-
TC*mdot(j)*cf(i,j);

        else
            %no flow

        end
    end
    for i=2:Nx-1
        % regenerator energy equations
        A(Nx+i,Nx+i)=Ac*L/Nx*(1-
eps)*rhor(i)*cmuoH(i,j)/dt+h(i,j)*as*Ac*L/Nx+2*kstat(i,j)*Ac*Nx/L; %energy
equation for center node
        A(Nx+i,Nx+i-1)=-kstat(i,j)*Ac*Nx/L; %energy equation for left node
        A(Nx+i,Nx+i+1)=-kstat(i,j)*Ac*Nx/L; %energy equation for right node
        A(Nx+i,i)=-h(i,j)*as*Ac*L/Nx; %energy equation for fluid
        B(Nx+i)=Ac*L/Nx*(1-eps)*rhor(i)*cmuoH(i,j)*Tr(i,j)/dt-Ac*L/Nx*(1-
eps)*rhor(i)*Tr(i,j)*dsdmuoH(i,j)*(muoH(i,j+1)-muoH(i,j))/dt; %right hand side
of energy equation
    end
    i=1; %hot end
    A(Nx+i,Nx+i)=Ac*L/Nx*(1-
eps)*rhor(i)*cmuoH(i,j)/dt+h(i,j)*as*Ac*L/Nx+kstat(i,j)*Ac*Nx/L;
    A(Nx+i,Nx+i+1)=-kstat(i,j)*Ac*Nx/L;
    A(Nx+i,i)=-h(i,j)*as*Ac*L/Nx;
    B(Nx+i)=Ac*L/Nx*(1-eps)*rhor(i)*cmuoH(i,j)*Tr(i,j)/dt-Ac*L/Nx*(1-
eps)*rhor(i)*Tr(i,j)*dsdmuoH(i,j)*(muoH(i,j+1)-muoH(i,j))/dt;
    i=Nx;
    A(Nx+i,Nx+i)=Ac*L/Nx*(1-
eps)*rhor(i)*cmuoH(i,j)/dt+h(i,j)*as*Ac*L/Nx+kstat(i,j)*Ac*Nx/L;
    A(Nx+i,Nx+i-1)=-kstat(i,j)*Ac*Nx/L;
    A(Nx+i,i)=-h(i,j)*as*Ac*L/Nx;
    B(Nx+i)=Ac*L/Nx*(1-eps)*rhor(i)*cmuoH(i,j)*Tr(i,j)/dt-Ac*L/Nx*(1-
eps)*rhor(i)*Tr(i,j)*dsdmuoH(i,j)*(muoH(i,j+1)-muoH(i,j))/dt;

    %%invert matrix A to calculate the temperature of the fluid and solid
    %%for the current time step then pull fluid and regenerator
    %%temperatures from the resulting X matrix.

    X=A\B; %the matrix X contains the fluid temp in rows 1 to Nx, and
regenerator temp in rows Nx + 1 to 2Nx

    %% extract the fluid and solid temps from the sparse matrix X using the
```

```
    %% matlab command 'full'

    i=1:Nx;
    Tf(:,j+1)=full(X(i));
    i=1:Nx;
    Tr(:,j+1)=full(X(Nx+i));

    if j==Nt %end of cycle, check for convergence
        %% calculate properties for Nt+1 time step
        j=Nt+1;
        [muf(:,j),kf(:,j),cf(:,j),rhof,hf(:,j),sf(:,j)]=fluidfun(Tf(:,j));
        Prf(:,j)=cf(:,j).*muf(:,j)./(kf(:,j)); %Prandtl number

[cmuoH(:,j),dsdmuoH(:,j),rhor,kr(:,j),sr(:,j),hr(:,j)]=magpropfun(xr,L,Tr(:,j)
,muoH(:,j),numlayer,mcm_inp,mcmfun);

        %calculate system performance for previous cycle
        TCedg=0.5*(1.5*Tf(Nx,1:Nt)-0.5*Tf(Nx-1,1:Nt))+0.5*(1.5*Tf(Nx,2:Nt+1)-
0.5*Tf(Nx-1,2:Nt+1)); %Fluid temperature at the hot edge of the bed.  This
temp is extrapolated from the last two nodes in the bed
        [mufCedg,kfCedg,cfCedg,rhof,hfCedg,sfCedg]=fluidfun(TCedg); %Use the
fluid temp at the cold end of the bed to determine fluid properties at the
cold end of the bed.
        hflux(Nx+1,1)=sum(mdot.*hfCedg')*tau/Nt; %net enthalpy flux at the
cold end of the bed
        ref_load=-hflux(Nx+1); %J
        THedg=0.5*(1.5*Tf(1,1:Nt)-0.5*Tf(2,1:Nt))+0.5*(1.5*Tf(1,2:Nt+1)-
0.5*Tf(2,2:Nt+1)); %Fluid temperature at the hot edge of the bed.  This temp
is extrapolated from the last two nodes in the bed
        [mufHedg,kfHedg,cfHedg,rhof,hfHedg,sfHedg]=fluidfun(THedg); %Use the
fluid temp at the cold end of the bed to determine fluid properties at the hot
end of the bed.
        heat_load=-sum(mdot.*hfHedg')*tau/Nt; %J
        %calculate pressure drop in the regenerator and pump work
        for j=1:Nt
            dWpump(:,j)=abs(mdot(j)/rhof*dP(:,j)); %W
            deltaP(j)=sum(dP(:,j));
        end
        Wpump=sum(sum(dWpump,1),2)*dt %pump work in J

        %calculate bypass flow from the regenerator and associated energy
        %losses
        dQby=pi*deltaP*dby^4/(128*muf_av*L);
        Qby=trapz(t(1:(Nt/2+1)),dQby(1:(Nt/2+1)));
        Vby=L*pi/4*dby^2; %bypass fluid volume in the regenerator
        qby=(Qby-Vby)*rhof*deltaUf; %heat loss due to bypass flow

        Ef=eps*rhof*hf*Ac*L/Nx; %fluid energy entrained in one bed of the
regenerator
        Er=(1-eps)*rhor(1)*hr*Ac*L/Nx; %regenerator energy for one bed
        dE_cycle=sum(abs(Er(:,Nt+1)-Er(:,1)))+sum(abs(Ef(:,Nt+1)-
Ef(:,1))) %absolute value of the change in energy over one cycle
        Wmag=dE_cycle-Wpump+heat_load-ref_load; %magnetic work during the
previous cycle
```

```
        Emax=max(sum(Ef,1)+sum(Er,1)); %maximum energy in the solid and fluid
during previous cycle
        Emin=min(sum(Ef,1)+sum(Er,1)); %minimum energy in the solid and fluid
during previous cycle
        err=abs(dE_cycle/(Emax-Emin)) %figure of merit for cyclical steady
state convergence
        count=count+1
        count2=count2+1;
        if count==1
            E0=Ef(Nt+1)+Er(Nt+1);
        end
        deltaE(count2)=dE_cycle/E0;
        if err<tol %system has reached steady state, exit while loop.
            %         if deltaU<tol
            done=1;
        else %steady state has not been achieved, continue to next cycle.
            j=0; A=0*A; B=0*B; %reset matrices A and B
            cycle=(1:1:extrapnum)';
            dE=mean(deltaE);
            Tr(:,1)=Tr(:,Nt+1); %initial regenerator temp for next cycle
            Tf(:,1)=Tf(:,Nt+1);  %initial fluid temp for next cycle
            Tr_log(:,count)=Tr(:,Nt+1);
            Tf_log(:,count)=Tf(:,Nt+1);
            Tr_log2(:,count2)=Tr(:,Nt+1);
            Tf_log2(:,count2)=Tf(:,Nt+1);
            if count2==extrapnum
              for i=1:Nx
                    P=polyfit(cycle,Tr_log2(i,:)',order);
                    Tlin=polyval(P,extlin);
                    Tr(i,1)=Tr_log2(i,extrapnum)+wt*(Tlin-
Tr_log2(i,extrapnum));
                    P=polyfit(cycle,Tf_log2(i,:)',order);
                    Tlin=polyval(P,extlin);
                    Tf(i,1)=Tf_log2(i,extrapnum)+wt*(Tlin-
Tf_log2(i,extrapnum));
                end
                Tr_log2=zeros(size(Tr_log2));
                Tf_log2=zeros(size(Tf_log2));
                count2=0;
                deltaE=zeros(extrapnum,1);
            end

        end
        %done=1
    end
    %     done=1
end

TCedg=0.5*(1.5*Tf(Nx,1:Nt)-0.5*Tf(Nx-1,1:Nt))+0.5*(1.5*Tf(Nx,2:Nt+1)-
0.5*Tf(Nx-1,2:Nt+1)); %Fluid temperature at the hot edge of the bed.  This
temp is extrapolated from the last two nodes in the bed
[mufCedg,kfCedg,cfCedg,rhof,hfCedg,sfCedg]=fluidfun(TCedg);
Tout_avg=trapz(t(1:Nt/2),TCedg(1:(Nt)/2)')/(t((Nt)/2)-t(1))%*pi/(2*mdot_amp)
eff=(TH-Tout_avg)/(TH-TC)
NTU=Nuf(1,1)*kf(1,1)*Ac*L*as/(dh*mdot_amp*cf(1,1));
```

```
% dwell=1/3;
% n_beds=6

U=mdot_amp*dwell*cf(1,1)*tau/(2*Ac*L*(1-eps)*rhor(1)*cmuoH(1,1));
Crat=Ac*L*(1-eps)*rhor(1)*cmuoH(1,1)/(mdot_amp*cf(1,1)*tau/2);
count=count
t_conv=toc %this determines how long the model took to converge

%%%Calculate dimensionless parameters
V=Ac*L;
cr_avg=mean(mean(cmuoH));
cf_avg=mean(mean(cf));
Cr=mean(rhor)*V*(1-eps)*cr_avg;
Cf=rhof*V*(eps)*cf_avg;
R=Cf/Cr;
lambda=tau/2*(1-dwell);
U=mdot_amp*cf_avg*lambda/(Cr+Cf);
mdot_max=max(mdot);
z=0;
for i=1:size(mdot)
    if mdot(i)==mdot_max
        z=z+1;
        Nu_flow(z)=Nuf(1,i);
    end
end
Nu_avg=mean(Nu_flow);
%NTU=Nu_avg*kf(1,19)*Ac*L*as/(dh*mdot_amp*cf_avg);

%% Calculate net enthalpy and entropy fluxes

for i=1:Nx
   hflux(i,1)=sum(mdot.*hf(i,1:Nt)')*tau/Nx;
   sflux(i,1)=sum(mdot.*sf(i,1:Nt)')*tau/Nx;
end
THedg=0.5*(1.5*Tf(1,1:Nt)-0.5*Tf(2,1:Nt))+0.5*(1.5*Tf(1,2:Nt+1)-
0.5*Tf(2,2:Nt+1)); %Fluid temperature at the hot edge of the bed.  This temp
is extrapolated from the last two nodes in the bed
[mufHedg,kfHedg,cfHedg,rhof,hfHedg,sfHedg]=fluidfun(THedg);
hflux(Nx+1,1)=sum(mdot.*hfCedg')*tau/Nt;

%Calculate system performance
ref_load=0; heat_load=0;
for i=1:Nt
    if mdot(i)>0
        ref_load=ref_load-mdot(i)*(hfCedg(i)-hfC)*dt; %refrigeration in J
supplied to the cold reservoir for one cycle by one bed
    end
    if mdot(i)<0
        heat_load=heat_load-mdot(i)*(hfHedg(i)-hfH)*dt; %heat transferred from
the hot reservoir in J to the surroundings for one cycle by one bed
    end
end
```

```
ref_cap=ref_load/tau*n_beds %refrigeration rate in W supplied to the cold
reservoir by the entire regenerator
heat_rej=heat_load*n_beds/tau %heat transfer rate from the hot reservoir in W
to the surroundings by the entire regenerator
Wmag=heat_load-ref_load-Wpump; %magnetic work in J
Wmotor=Wmag/n_motor % Work of the motor on J done by the electric motor for
each bed
Qpump=Wpump/(n_pump*tau)*n_beds; %rate of work applied to the pump in W for
all beds in the regenerator
COP=ref_load/(Wmotor+Wpump/n_pump) %coefficient of performance
COP_Carnot=(TC)/(TH-TC); %Carnot efficiency for a cycle operating between the
specified hot and cold reservoir temperatures

%% plot selected model results, if modelcheck is set to a value of 1.
if modelcheck==1
    resplot(t,xf,Tr,Tf,mdot,muoH,dwell,rhof)
end
```

Regenerator Correlations

```
%% This function calculates model parameters for several packing geometries
%% It accepts an input array named inputs and calculates the appropriate
%% hydraulic diameter, porosity and specific surface area.  The array
%% 'inputs' contains different information about the regenerator geometry
%% for each type of regenerator.  The order of variables in 'inputs' is
%%
%% For a packed sphere regenerator: 1. volumetric porosity
%%      2. dummy variable
%%      3. particle diameter
%%      4. dummy variable
%%
%% For parallel plate regenerators: 1. Dx, plate thickness in meters
%%      2. Px, plate spacing (from plate to plate, not flow channel length)
%%      in meters
%%      3. dummy variable
%%      4. dummy variable

function[dh,eps,as]=pack_geom(inputs,bedcorrfun);

geometry=func2str(bedcorrfun);

if (strcmp(geometry,'SphPart2')==1 | strcmp(geometry,'SphPart_SB_2par')==1 |
strcmp(geometry,'SphPart_SB_1par')==1)%spherical particle geometryt

    %% assign variable to elements in the inputs array

    eps=inputs(1);
    dp=inputs(3);

    %% calculate geometry-specific parameters

    dh=2/3*eps/(1-eps)*dp %m
    as=6*(1-eps)/dp %m^2/m^3
```

```
elseif(strcmp(geometry,'AlignRect')==1 |
strcmp(geometry,'AlignRect_ha')==1)%aligned rectangular plater regenerator

    %%parse the input variable

    Dx=inputs(1);
    Px=inputs(2);
    %processing...
    as=2/Px
    eps=1-Dx/Px;
    dh=4*eps/as

else
    error('geometry not yet coded or mismatch error with geometry and
inputs');
end

%% This function calculates the Nusselt number, friction factor, static
%% axial conduction that occurs simultaneously through the solid and fluid
%% regenerator matrix, and axial conduction due to axial dispersion in the
%% fluid for a regenerator construced of perfectly aligned parallel slots
%% where fluid flows.
%% many inputs for this function are contained in the array  named 'inputs'
%% The values from the array are assigned to individual variables and the
%% geometry-specific dimensionless numbers are calculated.  The processed
%% variables such as hydraulic diameter and porosity in the x direction are
%% generated by pack_geom.m.  See that function for more detail.  The first
%% four entries in the 'inputs' array are the unprocessed regenerator data
%% and they are not used by this function.  For AlignRect.m the array
%% 'inputs' has the following variables stored in the indices of the array:

%%  1       Dx, not used
%%  2       Px, not used
%%  3       dummy variable, not used
%%  4       dummy variable, not used
%%  5       as, not used
%%  6       eps, volumetric or overall porosity 0 < eps < 1
%%  7       dh, hydraulic diameter in meters
%%  8       cNu, Nusselt number scaling factor [dimensionless]
%%  9       cff, friction factor scaling factor [dimensionless]
%%  10     cnk, axial conduction and dispersion scaling factor
%%          [dimensionless].  This scaling factor applies to both the
%%          static conduction and axial dispersion.

function[Nu_corr,f,kstatic,kdisp]=AlignRect(inputs,Re,Pr,kf,kr,v,muf,rhof,cf,t
au);

eps=inputs(6); %volumetric porosity
cNu=inputs(8); %scaling factor for Nusselt number
cff=inputs(9); %scaling factor for friction factor
cnk=inputs(10); %scaling factor for axial conduction
[n m]=size(Re);
```

```
%% Calculate friction factor

f=cff*96./Re;

%% Calculate Nusselt number

Nu1=cNu*8.24*ones(size(Re));
Nu_corr=Nu1;


%%Calculate static conductivity and dispersion according to Aris (1956)

Ns=kr./kf;
kstatic=cnk*kf.*(Ns*(1-eps)+eps);
kdisp=cnk*kf.*(0.5*Pr.*Re).^2/210;

%% This function calculates the Nusselt number, friction factor, static
%% axial conduction that occurs simultaneously through the solid and fluid
%% regenerator matrix, and axial conduction due to axial dispersion in the
%% fluid for a regenerator constructed of equal diameter smooth spheres.
%% Many inputs for this function are contained in the array 'inputs'.  The
%% values from the array are assigned to individual variables and the
%% geometry-specific dimensionless numbers are calculated.
%% The inputs array can conain a variable number of inputs and therefore
%% can describe many different regenerator geometries.  The processed
%% variables such as hydraulic diameter and porosity in the x direction are
%% generated by pack_geom.m.  See that function for more detail.  The first
%% four entries in the 'inputs' array are the unprocessed regenerator data
%% and they are not used by this function.  For SphPart2.m the array
%% 'inputs' has the following variables stored in the indices of the array:

%%  1       dummy variable, not used
%%  2       dummy variable, not used
%%  3       dummy variable, not used
%%  4       dummy variable, not used
%%  5       dummy variable, not used
%%  6       eps, volumetric or overall porosity 0 < eps < 1
%%  7       dh, hydraulic diameter in meters
%%  8       cNu, Nusselt number scaling factor [dimensionless]
%%  9       cff, friction factor scaling factor [dimensionless]
%%  10     cnk, axial conduction and dispersion scaling factor
%%           [dimensionless].  This scaling factor applies to both the
%%           static conduction and axial dispersion.

function[Nu_corr,f,kstatic,kdisp]=SphPart2(inputs,Re,Pr,kf,kr,v,muf,rhof,cf,ta
u);

%% parse the inputs array to determine geometry-specific inputs

eps=inputs(6); %volumetric porosity
dh=inputs(7); %hydraulic diameter in meters
cNu=inputs(8); %Nusselt number scaling factor
cff=inputs(9); %friction factor scaling factor
```

```
cnk=inputs(10); %axial conduction and dispersion scaling factor

[Nx Nt]=size(Re); %determine the number of time steps and spartial steps in
the Reynolds number matrix

Re1=3*(1-eps)/2*Re; %Reynolds number based on particle diameter
dp=3/2*(1-eps)/eps*dh;

%% Calculate friction factor from Kaviany (1995)

for j=1:Nt
    f(:,j)=cff*(160./(eps*Re(:,j))+2.4/eps^2);
end

%%convert Nusselt correlation for Re1 and Nu1 to Re and Nu then correct the
%%Nusselt number correlation for internal temperature gradients

Nu1=cNu*(2+1.1*Re1.^(0.6).*Pr.^(1/3)); %from Wakao 1982, based on particle
diameter

% Calculate Biot number and the heat transfer degradation factor
Bi=(Nu1.*kf)./(2*kr);
%Bi=0;
Fo=kf*tau./(rhof*cf*(dp/2)^2);
chi=Fo.*exp(0.246196-0.84878*log(Fo)-0.05639*(log(Fo)).^2); %from J of Heat
Transfer paper
Nu1=Nu1./(1+chi.*Bi/5); %corrected heat transfer coefficient
Nu_corr=2/3*eps/(1-eps)*Nu1; %make definition of Nu consistent with hydraulic
diameter def

%%Calculate static conductivity according to Hadley (1986) and axial
%%dispersion from Kaviany (1995)

if eps<0.0827
    a0=10^(-4.898*eps);
elseif eps<0.298
    a0=10^(-.405-3.154*(eps-0.0827));
elseif eps<0.58
    a0=10^(-1.084-6.778*(eps-0.298));
end
f0=0.8+0.1*eps;
kstatic=cnk*kf.*((1-a0)*(eps*f0+kr./kf*(1-eps*f0))./(1-eps*(1-
f0)+kr./kf*eps*(1-f0))+a0*(2*(kr./kf).^2*(1-
eps)+(1+2*eps)*kr./kf)./((2+eps)*kr./kf+1-eps)); %W/m2-K, Hadley (1986) from
Kaviany
kdisp=cnk*.75*eps*kf.*Pr.*Re1; %W/m2-K, effective conduction in fluid due to
axial dispersion
```

Magnetocaloric Material Properties

```
%% This function calculates the properties of the magnetocaloric material
%% across the entire bed.  The bed may be composed of multiple layers and
```

```
%% each layer may occupy a different fraction of the length of the bed.
%% The range of nodes occupied by each layer is calculated and the
%% properties for each layer are then calculated by calling the appropriate
%% material property function.  numlayer is the number of layers in the bed
%% The array inputs is an array with dimension numlayer x 2.  The array
%% contains the following variables: TCurie and Lfrac.  TCurie is the first
%% column of inputs and Lfrac is the second column.  The order of the
%% layers in inputs goes from x=0 to x=L.  For example, the first layer
%% listed should occupy x=0 to x=Lfrac(1) in the regenerator.  The layers
%% must be put in order in the inputs array and mcmfunc cell array.
%% TCurie is a row vector that contains the Curie temperature of mcm material
%%  in each layer, TCurie must have numlayer elements in the array.  The
%%  units are K.
%% Lfrac is a row vector that contains the portion of the length of the
%%  regenerator bed occupied by each layer.  Lfrac must have numlayer
%%  elements in the array and they must add to zero.  Each element must be
%%  in the range 0-1.
%% mcmfunc is a cell array that contains the function handle for the
%%  material property function used to evaluate the properties of mcm in
%%  each layer.

function[cmuoH,dsdmuoH,rhor,kr,sr,hr]=mcmprops(x,L,Tr,muoH,numlayer,inputs,mcm
func);

%% parse the inputs array

TCurie=inputs(:,1);
Lfrac=inputs(:,2);
[Nx a]=size(x);

%% check inputs for errors

sumfrac=sum(Lfrac);
if sumfrac ~= 1
    fprintf('Fraction of Layers does not sum to 1')
end

if numlayer>Nx
    fprintf('Number of layers cannot be greater than number of spatial nodes')
end

[NT a]=size(TCurie);
[NL a]=size(Lfrac);
[Nmcm a]=size(mcmfunc);

if (NT ~= numlayer) || (NL ~= numlayer)
    fprintf('Number of elements in inputs does not equal number of layers\n')
end

%% if only one mcmfunction is given, the function assumes that every layer
%% is made of the same material

if Nmcm==1
```

```
    mcm=mcmfunc;
    for i=1:numlayer
        mcmfunc{i,1}=mcm{1};
    end
end

[Nmcm a]=size(mcmfunc);
if (numlayer ~= Nmcm)
    fprintf('Number of mcm functions does not equal number of layers\n')
end

%% calculate material properties for each layer, 1 - numlayer

xfrac=x/L; %dimensionless regenerator position
xlayer(1)=0; %x position of first layer boundary
j=0;
for i=1:numlayer
    j=j+1;
    numstart(i)=j; %node number of starting position of layer i
    xlayer(i+1)=xlayer(i)+Lfrac(i)*L; %x position of i+1 layer boundary
    while (x(j)<=xlayer(i+1)) & (j<Nx)
        j=j+1;
    end
    numfin(i)=j; %node number of ending position of layer i
    mcmfunction=mcmfunc{i}; %get mcm material function for node i
    Tri=Tr(numstart(i):numfin(i),:); %Tri is an array that contains the
regenerator temperatures that will be sent to the mcm property function
    muoHi=muoH(numstart(i):numfin(i),:); %muoHi is an array that contains the
magnetic field that will be sent to the mcm property function
    TCuriei=TCurie(i)*ones(numfin(i),1); %TCuriei is an array that contains
the local Curie temperature that will be sent to the mcm property function
    [cmuoH(numstart(i):numfin(i),:),dsdmuoH(numstart(i):numfin(i),:),rholayer,
klayer,sr(numstart(i):numfin(i),:),hr(numstart(i):numfin(i),:)]=mcmfunction(
Tri,TCuriei,muoHi);
    rhor(numstart(i):numfin(i))=rholayer;
    kr(numstart(i):numfin(i))=klayer;
end
kr=kr';
rhor=rhor';

%% This function calculates properties of gadolinium based on the mean
%% field theory.  The entropy as a function of temperature and magnetic
%% field was provided by Risoe National Lab.
% Ames labs.  The function interpolates entropy data for temperature and
%% magnetic field using a spline technique.  Material properties are
%% determined by numercially differentiating the entropy data.  Gd
%% has a Curie temp of approximately 293 K.
%% The temperature range for this function is 200-400 K and the magnetic
%% field range is 0-2 Tesla.  Because Gd is a pure substance, the Curie
%% temperature cannot be modified in this function.
%%
%% The function takes the following inputs:
%%      Tr      regenerator temperature in K with matrix dimensions Nx x Nt
%%      TCurie  Curie temperature of the regenerator in K with matrix
%%              dimension Nx x 1, this variable acts as a dummy in this
```

```
%%              function because Gd properties cannot be shifted by
%%              changing the composition
%%      muoH    magnetic field for each spatial and temporal step in Tesla.
%%              Matrix dimension is Nx x Nt

function[cmuoH,dsdmuoH,rhor,kr,sr,hr]=Gd_meanfield(Tr,TCurie,muoH);

load Gd_meanfield_entropy_small.mat; %load entropy data as a function of temp
and magnetic field

Tcur_ref=293;
delta=0.01; %Tesla
DELTA=0.01; %K

[n,mp]=size(Tr);

So=interp2(Barr,Tarr,entropy,muoH,Tr,'spline');
Sc1=interp2(Barr,Tarr,entropy,muoH,(Tr-DELTA),'spline');
Sc2=interp2(Barr,Tarr,entropy,muoH,(Tr+DELTA),'spline');
Sd=interp2(Barr,Tarr,entropy,(muoH+delta),Tr,'spline');

%numerically differentiate entropy data
cmuoH=Tr.*(Sc2-Sc1)/(2*DELTA); %J/kg-K
dsdmuoH=(Sd-So)/delta; %J/kg-K-Tesla
sr=So;

rhor=7900; %kg/m^3
kr=10.5; %W/m-K

%calculate enthalpy at beginning and end of cycle
hr=interp1(T_0,h_0,Tr,'pchip');
```

Calling Function for Regenerator Model

```
%%%
```

```
clear %clears the existing variable space before running the model

%Volume=.033; %L, total volume of the regenerator material
nbed=1; %number of beds in the regenerator
h=.02; %m, height of flow channel in regenerator
w=.02; %m, width of flow channel in regenerator
Ac=h*w; %m2, cross sectional area of the regenerator
L=.06; %m, length of each regenerator bed
bed_vol=Ac*L; %volume per bed
dr=1/3; %mass flow rate dwell ratio
unbal=0.0; %flow unbalance in regenerator
flow_ramp=0.1; %ramp period for fluid flow
muoH_max=1.499; %Tesla, maximum magnetic field generated by the magnetic
source
cnk=1; %axial conduction scaling factor
cff=1; %friction factor scaling factor
cNu=1; %Nusselt number scaling factor
TC=285; %K
TH=300; %K
tau=0.5; %sec, cycle duration
delay=15/360*tau; %sec, delay time in seconds from the beginning of the cycle
before the blow period begins
mdot_amp=.03; %kg/s,   mass flow rate amplitude
massflow_inp=[dr,delay,flow_ramp,unbal]; %inputs associated with the fluid
mass flow function

%inputs associated with the regenerator packing
pacRAW=[0.36, 0, .0005, 0]; %[eps, dummy, dp, dummy] for packed sphere
regenerator

%inputs associated with the magnetic field profile
maginp=[120,15,360/nbed,2,L];%[arc of magnet, arc of ramp, arc of each bed,
bed type, regenerator length]


%% Model parameters

Nx=30; %number of spatial steps
Nt=1000; %number of time steps
tol=.0002; %convergence tolerance

%% Define the user-defined functions called to determine properties

numlayer=1; %number of layers in the regenerator
mcm_inp=[294, 1]; %[Curie temp of layer, fraction of regerator occupied by
layer]
mcmfun={@GdScaledS15T15}; %property function used for each layer.  This array
must use the curly brackets {} to stay compatible with other matlab versions
fluidfun=@props_water; %the fluid is water
bedcorrfun=@SphPart2; %regenerator correlation function
muoHfun=@muoH_ramp2; %ramped field function
mcmpropfun=@Gdcom; %magnetocaloric material property function called by the
implicit function
```

```
massflowfun=@mdotsmoothunbal_delay; %fluid flow function

%%

modelcheck=0; %1=plot model results, 0=do not plot results



%% determine mass flow and magnetic field profiles

ii=1:Nx;
jj=0:Nt;
t_node=(jj(1:Nt)'+0.5)/Nt*tau; %time grid at center of time step
xr=L*(ii'-1/2)/Nx; %regenerator spatial grid
mdot=massflowfun(t_node,tau,mdot_amp,massflow_inp); %determines the mass flow
of fluid vs time
muoH=muoHfun(xr,t_node,tau,muoH_max,maginp); %determines magnetic field vs
time
muoH(:,Nt+2)=muoH(:,1); %fills beginning of next cycle muoH at end of muoH
array
muoH=muoH+.001; %offset magnetic field because the meanfield function has a
singularity at a field of 0


%% Call the AMR bed model

[Qpump,ref_cap,heat_rej,Tr,Tf,mdot,muoH]=AMRregen_3_8(L,Ac,tau,TC,TH,Nx,Nt,nbe
d,tol,mdot_amp,dr,cnk,cNu,cff,pacRAW,mcmpropfun,fluidfun,bedcorrfun,modelcheck
,mdot,muoH,numlayer,mcm_inp,mcmfun);

save modeloutput.mat

fprintf('\n Finsihed\n\n')
```

Mass Flow Function

```
%% This function generates a mass flow profile with two dwell periods and an
%% s-shaped transition to the maximum absolute mass flow rate.  This flow
%% can be unbalanced according to the unbalance input, which ranges from 0
%% to 1.  The mass flow in the positive direction begens at time = delay.
%%
%% The ramp in flow is smoothed by using a cubic function to go from 0
%% flow to a blow period.  This makes derivative of the mass flow rate
%% always continuous and makes the numerical model more stable.  Because
%% the ramped portions of the mass blow period reduce the total flow
%% through the bed during the blow period, the amplitude of the mass flow
%% rate is corrected to give the same total mass flow as an on/off flow.
%% The flow rate is never set to 0 because the implicit model
%% cannot handle a 0 mass flow rate and the same function is used by the
%% implicit and explicit models.
```

```
%%
%% The inputs to the function are as follows:
%%      time        time or temporal grid of one cycle of the system
%%      tau         time for one complete cycle (s)
%%      mdot_amp    maximum amplitude of the mass flow rate (kg/s)
%%      inputs      array that contains function specific flow
%%                  characteristics.  The array containts the folling
%%                  variables:
%%       dwell       dwell ratio in the range 0-1
%%       delay       delay time, in seconds, before first blow period
%%                   begins
%%       ramp        fraction of each blow period that is spent ramping up
%%                   or ramping down.  0 < ramp < 0.5
%%       unbal       unbalance fraction.  Fraction of flow in the negative
%%                   direction to flow in positive direction.
%%                   -1 < unbal < 1

function[mdot]=mdotsmoothunbal_delay(time,tau,mdot_amp,inputs);

%% parse inputs array

[Nt dummy]=size(time);
dwell=inputs(1); %[unitless]
delay=inputs(2); %s
ramp=inputs(3);
unbal=inputs(4)/2; %offset the flow in each direction by 0.5*unbalance

t1=delay;
t2=delay+tau/2*(1-dwell)*ramp;
t3=delay+tau/2*(1-dwell)-tau/2*(1-dwell)*ramp;
t4=delay+tau/2*(1-dwell);
t5=tau/2;

if (t5-t4)<tau/Nt
    t5=t5+tau/Nt;
end

[n,g]=size(time);
n=n-1;
if delay>(tau/2*dwell)
    fprintf('delay is too long\n')
end
begin=0;
fin=0;
mdot0=mdot_amp;
mdot_amp=mdot_amp*(1-unbal);
for j=0:n
    if(time(j+1,1)<t1)
        mdot(j+1,1)=.001*mdot_amp;
    elseif(time(j+1,1)<t2)
        mdot(j+1,1)=.001*mdot_amp-2*mdot_amp/(t2-t1)^3*(time(j+1)-
t1)^3+3*mdot_amp/(t2-t1)^2*(time(j+1)-t1)^2;
        if begin==0
            begin=j+1;
```

```
        end
    elseif(time(j+1,1)<t3)
        mdot(j+1,1)=mdot_amp;
    elseif(time(j+1,1)<t4)
        mdot(j+1,1)=.001*mdot_amp+2*mdot_amp/(t4-t3)^3*(time(j+1)-t3)^3-
3*mdot_amp/(t4-t3)^2*(time(j+1)-t3)^2+mdot_amp;
    elseif(time(j+1,1)<=t5)
        mdot(j+1,1)=.001*mdot_amp;
        if fin==0
            fin=j;
        end
    else
        time=time-t5;
        mdot_amp=-mdot0*(1+unbal);
        if(time(j+1,1)<t1)
            mdot(j+1,1)=.001*mdot_amp;
        elseif(time(j+1,1)<t2)
            mdot(j+1,1)=.001*mdot_amp-2*mdot_amp/(t2-t1)^3*(time(j+1)-
t1)^3+3*mdot_amp/(t2-t1)^2*(time(j+1)-t1)^2;
            if begin==0
                begin=j+1;
            end
        elseif(time(j+1,1)<t3)
            mdot(j+1,1)=mdot_amp;
        elseif(time(j+1,1)<t4)
            mdot(j+1,1)=.001*mdot_amp+2*mdot_amp/(t4-t3)^3*(time(j+1)-t3)^3-
3*mdot_amp/(t4-t3)^2*(time(j+1)-t3)^2+mdot_amp;
        elseif(time(j+1,1)<=t5)
            mdot(j+1,1)=.001*mdot_amp;

        end
    end
end

%% correct the amplitude of the mass flow rate to achieve the correct
%% average mass flow rate.

marea=trapz(time(begin:fin),mdot(begin:fin));
square=(time(fin)-time(begin))*mdot0*(1-unbal);
mdot=-square/marea*mdot;
```

Magnetic Field Profile Function

```
%This function calculates the magnetic field assuming a trapezoidal
%magnetization curve and that the magnetic field is uniform across the
%regenerator bed at any instant in time.  At the beginning of the cycle,
%the magnetic field starts at 0 Tesla and begins to ramp up.  The field
%ramps up, then levels off to the maximum field value, ramps down, and ends
%with a magnetic field of 0 Tesla.
%The inputs are described below
%x      spatial grid of the regenerator bed
%t      temporal grid of the cycle (time)
%tau    time take for one complete cycle
```

```
%muoH_max   maximum magnetic field
%muoH_inp   array that contains the following variables
%   1 arc_mag   arc occupied by the magnet (degrees)
%   2 arc_ramp  arc over which the magnetic field ramps to zero (degrees)
%
%The model calculates the magnetic field for the first spatial node in the
%bed and assigns that calculated value to all other nodes in the bed for
%each time step.  The length of the ramp length are assumed symmetric
%(equal ramp distance going from high to low as from low to high) and is
%variable.

function[muoH]=muoHfunction_ramp2(x,t,tau,muoH_max,muoH_inp);

[Nx,g]=size(x);
[Nt,g]=size(t);
arc_mag=muoH_inp(1);
arc_ramp=muoH_inp(2);

angle=t/tau*360; %convert time in cycle to an angle from 0-360
ang0=0; %beginning of ramp from low field to high field
ang1=arc_ramp+ang0; %beginning of flat high field section
ang2=arc_mag+ang1; %beginning of ramp from high field to low field
ang3=arc_ramp+ang2; %end of ramp from high field to low field

    for j=1:Nt
        if(angle(j)<ang1); %ramp up
            muoH(1,j)=muoH_max*(angle(j)-ang0)/arc_ramp;
        elseif(angle(j)>=ang1)&(angle(j)<=ang2); %high field
            muoH(1,j)=muoH_max;
        elseif(angle(j)>ang2)&(angle(j)<=ang3); %ramp down
            muoH(1,j)=muoH_max*(1-(angle(j)-ang2)/arc_ramp);
        else %zero field
            muoH(1,j)=0;
        end
        muoH(2:Nx,j)=muoH(1,j);
    end
```

Appendix A2 Single Blow Experiment Operating Instructions

The system schematic for the single blow test stand is shown in Figure A2.1. Each valve is numbered in Figure A2.1 for reference purposes. Valves 1, 3 and 4 are manual 3-way valves and Valve 2 is a solenoid valve. Bath 1 and Bath 2 are temperature controlled baths. BV 1 and BV 2 are bleeder valves used to purge air from the system. SV is a shutoff valve, and AF 1 and AF 2 are quick-connect air fittings. For the purpose of describing the state of each valve, each valve will be referred to as being in state 1 when the cold soak flow loop is used and position 2 when the main pump flows through the test section into the graduated cylinder. For example, when Valve 1, the on/off solenoid valve, is in the off position, it is in position 1. In Figure A2.1, Valve 1 is in Position 1 and Valve 4 is in Position 2. A photograph of the test stand is shown in Figure A2.2.

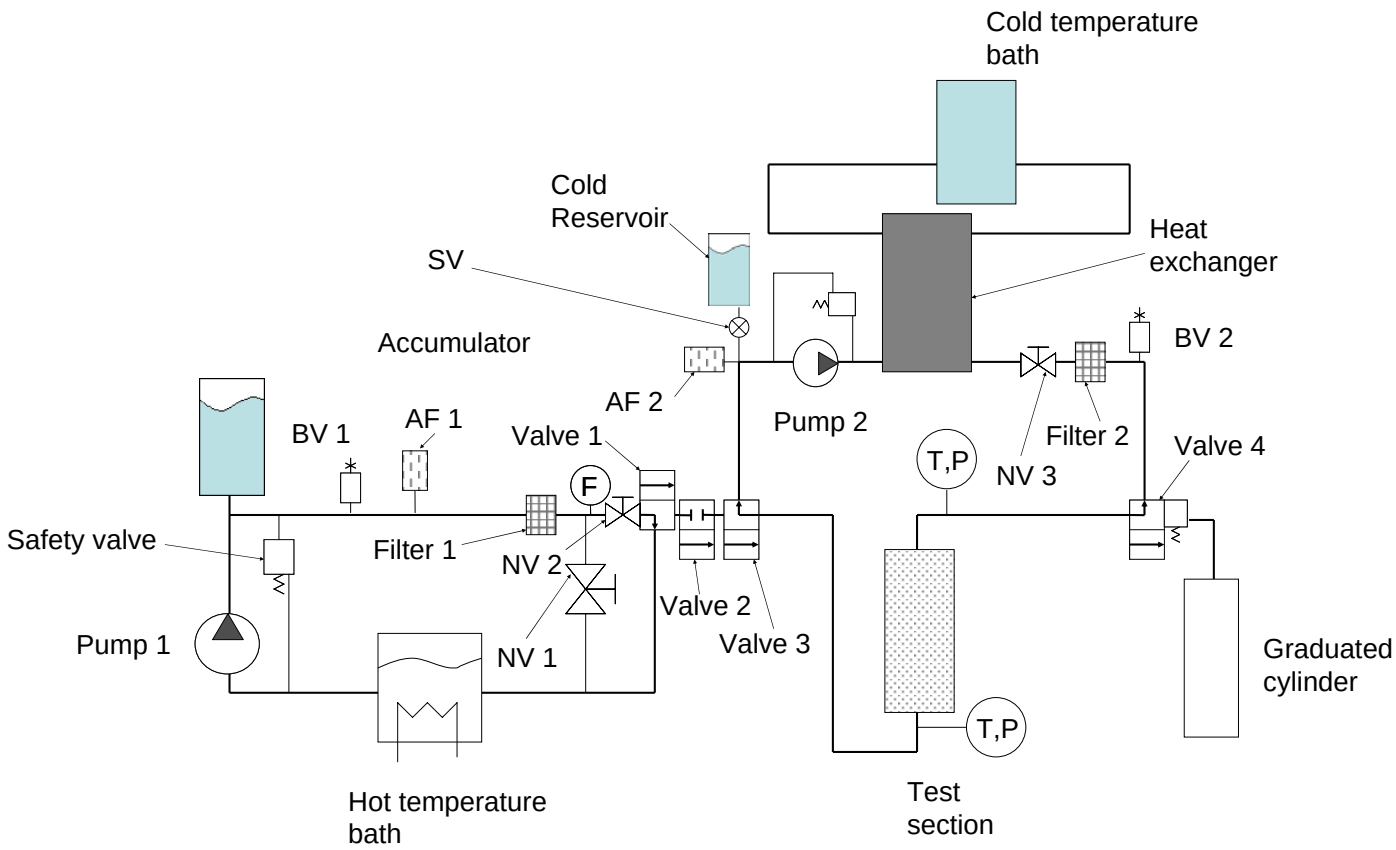

Figure A2.1. Schematic of the single blow test facility

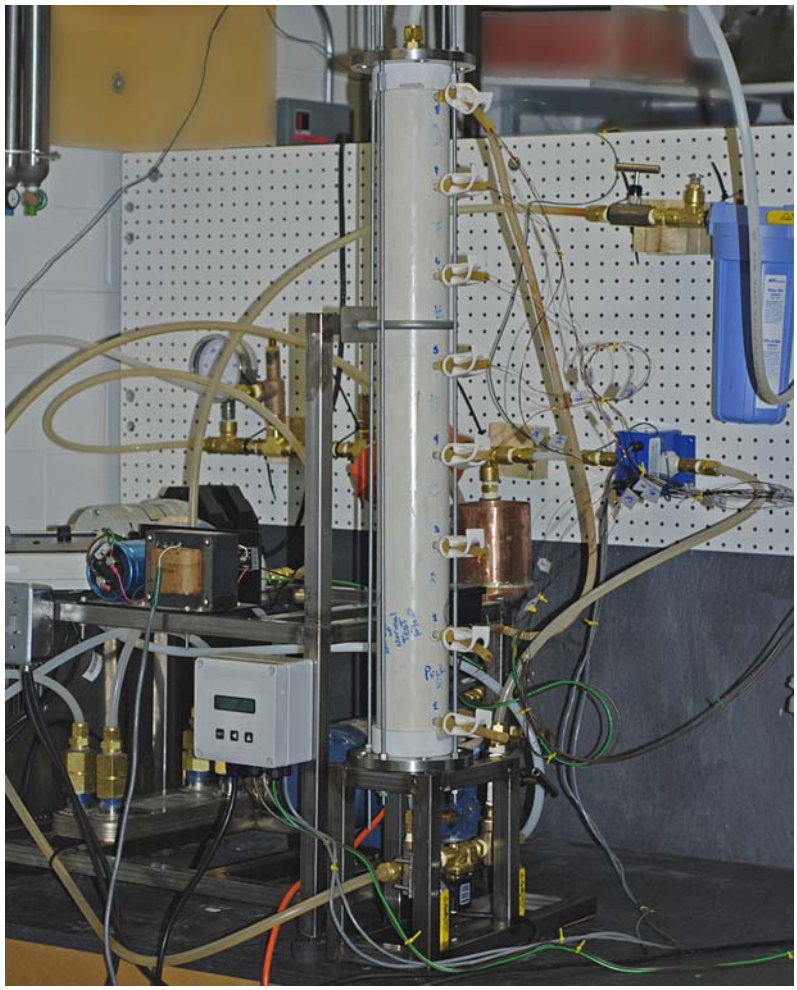

Figure A2.2. Single blow test facility

Below are operating procedures for the single blow test stand.

Filling the System

It is very important to system performance that the system have as few bubbles as possible. Bubbles tend to accumulate in the regenerator and can cause significant measurement error. It is acceptable if there are standing bubbles in the cold soak system that do not pass through the regenerator. However, any bubbles in the flow loop used to conduct an experiment must be purged.

The system should be as dry as possible before filling. Start with power to the pumps and controlled temperature baths off. The following steps should be taken to purge all air from the system during filling:

1. Begin with both pumps off and the valves in the following positions.

Valve Name	Position
Valve 1	2
Valve 2	1
Valve 3	1
Valve 4	1
NV 1	partially open
BV 1	closed
BV 2	open
SV	open

The valves should be positioned as shown in Figure A2.3. The flow schematic in this position is shown in Figure A2.1.

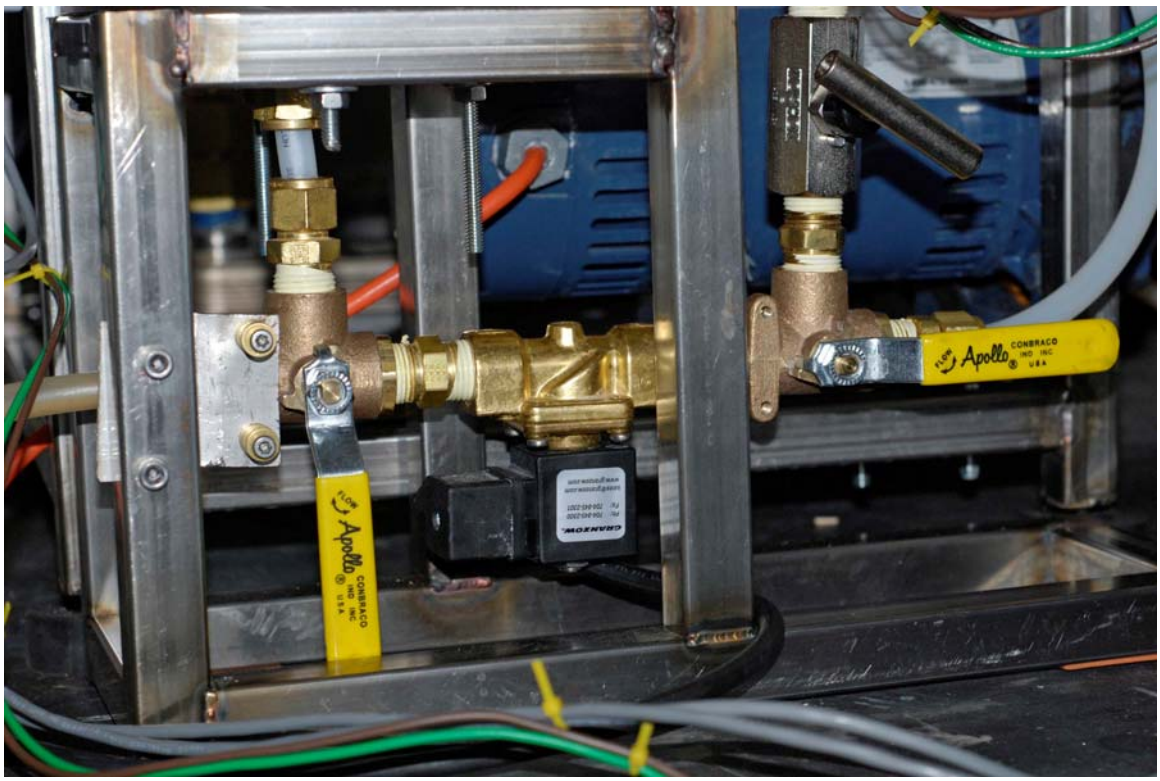

Figure A2.3. Photograph of 3-way valve positions during filling.

2. Fill Bath 1. Slowly fill the cold reservoir with the bleeder valve, BV 2, open. A photograph of BV 2 is shown in Figure A2.4. Ensure that the shut-off valve below the cold reservoir is open. Fill the cold reservoir then close BV 2. Pump 1 is self priming so no efforts to prime the pump are necessary.

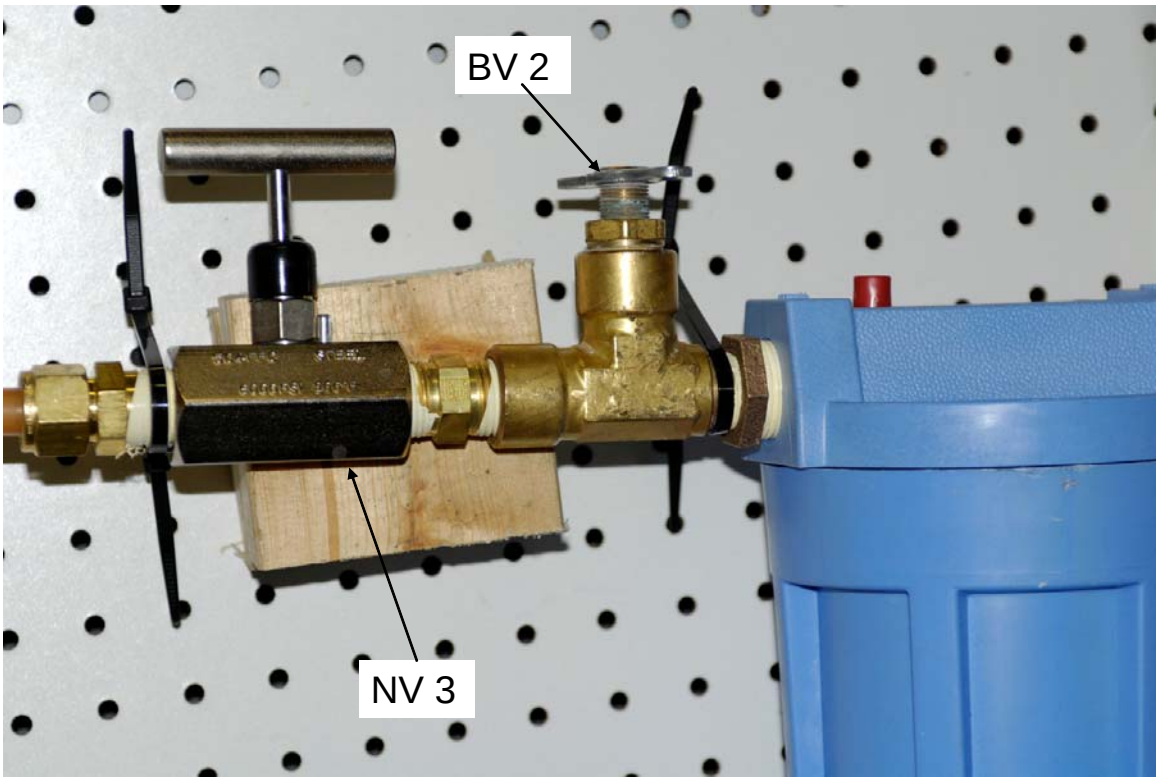

Figure A2.4. Photograph of bleed valve, BV 2.

3. Slowly increase the speed of Pump 1. Allow the pump to run until there are no visible bubbles in the return flow to Bath 1. Be sure that the fluid level in Bath 1 remains at an adequate level. Open valve 5 and allow the pump to run until there are no visible in the return flow to Bath 1. Crack BV 1 to purge any trapped air in the system. A photograph of BV 1 is shown in Figure A2.5.

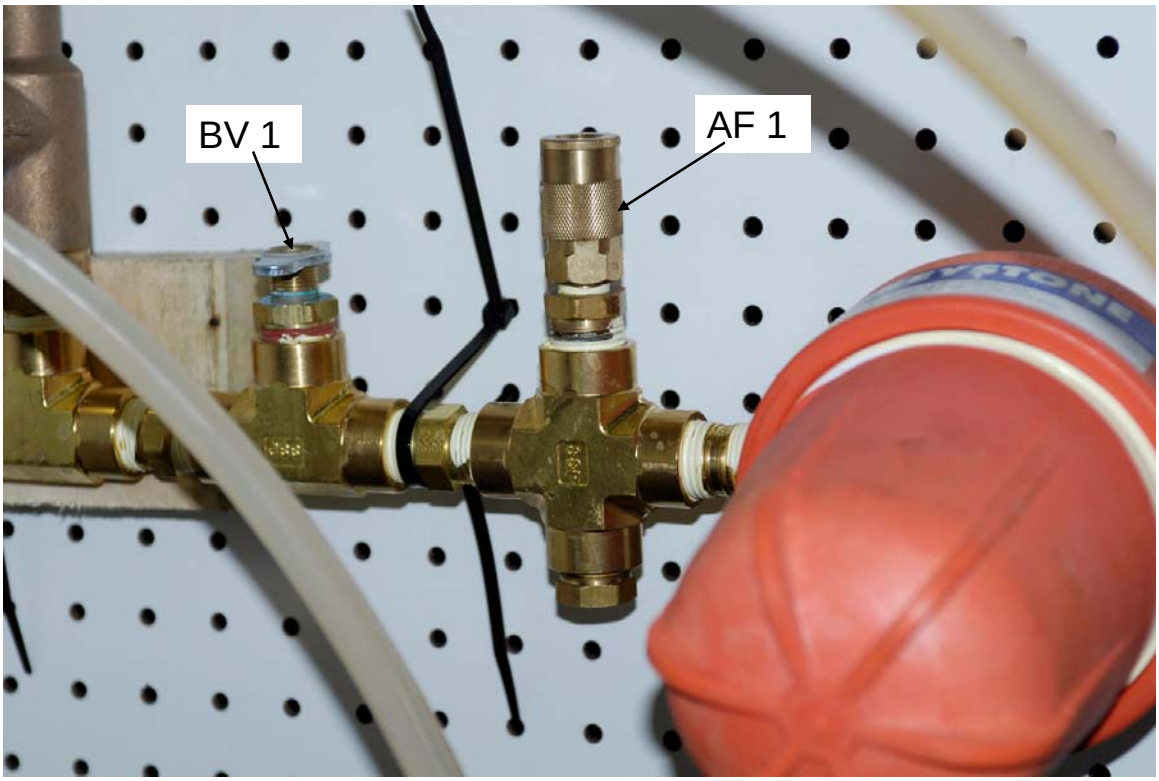

Figure A2.5. Photograph of bleed valve, BV 2.

4. Turn Pump 2 on to a slow flow rate and allow the pump to run. Add fluid to the cold reservoir as needed and be sure not to allow the level to drop below the bottom of the reservoir. Crack BV 2 while the pump is running and allow bubbles to escape. Add fluid to the cold reservoir as necessary. It may be necessary to start and stop the pump several times to purge some of the bubbles. It will likely be necessary to repeat step 3 in order to purge air from the regenerator.
5. Switch Valve 5 to position 2 by energizing the solenoid. Allow Pump 1 to run until there are no visible bubbles in the flow to the graduated cylinder. De-energize the solenoid and increase the pump speed. Switch the solenoid valve on and off several times until no additional bubbles flow out of the regenerator when the solenoid is energized.
6. There is often a bubble that gets trapped near valve 1. One way to purge this bubble is to run pump 1 at a moderate rate and slowly switch the position in valve 1 until the bubble is purged are reduced to a very small size that will not flow into the regenerator.

Emptying the System

If the fluid mixture is to be changed, it is necessary to purge as much of the fluid in the system as possible. All power to the pumps and controlled temperature baths should be off. The following steps should be taken to purge the system:

1. Drain Bath 1. Position the valves as follows:

Valve Name	Position
Valve 1	1
Valve 2	2
Valve 3	2
Valve 4	1
NV 1	closed
BV 1	closed
BV 2	closed
SV	open

2. Reverse polarity to the pump motor so it will pump in the opposite direction. Turn Pump 1 on and allow it to pump fluid from the regenerator and connecting piping into Bath 1. Turn Pump 1 off once fluid ceases to flow into Bath 1.
3. Close the cold reservoir shut-off valve, SV.
4. Apply a regulator hooked to shop air to the quick connect coupling, AF 1, and allow the compressed air to push the fluid out into the graduated cylinder. Move Valve 1 into position 2 and allow the compressed air to purge the fluid into Bath 1. Close Valve 5 and wait until liquid no longer exits into the graduated cylinder. Remove the regulator from AF 1.
5. Move Valve 3 into position 1. Move Valve 2, the solenoid valve, to position 1 by de-energizing it. Apply a regulator hooked to shop air to the quick connect coupling, AF 2, and open the bleeder valve, BV 2. A piece of ¼" tubing can be placed in the outlet of the bleeder valve to reduce fluid spray. Allow the compressed air to push the fluid out the bleeder valve for several minutes. Remember to drain the cold reservoir. This can be done by setting the air pressure to 0 and opening the shut-off valve, SV, to let the fluid drain into the piping. Increase the air pressure again to purge as much of the remaining fluid as possible. Remove the compressed air line from AF 2.
6. Empty the filters for the hot and cold systems. Inspect the filter elements and change them, if necessary.

Setting flow rate through regenerator

The flow rate through the regenerator can be controlled through a combination of varying the speed of pump 1, opening the bypass needle valve (NV1), setting the flow resistance to the regenerator by opening the needle valve upstream of the regenerator (NV2). The flow rate should be set in such a way as to maintain a sufficiently low pressure drop across the system and reduce the flow spike when the solenoid valve is opened. To set the flow rate through the regenerator:

1. Set the speed of pump 1. Generally it should be set to a value of 5 or higher.
2. Set the flow restriction of NV2.
3. Adjust the flow rate to the desired value by opening the bypass needle valve (NV1).
4. De-energize the solenoid valve (Valve 2), allow the system to stabilize, then re-energize it and ensure that the flow rate is still the desired value.

Temperature Soaking the System

Before each test, the system must be thermally soaked to achieve a uniform initial cold temperature in the test section and uniform initial warm temperature in the rest of the system. To thermally soak the system:

1. Before the system is set to cold soak mode, the flow rate through the regenerator must be set to the desired value in order to run the test after the system has been soaked. See above for setting flow rate before beginning the cold soak process.
2. Set the desired temperature of Bath 1 and Bath 2.
3. Set the valves to the following positions. It is generally best to switch the position of Valve 4 first.

Valve Name	**Position**
Valve 1	2
Valve 2	1
Valve 3	1
Valve 4	1
BV 1	closed
BV 2	closed

The valves should now be in the positions shown in Figure A2.6. The flow schematic for cold soak operation is shown in Figure A2.7.

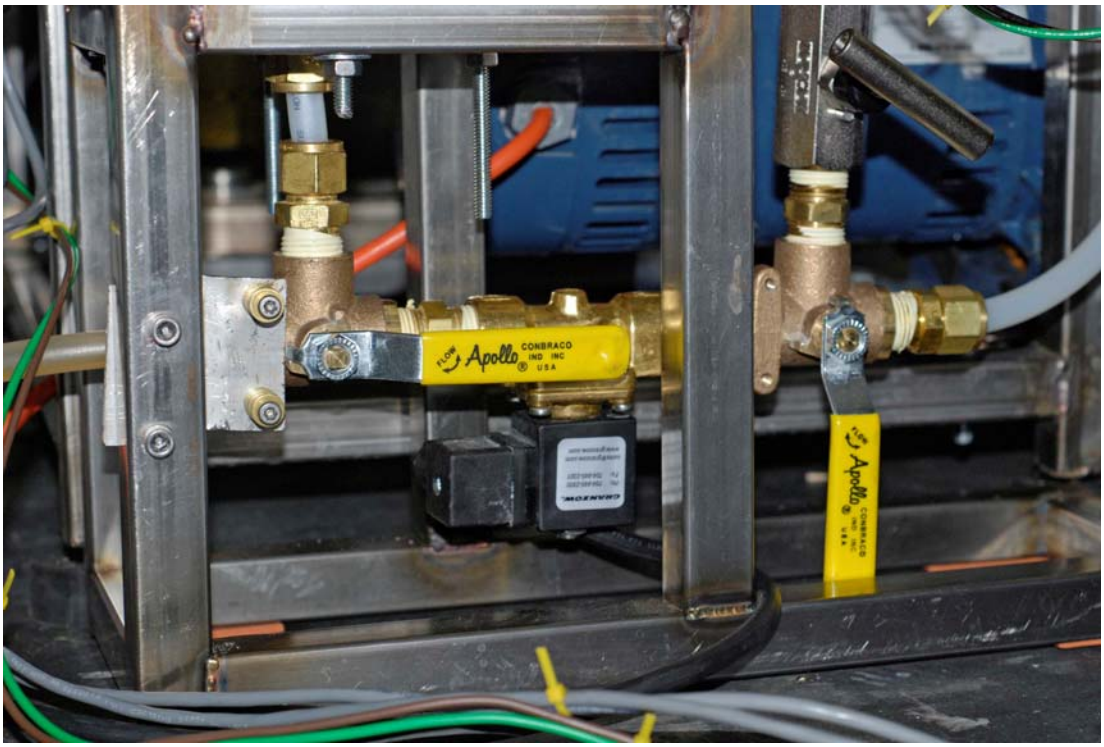

(a)

(b)

Figure A2.6. Photograph of (a) Valves 1 – 3 and (b) Valve 4 during the cold soak operation.

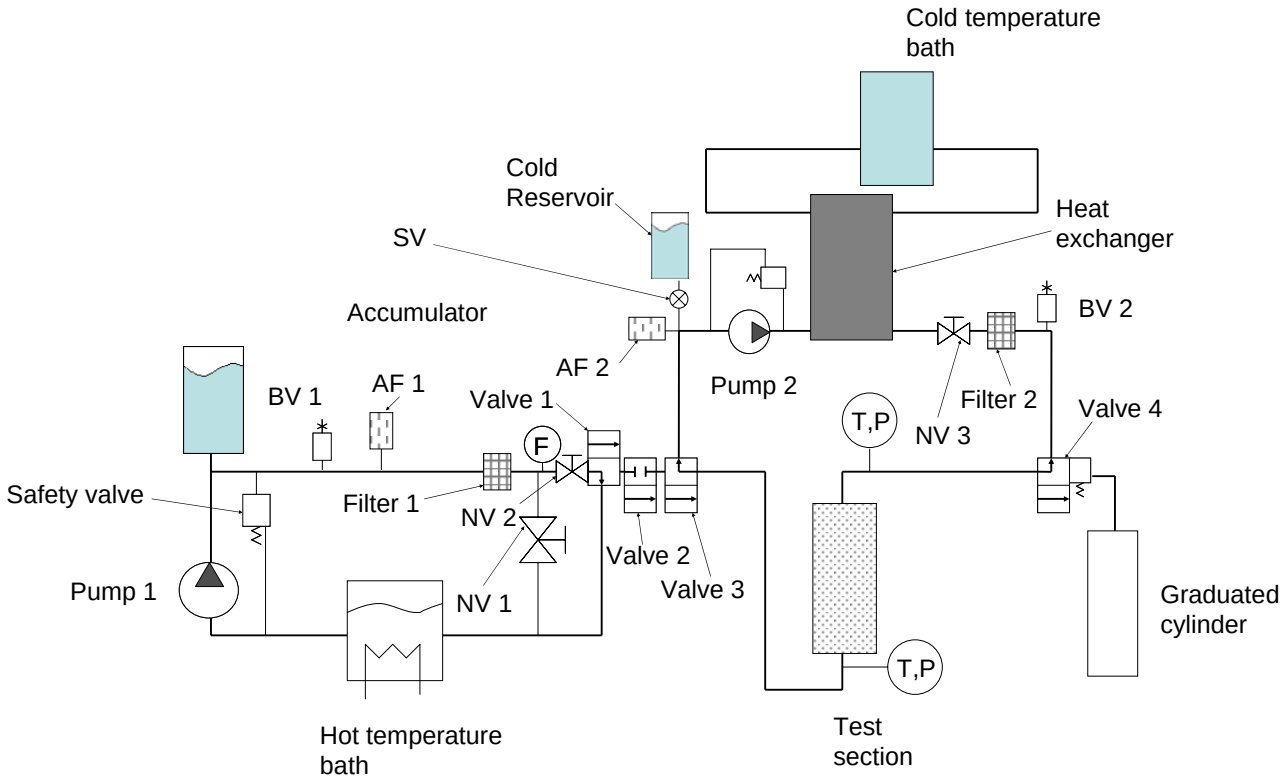

Figure A2.7. System flow schematic cold soak.

4. Turn on Pump 1 and Pump 2 and allow the entire system to reach thermal equilibrium. This will take approximately 15 minutes depending on the temperatures of the hot and cold reservoirs.

Running an Experiment

1. Ensure that Bath 1 and Bath 2 are set to the correct temperatures and that Pump 1 is set to the correct speed. Pump 2 should be turned off. The system should have attained thermal equilibrium in the soak mode and should not have been exposed to ambient temperature for an extended period of time.
2. Before the experiment begins, the valves should be in the following positions.

Valve Name	Position
Valve 1	1
Valve 2	1
Valve 3	2
Valve 4	2
BV 1	closed
BV 2	closed

The valves should be in the positions shown in Figure A2.8. The flow schematic for cold soak operation is shown in Figure A2.9.

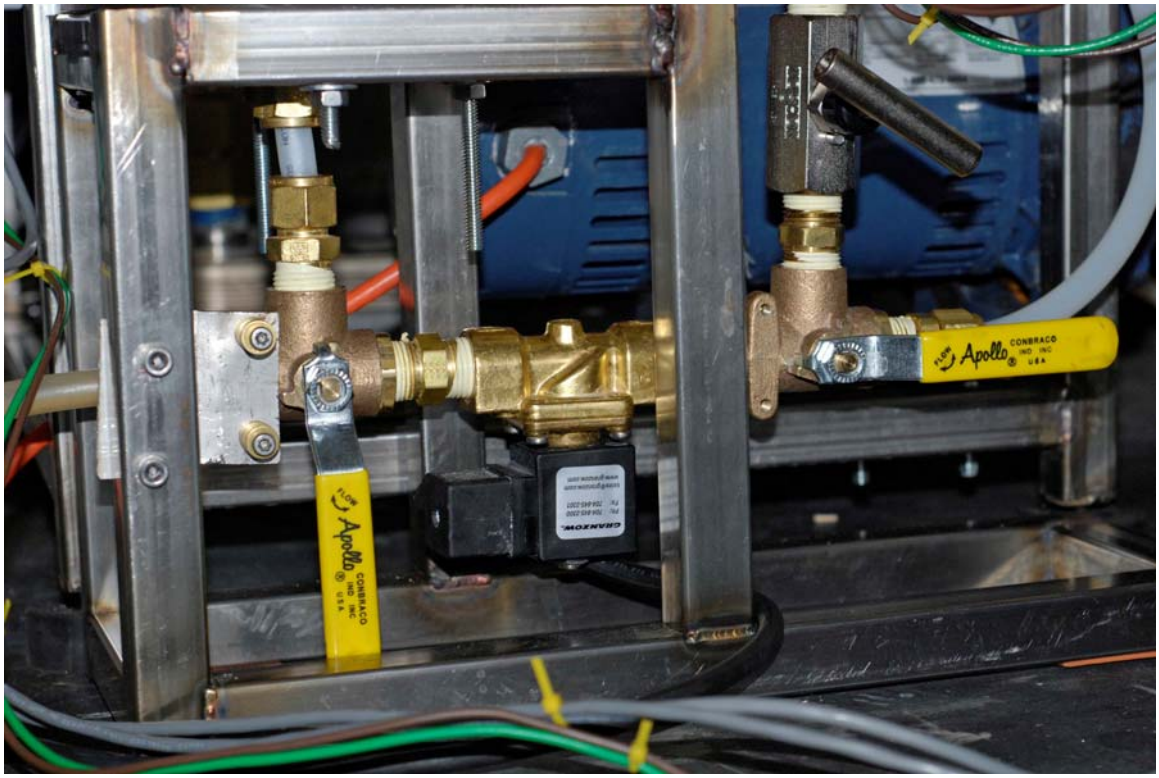

(a)

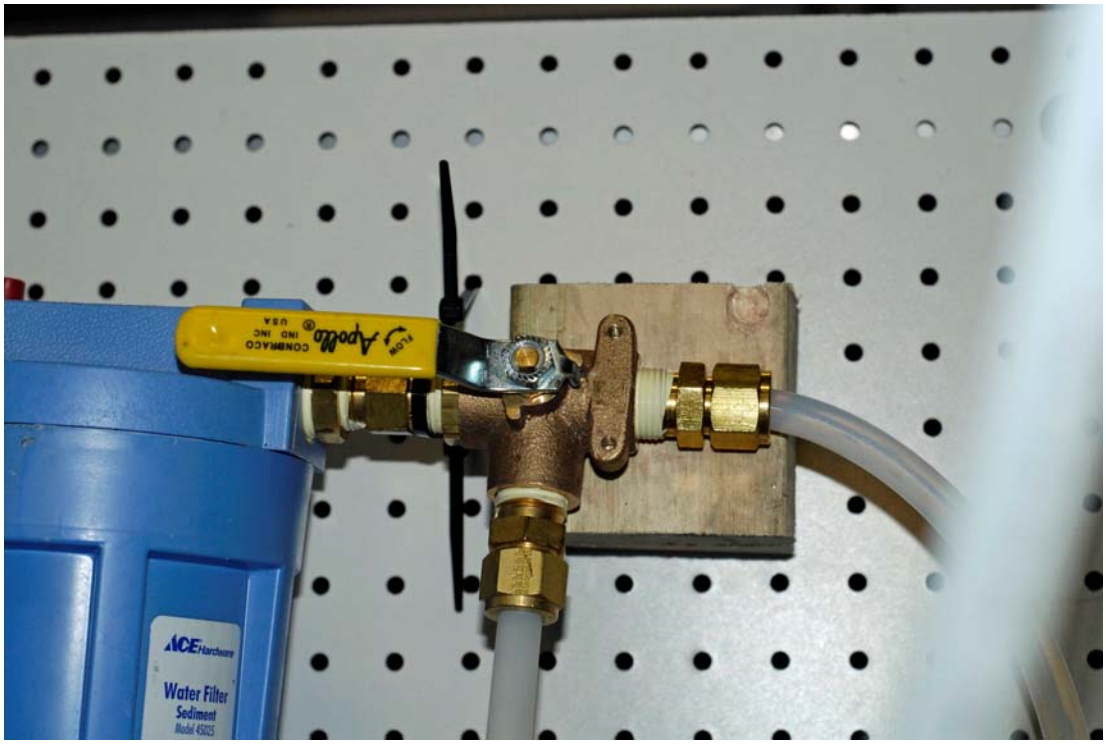

(b)

Figure A2.8. Photograph of (a) Valves 1 – 3 and (b) Valve 4 during an experiment.

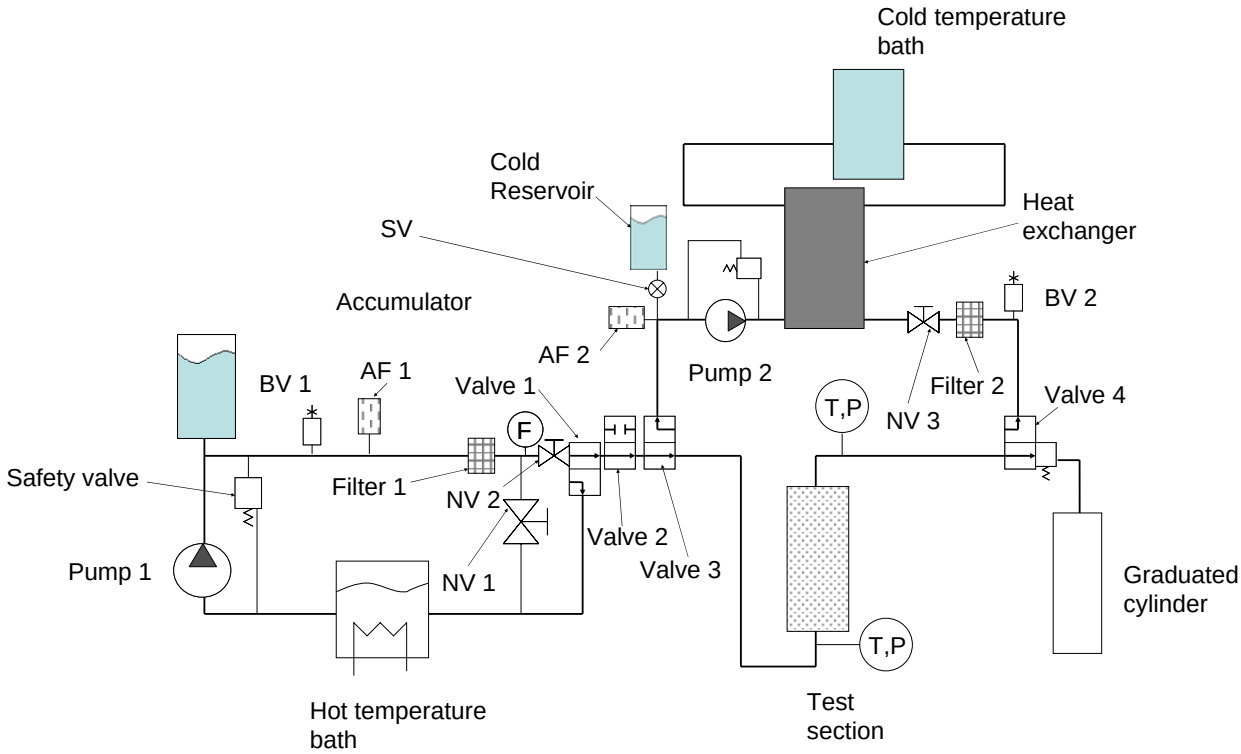

Figure A2.9. System flow schematic during an experiment.

3. Start data collection.
4. The test begins when Valve 2 (the solenoid valve) opens and allows fluid to flow from the pump to the test section.
5. After an appropriate amount of time, switch Valve 2 to Position 1 (closed) to stop the test.
6. Record the amount of fluid collected in the graduated cylinder and transfer the fluid to Bath 1.

Description of System Components

Label	Description	Function
safety valve	adjustable crack pressure check valve	relieve pressure on pump 1 to prevent failure
pump 1	peristaltic pump	pump used during experiment
pump 2	centrifugal pump	cold soak pump
BV 1	bleed valve	purge bubbles from main flow path
BV 2	bleed valve	purge bubbles from the cold soak circuit
AF 1	quick-connect air fitting	purge heat transfer fluid from the main flow loop
AF 2	quick-connect air fitting	purge from the cold soak circuit
Filter 1	water filter	protect flow meter from particulates
Filter 2	water filter	protect the regenerator and the cold soak circuit from particulates from pump 2
NV 1	needle valve	allows fluid to bypass the regenerator during an experiment, which allows for precise flow rate control and can reduce flow spikes when the solenoid valve is opened
NV 2	needle valve	controls the restriction of the regenerator in order to reduce flow spikes when the solenoid valve opens
NV 3	needle valve	controls the restriction of the cold soak circuit, which controls the flow rate through Filter 2 and the regenerator during the cold soak process
Valve 1	3 way valve	controls the direction of flow from pump 1
Valve 2	solenoid valve	is energized to provide a step change in flow across the regenerator
Valve 3	3 way valve	controls flow direction into the regenerator
Valve 4	3 way valve	controls flow direction out of the regenerator
SV	shut-off valve	allows the cold soak circuit reservoir to be shut off from the rest of the system
Heat exchanger	counter-flow heat exchanger	provides thermal communication between the cold temperature bath and the cold soak circuit
Cold reservoir	Reservoir	provides a fluid reservoir for the cold soak circuit and allows the cold soak circuit to be filled independently of the main circuit

Appendix A3 Rotary AMRR Prototype Experimental Results

time	RPM	FMc	Heater	Ppmp	Pci	Tco	Tci	Thi	Tho	Tamb	dT
sec		L/min	W	psi	psi	ºC	ºC	ºC	ºC	ºC	ºC
155.48	15.76	0.50	1.49	19.68	12.45	10.20	10.18	13.42	13.54	22.56	3.24
151.03	240.00	0.33	4.10	9.83	6.58	17.04	17.02	24.83	25.76	26.90	7.81
152.53	239.97	0.35	5.21	11.65	7.81	11.15	11.27	20.24	21.29	25.98	8.97
154.04	14.91	0.50	6.19	18.90	11.94	13.26	13.31	16.16	16.31	24.55	2.85
157.03	15.50	0.50	6.30	17.64	11.12	17.61	17.70	20.88	21.02	24.95	3.18
152.50	119.65	0.35	7.75	10.70	7.05	12.41	12.57	25.06	25.78	26.35	12.48
152.53	239.98	0.34	8.22	10.23	6.74	19.77	19.92	24.83	25.82	26.97	4.91
152.53	60.11	0.34	8.51	10.35	6.75	14.56	14.67	25.19	25.89	26.72	10.52
151.03	119.65	0.33	8.81	11.02	7.28	9.98	10.21	20.52	21.48	25.28	10.31
152.53	60.08	0.34	10.16	11.15	7.26	10.30	10.50	20.70	21.53	24.71	10.20
152.53	240.21	0.49	10.19	17.12	10.98	13.56	13.71	25.44	26.15	27.41	11.73
152.53	239.97	0.34	10.31	10.60	7.26	16.20	16.51	20.22	21.49	25.97	3.72
151.02	240.18	0.50	11.64	19.02	12.13	10.04	10.25	20.85	21.70	26.30	10.60
155.53	239.99	0.34	12.33	9.83	6.56	23.49	23.84	24.81	25.88	26.93	0.97
152.53	120.32	0.49	12.37	16.42	10.42	12.82	13.14	25.57	26.26	26.60	12.43
152.53	60.11	0.52	13.28	17.96	11.35	12.75	12.83	25.08	25.65	26.38	12.24
152.53	20.07	0.51	13.39	20.37	12.55	10.00	10.27	13.44	13.87	22.34	3.17
152.53	120.35	0.51	13.89	18.70	11.75	9.16	9.49	20.95	21.73	25.55	11.47
149.53	240.76	0.68	14.76	26.69	16.79	12.70	12.81	25.58	26.14	27.96	12.77
152.53	119.66	0.34	15.50	10.08	6.70	16.94	17.45	25.04	25.94	26.37	7.58
155.53	239.95	0.35	15.54	10.85	7.08	19.00	19.43	20.27	21.57	25.82	0.84
151.02	60.09	0.51	15.72	18.74	11.77	9.46	9.58	20.45	21.19	24.44	10.88
152.50	240.69	0.68	16.83	28.78	18.08	8.99	9.16	20.87	21.53	26.57	11.71
151.03	60.10	0.34	16.94	9.63	6.38	18.41	18.90	25.26	26.13	26.63	6.37
152.52	119.68	0.67	17.05	26.04	16.11	11.14	11.40	24.67	25.19	26.19	13.27
152.41	119.65	0.35	17.59	11.16	7.36	13.51	14.07	20.54	21.63	25.18	6.47
152.53	60.10	0.67	17.63	25.86	16.02	13.92	14.25	25.70	26.13	26.47	11.46
152.50	239.94	0.82	18.52	35.08	21.46	12.30	12.56	25.32	25.77	27.35	12.75
152.53	20.17	0.51	19.08	19.38	12.19	12.40	12.83	16.13	16.53	24.14	3.31
152.53	119.67	0.66	19.84	26.81	16.63	7.91	8.09	19.86	20.54	25.03	11.77
151.03	240.21	0.50	20.29	16.91	10.87	18.37	18.84	25.44	26.28	27.35	6.60
150.97	60.08	0.33	20.29	10.18	6.68	14.49	15.10	20.67	21.81	24.44	5.57
152.53	120.80	0.81	20.87	34.41	21.06	11.23	11.48	24.81	25.27	25.71	13.33
152.53	60.07	0.67	21.00	27.20	16.88	10.44	10.77	20.93	21.56	25.25	10.16
150.94	60.40	0.81	21.21	34.42	21.07	14.08	14.37	25.23	25.65	26.18	10.87
152.54	239.90	0.80	21.25	36.69	22.73	8.53	8.82	20.59	21.19	25.49	11.77
153.99	240.62	0.50	22.97	20.05	12.83	10.68	11.23	14.01	15.14	24.49	2.78
154.03	29.90	0.50	23.10	19.72	12.26	9.54	10.13	13.40	14.09	22.20	3.26
154.03	119.65	0.34	23.23	9.50	6.36	23.92	24.76	25.09	26.09	26.27	0.33
152.53	240.18	0.51	23.23	18.55	11.84	14.15	14.66	20.86	21.94	26.22	6.20
152.50	20.59	0.49	24.17	17.09	10.72	16.96	17.56	20.84	21.39	25.04	3.28
152.53	120.30	0.49	24.84	15.94	10.04	17.74	18.36	25.53	26.42	26.56	7.17

time	RPM	FMc	Heater	Ppmp	Pci	Tco	Tci	Thi	Tho	Tamb	dT
sec		L/min	W	psi	psi	ºC	ºC	ºC	ºC	ºC	ºC
151.04	120.79	0.80	24.84	35.74	21.96	8.10	8.49	20.12	20.67	24.22	11.63
151.03	60.39	0.82	24.98	36.80	22.38	10.45	10.77	20.52	20.99	24.54	9.75
155.53	60.09	0.34	25.30	9.41	6.22	23.78	24.62	25.23	26.27	26.44	0.61
152.53	40.15	0.50	25.58	19.78	12.40	9.46	10.09	13.37	14.31	22.24	3.28
149.53	159.97	0.50	25.86	19.94	12.80	9.43	10.03	13.33	14.31	22.88	3.29
154.03	119.66	0.35	26.37	10.52	7.00	18.87	19.80	20.67	21.98	25.02	0.86
152.53	60.12	0.50	26.60	16.23	10.20	17.88	18.40	25.09	25.90	26.25	6.69
152.53	240.65	0.50	27.51	19.07	12.19	12.27	12.90	15.91	17.09	24.57	3.01
151.02	60.48	0.50	27.56	19.57	12.23	9.50	10.22	13.37	14.38	22.35	3.15
152.53	119.93	0.50	27.65	19.70	12.04	9.63	10.24	13.24	14.28	22.64	3.00
152.53	120.33	0.51	27.90	17.67	11.17	13.95	14.63	20.88	21.97	25.73	6.25
154.02	240.64	0.52	28.19	18.35	11.68	16.88	17.53	20.73	21.90	26.75	3.20
152.53	80.33	0.51	29.12	19.72	12.29	9.71	10.44	13.29	14.41	22.45	2.86
151.03	240.76	0.67	29.61	25.25	15.87	17.84	18.34	25.59	26.37	27.90	7.25
153.97	159.91	0.50	29.97	18.69	11.65	11.82	12.55	15.81	16.94	24.07	3.25
152.49	30.22	0.51	29.97	19.29	11.98	11.96	12.69	15.99	16.81	23.64	3.30
152.50	240.21	0.51	30.36	16.80	10.83	24.24	24.99	25.52	26.45	27.25	0.53
153.98	60.07	0.34	30.42	10.12	6.62	19.55	20.62	20.77	22.08	24.21	0.15
151.03	60.09	0.51	31.38	17.83	11.19	13.84	14.44	20.55	21.58	24.42	6.10
152.53	120.38	0.49	32.94	18.20	11.52	12.02	12.85	15.87	17.03	23.98	3.02
153.99	160.13	0.49	32.99	16.95	10.88	16.77	17.62	20.77	21.96	26.15	3.15
152.53	240.69	0.68	33.46	27.29	17.19	13.65	14.23	20.90	21.89	26.53	6.67
153.97	40.47	0.51	33.62	19.01	11.85	11.91	12.78	15.86	16.95	23.47	3.08
152.54	119.69	0.66	34.20	24.23	14.96	16.39	17.05	24.65	25.41	26.13	7.60
153.98	240.17	0.51	34.69	17.68	11.19	19.69	20.57	20.90	22.13	25.98	0.33
151.03	60.21	0.50	34.96	18.75	11.70	11.74	12.66	15.82	16.86	23.51	3.16
152.53	80.41	0.51	34.96	19.06	11.95	11.59	12.49	15.79	16.90	23.73	3.30
151.03	60.11	0.66	35.23	24.38	15.09	18.40	19.06	25.67	26.36	26.45	6.61
154.03	30.56	0.51	35.89	17.59	10.93	16.55	17.46	20.84	21.78	25.00	3.38
152.53	239.93	0.81	36.99	33.20	21.30	18.12	18.68	25.29	26.00	27.27	6.62
152.53	120.18	0.50	37.11	17.40	10.96	16.88	17.83	20.92	22.15	25.38	3.09
155.52	120.31	0.51	37.21	15.82	9.97	24.50	25.46	25.59	26.61	26.45	0.14
152.53	40.48	0.50	39.19	17.33	10.81	16.67	17.67	20.81	21.93	25.03	3.14
152.53	59.89	0.50	39.20	17.13	10.74	16.65	17.67	20.87	22.05	25.08	3.20
152.52	119.66	0.67	39.65	26.09	16.17	12.67	13.19	19.95	20.98	24.90	6.76
152.53	80.20	0.51	39.71	17.46	11.12	16.85	17.87	20.88	22.05	25.09	3.00
152.53	60.11	0.51	39.94	16.15	10.12	23.88	24.80	25.18	26.17	25.97	0.38
152.52	120.80	0.81	41.69	32.91	20.13	16.12	16.77	24.83	25.56	25.61	8.06
154.03	120.34	0.51	41.81	16.91	10.71	19.65	20.71	20.94	22.20	25.86	0.22
152.53	60.08	0.67	41.87	26.16	15.81	14.38	15.15	20.95	21.90	25.29	5.80
151.02	60.40	0.81	42.40	33.08	20.18	18.41	19.11	25.26	25.95	26.11	6.15
152.51	239.90	0.82	42.64	36.41	22.39	13.05	13.71	20.66	21.50	25.51	6.94
154.03	240.73	0.67	44.33	24.60	15.47	24.28	25.12	25.58	26.53	27.69	0.46
154.03	60.10	0.51	47.06	16.99	10.72	19.06	20.13	20.60	21.88	24.16	0.47
152.53	120.79	0.80	49.60	33.76	20.68	12.88	13.70	20.16	21.06	24.32	6.46
152.54	60.40	0.79	49.91	33.81	20.55	14.20	15.04	20.58	21.44	24.59	5.53

time	RPM	FMc	Heater	Ppmp	Pci	Tco	Tci	Thi	Tho	Tamb	dT
sec		L/min	W	psi	psi	ºC	ºC	ºC	ºC	ºC	ºC
155.53	240.66	0.68	50.17	26.24	16.44	19.11	20.07	20.90	22.11	26.41	0.83
152.53	119.68	0.68	51.28	24.22	14.99	23.46	24.52	24.68	25.64	26.01	0.16
156.99	60.09	0.67	52.80	23.59	14.69	24.34	25.44	25.70	26.60	26.31	0.26
154.03	239.95	0.81	55.48	32.52	20.15	24.21	25.13	25.29	26.20	26.96	0.16
155.53	119.66	0.67	59.37	25.12	15.57	18.60	19.53	20.01	21.32	24.60	0.48
152.53	120.79	0.80	62.51	31.15	19.11	23.64	24.74	24.82	25.80	25.31	0.08
157.03	60.09	0.67	62.80	25.14	15.63	19.47	20.73	20.98	22.21	25.31	0.25
154.03	60.42	0.81	63.52	32.03	19.34	23.94	25.08	25.29	26.20	25.92	0.22
154.03	239.85	0.80	63.82	33.33	20.51	19.54	20.61	20.69	21.84	25.30	0.09
155.48	120.78	0.82	74.30	33.82	20.65	18.50	19.78	20.14	21.31	24.23	0.37
155.53	60.44	0.81	74.93	33.96	20.57	18.84	20.16	20.65	21.82	24.54	0.48